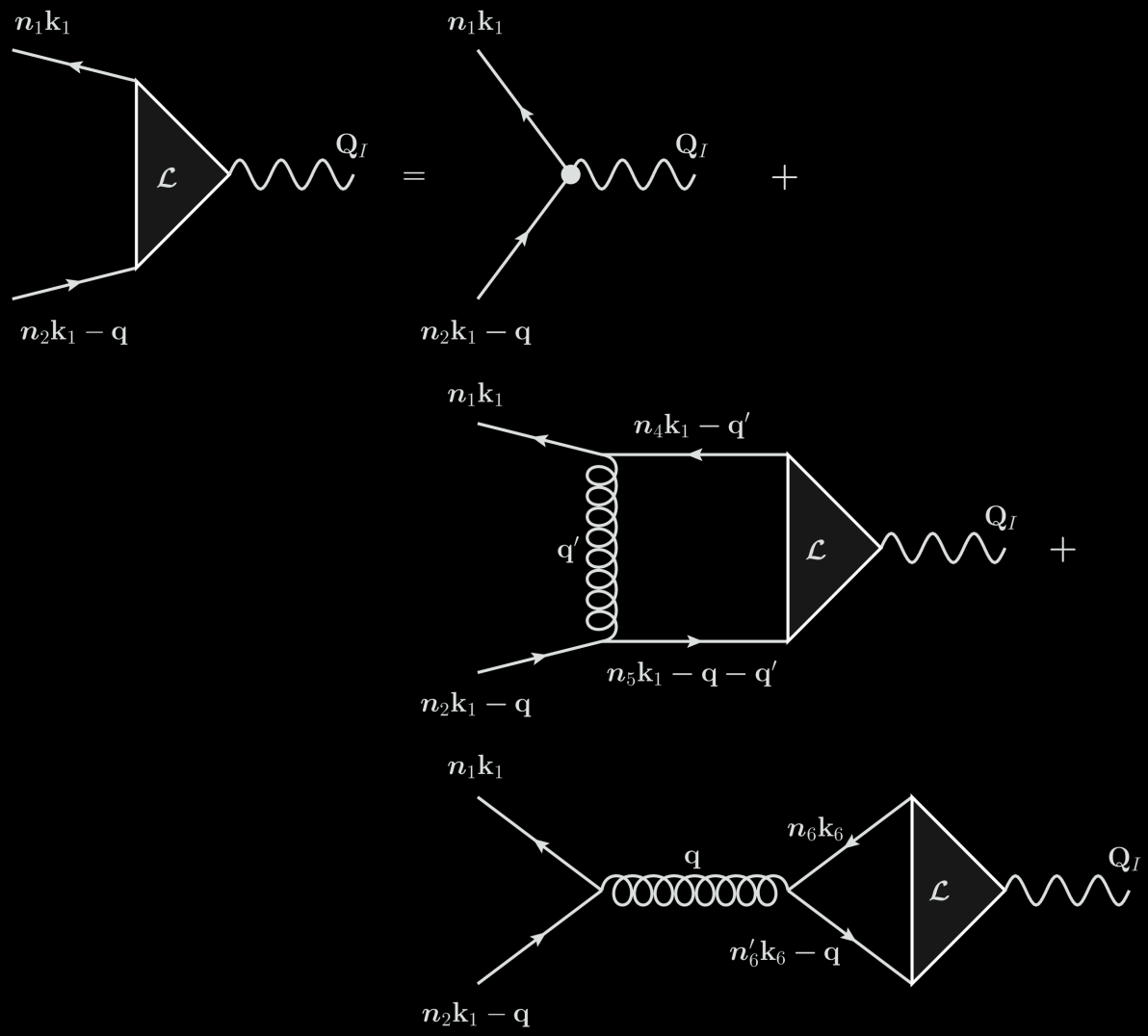

Pedro Miguel Monteiro Campos de Melo

AB-INITIO APPROACH TO PHOTOLUMINESCENCE BASED ON GREEN'S FUNCTION THEORY

Tese de Doutoramento em Física, ramo de Física da Matéria Condensada, orientada pelo Dr. Andrea Marini e pela Drª. Myrta Grüning e apresentada ao Departamento de Física da Faculdade de Ciências e Tecnologia da Universidade de Coimbra

Maio de 2017

· U C ·

Universidade de Coimbra

· U C ·

Ab-initio approach to photoluminescence based on Green's function theory

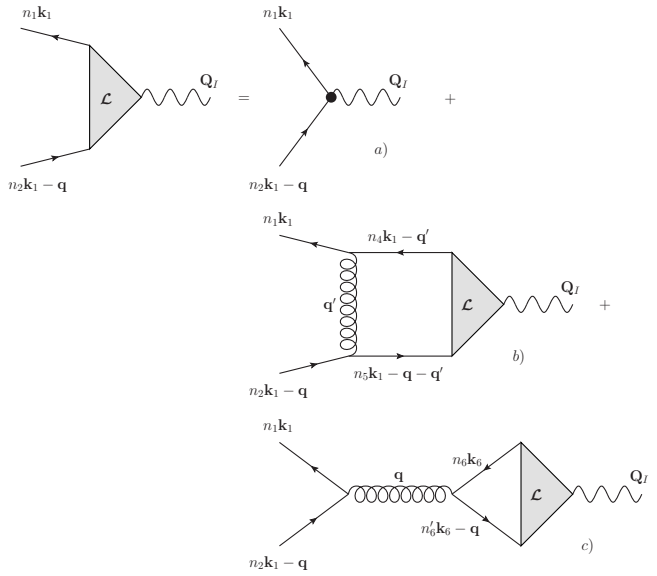

Supervisers: Dr. Andrea Marini and Dr. Myrta Grüning

Pedro Miguel Monteiro Campos de Melo

Department of Physics

Faculty of Sciences and Technology

University of Coimbra

May 2017

Declaration

This work was funded by the UE/FEDER, through Programa Operacional Factores de Competitividade - COMPETE and by National Funds through FCT - Fundação ao para a Ciência e Tecnologia, by Grant No. SFRH/BD/84032/2012.

“Only in silence the word,

Only in dark the light,

Only in dying life:

Bright the hawk’s flight

On the empty sky.

-The Creation of Éa”

Ursula K. Le Guin, *A Wizard of Earthsea*

Acknowledgements

It seems that the complexity of a given task increases the number of people to whom you are thankful. As the full list would be too large, below I would like to thank the "eigenvectors" with the highest contributions to the spectrum that is this thesis.

To my adviser Dr. Andrea Marini, the one true king of YAMBO. I do not think there is enough room to thank you, since not only this project would not be possible without you, but also because your patience (or sometimes the lack of it), your almost infinite energy, and your constant drive to achieve results were instrumental to its completion. I truly hope that my experience with you has made me a better scientist.

To my other adviser Dr. Myrta Grüning, to whom this thesis owns its existence and present form. Even though you were far away, you always kept interested in my work and I could always count upon your help and advice.

To Davide Sangalli, not only for the help with the great wondrous beast that is YAMBO, but also for the many discussions about almost everything ranging from Physics, Maths, and everyday life. Your companionship as a housemate more than made up for you innate ability to get us lost and for being quite possibly the worst Italian teacher I have ever had.

To Alejandro Molina-Sanchez for his help with the numerical calculations. I thank as well the Theoretical Solid-State Physics Group group from the Physics and Materials Science Research Unit of the University of Luxembourg, for their welcoming and support during my short stays with them. Special thanks go to the developers of Yambopy, Henrique,

Alejandro, Fulvio, and Alexandre. Without it, managing and submitting tasks to supercomputers would be a rather more tedious task.

To Fernando Nogueira who first introduced me to the world of Density Functional Theory and Many-body Perturbation Theory. Although you had no idea of the creature you were about to unleash, I have to say that this has been a fascinating trip through the world of theoretical and computational Solid State Physics.

A Francesco, Paola e Giuseppe, per la simpatia e la pazienza dimostrata a questo portoghese che di fatto ha sempre pagato il biglietto su ogni mezzo di trasporto pubblico a Roma.

To my friends in Coimbra and elsewhere for all the time we spent together. Whether or not we should have been working during those periods is a matter for another thesis altogether.

To my family, for everything.

Abstract

In this work we derive a full ab-initio theory for photoluminescence (PL) based on Non-equilibrium Green's function theory (NEGF). We begin from the second quantisation Hamiltonian for the particles which intervene in the dynamics after the system is driven out-of-equilibrium by a laser pulse, considering all possible interactions. Using the functional differentiation technique we arrive at a set of integro-differential equations for the propagators of electrons, phonons, and photons which extends and generalises Hedin's set of equations.

We then recover the Baym-Kadanoff equations (BKE) for the electronic lesser Green's function and show that the interactions which affect the electronic degrees of freedom (electron-electron, electron-phonon, and electron-photon) can be reduced to a GW like self-energy. We treat the coherent scattering terms responsible for the elemental excitations within the Coulomb-hole Screened-Exchange (COHSEX) approximation. We simplify the functional dependence of dynamical scattering terms and remove contributions from memory effects by applying the Generalised Baym-Kadanoff ansatz and the Completed collision approximation. We further simplify the BKE by introducing the Low-intensity approximation which assumes that a low density of excited carriers is created by the laser pump during experimental measurements. This leads to the recovering of the Boltzman limit of the BKE but with time-dependent lifetimes for each decay channel.

Next we connect the macroscopic measured quantity-the divergence of the Poynting vector-with the functions which contain the information on the microscopic interaction. For this we derive the Bethe-Salpeter equation for the electron-photon correlation by performing the analytic

continuation to the real axis using Langreth's theorem. Within the COHSEX approximation we obtain the pair-photon lesser and greater correlation function in a matrix form and analyse the pole structure of the correlation function. This allowed us to select the contributions to the emission spectrum.

Finally we implement this approach in YAMBO and apply it to PL in monolayer hBN and WS_2. Within the Tamm-Dancoff and the non-interacting particle approximations, the spectra obtained properly describe the dynamics of the systems when changing the frequency and duration of the laser pump and the temperature of the sample. For WS_2 we predict a Stokes shift of at most 0.03 eV and obtain the position of the emission peak within 0.1-0.2 eV of the reported experimental values.

Resumo

Neste trabalho apresentamos a derivação de uma teoria de primeiros princípios baseada no formalismo de funções de Green fora do equilíbrio para a fotoluminescência (PL). Começamos com a segunda quantização no Hamiltoniano de todas as partículas que intervêm na dinâmica do sistema após este ser levado para um estado excitado por um laser, e considerando todas as interações possíveis. Através da técnica da diferenciação funcional chegamos a um sistema de equações integro-diferenciais para os propagadores de electrões, fonões e fotões, que extende e generaliza o sistema de equações de Hedin.

A seguir, recuperamos a equação de Kadanoff-Baym (BKE) para a função de Green eléctrica "menor" e provamos que as interacções que afectam os graus de liberdade dos electrões (electrão-electrão, electrão-fonão, electrão-fotão) podem ser descritas a uma energia-própria do tipo GW. Os termos coerentes de dispersão, que são responsáveis pelas excitações elementares, são tratados ao nível da aproximação Coulomb-hole Screened-Exchange (COHSEX). A dependência funcional dos termos de dispersão dinâmica é simplificada e os efeitos de memória são removidos, através da aplicação do ansatz generalizado de Baym-Kadanoff e da aproximação de Colisões Completas. A simplificação da BKE é levada adiante com a introdução da aproximação de baixa intensidade, o que pressupõe que uma baixa densidade de transportadores excitados é criada pelo laser durante as medições experimentais. Isto permite-nos recuperar a equação de Bolztman, mas agora com constantes de decaimento dependentes do tempo para cada fenómeno de dissipação.

Depois fazemos a conexão entre a quantidade macroscópica que é medida - a divergência do vector de Poynting - e as funções que contêm

a informação sobre as interacções ao nível microscópico. Para este fim derivamos a equação de Bethe-Salpeter para o caso da correlação entre electrões e fotões, utilizando a continuação analítica e o teorema de Langreth, que nos permitem passar do plano imaginário para o eixo real temporal. As funções maior e menor de correlação par-fotão são obtidas, dentro da aproximação COHSEX, e reduzidas a uma forma matricial. Estas matrizes são depois usadas para analisar as propriedades analíticas das funções de correlação, o que nos permite seleccionar as contribuições para o espectro de emissão.

No fim, implementamos este formalismo no YAMBO e usamo-lo para obter o espectro de PL em camadas isoladas de hBN e WS_2. No limite das aproximações de Tamm-Dancoff e de partículas não interactuantes, os espectros obtidos descrevem correctamente a dinâmica do sistema consoante a energia e duração do laser e da temperatura da amostra. Prevemos para o WS_2 um desvio de Stokes até os 0.03 eV e obtemos para a posição do pico de emissão valores que se encontram entre 0.1 a 0.2 eV afastados dos valores encontrados na literatura experimental.

Contents

CONTENTS

Chapter 1

Introduction

"Begin at the beginning," the King said, very gravely, "and go on till you come to the end: then stop."

Lewis Carrol, *Alice in Wonderland*

1.1 Photoluminescence

Luminescence is the spontaneous emission of radiation by a system after excitation from an external source. Depending on the source which drove the system out of equilibrium we get different designations for the emission of light: thermoluminescence, if it is caused by heating the system; chemiluminescence, if it is due to a chemical reaction; and so on. For the specific case where the excitation is caused by photo-absorption (electromagnetic radiation) the process is called photoluminescence (PL).

Photoluminescence and has a wide range of technological applications, such as the use of luminescent molecules as markers in *in vivo* imagining techniques. In Fig. 1.1 we can see an example of such a molecule, toluene, where different solutions are irradiated with UV light. In the every-day life, materials which have luminescent properties can be used for lightning or in screens.

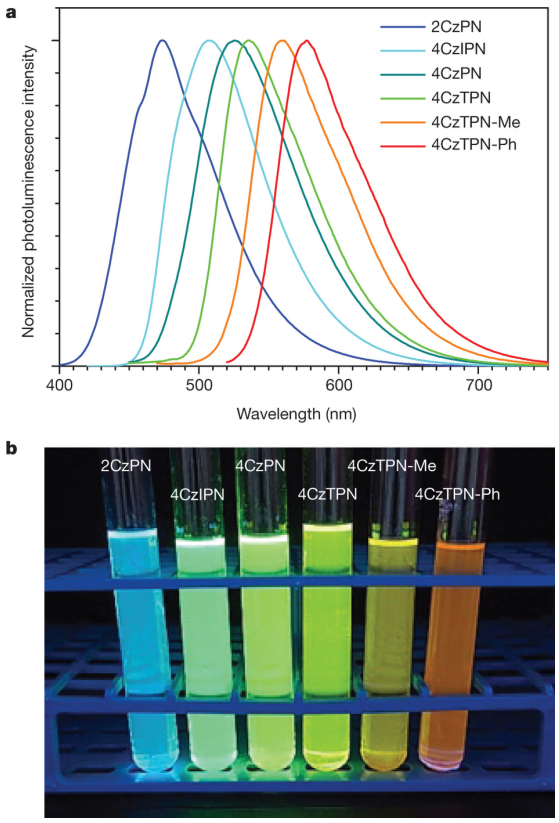

Figure 1.1: a) Photoluminescence spectra measured in toluene. b) Photograph under irradiation at 365 nm [1].

Biological and technological applications of photoluminescence are dependent on the possibility of tuning or increasing the frequency of the emitted light. This inevitably requires a deep knowledge of the complex interplay of the dynamics after excitation by electromagnetic radiation. If we are interested in simulating a photo-luminescent material, a possible way to do so is through *ab-initio* computational electronic structure methods, which have already demonstrated their usefulness in quantitative predictions without the need of external *ad-hoc* parameters.

We can also wish to study luminescent system with potential technological applications in the laboratory. Through spectroscopic techniques we can obtain a wide range of information about the interplay of dynamical processes which occur in the system before and during light emission. Various sophisticated methods allow us to study different properties of a given material after it has been irradiated

by light. Three commonly used techniques and what they allow us to study are, for instance:

- Time-resolved photoluminescence (TR-PL) - recombination kinetics, surface recombination, transport dynamics;
- Spatial-resolved photoluminescence (SR-PL) - inhomogeneities and transport properties;
- Time-spatial-resolved photoluminescence (TSR-PL) - carrier transport dynamics.

In this work we will be focusing on the theoretical description and simulation of TR-PL experiments, which are often carried out using a pump and probe laser fields.

1.2 Pump and Probe experiments and Photoluminescence

The impressive progress in ultrafast and ultrastrong laser-pulse technology has paved the way to non-equilibrium (NEQ) femtosecond spectroscopies [2–6]. Unlike conventional spectroscopies, the sample is driven away from equilibrium by a strong laser pulse (the pump) and then probed with a weaker field (the probe). This second field is used to monitor a wealth of physical properties of the material in order to disclose the complex properties of the excited system trough the different phases of the real-time evolution [7, 8]. Indeed, experiments are carried out using pump pulses with frequency in the infrared-ultraviolet range and ultrashort probe pulses (down to a few hundreds of attoseconds). By varying the delay between the pump and the probe pulses one can monitor the excited-state dynamics in a wide range of energies and time scales.

In Fig. 1.2 we can see a schematic representation of the elemental processes which are induced by the perturbation with a strong[1] laser field. There, an ex-

[1] This is a relative term. Usually experiments are carried out with lasers whose intensity is much lower than the one needed to destroy the electronic structure of the material, but is still capable of creating a population of excited particles which is around 10% to 20% of the total population of particles in the material.

ternal laser pulse first excites a certain density of carriers from the valence to the conduction bands. The duration of this process is directly controlled by the duration of the laser field. In addition, the density of carriers is dictated by the intensity of the laser that also controls the amount of energy transferred to electrons and holes [7–13].

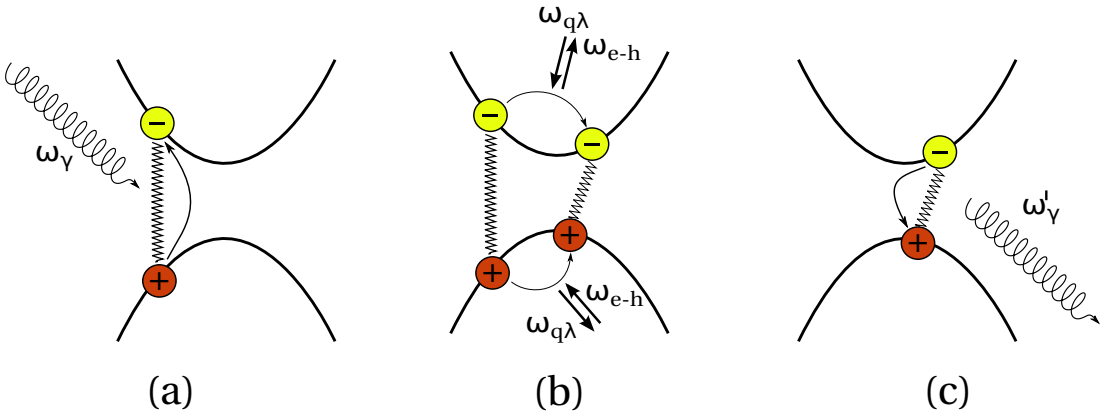

Figure 1.2: Schematic representation of the different processes induced by the interaction of a material with a short and intense laser pulse. The action of the laser creates electron-hole pairs [process (a)]. These pairs interact trough the screened Coulomb interaction (zig-zag line) creating transient excitonic states. After the photo-excitation the carriers undergo repeated collisions with other carriers and with the lattice [process (b)]. During these processes phonons and electron-hole pairs are emitted and/or absorbed. Finally, after pico to microseconds, the excited carriers eventually relax to the ground state emitting photons [process (c)]. ω_γ and ω'_γ are photon energies, $\omega_{\mathbf{q}\lambda}$ is a phonon energy, and $\omega_{\mathrm{e-h}}$ represents and electron-hole pair energy.

Already during this first step static and coherent correlation effects play a crucial role. As an example, it is well known that the absorption of light is accompanied by the formation of excitonic states [14], i.e., bound electron-hole pairs created by the initial laser excitation. Nevertheless, at this stage the quantisation of the electromagnetic field is not necessary and indeed, in studying simple optical absorption the simpler classic treatment is commonly adopted [14, 15].

After the photo-excitation (panel b)) the carriers will relax by dissipating and transferring energy among themselves and to the lattice. During this first step of the dynamics (which can be as long as few pico-seconds) the ensemble of electrons interact via repeated collisions mediated by the Coulomb (e-e) and the electron-

phonon (e-p) interactions. Indeed, the complex interaction of the carriers with the lattice imposes the quantisation of the atomic oscillations in the form of phonon modes. These then enter naturally in the dynamics and must be included in a coherent framework together with the excitonic effects.

The last step in the dynamics (panel c)) of the photo-excited carriers is the recombination with the consequent spontaneous light emission, which requires the quantisation of the electromagnetic field. As a consequence, it is evident that a comprehensive description of all phases of the dynamics following a photo-excitation event require the simultaneous quantistic treatment of electron, phonons and photons. This is well beyond the state-of-the art and it represents one of the goals of the present work.

In a typical pump and probe experiment (P&p), a weaker and perturbative second laser pulse is used to probe the system at any time between the processes (a) and (c) of Fig. 1.2. A wealth of time-dependent observables are then measured experimentally, such as: the change in the absorption of the probe induced by the pump (transient absorption) [16–18]; the time-dependent light emission spectrum [19]; and the time-dependent photo-electron spectrum [20, 21].

We should point out that in a real material the situation is rather more complex. The presence of impurities, bound excitons, defects, for example, can result in the quenching of peaks in the spectrum, as new non-radiative channels are open to the electrons, and give rise to additional peaks, since electron-hole pairs will have access to extra recombination channels.

1.3 Theoretical state of the art

1.3.1 Ground state theories

The most up-to-date scheme to calculate and predict the ground- and excited-state properties of a wide range of materials is based on the merging of Density-Functional-Theory (DFT) [23] with Many-Body Perturbation Theory (MBPT) [14]. DFT is a broadly used *ab-initio* ground-state theory, that allows us to quickly and accurately compute the electronic density and total energy without adjustable parameters, for a wide range of materials. The application of standard perturbation theory to DFT gives the so-called Density-Functional Perturbation Theory

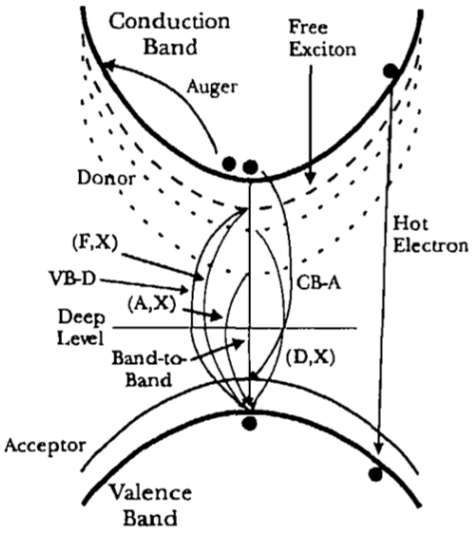

Figure 1.3: Illustrative scheme for possible radiative recombination processes in a real material [22].

(DFPT) [24, 25]. DFPT is a powerful computational tool for the direct treatment of phonons. However, the DFT computation of excited electronic states properties, like band-gap energies, remains out of reach for the formalism [23], as it is a ground state theory. As a result, MBPT is often a preferred alternative to DFT for that purpose. It is based on the accurate treatment of correlation effects by means of the Green's function formalism. MBPT is formally correct and leads to a close agreement with experiment [26], but is extremely computationally demanding. A natural way to solve this issue is to merge the quick DFT calculation with the accurate MBPT one. This method is often referred to as *ab-initio* Many-Body Perturbation Theory (*ai*-MBPT) [14]. In this method, DFT provides a suitable single-particle basis for the MBPT scheme, facilitating the study of realistic systems starting from their atomic structure rather than having to recur to models. This method has been applied successfully, for example, to correct the well-known band-gap underestimation problem of DFT [27].

Therefore, as far as equilibrium properties are concerned, the theoretical and methodological developments have constantly contributed to create a consistent and efficient framework that can now count on a number of well established standards and codes.

1.3.2 Out-of-equilibrium theories

The situation in the out-of-equilibrium case is rather different. Indeed the standard tools of equilibrium MBPT cannot be applied and one has to switch to more advanced non-equilibrium Green's function (NEGF) techniques. From a purely theoretical point of view the NEGF theory has been extensively studied and reviewed in many books [10–13]. Nevertheless its development has been mainly confined to simple models or specific models suitable to interpret specific properties. A merging with DFT, in the NEGF case, is still at the very beginning and an inclusive approach is lacking. As a main consequence there are few standard numerical tools which can be used even by non-experts or experimentalists to support their observations. This is one of the main motivations of the present work.

The NEGF theory is indeed, as far as the electron-electron (e-e) interaction is concerned, at an excellent level of development. By using the Keldysh contour formalism [28] we can obtain the Baym-Kadanoff equations (BKE) that govern the electronic motion. The fundamental ingredient of the BKE is the self-energy, which embodies all the information on the many-particle interaction. The self-energy can be calculated from single-particle quantities [28]. The BKE can also be reduced to a Boltzmann-like equation in the Markovian limit [28].

The e-p interaction has been widely studied both at equilibrium and out-of-equilibrium. In equilibrium the MBPT approach has been applied and reviewed in Ref. [29]. In this case the nuclear effects are included by deriving a full set of self-consistent equations for the screened interaction and the self-energy operator. Also the merging of MBPT and DFT has been studied [30, 31] and applied [32–36]. In the out-of-equilibrium case the theory is well known as well and it leads to a combined description of both the electronic and phononic dynamics [11, 37, 38]. In this case the merging with DFT has been only very recently introduced within the simplified Markovian limit [39] or in the more general scheme based on the Generalised Baym-Kadanoff ansatz (GBKA) and on the Completed Collision approximation (CCA) [21, 40].

It is crucial to note, at this point, that in all the above cases the electron-photon (e-γ) interaction is neglected and the electromagnetic interaction is treated

classically. This approach is suitable unless we are not interested in the long-time carrier dynamics and in the transient light emission spectrum.

Another family of theoretical studies is connected to the bridging of the very general theories based on the NEGF with the actual experiments that are performed in a typical P&p setup.

The case of the carrier dynamics is the most natural and easy to introduce as it is a simple by-product of the BKE. Once that GBKA and the CCA are applied the equation of motion for the electronic occupations is obtained [21, 37–40].

The time-resolved light absorption of the probe field has been studied within the NEGF formalism in Ref. [41]. Starting from the BKE and introducing an adiabatic approximation, an equation of motion for the linear response function is derived and shown to reduce to the well-known Bethe-Salpeter Equation (BSE) in the absence of the pump field or when this is weak enough to be possible to apply the low-intensity regime approximation (LIA). Both the LIA and the adiabatic ansatz will be introduced and extensively used in this work.

In order to study photoluminescence (PL) the inclusion of the e-e and e-p interactions is not enough. Indeed light emission is possible only when also the electromagnetic field is quantised and it appears as a evolving term in the BKE. As in the e-e and e-p cases also the inclusion of the e-γ interaction has been studied [42–44]. In those works the theory is bridged with the BSE but the e-p interaction, and therefore the photo-excited carriers relaxation, is neglected. Alternatively e-p interaction has been included [43, 45, 46] but, in that case, neglecting the e-e interaction and, therefore, the formation of excitonic states.

A field that has been developed in parallel to MBPT is the one based on time-dependent DFT (TD-DFT). Here the most used tool is the time-dependent Kohn-Sham equation [23] that has been applied to study out-of-equilibrium regimes [47, 48]. TD-DFT provides an alternative and powerful tool where, however, the description of e-e and e-p interactions is quite problematic. Indeed, TD-DFT has been mainly applied to low-dimensional systems [49] or to study very short-time effects [50] where relaxation, dissipation and formation of excitonic states can be, within specific approximations, neglected. Quantised electromagnetic fields have also been recently introduced within DFT [51].

1.4 Main goals and work outline

The main goal of this work is to derive from NEGF a theoretical framework with which we can treat PL and connect it with a feasible first principles computational approach. In order to do so, we must begin by creating a complete theoretical framework which describes in a quantistic way the dynamics of electrons, phonons, and photons and the interactions between them. Following that, we must focus on deriving a connection between the PL spectrum and the quantities which contain information on the dynamics of the excited system. Once that is accomplished, the necessary equations should be implemented in the code YAMBO [52] and then tested in a set of materials under different excitation conditions in order to confirm the validity of what was implemented in the code and the equations which were derived.

In this chapter we have introduced the basic concepts of photoluminescence and the basics of an TR-PL experiment used to study this phenomena. We have also discussed the essencial processes involved in a P&p experiment and the state of the art at which their description is currently.

In chapter 2 we lay down the theoretical foundations which support this work within th Keldysh contour formalism. We arrive at an extension of Hedin's set of equations which includes the functions associated with photons and phonons.

In chapter 3 we obtain the Baym-Kadanoff equation for the electronic density. With the simplifications introduced by the GBKA and the CCA we are able to derive a closed set of equations for the reducible electronic polarisation and the transverse polarisation function.

In order to compute the PL signal, we study in chapter 4 expected pole structure of the emission spectrum within the non-interacting particle approximation and the excitonic picture of the Bethe-Salpeter equation (BSE). Using these results, we derive in chapter 5 the connection between the divergence of the Poynting vector and the density-density correlation function.

The resulting equations have been implemented in the code YAMBO. In order to test the code and the equations, we have performed a series of tests on two monolayers, hexagonal Boron-nitride (hBN) and tungsten disulphide (WS_2). These results are presented in chapter 6.

We present the main conclusions of this work in chapter 7. Also, in the appendices we present complementary information about the (TD)-DFT, MBPT and NEGF theories (see Appendix A), some conventions on linear algebra which are used in chapter 2 (see Appendix C). We also show the main arguments behind the merging between DFT and MBPT in Appendix B, and in Appendix D we describe the technical details for the inversion algorithms needed to compute the PL spectrum coming from the BSE.

1.5 Note on the content

Some of the work presented in this thesis, aside some modifications and corrections, has already been published in Ref [53]. Namely Sections 1.2 and 1.3, Chapters 2 and 3, and Appendices B and C.

Chapter 2

Propagators and response functions on the Keldysh contour

"It's no use going back to yesterday, because I was a different person then."

Lewis Carroll, *Alice in Wonderland*

2.1 The quantisation of electrons, nuclei, and photons

We start with the non relativistic Hamiltonian of a system of interacting electrons moving under the action of an external electromagnetic field and of the internal electron-nucleus interaction:

$$\hat{H} = \hat{H}_0 + \hat{H}_{\mathrm{int}}, \tag{2.1a}$$

$$\hat{H}_0 = \sum_i h\left(\hat{\mathbf{r}}_i\right) + \hat{T}_{\mathrm{n}} + \hat{H}_\gamma + \hat{H}_{\mathrm{n-n}}, \tag{2.1b}$$

$$\hat{H}_{\mathrm{int}} = \hat{H}_{\mathrm{e-e}} + \hat{H}_{\mathrm{e-n}} + \hat{H}_{\mathrm{e-}\gamma}. \tag{2.1c}$$

Equations (2.1a) to (2.1c) include terms describing the single-particle dynamics ($\hat{T}_{\mathrm{n}}$ and $\hat{H}_\gamma$) and interaction terms due to the mutual interaction of electrons,

nuclei and photons ($\hat{H}_{\mathrm{n-n}}$, $\hat{H}_{\mathrm{e-n}}$, $\hat{H}_{\mathrm{e-e}}$ and $\hat{H}_{\mathrm{e-}\gamma}$). In the above equation, $h\left(\mathbf{r}\right)$ represents the single-particle operator and it is summed over the electronic positions $\mathbf{r}_i$.

Depending on the choice of the non-interacting part of the Hamiltonian, h can include, aside from the kinetic part, some kind of initial correlation in the form of a mean-field potential. This is an essential ingredient in the merging of many-body techniques with *ab-initio* methods.

The electronic and nuclear kinetic parts are

$$\hat{T}_{\mathrm{e}} = -\frac{1}{2}\int \mathrm{d}^3\mathrm{r}\,\hat{\psi}^{\dagger}(\mathbf{r})\nabla^2\hat{\psi}(\mathbf{r}), \tag{2.2a}$$

$$\hat{T}_{\mathrm{n}} = -\sum_{\mathbf{R}}\frac{\nabla^2_{\mathbf{R}}}{2M_{\mathbf{R}}}, \tag{2.2b}$$

with $\mathbf{R}$ the generic position of the nucleus with mass $M_{\mathbf{R}}$. In Eq. (2.2a) $\hat{\psi}(\mathbf{r})$ and $\hat{\psi}^{\dagger}(\mathbf{r})$ are, respectively, the electron creation and annihilation operators in the Schrödinger's picture. The spinorial degrees of freedom are not considered here to keep the notation as simple as possible. The extension of the present theory to include their effect can be done starting from Pauli's equation and using the minimal coupling transformation. We also use the convention of representing vectors with a bold symbol (like $\mathbf{A}$) and tensors using a double arrow over-script (like $\overleftrightarrow{\mathcal{D}}$). Through this work band indices will be represented by a Latin subscript $(i, j, ...)$, while Cartesian directions and branch indices will be denoted by Greek labels $(\alpha, \beta, ...)$.

$\hat{H}_{\gamma}$ is the non-interacting Hamiltonian for the transverse photons

$$\hat{H}_{\gamma} = \sum_{\mathbf{q},\lambda}\omega_{\mathbf{q}}\hat{d}^{\dagger}_{\mathbf{q},\lambda}\hat{d}_{\mathbf{q},\lambda}, \tag{2.3}$$

with $\mathbf{q}$ and $\omega_{\mathbf{q}}$ the photon's momentum and energy, λ its polarisation, and $\hat{d}^{\dagger}_{\mathbf{q},\lambda}$ and $\hat{d}_{\mathbf{q},\lambda}$ the creation and annihilation operators, respectively (also in Schrödinger's picture).

The first group of interaction terms, $\hat{H}_{\text{n-n}}$ and $\hat{H}_{\text{e-e}}$, describe the nuclear-nuclear and e-e interactions, respectively. Those do not make the different sub-spaces of electron, nuclei and photons interact but build up internal (purely electronic and

nuclear) correlation effects:

$$\hat{H}_{\mathrm{e-e}} = \frac{1}{2}\int \mathrm{d}^3r\,\mathrm{d}^3r'\,\hat{\psi}^\dagger(\mathbf{r})\hat{\psi}^\dagger(\mathbf{r}')v(\mathbf{r}-\mathbf{r}')\hat{\psi}(\mathbf{r}')\hat{\psi}(\mathbf{r}), \tag{2.4}$$

with $v\left(\mathbf{r}-\mathbf{r}'\right)$ the bare Coulomb potential. The nucleus-nucleus interaction reads as:

$$\tilde{H}_{\mathrm{n-n}} = \frac{1}{2}\sum\nolimits'_{\mathbf{R},\mathbf{R}'} Z_{\mathbf{R}} Z_{\mathbf{R}'} v\left(\mathbf{R}-\mathbf{R}'\right), \tag{2.5}$$

with $\sum'_{ij} = \sum_{i\neq j}$ and $Z_{\mathbf{R}}$ the nucleus atomic number.

The e-γ interaction, $\hat{H}_{\mathrm{e}-\gamma}$, is given by

$$\hat{H}_{\mathrm{e}-\gamma} = -\frac{1}{c}\int \mathrm{d}^3r\,\hat{\mathbf{A}}(\mathbf{r})\cdot\hat{\mathbf{J}}(\mathbf{r}) + \frac{1}{2c^2}\int \mathrm{d}^3r\,\hat{\rho}(\mathbf{r})\hat{\mathbf{A}}^2(\mathbf{r}). \tag{2.6}$$

Here, the paramagnetic electronic current and the density are defined as

$$\hat{\mathbf{J}}(\mathbf{r}) = \frac{1}{2\mathrm{i}}\left[\hat{\psi}^\dagger(\mathbf{r})\nabla\hat{\psi}(\mathbf{r}) - \mathrm{c.c.}\right], \tag{2.7a}$$

$$\hat{\rho}(\mathbf{r}) = \hat{\psi}^\dagger(\mathbf{r})\hat{\psi}(\mathbf{r}). \tag{2.7b}$$

We work in the second quantisation formalism and introduce a suitable single-particle basis with orthonormal wave-functions $\{\varphi_i\left(\mathbf{r}\right)\}$. Then, the creation and annihilation field-operators $\hat{\psi}^\dagger\left(\mathbf{r}\right)$ and $\hat{\psi}\left(\mathbf{r}\right)$ for a particle at position r in space are expanded according to

$$\hat{\psi}\left(\mathbf{r}\right) = \sum_i \varphi_i\left(\mathbf{r}\right)\hat{c}_i. \tag{2.8}$$

The one-particle density-matrix operator takes the form

$$\hat{\rho}(\mathbf{r},\mathbf{r}') = \hat{\psi}^\dagger(\mathbf{r})\hat{\psi}(\mathbf{r}') = \sum_{ij}\varphi_i^*(\mathbf{r})\varphi_j(\mathbf{r}')\hat{\rho}_{ji}, \tag{2.9}$$

with $\hat{\rho}_{ji} = \hat{c}_i^\dagger\hat{c}_j$.

The first important step is the quantisation of the electromagnetic field that, as it will be clear shortly, will appear as an explicit ingredient of the time evolution. We start by rewriting the vector potential of the electromagnetic radiation in terms of photon creation and annihilation operators

$$\hat{\mathbf{A}}(\mathbf{r}) = \sum_{\mathbf{G},\mathbf{q},\lambda}\left(\frac{2\pi c^2}{\omega_{\mathbf{q}+\mathbf{G}}\Omega}\right)^{\frac{1}{2}}\left[\hat{d}_{\mathbf{q}+\mathbf{G},\lambda}e^{\mathrm{i}(\mathbf{q}+\mathbf{G})\cdot\mathbf{r}} + \hat{d}^\dagger_{\mathbf{q}+\mathbf{G},\lambda}e^{-\mathrm{i}(\mathbf{q}+\mathbf{G})\cdot\mathbf{r}}\right]\mathbf{e}_\lambda(\mathbf{q}+\mathbf{G}), \tag{2.10}$$

with Ω being the volume of the lattice and $\mathbf{e}_\lambda(\mathbf{q}+\mathbf{G})$ the polarisation vectors orthogonal to the photon's momentum $\mathbf{q}+\mathbf{G}$.

We aim at describing any kind of system by using a super-cell approach. This means that the periodic part of the system (if any) is represented by a unit cell of volume Ω_s containing N momenta $\mathbf{q}$ ($\Omega \equiv N\Omega_s$). This unit cell is periodically repeated displaced of a generic vector $\mathbf{G}$ of the reciprocal lattice. In the case of isolated systems $N=1$ and Ω_s is chosen large enough to avoid spurious interactions.

The e-p interaction arises from the term $\hat{H}_{\mathrm{e-n}}$ where the nuclear and electronic densities are coupled via the Coulomb interaction

$$\hat{H}_{\mathrm{e-n}} = -\int \mathrm{d}^3\mathrm{d}^3R\, \frac{\hat{\rho}(\mathbf{r})\hat{N}(\mathbf{R})}{|\mathbf{r}-\mathbf{R}|}. \tag{2.11}$$

$\hat{N}(\mathbf{R})$ is the nuclear density operator that we take as the counterpart of the electronic case. The actual definition of the nuclear density is a delicate issue that has been already discussed in Ref. [29].

2.2 Coupling to external perturbations

The Hamiltonian H describes the complete dynamics of the coupled systems of electrons, photons and phonons. In order to rewrite this dynamics in the form of equations of motion for the corresponding Green's functions we can use two equivalent paths. One is based on the standard diagrammatic technique [54] which constructs approximations for the different terms of the theory by using a geometrical and graphical approach. An alternative approach, that we follow here, is based instead on the equation of motion approach [55]. This methods leads, both in the equilibrium and the out-of-equilibrium regimes, to a closed set of integro-differential equations that at the equilibrium are known as Hedin's equations [56].

In order to extend these equations to account for the correlated dynamics of electrons, photons and phonons in an out-of-equilibrium context we start by discussing some key aspects of the purely electronic case. In the equation of motion approach the Hamiltonian is perturbed with a fictitious time-dependent term

$$\hat{H}(t) = \hat{H} + \hat{H}_{\mathrm{ext}}(t). \tag{2.12}$$

In the original derivation of Hedin's equations [55] $\hat{H}_{\text{ext}}(t)$ describes the coupling of the electronic charge with an external fictitious field $\phi_{\text{ext}}(\mathbf{r},t)$ that, at the end of the derivation, is set to zero:

$$\hat{H}_{\text{ext}}(t) = \int \mathrm{d}^3 r\, \phi_{\text{ext}}(\mathbf{r},t)\, \hat{\rho}(\mathbf{r},t)\,. \tag{2.13}$$

Now the problem is that this perturbation cannot be used in the present case where we want to describe a quantised electromagnetic field. The reason is that the vector potential is now quantised and it cannot be set to zero at the end of the calculations. This is connected to the existence of a vacuum energy of the electromagnetic field.

To solve this problem we follow a different path. We notice that the external potential $\phi_{\text{ext}}(\mathbf{r},t)$ is solution of the Poisson equation

$$\nabla^2 \phi_{\text{ext}}(\mathbf{r},t) = -4\pi \rho_{\text{ext}}(\mathbf{r},t)\,. \tag{2.14}$$

The solution of Eq. (2.14) can be rewritten in integral form

$$\phi_{\text{ext}}(\mathbf{r},t) = \int \mathrm{d}^3 r'\, v\left(\mathbf{r}-\mathbf{r}'\right) \rho_{\text{ext}}\left(\mathbf{r}',t\right), \tag{2.15}$$

that, plugged into Eq. (2.13), yields

$$\hat{H}_{\text{ext}}(t) = \int \mathrm{d}^3 r\ \hat{\phi}'(\mathbf{r})\, \rho_{\text{ext}}(\mathbf{r},t)\,, \tag{2.16}$$

with ρ_{ext} the inhomogeneous part of Eq. (2.14) and $\hat{\phi}'(\mathbf{r})$ is the potential operator corresponding to $\hat{\rho}(\mathbf{r})$.

By comparing Eq. (2.13) with Eq. (2.16) we notice that, now, the potential can be quantised and the external charge set to zero. As it will be clear in the following, these two procedures are equivalent, as far as the solely electronic limit is concerned.

Another important aspect is that we can now couple the external test charge to the potential generated by both the nuclear and the electronic charges:

$$\hat{\phi}(\mathbf{r},t) = \int \mathrm{d}^3 r'\, v\left(\mathbf{r}-\mathbf{r}'\right)\left[\hat{\rho}\left(\mathbf{r}'\right) - \hat{N}(\mathbf{r}')\right] = \int \mathrm{d}^3 r'\, v\left(\mathbf{r}-\mathbf{r}'\right)\hat{n}(\mathbf{r}'), \tag{2.17}$$

where $\hat{n} = \hat{\rho} - \hat{N}$ is the total internal density of the system, since now we have to account for the quantised nuclei as well. By following Ref. [29] we introduce

an external perturbation of the nuclear density, $N_{\rm ext}\left(\mathbf{R},t\right)$, that is coupled, via Eq. (2.15), to the electric potential generated by the nuclei, $\hat{V}_{\rm n}\left(\mathbf{r},t\right)$.

A similar procedure can be applied to the perturbation induced by an external vector potential by using the equation of motion

$$\left(\frac{1}{c^2}\partial_t^2-\nabla^2\right)\mathbf{A}_{\rm ext}\left(\mathbf{r},t\right)=\frac{4\pi}{c}\mathbf{J}^{\perp}_{\rm ext}\left(\mathbf{r},t\right). \tag{2.18}$$

In this way the total interaction part of the Hamiltonian looks like

$$\hat{H}_{\rm ext}(t)=\int \mathrm{d}^3r\,\hat{\phi}(\mathbf{r},t)\rho_{\rm ext}(\mathbf{r},t)-\frac{1}{c}\int \mathrm{d}^3r\,\hat{\mathbf{A}}(\mathbf{r})\cdot\mathbf{J}_{\rm ext}(\mathbf{r},t)- \int \mathrm{d}^3R\,\hat{V}_{\rm n}(\mathbf{r})N_{\rm ext}(\mathbf{r},t). \tag{2.19}$$

The last term in Eq. (2.19) describes the coupling with the nuclear motion. This was first introduced by Baym in Ref. [57] and also used in Ref. [29]. Here, we work with a fictitious external density in order to maintain coherence with the other perturbative terms. As it will be clear later on, we use these external quantities to decouple the dynamics of electrons, nuclei, and photons. In Eq. (2.19) we have neglected the second term on the right hand side of Eq. (2.6). The reason is that this term is multiplied by $1/c^2$ and therefore, for a given order in the perturbative expansion it leads to correction much smaller than those induced by the $\mathbf{A}\cdot\mathbf{J}$ term. From a diagrammatic point of view the $\rho\mathbf{A}^2$ term is responsible of a series of diagrams well-known and studied in the e-p problem [30], where they arise from the second-order e-p interaction. In the e-γ case, however, these diagrams can be safely neglected.

2.3 Green's functions and the Keldysh contour

The time evolution in non-equilibrium processes is more complicated than for equilibrium systems because it is not guaranteed that after an arbitrarily long enough time the system will return to the ground state. The extension of Hedin's equations to an out-of-equilibrium system can be done by defining a contour in the complex plane known as the Keldysh contour [11]. The contour runs as shown in Fig. 2.1 with the upper (positive) branch running from an instant t_0 where the system is assumed to be at equilibrium to an unknown state. The system is brought

back to equilibrium via the lower (negative) branch and it is this mathematical description for the time evolution which allows us to have all the necessary rules to derive a system of equations similar to the original one of Hedin's [11].

The Green's function $G(1,2)$ for non-equilibrium processes is defined on the Keldysh contour [12]:

$$G(1_\alpha, 2_\beta) = -\mathrm{i}\beta \frac{\mathrm{Tr}\left\{\rho_0 \mathrm{T}_C\left[\hat{S}_C \hat{\psi}_I(1_\alpha)\,\hat{\psi}_I^\dagger(2_\beta)\right]\right\}}{\mathrm{Tr}\left\{\rho_0 \hat{S}_C\right\}}, \tag{2.20}$$

where the subscripts $\alpha,\ \beta = \pm 1$ indicate the branch on the Keldysh contour where the time argument of the respective operator is located. The operator T_C is the contour time ordering operator. In Eq. (2.20) we introduce the compact notation $1 \equiv (\mathbf{r}_1, t_1)$. Note that the time t runs on the Keldysh contour.

The transition from the Heisenberg picture (where the electron operators are usually defined) to the interaction one is done via the following expression

$$\hat{O}(t_\alpha) = \hat{S}(-\infty, t_\alpha)\,\hat{O}_I(t_\alpha)\,\hat{S}(t_\alpha, -\infty), \tag{2.21}$$

where $\hat{O}$ is a generic operator and

$$\hat{S}\left(t_\alpha, t'_\alpha\right) = \mathrm{T}_\alpha \mathrm{exp}\left[-\mathrm{i}\alpha \int_{t'_\alpha}^{t_\alpha} \mathrm{d}\tau\, \hat{H}^\alpha_{\mathrm{ext},I}(\tau)\right]. \tag{2.22}$$

Note that, in Eq. (2.22), the time arguments lie on a single time branch of the

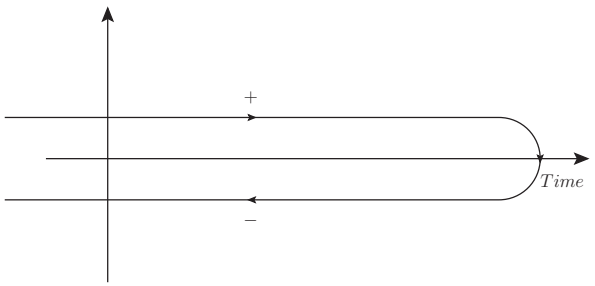

Figure 2.1: The Keldysh contour. Any time index runs on the contour which defines a natural time ordering that only in the upper branch is equivalent to the ordering in the standard real-time axis.

Keldysh contour. This implies that we can introduce a branch specific evolution

operator, $\hat{S}_\alpha(t,t') \equiv \hat{S}(t_\alpha, t'_\alpha)$. With this definition the overall time evolution operator, $\hat{S}_C$, entering Eq. (2.20) can be rewritten as

$$\hat{S}_C = \hat{S}_-(-\infty,\infty)\hat{S}_+(\infty,-\infty), \tag{2.23}$$

and we have that the expectation value of $\hat{O}$ taken on the contour is

$$\langle \hat{O}(1)\rangle_C = \frac{\mathrm{Tr}\left\{\rho_0 \mathrm{T}_C\left[\hat{S}_C \hat{O}_I(1)\right]\right\}}{\mathrm{Tr}\left\{\rho_0 \hat{S}_C\right\}}. \tag{2.24}$$

The structure of Eq. (2.20) with respect to the position of the time arguments on the Keldysh contour defines the different kind of Green's functions:

$$G(1_+, 2_+) \equiv G_{\mathtt{c}}(1,2), \tag{2.25a}$$
$$G(1_-, 2_+) \equiv G^<(1,2), \tag{2.25b}$$
$$G(1_+, 2_-) \equiv G^>(1,2), \tag{2.25c}$$
$$G(1_-, 2_-) \equiv G_{\tilde{\mathtt{c}}}(1,2). \tag{2.25d}$$

In Eqs. (2.25a) to (2.25d), $G_{\mathtt{c}}$ is the time-ordered or causal Green's function, $G^<$ and $G^>$ are the lesser and greater Green's functions, and $G_{\tilde{\mathtt{c}}}$ is the anti-time-ordered Green's function.

2.4 Equation of motion for the Green's function on the Keldysh contour

In order to obtain the equation of motion for G we start from $\mathrm{i}\partial_{t_1} G(1_\alpha, 2_\beta)$. From Eqs. (2.20) and (2.25a) we get

$$\begin{aligned}\partial_{t_1}\mathrm{T}_C\left[\hat{S}_C\hat{\psi}_I(1_\alpha)\hat{\psi}_I^\dagger(2_\beta)\right] &= \delta(1_\alpha - 2_\beta)\,\mathrm{T}_C\left[\hat{S}_C\right] + \mathrm{T}_C\left[\hat{S}_C\partial_{t_1}\hat{\psi}_I(1_\alpha)\hat{\psi}_I^\dagger(2_\beta)\right] \\ &+ \mathrm{i}\alpha\mathrm{T}_C[\hat{S}_C\hat{H}_{\mathrm{ext}}(t_{1\alpha})\hat{\psi}_I(1_\alpha)\hat{\psi}_I^\dagger(2_\beta)] - \mathrm{i}\alpha\mathrm{T}_C[\hat{S}_C\hat{\psi}_I(1_\alpha)\hat{H}_{\mathrm{ext}}(t_{1\alpha})\hat{\psi}_I^\dagger(2_\beta)].\end{aligned} \tag{2.26}$$

In the second term of the right-hand side of Eq. (2.26) we have the time derivative of the electron annihilation operator that is, in the interaction picture,

$$\mathrm{i}\partial_{t_1}\hat{\psi}_I(1) = \left[\hat{\psi}_I(1), \hat{H}_I(t_1)\right] = \left[\hat{h}(1) - \frac{\mathrm{i}}{c}\hat{\mathbf{A}}(1)\cdot\nabla_1 + \hat{\phi}(1)\right]\hat{\psi}_I(1). \tag{2.27}$$

$\hat{H}_I$ is the representation, in the interaction picture, of $\hat{H}_{\rm ext}\left(t\right)$, defined in Eq. (2.12), while the third and fourth terms in Eq. (2.26) give

$$\mathrm{i}\alpha\mathrm{T}_C[\hat{S}_C\hat{H}_{\rm ext}(t_1)\hat{\psi}_I\left(1_\alpha\right)\hat{\psi}_I^\dagger\left(2_\beta\right)]-\mathrm{i}\alpha\mathrm{T}_C[\hat{S}_C\hat{\psi}_I\left(1_\alpha\right)\hat{H}_{\rm ext}(t_1)\hat{\psi}_I^\dagger\left(2_\beta\right)]= \\ =-\mathrm{i}\alpha\phi_{\rm ext}(1)\mathrm{T}_c[\hat{S}_c\hat{\psi}(1_\alpha)\hat{\psi}^\dagger(2_\beta)]. \quad (2.28)$$

Equations (2.26)-(2.28), finally, lead to the following equation of motion for G:

$$\left[\mathrm{i}\partial_{t_1}-\hat{h}\left(1\right)-\frac{\mathrm{i}}{c}\left\langle\hat{\mathbf{A}}\left(1_\alpha\right)\right\rangle_C\cdot\nabla_1-U\left(1_\alpha\right)\right]G\left(1_\alpha,2_\beta\right)=\delta\left(1_\alpha-2_\beta\right)+ \\ \mathrm{i}\frac{\delta G\left(1_\alpha,2_\beta\right)}{\delta\rho_{\rm ext}\left(3_\gamma\right)}\bigg|_{3_\gamma=1_\alpha}-\nabla_1\cdot\frac{\delta G\left(1_\alpha,2_\beta\right)}{\delta\mathbf{J}_{\rm ext}\left(3_\gamma\right)}\bigg|_{3_\gamma=1_\alpha}. \quad (2.29)$$

In Eq. (2.29) we defined the total potential

$$U\left(1\right)=\phi_{\rm ext}\left(1\right)+\left\langle\hat{\phi}\left(1\right)\right\rangle_C, \quad (2.30)$$

and used the following identities for the functional derivatives

$$\frac{\delta G\left(1_\alpha,2_\beta\right)}{\delta\rho_{\rm ext}\left(3_\gamma\right)}=\mathrm{i}\gamma\left\langle\hat{\phi}_\gamma\left(3_\gamma\right)\right\rangle_C G\left(1_\alpha,2_\beta\right)-\beta\gamma\left\langle\hat{\phi}\left(3_\gamma\right)\hat{\psi}\left(1_\alpha\right)\hat{\psi}^\dagger\left(2_\beta\right)\right\rangle_C, \quad (2.31)$$

and

$$\frac{\delta G\left(1_\alpha,2_\beta\right)}{\delta\mathbf{J}_{\rm ext}\left(3_\gamma\right)}=\mathrm{i}\frac{\gamma}{c}\left\langle\hat{\mathbf{A}}\left(3_\gamma\right)\right\rangle_C G\left(1_\alpha,2_\beta\right)+\frac{\beta\gamma}{c}\left\langle\hat{\mathbf{A}}\left(3_\gamma\right)\hat{\psi}\left(1_\alpha\right)\hat{\psi}^\dagger\left(2_\beta\right)\right\rangle_C. \quad (2.32)$$

Equation (2.29) can also be used to define the noninteracting Green's function in order to rewrite it as Dyson equation or, alternatively, as BKE. Indeed we start by noticing that G_0 is the solution of Eq. (2.29) when $\frac{\delta G}{\delta\rho_{\rm ext}}=\frac{\delta G}{\delta\mathbf{J}_{\rm ext}}=0$:

$$\left[\mathrm{i}\partial_{t_1}-h_{\rm tot}\left(1_\alpha\right)\right]G_{0,\mathrm{H}}\left(1_\alpha,2_\beta\right)=\delta\left(1_\alpha-2_\beta\right), \quad (2.33)$$

with

$$h_{\rm tot}\left(1\right)=h\left(1\right)-\frac{\mathrm{i}}{c}\left\langle\hat{\mathbf{A}}\left(1\right)\right\rangle_C\cdot\nabla_1-U\left(1\right). \quad (2.34)$$

Equations (2.33) and (2.34) imply that

$$G_{0,\mathrm{H}}^{-1}\left(1_\alpha,2_\beta\right)=\left[\mathrm{i}\partial_{t_1}-h_{\rm tot}\left(1_\alpha\right)\right]\delta\left(1_\alpha-2_\beta\right). \quad (2.35)$$

Here the subscript "H" in Eq. (2.33) indicates that contributions from the Hartree self-energy are already included in the zeroth order Green's function. We can

remove this contribution from the zeroth order by defining the Hartree self-energy, Σ_{H}, which is given by

$$\begin{aligned}\Sigma_{\mathrm{H}}(1,2) &= \Sigma_{\mathrm{H}}^{\parallel}(1,2) + \Sigma_{\mathrm{H}}^{\perp}(1,2) \\ &= \delta(1,2)\left[-\mathrm{i}w_0(1,3)G(3,3^+) + \frac{1}{c}\mathbf{A}_{\mathrm{ind}}\cdot\mathbf{\Pi}(1,1')G(1,1')|_{1'=1^+}\right], \quad (2.36)\end{aligned}$$

where we have used $w_0(1,3) = \delta(t_1,t_3)v(\mathbf{r}_1-\mathbf{r}_3)$ and $\mathbf{A}_{\mathrm{ind}}$ stands for the induced vector potential. The first term on the right-hand-side corresponds to the longitudinal Hartree self-energy, $\Sigma_{\mathrm{H}}^{\parallel}$, while the second term is the transverse Hartree self-energy, $\Sigma_{\mathrm{H}}^{\perp}$. We will analyse later on the implications which arise from these terms. With this, we can recover the usual zeroth order Green's function, $G_0(1,2)$, which is the solution of the differential equation

$$\left[\mathrm{i}\partial_{t_1} - h_{\mathrm{ext}}\left(1_\alpha\right)\right] G_0\left(1_\alpha, 2_\beta\right) = \delta\left(1_\alpha - 2_\beta\right), \quad (2.37)$$

with

$$h_{\mathrm{ext}}\left(1\right) = h\left(1\right) - \frac{\mathrm{i}}{c}\mathbf{A}_{\mathrm{ext}}\left(1\right)\cdot\nabla_1 - \phi_{\mathrm{ext}}\left(1\right). \quad (2.38)$$

By using Eq. (2.36) and Eq. (2.37) we can further rewrite Eq. (2.29) in terms of the bare and of the fully interacting Green's functions. This is clearly a step towards the final form of the Dyson-type equation:

$$\begin{aligned}G\left(1_\alpha, 2_\beta\right) &= G_0\left(1_\alpha, 2_\beta\right) + G_0\left(1_\alpha, 4_\sigma\right) \\ &\times\left[\Sigma_{\mathrm{H}}(4_\sigma,3_\gamma)G(3_\gamma,2_\beta) + \mathrm{i}\frac{\delta G\left(4_\sigma,2_\beta\right)}{\delta\rho_{\mathrm{ext}}\left(3_\gamma\right)}\bigg|_{3_\gamma=4_\sigma} - \nabla_1\cdot\frac{\delta G\left(4_\sigma,2_\beta\right)}{\delta\mathbf{J}_{\mathrm{ext}}\left(3_\gamma\right)}\bigg|_{3_\gamma=4_\sigma}\right]. \quad (2.39)\end{aligned}$$

The electromagnetic field and the nuclei are now quantised, so the entire theoretical scheme is closed only when the equations of motion for their propagators are introduced. It is interesting to note that all different effects induced by the mutual interactions (e-e, e-p, e-γ) will mix together in the dressing of the total fields connected to the external sources. This dressing involves the ensemble of electrons, photons, and phonons via oscillations (collective and not) described by the corresponding response functions.

As it will be clear, in difference with the well known purely electronic case new response and vertex functions must be introduced.

2.5 Equation of motion for the electromagnetic potentials

The equation of motion for the fields are obtained by taking the macroscopic average of U and $\langle\hat{\mathbf{A}}\rangle$. From classical electrodynamics, we know that the scalar potential U is the solution of the Poisson equation

$$\nabla^2 U(1) = -4\pi[\rho_{\text{ext}}(1) + \langle\hat{n}(1)\rangle_C], \tag{2.40}$$

while the expectation value of the vector potential $\langle\hat{\mathbf{A}}\rangle$ satisfies the equation of motion

$$\left(\frac{1}{c^2}\partial_{t_1}^2 - \nabla_1^2\right)\langle\hat{\mathbf{A}}\,(1)\rangle_C = \frac{4\pi}{c}\mathbf{J}_{\text{tot}}^{\perp}\,(1) = \frac{4\pi}{c}\int \mathrm{d}2\,\overleftrightarrow{\delta}^{\perp}\,(1,2)\,\mathbf{J}_{\text{tot}}\,(2)\,. \tag{2.41}$$

The $\perp$ superscript means that only the transverse part of the current enters in the Eq. (2.41). This is obtained from the total current vector using the transverse delta function

$$\delta_{\alpha\beta}^{\perp}\,(1,2) = \delta\,(t_1 - t_2)\left[\delta(\mathbf{r}_1 - \mathbf{r}_2)\delta_{\alpha\beta} + \frac{1}{4\pi}\frac{\partial}{\partial r_{1,\alpha}}\left(\frac{1}{|\mathbf{r}_1 - \mathbf{r}_2|}\frac{\partial}{\partial r_{2,\beta}}\right)\right]. \tag{2.42}$$

2.6 Response and vertex functions, and self-energies

The equation of motion for G, Eq. (2.29), is still written in an obscure way and the different physical ingredients describing the complex many-body dynamics are hidden inside the functional derivatives $\left[\frac{\delta G(4_\sigma,2_\beta)}{\delta\rho_{\text{ext}(3)}}\right.$ and $\left.\frac{\delta G(4_\sigma,2_\beta)}{\delta\mathbf{J}_{\text{ext}}(3_\gamma)}\right]$. In this section we investigate the structure of these derivatives by introducing the longitudinal and transverse response function and vertex functions.

We start by noticing that, as a consequence of the Green's function definition, it follows that

$$G\,(1_\alpha, 2_\beta)\,G^{-1}\,(2_\beta, 3_\gamma) = \delta\,(1_\alpha - 2_\beta) \Rightarrow \frac{\delta G\,(1_\alpha, 2_\beta)}{\delta h\,(3_\gamma)} = \\ = -G\,(1_\alpha, 4_\eta)\left[\frac{\delta G^{-1}\,(4_\eta, 5_\xi)}{\delta h\,(3_\gamma)}\right] G\,(5_\xi, 2_\beta)\,, \tag{2.43}$$

for any well behaved function h. In Eq. (2.43) we have introduced the *right* G^{-1} function that acts on the right arguments of G. Note that an alternative formulation can be introduced by using the *left* G^{-1} defined in such a way that $G^{-1}(1_\alpha, 2_\beta) G(2_\beta, 3_\gamma) = \delta(1_\alpha - 2_\beta)$ [55].

We can now apply a second rule that states that:

$$\frac{\delta G^{-1}(4_\eta, 5_\xi)}{\delta h(3_\gamma)} = \frac{\delta G^{-1}(4_\eta, 5_\xi)}{\delta g(6_\sigma)} \frac{\delta g(6_\sigma)}{\delta h(3_\gamma)}. \tag{2.44}$$

From Eqs.(2.43) and (2.44) we get that, by using $h = \rho$ and $g = U$ [see Eq. (2.30)],

$$\left.\frac{\delta G(1_\alpha, 2_\beta)}{\delta \rho_{\text{ext}}(3_\gamma)}\right|_{3_\gamma = 1_\alpha} = G(1_\alpha, 4_\eta)\, \tilde{\gamma}(4_\eta, 5_\xi, 6_\sigma)\, W(6_\sigma, 1_\alpha)\, G(5_\xi, 2_\beta). \tag{2.45}$$

With Eq. (2.45) we can introduce the scalar (longitudinal) part of the total self-energy operator, Σ_{long}, defined as:

$$\mathrm{i} \left.\frac{\delta G(1_\alpha, 2_\beta)}{\delta \rho_{\text{ext}}(3_\gamma)}\right|_{3_\gamma = 1_\alpha} = \Sigma^{\parallel}_{\mathbf{xc}}(1_\alpha, 3_\gamma)\, G(3_\gamma, 2_\beta), \tag{2.46}$$

and, from Eq. (2.45), it follows that

$$\Sigma^{\parallel}_{\mathbf{xc}}(1_\alpha, 2_\gamma) \equiv G(1_\alpha, 3_\gamma)\, \tilde{\gamma}(3_\gamma, 2_\beta, 4_\sigma)\, W(4_\sigma, 1_\alpha). \tag{2.47}$$

The definition of the self-energy operator naturally introduces scalar response function

$$W(1,2) = \frac{\delta U(1)}{\delta \rho_{\text{ext}}(2)}, \tag{2.48}$$

and the irreducible longitudinal vertex function $\gamma(1,2,3)$

$$\tilde{\gamma}(1,2,3) = -\frac{\delta G^{-1}(1,2)}{\delta U(3)}. \tag{2.49}$$

A similar procedure can be applied to the other derivative that appears in Eq. (2.29), $\frac{\delta G}{\delta \mathbf{J}_{\text{ext}}}$. At difference with the charge derivative this new term is a vector and we use Greek symbols $(\alpha, \beta, ...)$ to label its Cartesian components. By applying the following substitutions to Eqs.(2.43) and (2.44)

$$\frac{\delta}{\delta \rho_{\text{ext}}} \Rightarrow \frac{\delta}{\delta J_{\text{ext},\alpha}}, \tag{2.50a}$$

$$\frac{\delta}{\delta U} \Rightarrow \frac{\delta}{\delta A_\alpha}, \tag{2.50b}$$

we get that

$$\left.\frac{\delta G\left(1_\alpha,2_\beta\right)}{\delta J_{\mathrm{ext},\lambda}\left(3_\gamma\right)}\right|_{3_\gamma=1_\alpha}=-\sum_{\theta=1}^{3}G\left(1_\alpha,4_\eta\right)\frac{\delta G^{-1}\left(4_\eta,5_\xi\right)}{\delta\left\langle\hat{A}_\theta\left(6_\sigma\right)\right\rangle_C}\frac{\delta\left\langle\hat{A}_\theta\left(6_\sigma\right)\right\rangle_C}{\delta J_{\mathrm{ext},\lambda}\left(1_\alpha\right)}G\left(5_\xi,2_\beta\right) \tag{2.51}$$

Equation (2.51) allows us to introduce the second important term in the total self-energy corresponding to its transverse contribution, $\Sigma_{\mathrm{xc}}^{\perp}$:

$$\begin{aligned}\Sigma_{\mathrm{xc}}^{\perp}\left(1_\alpha,2_\beta\right)&=-\nabla_i\left.\frac{\delta G\left(1_\alpha,2_\beta\right)}{\delta J_{\mathrm{ext},\lambda}\left(3_\gamma\right)}\right|_{3_\gamma=1_\alpha}=\\&=\mathrm{i}\,\Pi_i\left(1,3\right)\left.\sum_{\theta=1}^{3}G\left(1_\alpha,4_\eta\right)\tilde{\Gamma}_\theta\left(4_\eta,5_\xi,6_\sigma\right)\mathcal{D}_{\theta\lambda}\left(6_\sigma,3_\beta\right)G\left(5_\xi,2_\beta\right)\right|_{3_\gamma=1_\alpha}.\end{aligned} \tag{2.52}$$

where

$$\boldsymbol{\Pi}\left(1,2\right)=-\frac{\mathrm{i}}{2}\left(\nabla_1-\nabla_2\right)=\boldsymbol{\Pi}\left(1\right)+\boldsymbol{\Pi}^*\left(2\right). \tag{2.53}$$

The transverse self-energy, Eq. (2.52) further introduces two functions. The transverse photon propagator, which we will call $\overleftrightarrow{\mathcal{D}}\left(1,2\right)$,

$$\overleftrightarrow{\mathcal{D}}\left(1,2\right)=-\frac{c}{4\pi}\frac{\delta\left\langle\hat{\mathbf{A}}\left(1\right)\right\rangle_C}{\delta\mathbf{J}_{\mathrm{ext}}\left(2\right)}, \tag{2.54}$$

and the transverse vertex (vectorial) function $\boldsymbol{\Gamma}$,

$$\tilde{\boldsymbol{\Gamma}}\left(1,2,3\right)=-\frac{4\pi}{c}\frac{\delta G^{-1}\left(1,2\right)}{\delta\left\langle\hat{\mathbf{A}}\left(3\right)\right\rangle}. \tag{2.55}$$

We notice now that the longitudinal screened potential and vertex are connected, via Eq. (2.40), to the *total* density. This includes both an electronic and a nuclear component. It is then clear that the nuclear motion enters directly in the electronic dynamics via the longitudinal components.

This sharp separation between longitudinal and transverse components of the theory is the consequence of using the Coulomb gauge. Although the latter allows the electromagnetic field to be separated into two independent parts the entire theory still follows the same structure as its version without quantised fields which was presented in Section A.1.2, that is, we can still define a set of equations analogous to the one of Hedin. As we will see shortly, the final expression for the self-energy will also be split in a longitudinal and in a transverse part.

The final step of this section is obtained by using Eqs.(2.52) and (2.49) to define the total self-energy, $\Sigma = \Sigma_{\text{long}} + \Sigma_{\text{trans}}$. This can be introduced in Eqs.(2.39) and (2.29) to obtain the final form of the equation of motions for the G written as time-derivative

$$\left[\mathrm{i}\partial_{t_1} - h_{\text{ext}}(1)\right] G(1_\alpha, 2_\beta) = \delta(1_\alpha - 2_\beta) + \Sigma(1_\alpha, 3_\gamma) G(3_\gamma, 2_\beta), \tag{2.56}$$

and as Dyson-type equation

$$G(1_\alpha, 2_\beta) = G_0(1_\alpha, 2_\beta) + G_0(1_\alpha, 3_\gamma) \Sigma(3_\gamma, 4_\eta) G(4_\eta, 2_\beta). \tag{2.57}$$

Equations (2.56) and (2.57) are equivalent and represent two different formulations of the KBE.

From the equation of motion for the scalar and for the vector potential we can now derive the equations governing the response functions. Indeed these functions describe the change in the observables due to the total (external plus induced) perturbations and provide a connection between Eq. (2.40), (2.41), and (2.29). In the following sections we analyse separately the two contributions: transverse (photon-induced) and longitudinal (electronic and phonon-mediated).

2.7 The photon-induced response function

The photon-induced response function represents the transverse photon propagator. We start from Eq. (2.41) and divide the total current in an external and an induced part: $\mathbf{J}_{\text{tot}} = \mathbf{J}_{\text{ext}} + \mathbf{J}_{\text{ind}}$. Thus, we can express the solution of Eq. (2.41) as

$$\langle \hat{\mathbf{A}}(1) \rangle_C = -\frac{4\pi}{c} \int \mathrm{d}2 \overleftrightarrow{\mathcal{D}}_0(1,2) \left[\mathbf{J}_{\text{ext}}(2) + \mathbf{J}_{\text{ind}}(2)\right], \tag{2.58}$$

where $\mathcal{D}_0(1,2)$ is the free transverse photon propagator, solution of

$$\left(\frac{1}{c^2}\partial_{t_1}^2 - \nabla_1^2\right) \overleftrightarrow{\mathcal{D}}_0(1,2) = \overleftrightarrow{\delta}^{\perp}(1,2). \tag{2.59}$$

By applying the chain rule, Eq. (2.43) we derive the equation of motion for the transverse photon propagator

$$\overleftrightarrow{\mathcal{D}}(1,2) = \overleftrightarrow{\mathcal{D}}_0(1,2) + \overleftrightarrow{\mathcal{D}}_0(1,3) \overleftrightarrow{\tilde{P}}(3,4) \overleftrightarrow{\mathcal{D}}(4,2), \tag{2.60}$$

where we have defined the irreducible transverse photon polarisation $\overleftrightarrow{\tilde{P}}(3,4)$:

$$\overleftrightarrow{\tilde{P}}(1,2) = -\frac{4\pi}{c}\frac{\delta \mathbf{J}_{\mathrm{ind}}(1)}{\delta \langle \hat{\mathbf{A}}(2)\rangle_C}. \tag{2.61}$$

To obtain the equation for the transverse polarisation we need a microscopic expression for the induced current, $\mathbf{J}_{\mathrm{ind}}$. This is related to the electronic Green's function by

$$\mathbf{J}_{\mathrm{ind}}(1) = \langle \hat{\mathbf{J}}(1)\rangle_C - \langle \hat{\rho}(1)\,\hat{\mathbf{A}}(1)\rangle_C = \mathrm{i}\boldsymbol{\Pi}\left(1,1'\right) G\left(1,1'\right)|_{1'=1^+}. \tag{2.62}$$

In deriving Eq. (2.62) we have omitted the $\rho\mathbf{A}$ term as we are considering averages on states with a fixed population of photons such that $\langle d^\dagger_{\mathbf{q}+\mathbf{G},\lambda}\rangle_C = \langle d_{\mathbf{q}+\mathbf{G},\lambda}\rangle_C = 0$. This implies that $\langle \hat{\rho}(1)\,\hat{\mathbf{A}}(1)\rangle_C = 0$. From Eqs.(2.61) and (2.54), we finally get a closed expression for the transverse photon polarisation

$$\tilde{P}_{\alpha\beta}(1,2) = -\mathrm{i}\Pi_\alpha\left(1,1'\right) G(1,3)\,\tilde{\Gamma}_\beta(3,4,2)\,G\left(4,1'\right)|_{1'=1}. \tag{2.63}$$

2.8 Phonon-induced response function

We now look into the screened Coulomb interaction W defined in Eq. (2.48). By using Eq. (2.30), we obtain

$$\begin{aligned} W(1,2) = w_0(1,2) + w_0(1,2)\left[\frac{\delta\langle\hat{\rho}(3)\rangle_C}{\delta\rho_{\mathrm{ext}}(2)} - \frac{\delta\langle\hat{N}(3)\rangle_C}{\delta\rho_{\mathrm{ext}}(2)}\right] = \\ = w_0(1,2) + w_0(1,3)\left[\tilde{p}_{\mathrm{e}}(3,4)W(4,2) - \frac{\delta\langle\hat{N}(3)\rangle_C}{\delta\rho_{\mathrm{ext}}(2)}\right], \end{aligned} \tag{2.64}$$

where $w_0(1,2) = \delta(t_1 - t_2)/|\mathbf{r}_1 - \mathbf{r}_2|$ is the bare Coulomb interaction, and p_{e} is the irreducible longitudinal electronic polarisation:

$$\tilde{p}_{\mathrm{e}}(1,2) = \frac{\delta\langle\hat{\rho}(1)\rangle_C}{\delta U(2)}. \tag{2.65}$$

Equation (2.64) includes two contributions. The first term in the square brackets comes from the electronic density (via p_e) and the second term from the nuclear density (via $\delta N/\delta\rho$). Thus, by following Ref. [29], we separate W into an electronic plus a nuclear part.

The electronic polarisation is still defined, as in the purely electronic case [55], in terms of the electronic component of the total density

$$\langle\hat{\rho}(1)\rangle_C = -\mathrm{i}G(1,1^+), \tag{2.66}$$

from which it immediately follows that

$$\tilde{p}_\mathrm{e}(1,2) = \mathrm{i}G(1,2)\tilde{\gamma}(3,4,2)G(4,1). \tag{2.67}$$

Again, in the derivation of Eq. (2.67) we used Eq. (2.43).

The last term on the right-hand-side of Eq. (2.64) is due to the change in the nuclear density induced by a change of the purely electronic part of the external charge. Indeed, this is the source of e-p interaction that describes the link between the nuclear motion and the electronic dynamics:

$$\frac{\delta\langle\hat{N}(3)\rangle_C}{\delta\rho_\mathrm{ext}(2)}. \tag{2.68}$$

In order to link this quantity to the microscopic correlation functions we need to introduce the nuclear density-density correlation function, D, given by

$$D(1,2) = -\mathrm{i}\langle\Delta\hat{N}(1)\Delta\hat{N}(2)\rangle_C, \tag{2.69}$$

where the fluctuation of an operator is expressed as $\Delta\hat{O} = \hat{O} - \langle\hat{O}\rangle$.

It is now possible to define an equation for D thanks to the introduction of the external nuclear charge N_ext in Eq. (2.19). As the interaction with the electronic density is $\int \mathrm{d}^3r\,\hat{\phi}(\mathbf{r},t)\rho_\mathrm{ext}(\mathbf{r},t)$, it follows that

$$\frac{\delta\langle\hat{N}(1)\rangle_C}{\delta\rho_\mathrm{ext}(2)} = -\mathrm{i}\langle\Delta\hat{N}(1)\Delta\hat{\phi}(2)\rangle_C. \tag{2.70}$$

If now we use the solution of the Poisson equation to rewrite $\Delta\hat{\phi}$ in terms of charge variations, we get

$$\frac{\delta\langle\hat{N}(1)\rangle_C}{\delta\rho_\mathrm{ext}(2)} = \mathrm{i}w_0(2,3)\left[\langle\Delta\hat{N}(1)\Delta\hat{N}(3)\rangle_C - \langle\Delta\hat{N}(1)\Delta\hat{\rho}(3)\rangle_C\right]. \tag{2.71}$$

Using the same procedure of above we can evaluate a similar derivative, $\frac{\delta\langle\hat{n}(1)\rangle}{\delta N_\mathrm{ext}(2)}$. In this case the interaction with N_ext is $\int \mathrm{d}^3r\,\hat{V}_\mathrm{n}(\mathbf{r})N_\mathrm{ext}(\mathbf{r},t)$. It follows then that

$$\frac{\delta\langle\hat{n}(1)\rangle_C}{\delta N_\mathrm{ext}(2)} = -\mathrm{i}\langle\Delta\hat{n}(1)\Delta\hat{V}_\mathrm{n}(2)\rangle_C. \tag{2.72}$$

By using again the solution of the Poisson equation we get that

$$\frac{\delta \langle \hat{N}(3) \rangle}{\delta \rho_{\mathrm{ext}}(2)} = -\frac{\delta \langle \hat{n}(3) \rangle}{\delta N_{\mathrm{ext}}(2)}. \tag{2.73}$$

We can now easily evaluate Eq. (2.68) via Eq. (2.73). Taking into account the definition of $\hat{n}$ we can use the functional derivative chain rule to obtain a Dyson-type equation

$$\begin{aligned} w_0(1,3)\frac{\delta \langle \hat{n}(3) \rangle}{\delta N_{\mathrm{ext}}(2)} &= w_0(1,3)D(3,4)w_0(4,2) + w_0(1,3)\frac{\delta \langle \hat{\rho}(3) \rangle}{\delta N_{\mathrm{ext}}(2)} \\ &= w_0(1,3)D(3,4)w_0(4,2) + w_0(1,3)\frac{\delta \langle \hat{\rho}(3) \rangle}{\delta U(4)}\frac{\delta U(4)}{\delta \langle \hat{n}(5) \rangle}\frac{\delta \langle \hat{n}(5) \rangle}{\delta N_{\mathrm{ext}}(2)} \\ &= w_0(1,3)D(3,4)w_0(4,2) + w_0(1,3)\tilde{p}_{\mathrm{e}}(3,4)w_0(4,5)\frac{\delta \langle \hat{n}(5) \rangle}{\delta N_{ext}(2)}. \end{aligned} \tag{2.74}$$

Iterating the equation leads to the following solution:

$$w_0(1,3)\frac{\delta \langle \hat{n}(3) \rangle}{\delta N_{\mathrm{ext}}(2)} = \left[1 - w_0\tilde{p}_{\mathrm{e}}\right]^{-1}(1,3)w_0(3,4)D(4,5)w_0(5,2), \tag{2.75}$$

which we can then insert in Eq. (2.64) to obtain the final expression for the total screened interaction

$$\begin{aligned} W(1,2) = w_0(1,2) + w_0(1,3)\tilde{p}_{\mathrm{e}}(3,4)W(4,2) \\ + \left[1 - w_0\tilde{p}_{\mathrm{e}}\right]^{-1}(1,3)w_0(3,4)D(4,5)w_0(5,2). \end{aligned} \tag{2.76}$$

Solving Eq (2.76) in order to W leads to two separate contributions

$$W(1,2) = W_{\mathrm{e}}(1,2) + W_{\mathrm{ph}}(1,2). \tag{2.77}$$

The first term, W_{e}, accounts for the interactions among the electrons and has no direct contribution from the nuclei

$$W_{\mathrm{e}}(1,2) = \left[1 - w_0\tilde{p}_{\mathrm{e}}\right]^{-1}(1,3)w_0(3,2), \tag{2.78}$$

while the second term introduces the effects of the contribution from the nuclear density fluctuations

$$W_{\mathrm{ph}}(1,2) = \left[1 - w_0\tilde{p}_{\mathrm{e}}\right]^{-1}(1,3)W_{\mathrm{e}}(3,4)D(4,5)w_0(5,2). \tag{2.79}$$

2.9 Vertex functions

In Eqs. (2.45) and (2.51), we have introduced a longitudinal and a transverse vertex function, both irredubicle. The equations of motion that govern their dynamics can be easily found by differentiating the inverse of the Dyson equation, Eq. (2.39)

$$G^{-1}(1,2) = G_0^{-1}(1,2) - \Sigma(1,2). \tag{2.80}$$

Thus we can write for the irreducible longitudinal vertex, given by Eq. (2.49), the following equation

$$\tilde{\gamma}(1,2,3) = \delta(1,2)\delta(1,3) + \frac{\delta\left[\Sigma_{\mathbf{xc}} + \Sigma_{\mathbf{H}}^{\perp}\right](1,2)}{\delta G(4,5)} G(4,6)\tilde{\gamma}(6,7,3)G(7,5), \tag{2.81}$$

and for the irreducible transverse part [Eq. (2.54)] we have that

$$\begin{aligned}\tilde{\mathbf{\Gamma}}(1,2,3) = -\frac{4\pi}{c}\mathbf{\Pi}(1,1')\delta(1,3)\delta(1',2)|_{1'=1^+} \\ + \frac{\delta\left[\Sigma_{\mathbf{xc}} + \Sigma_{\mathbf{H}}^{\parallel}\right](1,2)}{\delta G(4,5)} G(4,6)\tilde{\mathbf{\Gamma}}(6,7,3)G(7,5),\end{aligned} \tag{2.82}$$

Vertex and response functions are the ingredients we need to close the equation of motion for the Green's function in a set of integro-differential equations. At this stage, it is important to note that through the functional derivative $\frac{\delta\Sigma}{\delta G}$ all interactions mix together in a complex dynamics.

2.10 Final form of the Hedin's equations

We are now ready to present the full set of the Hedin's equations. The first equation gives us the electron propagator G:

$$G(1,2) = G_0(1,2) + G_0(1,3)\Sigma(3,4)G(4,2). \tag{2.83}$$

The second equation allows us to obtain the self-energy

$$\begin{aligned}\Sigma(1,2) = \delta(1,2)\left[-\mathrm{i}w_0(1,3)G(3,3^+) + \frac{1}{c}\mathbf{A}_{\mathrm{ind}}\cdot\mathbf{\Pi}(1,1')G(1,1')|_{1'=1^+}\right] \\ + \mathrm{i}\left[G(1,3)\gamma(3,2,4)W(4,1^+) + \sum_{\alpha,\beta=1}^{3}\Pi_\alpha(1,1')G(1,3)\Gamma_\beta(3,2,4)\mathcal{D}_{\beta\alpha}(4,1')\right]\Bigg|_{1'=1},\end{aligned} \tag{2.84}$$

in which, with respect to the original Hedin's equations, the second and fourht terms on the right-hand-side are now present, due to the quantisation of the EM field. The fourth and fifth equations describe the screened Coulomb interaction

$$W(1,2) = W_{\mathrm{e}}(1,2) + W_{\mathrm{ph}}(1,2), \tag{2.85}$$

and the transverse photon propagator

$$\overleftrightarrow{\mathcal{D}}(1,2) = \overleftrightarrow{\mathcal{D}}_0(1,2) + \overleftrightarrow{\mathcal{D}}_0(1,3)\overleftrightarrow{\tilde{P}}(3,4)\overleftrightarrow{\mathcal{D}}(4,2). \tag{2.86}$$

In order to evaluate them, we need the longitudinal

$$\tilde{p}_{\mathrm{e}}(1,2) = \mathrm{i}G(1,2)\tilde{\gamma}(3,4,2)G(4,1), \tag{2.87}$$

and transverse polarisation

$$\tilde{P}_{\alpha\beta}(1,2) = \mathrm{i}\Pi_{\alpha}(1,1')G(1,3)\tilde{\Gamma}_{\beta}(3,4,2)G(4,1')|_{1'=1}. \tag{2.88}$$

These equations form the sixth and seventh Hedin's equations that introduce the corresponding vertex functions, whose equations of motion represent the last two Hedin equations:

$$\tilde{\gamma}(1,2,3) = \delta(1,2)\delta(1,3) + \frac{\delta\tilde{\Sigma}^{\parallel}(1,2)}{\delta G(4,5)}G(4,6)\tilde{\gamma}(6,7,3)G(7,5), \tag{2.89}$$

and

$$\tilde{\mathbf{\Gamma}}(1,2,3) = -\frac{4\pi}{c}\mathbf{\Pi}(1,1')\delta(1,3)\delta(1',2)|_{1'=1^+} + \frac{\delta\tilde{\Sigma}^{\perp}(1,2)}{\delta G(4,5)}G(4,6)\tilde{\mathbf{\Gamma}}(6,7,3)G(7,5), \tag{2.90}$$

and where we have defined, to simplify the notation,

$$\tilde{\Sigma}^{\parallel}(1,2) = \Sigma_{\mathbf{xc}}(1,2) + \Sigma^{\perp}(1,2), \tag{2.91}$$

and

$$\tilde{\Sigma}^{\perp}(1,2) = \Sigma_{\mathbf{xc}}(1,2) + \Sigma^{\parallel}(1,2). \tag{2.92}$$

The only missing term is the equation of motion for D, the nuclear density-density correlation function. However it has been shown [29] that the electronic and nuclear parts of Hedin's equations can be safely decoupled. As a consequence

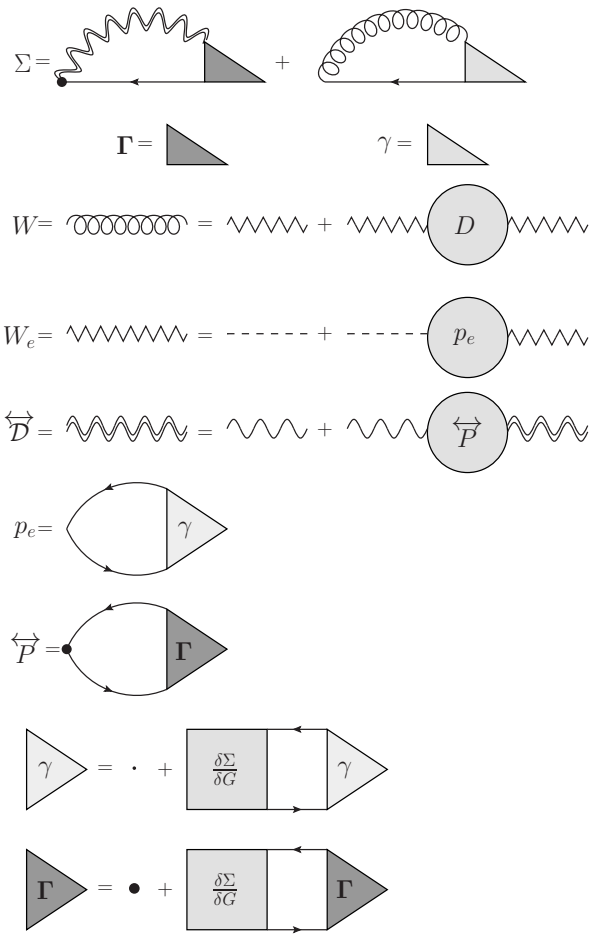

Figure 2.2: Diagrammatic representation of the Hedin's equations. The bullet represents a $\mathbf{\Pi}$ differential operator, defined in Eq. (2.53).

the D propagator can be thought as to be given and the purely electronic and photonic components of Hedin's equations can be solved self-consistently. We have represented the new set of Hedin's equations in diagrammatic form in Fig. 2.2 and in schematic form in Fig. 2.3. The latter representation also provides a method to solve the equations self-consistently. Starting from a reasonable approximation for the longitudinal and transverse parts of the self-energy Σ, we can evaluate the longitudinal and the transverse vertex, respectively, $\tilde{\gamma}$ and $\tilde{\mathbf{\Gamma}}$. Then we can obtain the longitudinal and transverse irreducible polarisations, $\tilde{p}_{\mathrm{e}}$ and $\overleftrightarrow{\tilde{P}}$ and incorporate the results in the photon propagator $\overleftrightarrow{\mathcal{D}}$ and, assuming that we have a good

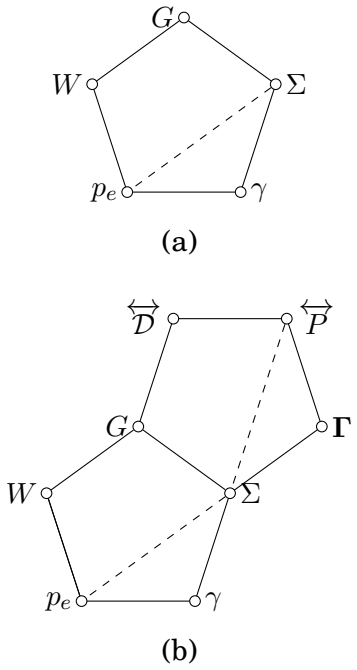

Figure 2.3: Schematic representation of the different formulations of Hedin's equations. (a) Longitudinal case. This is widely used in the literature in its equilibrium and out-of-equilibrium versions. When the interaction with the quantised electromagnetic field is switched on, a new pentagon must be added [case (b)] where the corners are the photon propagator and the transverse electronic polarisation and vertex function. The dashed lines correspond to the generalised GW approximation where all vertex functions are neglected.

description for the nuclear oscillations in the form of the phonon propagator D, the screened longitudinal interaction W. Finally, we can obtain the expression for the Green's function, G. This is analogous to the usual description for a self-consistent MBPT calculation, only that in this case we have two sub-cycles to evaluate: one for the transverse and another for the longitudinal electromagnetic field.

2.11 The *GW* approximation

The GW approximation [27] is based on the assumption that the corrections to the vertex can be ignored. In the present case, it corresponds to ignore the second term in Equations (2.89) and (2.90) so that the vertex functions acquire a simple

form:

$$\tilde{\mathbf{\Gamma}}^{GW}(1,2,3) = -\frac{4\pi}{c}\mathbf{\Pi}(1,1')\delta(1,3)\delta(1',2)|_{1'=1^+}, \tag{2.93}$$

and

$$\tilde{\gamma}^{GW}(1,2,3) = \delta(1,2)\delta(1,3). \tag{2.94}$$

As a consequence both the longitudinal and transverse polarisation functions turn into an independent-particle representation

$$\tilde{p}_{\mathrm{e}}^{GW}(1,2) = \mathrm{i}G(1,2)G(2,1), \tag{2.95}$$

and

$$\tilde{P}_{\alpha\beta}^{GW}(1,2) = \mathrm{i}\Pi_\alpha(1,1')G(1,2)\Pi_\beta(2)G(2,1')|_{1'=1}. \tag{2.96}$$

The final expression for the electronic exchange-correlation part of the self-energy in the GW approximation is then given by

$$\Sigma_{\mathbf{xc}}^{GW}(1,2) = \mathrm{i}\left[G(1,2)W(2,1) + \sum_{\alpha,\beta=1}^{3}\Pi_\alpha(1,1')G(1,2)\Pi_\beta(2)\mathcal{D}_{\beta\alpha}(2,1')\right]\Bigg|_{1'=1}. \tag{2.97}$$

The longitudinal GW self-energy has been extensively studied and its formulation for the e-e and e-p parts are well known.

2.12 The reducible representation and the Hartree self-energy

In the previous section we focused on the irreducible functions, i.e. functional derivatives of G or G^{-1} with respect to the total longitudinal potential $U(1)$ or the total vector potential $\langle A(1)\rangle$. As we saw in the the equations for the irreducible vertices [see Eqs. (2.81) and (2.82)] this means that the corresponding longitudinal/transverse Hartree component of the self-energy does not appear in kernel of the longitudinal/transverse vertex. We saw in Eq. (2.36) that we can write

$$\Sigma_{\mathbf{H}}^{\parallel}(1,2) = -\mathrm{i}\delta(1,2)w_0(1,3)G(3,3^+) \tag{2.98}$$

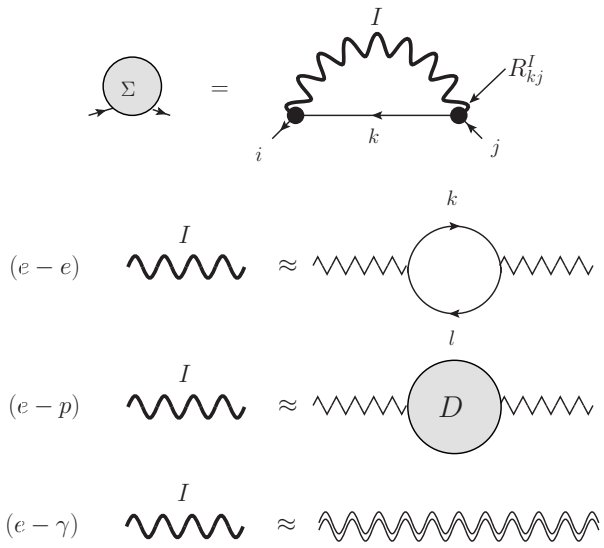

Figure 2.4: The generalised GW approximation for the three kind of interactions: e-e, e-p, and e-γ. The wiggled propagator in the e-e case represents a statically screened interaction, as explained in Ref. [40].

for the longitudinal Hartree self-energy, and

$$\Sigma^{\perp}_{\mathrm{H}}(1,2) = \delta(1,2)\frac{1}{c}\mathbf{A}_{\mathrm{ind}}(1)\cdot\boldsymbol{\Pi}(1,1')G(1,1')|_{1'=1^+} \tag{2.99}$$

for the transverse Hartree self-energy. By using Eq. (2.58) we can easily express the induced vector-potential as

$$\mathbf{A}_{\mathrm{ind}}(1) = -\frac{4\pi}{c}\overleftrightarrow{\mathcal{D}}_0(1,2)\mathbf{J}_{\mathrm{ind}}(2), \tag{2.100}$$

thus allowing us to rewrite Eq. (2.99) as

$$\Sigma^{\perp}_{\mathrm{H}}(1,2) = \delta(1,2)\frac{4\pi\mathrm{i}}{c^2}\left[\boldsymbol{\Pi}(1,1')G(1,1')\right]_{1'=1^+}\overleftrightarrow{\mathcal{D}}_0(1,3)\left[\boldsymbol{\Pi}(3,3')G(3,3')\right]_{3'=3^+}, \tag{2.101}$$

which can be taken as the energy coming from the interaction between the induced currents in the material.

Before progressing we should first present the formulations of the extended system of Hedin's equations using the reducible functions, as it is usually done in the equilibrium formalism. We start by noticing that, if in the derivation of the equation of motion for $\overleftrightarrow{\mathcal{D}}$ we use $\mathbf{A}_{\mathrm{ext}}$ in the chain rule, we then obtain

$$\overleftrightarrow{\mathcal{D}}(1,2) = \overleftrightarrow{\mathcal{D}}_0(1,2) + \overleftrightarrow{\mathcal{D}}_0(1,3)\overleftrightarrow{P}(3,4)\overleftrightarrow{\mathcal{D}}_0(4,2), \tag{2.102}$$

where $\overleftrightarrow{P}$ is the reducible transverse polarisation, given by

$$\overleftrightarrow{P}(1,2) = -\frac{4\pi}{c}\frac{\delta \mathbf{J}_{\text{ind}}(1)}{\delta \mathbf{A}_{\text{ext}}(2)} = \mathrm{i}\Pi_\alpha(1,1')G(1,3)\Gamma_\beta(3,4,2)G(4,1')|_{1'=1}. \tag{2.103}$$

In the equation above we have introduced the reducible transverse vertex, $\mathbf{\Gamma}$ which is given by

$$\begin{aligned}\mathbf{\Gamma}(1,2;3) &= -\frac{4\pi}{c}\frac{\delta G^{-1}(1,2)}{\delta \mathbf{A}_{\text{ext}}(3)} \\ &= \frac{4\pi}{c}\mathbf{\Pi}(1,1')\delta(1,3)\delta(1',2)|_{1'=1^+} + \frac{\delta\Sigma(1,2)}{\delta G(4,5)}G(4,6)\mathbf{\Gamma}(6,7,3)G(7,5),\end{aligned} \tag{2.104}$$

and unlike in Eq. (2.82), here the kernel in the second term on the right hand side has the full contribution of all the parts of the self-energy. A similar set of equations can be derived for the reducible longitudinal functions. We start from the reducible longitudinal polarisation p_{e}

$$p_{\text{e}}(1,2) = \frac{\delta\langle\hat{\rho}(1)\rangle}{\delta\phi_{\text{ext}}(2)} = \mathrm{i}G(1,3)\gamma(3,4,2)G(4,1), \tag{2.105}$$

which immediately leads to the definition of the reducible longitudinal vertex γ

$$\gamma(1,2;3) = -\frac{\delta G^{-1}(1,2)}{\delta\phi_{\text{ext}}(3)} = \delta(1,2)\delta(1,3) + \frac{\delta\Sigma(1,2)}{\delta G(4,5)}G(4,6)\gamma(6,7,3)G(7,5). \tag{2.106}$$

As it is in equilibrium theory, we can easily derive a relation between the reducible and irreducible polarisations. For the longitudinal case we obtain the usual relation

$$\begin{aligned}p_{\text{e}}(1,2) = \frac{\delta\langle\hat{\rho}(1)\rangle}{\delta U(3)}\frac{\delta U(3)}{\delta\phi_{\text{ext}}(2)} &= \tilde{p}_{\text{e}}(1,3)\left[\delta(3,2) + w_0(3,4)\frac{\delta\langle\hat{\rho}(4)\rangle}{\delta\phi_{\text{ext}}(2)}\right] \\ &= \tilde{p}_{\text{e}}(1,2) + \tilde{p}_{\text{e}}(1,3)w_0(3,4)p_{\text{e}}(4,2),\end{aligned} \tag{2.107}$$

while for the transverse case we get that

$$\begin{aligned}\overleftrightarrow{P}(1,2) = -\frac{4\pi}{c}\frac{\delta\langle\hat{\mathbf{J}}_{\text{ind}}(1)\rangle}{\delta\langle\hat{\mathbf{A}}(3)\rangle}\frac{\delta\langle\hat{\mathbf{A}}(3)\rangle}{\delta\mathbf{A}_{\text{ext}}(2)} &= \overleftrightarrow{\tilde{P}}(1,3)\left[\delta(3,2) - \frac{4\pi}{c}\overleftrightarrow{\mathcal{D}}_0(3,4)\frac{\delta\langle\hat{\mathbf{J}}_{\text{ind}}(4)\rangle}{\delta\mathbf{A}_{\text{ext}}(2)}\right] \\ &= \overleftrightarrow{\tilde{P}}(1,2) + \overleftrightarrow{\tilde{P}}(1,3)\overleftrightarrow{\mathcal{D}}_0(3,4)\overleftrightarrow{P}(4,2)\end{aligned} \tag{2.108}$$

In the equilibrium formulation of the theory, where the vector potential is not quantised, there is no need to distinguish between the longitudinal and transverse parts of the self-energy. However, we see from Eq. (2.101) that the corresponding transverse Hartree term would be expanded in powers of $1/c^2$, making it negligible unless the microscopic paramagnetic currents are very intense.

2. PROPAGATORS AND RESPONSE FUNCTIONS ON THE KELDYSH CONTOUR

Chapter 3

The time dependent BSE

"Would you tell me, please, which way I ought to go from here?"
"That depends a good deal on where you want to get to," said the cat.

Lewis Carroll, *Alice in Wonderland*

3.1 A simplified formulation using a single–time density matrix representation

The BKE [Eq. (2.56)] is very hard to solve for practical applications and in realistic materials. The reason is the complex two–times dependence and spatial non–locality that enormously increases the complexity of the problem compared to the more common methods used in the *ai*–MBPT scheme [14].

An approach that is attracting great interest is based on the reduction of the complex equation for $G(1_\alpha, 2_\beta)$ in a closed equation for the density matrix, $\rho(1) \equiv -iG(1_-, 1_+) = -iG^<(1,2)$. This approach is based on the GBKA [58] [Eq. (3.21b)] and, in the most recent approaches, on the CCA [40, 41, 59].

The aim of this section is to extend the derivation of a simplified KBE to the general case of the simultaneous presence of e-e, e-p, and e-γ interactions.

We start by expressing all quantities in the second quantisation basis

$$G(1,2) = \sum_{i,j} \phi_i^*(\mathbf{r}_1)\,\phi_j(\mathbf{r}_2)\,G_{ij}(t_1,t_2)\,, \tag{3.1}$$

$$\Sigma(1,2) = \sum_{i,j} \phi_i^*(\mathbf{r}_1)\,\phi_j(\mathbf{r}_2)\,\Sigma_{ij}(t_1,t_2)\,, \tag{3.2}$$

in such a way to remove the spatial dependence and concentrate our attention on the time arguments.

In this single-particle basis, the KBE for $G^<(t,t')$ can be rewritten in a compact, matrix-like form:

$$\left[\mathrm{i}\partial_t - h_{\mathrm{ext}}(t)\right] G^<(t,t') = \int d\bar{t}\,\left[\Sigma^r(t,\bar{t})\,G^<(\bar{t},t') + \Sigma^<(t,\bar{t})\,G^a(\bar{t},t')\right] + \text{H.c.}, \tag{3.3}$$

and its adjoint

$$\mathrm{i}\partial_{t'}G^<(t,t') - G^<(t,t')\,h_{\mathrm{ext}}(t') = \int d\bar{t}\,\left[G^r(t,\bar{t})\,\Sigma^<(\bar{t},t') + G^<(t,\bar{t})\,\Sigma^a(\bar{t},t')\right] + \text{H.c.}. \tag{3.4}$$

In Eqs.(3.3) and (3.4) the retarded/advanced functions carry a superscript r/a and are defined in terms of the lesser and greater functions according to

$$X^r(t,t') = [X^a(t',t)]^\dagger = \theta(t-t')\left[X^>(t,t') - X^<(t,t')\right], \tag{3.5}$$

where X can be G, Σ or any other two-time correlation function.

By adding the Eqs. (3.3) and (3.4), and taking the derivative on the macroscopic time-axis, $T = (t+t')/2$ we get the equation of motion for $\rho(T) = -iG^<(T,T)$

$$\frac{d}{dT}\rho(T) + \mathrm{i}\left[h_{\mathrm{ext}}(T)\,,\rho(T)\right] = -S\left[\{G\},\{\Sigma\}\right](T)\,, \tag{3.6}$$

where all the self-energy effects are embodied in the complex collision integral, given by $S\left[\{G\},\{\Sigma\}\right](T)$ that is still a function of the $\lessgtr$ two-times Green's functions and self-energies:

$$S\left[\{G\},\{\Sigma\}\right](T) = \int d\bar{t}\,\left[\Sigma^>(T,\bar{t})\,G^<(\bar{t},T) + G^<(T,\bar{t})\,\Sigma^>(\bar{t},T) - (\lessgtr\rightleftarrows\gtrless)\right]. \tag{3.7}$$

In Eq. (3.7), the $(\lessgtr\rightleftarrows\gtrless)$ indicates that the second part of the integral is obtained from the first part by exchanging $>(<)$ with $<(>)$. Such splitting has already been discussed in Refs. [15] and [40].

The collision integral includes contributions from self-energies which can be local or nonlocal in time, $\Sigma(t,t') = \Sigma_s(t)\,\delta(t-t') + \Sigma_c(t,t')$. The local part of the self-energy defines a coherent part of S moving out of the time integral:

$$S[\{G\},\{\Sigma\}](T) = S^{\mathrm{coh}}(T) + S^{\mathrm{dyn}}[\{G\},\{\Sigma\}](T). \tag{3.8}$$

The dynamical integral requires some approximations in order to reduce it to a functional of only the density. Such approximations will be introduced shortly.

The coherent part is embodied in the $h_{\mathrm{ext}}(t)$ term which turns into

$$\mathrm{i}\left[h_{\mathrm{ext}}(T),\rho(T)\right] + S[\{G\},\{\Sigma\}](T) = \mathrm{i}\left[h(T),\rho(T)\right] + S^{\mathrm{coh}}[\rho](T) + \\ + S^{\mathrm{dyn}}[\{G\},\{\Sigma\}](T), \tag{3.9}$$

with

$$S^{\mathrm{coh}}[\rho](T) = \mathrm{i}\left[\Sigma_s(T),\rho(T)\right]. \tag{3.10}$$

The different possible approximations to Σ_s reflect the different kind of physics introduced in the dynamics and can already account for important effects. Different cases can be considered:

(i) A mean-field potential that mimics the correlation effects. An example is DFT, where $\Sigma_s(t)$ is local in space and given by the sum of the Hartree and exchange-correlation potential.

(ii) HF self-energy. In this case the exclusion principle and quantum statistics (the requirement for the electronic wave function to be antisymmetric) are included. The Hartree-Fock (HF) self-energy reads:

$$\left[\Sigma_s(t)\right]_{pq} = V^{pq}_{mn}\rho_{nm}(t), \tag{3.11}$$

with the four-index tensor $V^{ij}_{mn} = 2\left[w_0\right]_{imnj} - \left[w_0\right]_{imjn}$ and $\left[w_0\right]_{imnj}$ the two-electron bare Coulomb integrals:

$$\left[w_0\right]_{imnj} \equiv \int d\mathbf{r}\,d\mathbf{r}'\phi_i^*(\mathbf{r})\,\phi_m^*(\mathbf{r}')\,v(\mathbf{r}-\mathbf{r}')\,\phi_n(\mathbf{r}')\,\phi_j(\mathbf{r}). \tag{3.12}$$

(iii) Hartree plus a Coulomb Hole and Screened Exchange (COHSEX) self-energy. In this case correlation is included using a linear-response approximation, but dynamical effects are neglected. The COHSEX self-energy reads as

$$\left[\Sigma_s(t)\right]_{pq} = V^{pq}_{mn}(t)\,\rho_{nm}(t), \tag{3.13}$$

with, now $V(t)_{\substack{ij\\mn}} = 2[w_0]_{imnj} - W[\rho(t)]_{imjn}$ and W the screened Coulomb hole potential. This is routinely calculated in the random-phase approximation (RPA) where

$$W[\rho](\mathbf{r},\mathbf{r}') \equiv \int d\overline{\mathbf{r}}\, \varepsilon^{-1}_{\mathrm{RPA}}[\rho](\mathbf{r},\overline{\mathbf{r}})\, w_0(\overline{\mathbf{r}}-\mathbf{r}'). \tag{3.14}$$

The choice of the local part of the self-energy is essential as it already describes a large part of the level of correlation embodied in the many-body dynamics. It has been formally proved, for example, that in the linear regime the COHSEX self-energy describes excitonic effects and reduces Eq. (3.6) to the well known Bethe-Salpeter equation [15].

The collision integral $S^{\mathrm{dyn}}(T)$ in Eq. (3.9) is nonlocal in time and its functional form is uniquely determined once an approximation for the correlation self-energy, Σ_c, is made. Let us consider here the GW approximation [Eq. (2.97)] that can be rewritten, by using Eq. (3.1), in a very general and compact form as

$$\Sigma^{\lessgtr}_{ij}(t,t') = \mathrm{i}\sum_I \left[(R^I)^\dagger G^{\lessgtr}(t,t')\, R^I\right]_{ij} W^{\lessgtr}_I(t,t'). \tag{3.15}$$

In Eq. (3.15), R^I and G are matrices [see Eqs. (3.1) and (3.2)] and the product in the square brackets represents a matrix multiplication. In Eq. (3.15), and from this point onward, we use the Einstein convention that repeated indices are summed over. W_I, instead, is a scalar function. R_I and W have different definitions depending on the kind of interaction they are describing.

(a) In the e-p case $I = (\mathbf{q}\lambda)$ and represents the phonon branch (λ) and momentum ($\mathbf{q}$) pair. It follows that

$$R^I_{ij} = R^{(\mathbf{q}\lambda)}_{ij} \equiv \int d\mathbf{r}\phi^*_i(\mathbf{r})\, \partial_{\mathbf{q}\lambda} V_n(\mathbf{r})\, \phi_j(\mathbf{r}), \tag{3.16}$$

with $\partial_{\mathbf{q}\lambda}$ the derivative of the bare ionic potential (V_n) along the phonon state $(\mathbf{q}\lambda)$. Note that, if the present formalism is applied on top of DFT, $V_n(\mathbf{r})$ is replaced by the dressed self-consistent derivative of the DFT ionic potential as discussed in Ref. [30].

(b) In the e-γ case the I index represents the photon polarisation index (λ) and momentum ($\mathbf{q}$) and

$$R^I_{ij} = \int d\mathbf{r}\, e^{\mathrm{i}\mathbf{q}_I\cdot\mathbf{r}} \phi^*_i(\mathbf{r})\, (\mathbf{e}_\lambda\cdot\nabla)\, \phi_j(\mathbf{r}). \tag{3.17}$$

(c) In the e-e case the derivation of the analytic expression for R^I is more mathematically involved. At the same time, however, this procedure has been extensively studied in the literature. We take as reference [40, 60] to rewrite the out-of-equilibrium screened e-e interaction as an effective interaction with a time-dependent plasma of electron-hole pairs with scattering amplitudes given by

$$R_{ij}^{I}=\int d\mathbf{r}\,\phi_{i}^{*}\left(\mathbf{r}\right)W\left[\rho\right]\left(\mathbf{r},\mathbf{r}'\right)\phi_{j}\left(\mathbf{r}\right)\left[\Phi_{I}\left(\mathbf{r}'\right)\right], \tag{3.18}$$

where $I=(k,l)$ and $\Phi_{I}\left(\mathbf{r}\right)\equiv\phi_{k}^{*}\left(\mathbf{r}\right)\phi_{l}\left(\mathbf{r}\right)$. In this case, indeed, the elemental excitations are electron-hole pairs (k,l).

In all of the three cases above, W has the form

$$W_{I}^{\lessgtr}\left(t,t'\right)\equiv W_{I}^{\lessgtr}\left(t-t'\right)\equiv\left(-\mathrm{i}\right)N_{I}^{\pm}e^{\pm\mathrm{i}\omega_{I}\left(t-t'\right)}. \tag{3.19}$$

In Eq. (3.19), $N_I^{\pm}$ acquires different meanings depending on the interaction. In the e-p case it represents the occupation of the phonon bath at a given temperature that, for simplicity, we assume to follow Bose-Einstein statistics[1]. As such, in the e-p and e-γ cases we will have that $N_{I}^{+}=N_{I}\left(\beta\right)+1$ and $N_{I}^{-}=N_{I}\left(\beta\right)$, where $N_{I}\left(\beta\right)$ is the Bose occupation and $\beta=1/k_{B}T_{lt}$, with k_B the Boltzmann constant and T_{lt} the lattice temperature. In the e-e case then $N_{kl}^{+}=\rho_{kk}\left(t\right)\left[1-\rho_{ll}\left(t\right)\right]$ and $N_{kl}^{-}=\rho_{ll}\left(t\right)\left[1-\rho_{kk}\left(t\right)\right]$. By using Eq. (3.19) into Eq. (3.15) we get that

$$\Sigma_{ij}^{\lessgtr}\left(t,t'\right)=\sum_{I}\left[\left(R^{I}\right)^{\dagger}G^{\lessgtr}\left(t,t'\right)R^{I}\right]_{ij}N_{I}^{\pm}e^{\pm\mathrm{i}\omega_{I}\left(t-t'\right)}. \tag{3.20}$$

3.2 Generalised Baym-Kadanoff ansatz

Now that $W^{\lessgtr}$ is rewritten in Eq. (3.19) as a function of the time difference, in order to close Eq. (3.6) in the space of the single-time density matrices we introduce the

[1] In order to have a full time evolving picture where the occupation functions of photons and phonons are time dependent and different from the distributions at equilibrium we would need to carry out an extended derivation by taking into account the simultaneous set of equations of motion for the occupation functions of electrons, phonons, and photons.

generalised Baym-Kadanoff ansatz. The GBKA is an ansatz for $G^{\lessgtr}$ which turns it, and hence the collision integral, into a functional of ρ and $G^{r/a}$:

$$G^{<}(t,t') = -G^{r}(t-t')\rho(t') + \rho(t)G^{a}(t-t'), \tag{3.21a}$$

$$G^{>}(t,t') = +G^{r}(t-t')\bar{\rho}(t') - \bar{\rho}(t)G^{a}(t-t'), \tag{3.21b}$$

where $\bar{\rho} = 1 - \rho$. It is necessary to express the propagator G^{r} as a functional of ρ, so that we can transform $S^{\mathrm{dyn}}(t)$ into a functional of the density matrix, and by doing that closing Eq. (3.6). Reasonable approximations to the propagator will depend on the system which we are studying, with one of the most common being the quasi-particle (QP) propagator

$$G^{r}(t,t') = -\mathrm{i}\theta(t-t')Te^{-\mathrm{i}\int_{t'}^{t} d\bar{t}\, h^{\mathrm{qp}}(\bar{t})}. \tag{3.22}$$

In the case of (small) finite systems, the choice $h^{\mathrm{qp}} = h^{\mathrm{eq}}$ (usually h^{eq} is the HF single-particle Hamiltonian) is a good choice[1]. For extended systems, however, relaxation requires a damping factor which we lack in h^{eq}, thus preventing the system to relax. In these cases we can correct the propagator by adding non-Hermitian terms given by the quasi-particle lifetimes $h^{\mathrm{qp}} = h^{\mathrm{eq}} + \mathrm{i}\eta$ [33, 40, 61, 63, 64].

By using Eq. (3.20) we rewrite $S^{\mathrm{dyn}}(T)$ as:

$$\begin{aligned} S_{ij}^{\mathrm{dyn}}[\{G\},\{\Sigma\}](T) &\equiv S_{ij}^{\mathrm{dyn}}[\{G\}](T) \\ &= \mathrm{i}\sum_{I}\int dt\Big\{\Big[\left(R^{I}\right)^{\dagger} G^{>}(T,t')R^{I}G^{<}(t',T)\Big]_{ij} W_{I}^{>}\left(T-t'\right) \\ &\quad + \Big[G^{<}(T,t')\left(R^{I}\right)^{\dagger} G^{>}(t',T)R^{I}\Big]_{ij} W_{I}^{>}\left(t'-T\right) - (\lessgtr)\Big\}, \end{aligned} \tag{3.23}$$

and, finally, we use Eqs. (3.21b) and (3.21b′), to rewrite the first terms of Eq. (3.23):

$$\begin{aligned} &\Big[\left(R^{I}\right)^{\dagger} G^{>}(T,t')R^{I}G^{<}(t',T)\Big]_{ij} W_{I}^{>}\left(T-t'\right) \\ &\quad = (-\mathrm{i})\sum_{\pm}\Big[\left(R^{I}\right)^{\dagger} G^{\mathrm{r}}(T-t')\bar{\rho}\left(t'\right) R^{I}\rho\left(t'\right) G^{\mathrm{a}}(t'-T)\Big]_{ij} N_{I}^{\pm} e^{\pm\omega_{I}(T-t')}, \end{aligned} \tag{3.24}$$

with $\bar{\rho}_{ij}(T) \equiv \delta_{ij} - \rho_{ij}(T)$. We now notice that, because of the time ordering of $G^{r/a}$, the integral in Eq. (3.23) runs between $-\infty$ and T.

[1] This means that any deviation introduced by fast dynamics and e-e and e-p interactions is ignored [61, 62].

In order to obtain a final expression that can be easily compared with the Boltzmann equation we use a drastic but simple approximation for $G^{\mathrm{r/a}}$ based on the non-interacting approximation:

$$G_{ij}^{r}\left(T\right)\approx-\mathrm{i}\theta\left(T\right)e^{-\mathrm{i}\varepsilon_{i}T}\delta_{ij}. \tag{3.25}$$

Equation (3.25) allows us to carry on to the final steps of the derivation in a more comfortable way by introducing the scattering matrix S_{ij}^{Is} as

$$S_{ij}^{Is}\left(T\right)\equiv-\mathrm{i}\int_{-\infty}^{T}dt\left[e^{-\mathrm{i}s\omega_{I}t}\left(R_{ki}^{I}\right)^{*}e^{\mathrm{i}(\varepsilon_{j}-\varepsilon_{k})(T-t)}\right]\times\underbrace{\left[\overline{\rho}_{kl}\left(t\right)R_{ln}^{I}\rho_{nj}\left(t\right)N_{I}^{-s}-\rho_{kl}\left(t\right)R_{ln}^{I}\overline{\rho}_{nj}\left(t\right)N_{I}^{s}\right]}_{\xi_{kj}^{Is}\left(t\right)}. \tag{3.26}$$

In Eq. (3.26), we have also defined the $\xi_{kj}^{Is}\left(t\right)$ function. The $S^{\mathrm{dyn}}\left(T\right)$ can be finally rewritten in terms of S as

$$S_{ij}^{\mathrm{dyn}}\left(T\right)\equiv\mathrm{i}\sum_{I,\pm}\left[e^{\mathrm{i}s\omega_{I}T}S_{ij}^{Is}\left(T\right)+\mathrm{H.c.}\right]. \tag{3.27}$$

3.3 Completed collision approximation

The time integral in Eq. (3.26) can be removed analytically by using the completed collision approximation. This is based on the *adiabatic* ansatz introduced in Ref. [41] which is based on the assumption that the characteristic time scales of the electronic dynamics are much longer compared to the time window where the physical properties are calculated. We will discuss more in detail the adiabatic ansatz in the next sections. Here we just formulate it by approximating $\xi_{kj}^{Is}\left(t\right)\approx\xi_{kj}^{Is}\left(T\right)$ in Eq. (3.26), so to take it outside the time integral. At this point, this can be solved analytically leading to the final expression for the S function:

$$S_{ij}^{Is}\left(T\right)\approx\left(-\mathrm{i}\right)\left(R_{ki}^{I}\right)^{*}\frac{e^{-\mathrm{i}s\omega_{I}T}}{\varepsilon_{k}-\varepsilon_{j}-s\omega_{I}+\mathrm{i}0^{+}}\xi_{kj}^{Is}\left(T\right). \tag{3.28}$$

By plugging Eq. (3.28) into (3.27) we get the final, explicit, form of $S^{\mathrm{dyn}}\left(T\right)$:

$$S_{ij}^{\mathrm{dyn}}\left(T\right)=-\mathrm{i}\sum_{Is}\left[\frac{\left(R_{ki}^{I}\right)^{*}\overline{\rho}_{kl}\left(T\right)R_{ln}^{I}\rho_{nj}\left(T\right)N_{I}^{-s}-\left(R^{I}\right)_{ik}^{\dagger}\rho_{kl}\left(T\right)R_{ln}^{I}\overline{\rho}_{nj}\left(T\right)N_{I}^{s}}{\left(\varepsilon_{k}-\varepsilon_{j}-s\omega_{I}-\mathrm{i}0^{+}\right)}-\mathrm{H.c.}\right]. \tag{3.29}$$

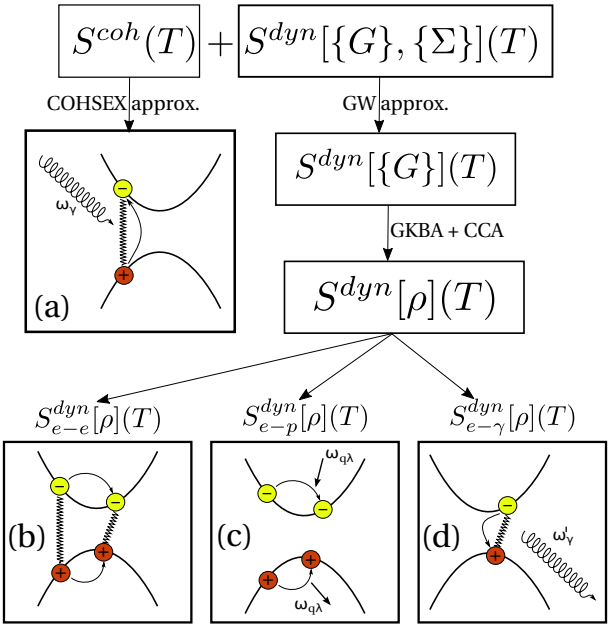

Figure 3.1: Schematic representation of the different links between the terms of Eq. (3.31) and the most elemental physical processes occurring in a typical pump-and-probe experiment: the photo excitation (a), the relaxation via e-e scattering (b), the relaxation and dissipation via e-p scattering (c), and the final, slow, radiative recombination (d). It is crucial to note that the use of Σ_{COHSEX} allows to include excitonic effects (caused by the electron-hole attraction) in all the processes.

Equation (3.29) represents an important result of this work. It shows that for any kind of interaction (e-e, e-p, e-γ) the scattering term of the equation of motion for the density matrix can be rewritten in a closed form. Now, before moving to the next section where we will turn Eq. (3.29) into a working scheme to calculate several quantities, we want to analyse in detail the structure of S^{dyn} in order to draw its very general properties. In simple terms Eq. (3.29) represents an elemental scattering event, where an initial state (i) is scattered in a series of states [(k), (l), (n), and finally (j)] via the emission/absorption of an elemental excitation (photon, e-h pair, phonon).

In order to see this graphically, we proceed as follows. We associate a density matrix $\rho_{ij}(T)$ with a single line connecting the state j to the state i, while $\overline{\rho}_{ij}(T)$ is represented by a double line. A large circle (◯) will represent a generic interaction matrix R^I. A label $\overline{I}$ will denote an adjoint matrix $\left(R^I\right)^\dagger$. A wiggled line, instead,

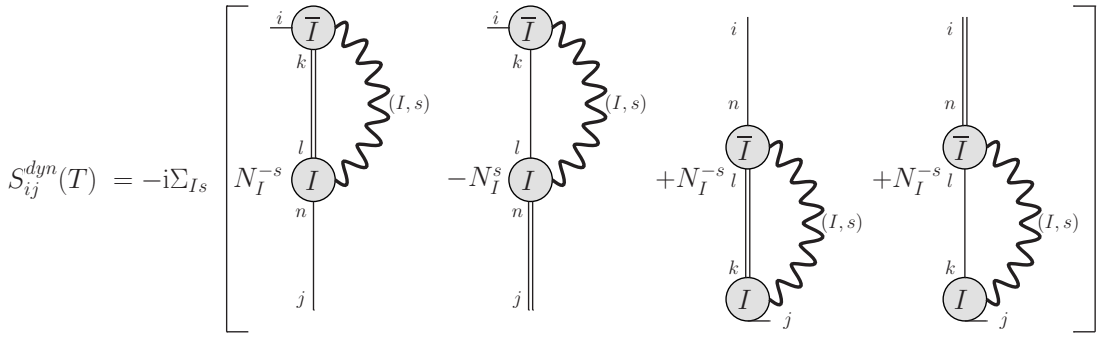

Figure 3.2: Graphical representation of Eq. (3.29). A single line represents the density matrix ρ, while the double line is its adjoint, $\overline{\rho}$. The wiggled line, in the spirit of Fig. 2.4, represents a generic interaction propagator.

represents the propagation of an excitation (I, s). By using these simple rules $S_{ij}^{\mathrm{dyn}}(T)$ can be graphically represented as shown in Fig. 3.2.

Now, the next step is to link the properties of $S^{\mathrm{dyn}}(T)$ to the actual quantities that are measured in a typical pump-and-probe experiment. The procedure that reduces the complex dynamical equation to the simple Eq. (3.29) form is schematically represented in Fig. 3.1.

3.4 Carrier dynamics, transient absorption, and light emission in the adiabatic regime

In the typical experiment sketched in Fig. 1.2, a strong pump laser field is followed by a second weaker probe field whose physical properties are measured as a function of the pump-probe temporal delay. The low intensity of the probe and pump field and their temporal duration and delay can be used to simplify further the equations. Those are the physical basis for the low-intensity approximation and for the introduction of the adiabatic ansatz regime. These two special regimes are motivated by well-defined physical arguments that are introduced in this section.

The aim of this section is to use the fact that Eq. (3.29) is closed in the space of the density matrices and rewrite all possible observables relevant to the dynamics schematically represented in Fig. 1.2 as functions of the time-dependent density matrix.

3.4.1 Adiabatic ansatz

The adiabatic ansatz has been first introduced in Ref. [41] and in the following we present a short review in order to introduce the physical basis for the low-intensity and completed collision approximations. The temporal geometry of the pump and probe fields must appear explicitly in Eq. (2.19) connected to two components of the external charge

$$\rho_{\mathrm{ext}}(1) = \rho^{p}_{\mathrm{ext}}(1) + \rho^{P}_{\mathrm{ext}}(1), \tag{3.30}$$

with $\rho^{P/p}$ referring to, respectively, the pump/probe components of the external charge. These terms define the pump and probe fields, $\mathbf{E}^{P/p}(1) = -\nabla\phi^{P/p}_{\mathrm{ext}}(1)$. In a P&p experiment we have that, in general, $|\mathbf{E}^{P}| \gg |\mathbf{E}^{p}|$ and the two fields are separated by a temporal delay τ.

The delay time τ is a crucial ingredient of the dynamics. Indeed the pump field excitation induces several processes with different time-scales. The laser excitation induces off-diagonal matrix elements of the density matrix ρ_{ij}, which in turn corresponds to a laser-induced current $\mathbf{J}(1) = \sum_{ij}\mathbf{j}_{ij}(\mathbf{r}_1)\rho_{ji}(t_1)$, with $\mathbf{j}_{ij}$ the matrix elements of Eq. (2.7a). The time-scale which describes the decay of the polarisation and of the current, τ_{pol}, is dictated by relaxation processes.

At the same time, the pump excites electrons from the valence to the conduction bands and these carriers first relax towards the band minimum (in the case of electrons) and band maximum (in the case of holes). This relaxation occurs on a time scale τ_{carr}. Thus, after a time $\tau_{\max} = \max(\tau_{\mathrm{pol}}, \tau_{\mathrm{carr}})$, we may say that the system is in a quasi-stationary state. In this regime the time to relax back to the ground state is dictated by e-γ scattering and can be of the order of picoseconds.

The key assumption of the adiabatic ansatz is that the delay τ is chosen in such a way that, for times $t \approx \tau$, we have that $\rho(t + \Delta t) \approx \rho(t)$, if $\Delta t \ll \tau_{\max}$. The fundamental idea of such approximation is that, during the measurement process, the non-equilibrium configuration of the system is frozen.

By using Eq. (3.30) in the external interaction term of h, we can now make explicit the different terms contributing to Eq. (3.6). We start by using the COHSEX for the coherent part, and by splitting S^{dyn} in the three terms induced by the

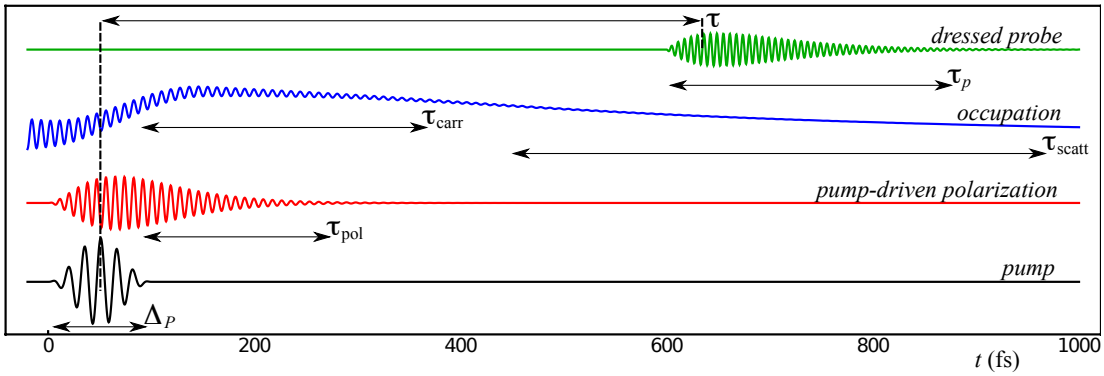

Figure 3.3: Depiction of the characteristic times which control a pump-and-probe experiment: Δ_{P} is the duration of the laser pump; τ_{p} is the lifetime of the dressed probe; τ_{carr} the time needed for occupations to stabilise; τ_{pol} is the duration in which the polarisation dephases; τ_{scatt} is the time needed to return to an equilibrium state. The delay between the pump and the probe fields, τ, is also displayed. Picture taken from Ref. [41].

different possible interactions

$$\frac{d}{dT}\rho\left(T\right)+\mathrm{i}\left[h_{\mathrm{ext}}\left(T\right),\rho\left(T\right)\right] = -S^{\mathrm{coh}}\left[\rho\right]\left(T\right)-S_{e-e}^{\mathrm{dyn}}\left[\rho\right]\left(T\right)-S_{e-p}^{\mathrm{dyn}}\left[\rho\right]\left(T\right)-S_{e-\gamma}^{\mathrm{dyn}}\left[\rho\right]\left(T\right). \quad (3.31)$$

The physical contents of the above equations are made clear by Eq. (3.29). In all the three cases the elemental process described by S^{dyn} is a single transition from the electronic state i to the electronic state j by spanning all possible intermediate states composed by an electron in the level k and a plasma (e-e case), phonon (e-p case), and photon (e-γ) excitation. The fact that it is a single transition is a consequence of the use of a GW approximation.

We start by noticing that, when the external pump and probe fields are zero, ρ is diagonal:

$$\rho_{ij}\left(T\right)|_{\mathbf{E}^{P}=\mathbf{E}^{p}=\mathbf{0}}=\delta_{ij}f_{i}. \quad (3.32)$$

Equation (3.31) is a non-linear equation whose non-linearity is driven by the pump field. This non-linearity mixes the diagonal and off-diagonal components of ρ creating a complex interplay between the induced carrier occupations and the related polarisation. However, in the case of a low-intense pumping field, if the system has

reached the quasi-stationary state, we can approximate in the right-hand side of Eq. (3.29):

$$\rho_{kl}(T) \approx \delta_{kl} f_k(T), \tag{3.33a}$$

$$\overline{\rho}_{kl}(T) \approx \delta_{kl} [1 - f_k(T)]. \tag{3.33b}$$

We will refer to this set of approximations as low-intensity approximation (LIA). This is a well-established physical regime used in a wealth of experimental setups where the density of carriers created in the conduction bands is low enough to not alter substantially the physical properties of the material.

3.4.2 Carrier dynamics

In the LIA, the complex structure of the dynamical kernel in Eq. (3.29) can be further reduced to a compact and simple form:

$$S_{ij}^{\mathrm{dyn}}(T) \approx S_{ij}^{\mathrm{dyn}}(T)\Big|_{\mathrm{LIA}} = \mathrm{i}\sum_n \Big[\gamma_{ijn}^{(-)}(T)\,\rho_{nj}(T) + \rho_{in}(T)\,\gamma_{nij}^{(+)}(T) - \tilde{\gamma}_{ijn}^{(-)}(T)\,\overline{\rho}_{nj}(T) - \overline{\rho}_{in}(T)\,\tilde{\gamma}_{nij}^{(+)}(T)\Big], \tag{3.34}$$

with

$$\gamma_{ijn}^{(\pm)}(T) = (-\mathrm{i})\sum_{Is} \frac{\left(R_{ki}^I\right)^* f_k(T)\, R_{kn}^I N_I^{-s}}{(\varepsilon_k - \varepsilon_j - s\omega_I \pm \mathrm{i}0^+)}, \tag{3.35a}$$

$$\tilde{\gamma}_{ijn}^{(\pm)}(T) = (-\mathrm{i})\sum_{Is} \frac{\left(R_{ki}^I\right)^* (1 - f_k(T))\, R_{kn}^I N_I^{s}}{(\varepsilon_k - \varepsilon_j - s\omega_I \pm \mathrm{i}0^+)}. \tag{3.35b}$$

In obtaining Eqs. (3.34), (3.35a), and (3.35b) we have used the LIA only on the internal density matrices as their indexes are free and do not impose the S^{dyn} to be diagonal.

We can now link Eq. (3.31) to the complex dynamics we were aiming at describing at the beginning of this work, schematically represented in Fig. 1.2. Physically, the different contributions to S^{dyn} represent the different channels that concur to the dynamics following the primary pump excitation. To see in practice their effect we move to the splitting of Eq. (3.31) in carrier and polarisation dynamics.

The equation of motion for the carrier occupations is readily obtained by taking the diagonal components of the ρ, solution of Eq. (3.31). In this case, the diagonal components of S^{dyn} acquire a simple interpretation. Indeed, from Eqs. (3.34), (3.35a), and (3.35b) it immediately follows that

$$\begin{aligned} S_{ii}^{\mathrm{dyn}}(T)\Big|_{\mathrm{LIA}} = 2\pi \sum_{Isk} |R_{ki}^{I}|^2 \big[& (1 - f_k(T)) f_i(T) \delta(\varepsilon_i - \varepsilon_k - s\omega_I) N_I^{-s} \\ & - f_k(T) (1 - f_i(T)) \delta(\varepsilon_i - \varepsilon_k - s\omega_I) N_I^{s} \big] \\ & = \sum_I \gamma_i^{(I,e)}(T) \rho_{ii}(T) - \gamma_i^{(I,h)}(T) \overline{\rho}_{ii}(T). \end{aligned} \tag{3.36}$$

Equation (3.36) represents a generic Markovian scattering of the electron/hole [labelled by the (e/h) superscripts] in the state i to the generic state k mediated by the emission ($s = +1$) or absorption ($s = -1$) of a generic boson of energy ω_I. In the e-e case, this boson is an additional electron-hole pair. In the e-p case the boson is a phonon, and in the e-γ channel it is a photon.

In the e-p and e-e cases, Eq. (3.36) reduces to the equation derived previously [40] and applied to the interpretation of the time-resolved two-photon photon-emission experiment of bulk silicon [21]. However, the present case extends the derivation to the e-γ channel. This extension defines in a pure NEQ framework the radiative electron/hole lifetimes. At difference with the usual formulation [65] the γ_i lifetimes are time-dependent and depend on the time fluctuations of the carrier occupations. Moreover, by means of the presence of S^{coh}, the coupling with the external laser field is correctly described.

3.4.3 Light absorption

Starting from the equilibrium condition, an external field will induce an electronic dipole defined as the expectation value of the dipole operator, which in turn is defined in terms of the density matrix

$$\hat{d} = \eta_p \cdot \hat{\mathbf{d}} \equiv \int d\mathbf{r}\, (\eta_p \cdot \mathbf{r}) \hat{\rho}(\mathbf{r}, \mathbf{r}) = d_{ij} \hat{\rho}_{ji}, \tag{3.37}$$

with $d_{ij} = \int d\mathbf{r}\, \varphi_i^*(\mathbf{r})(\eta_p \cdot \mathbf{r}) \varphi_j(\mathbf{r})$ the dipole matrix elements. For simplicity, in Eq. (3.37), we have assumed that the pump and probe fields are polarised along

the $\eta_{\mathbf{p}}$ direction. The time-dependent expectation value of the dipole operator, $d\left(T\right)$, is then given by

$$d\left(T\right)=\langle\Psi\left(T\right)|\hat{d}|\Psi\left(T\right)\rangle=d_{ij}\langle\Psi\left(T\right)|\hat{\rho}_{ji}|\Psi\left(T\right)\rangle, \tag{3.38}$$

and can be calculated using the electronic reducible polarisation function $p_{\mathrm{e}}(1,2)$ as

$$\delta d\left(T\right)=d_{ij}\int dt'p_{\substack{ji\\lk}\mathrm{,e}}\left(T,t'\right)d_{kl}E_{p}\left(t'\right)=\int dt'\left[d\circ\chi\left(T,t'\right)\circ d\right]E_{p}\left(t'\right). \tag{3.39}$$

In Eq. (3.39) we used the conventions listed in App. C [see Eq. (C.2)].

The absorption coefficient $\mathfrak{S}^{\tau}\left(\omega\right)$ can be easily calculated from the density-density linear response function, χ, as [41]

$$\mathfrak{S}^{\tau}\left(\omega\right)=-2\omega|e\left(\omega\right)|^{2}\Im\left[d\circ\chi^{\tau}\left(\omega\right)\circ d\right], \tag{3.40}$$

with $\chi^{\tau}\left(\omega\right)$ defined in Sec.3.5 and obtained from $\chi\left(t,t'\right)$ by applying the adiabatic ansatz. The problem is now how to calculate χ.

From Eq. (3.39) and the definition of the total (external plus induced) scalar field [Eq. (2.30)] we know that the matrix components of the reducible electronic polarisation function can be written as

$$\chi_{\substack{ji\\lk}}\left(t,t'\right)=-\mathrm{i}\theta\left(t-t'\right)\langle\Psi_{g}|\left[\hat{c}_{iH}^{\dagger}\left(t\right)\hat{c}_{jH}\left(t\right),\hat{c}_{kH}^{\dagger}\left(t'\right)\hat{c}_{lH}\left(t'\right)\right]|\Psi_{g}\rangle, \tag{3.41}$$

which, together with its irreducible counter-part $\tilde{\chi}$, can be rewritten respectively as derivatives of the time-dependent density-matrix with respect to the total or the external potential

$$\tilde{\chi}_{\substack{ji\\lk}}\left(t,t'\right)=\frac{\delta\rho_{ij}\left(t\right)}{\delta U_{kl}\left(t'\right)}, \tag{3.42a}$$

$$\chi_{\substack{ji\\lk}}\left(t,t'\right)=\frac{\delta\rho_{ij}\left(t\right)}{\delta\phi_{kl}^{\mathrm{ext}}\left(t'\right)}. \tag{3.42b}$$

The derivation of the equation of motion for both χ and $\tilde{\chi}$ is obtained by applying the functional derivatives to the equation of motion for $\rho\left(T\right)$[1]:

$$\frac{d}{dt}\left\{\frac{\delta\rho_{ji}\left(t\right)}{\delta\phi_{kl}^{\mathrm{ext}}\left(t'\right)}\right\}=\frac{\delta}{\delta\phi_{kl}^{\mathrm{ext}}\left(t'\right)}\left\{-\mathrm{i}\left[h_{\mathrm{ext}}\left(t\right),\rho\left(t\right)\right]_{ji}-S_{ji}^{\mathrm{coh}}\left[\rho\right]\left(t\right)-S_{ji}^{\mathrm{dyn}}\left[\rho\right]\left(t\right)\right\}. \tag{3.43}$$

[1]The time derivative operator and the functional derivative operator can be exchanged since we are considering a variation in the functional dependence due to a change in the functions, but not in the coordinates.

The first term on the right-hand side of Eq. (3.43) is

$$\frac{\delta}{\delta\phi_{kl}^{\mathrm{ext}}\left(t'\right)}\left\{\left[h_{\mathrm{ext}}\left(t\right),\rho\left(t\right)\right]_{ji}\right\}=\left[\delta_{jk}\rho_{li}\left(t\right)-\rho_{jk}\left(t\right)\delta_{li}\right]\delta\left(t-t'\right)+\left[h_{\mathrm{ext}}\left(t\right),\tilde{\chi}\left(t,t'\right)\right]_{\substack{ji\\lk}}, \tag{3.44}$$

where we have used the compact form given by Eq. (C.4) to write the last term of Eq. (3.44). The derivative of S^{coh} can be evaluated within the COHSEX approximation for Σ_s, Eq. (3.13),

$$\frac{\delta S_{ji}^{\mathrm{coh}}\left(t\right)}{\delta\phi_{kl}^{\mathrm{ext}}\left(t'\right)}=\mathrm{i}\left[\frac{\delta\Sigma^{s}(t)}{\delta\phi_{kl}^{\mathrm{ext}}\left(t'\right)},\rho(t)\right]_{ji}=\mathrm{i}\left[K_{s}\circ\tilde{\chi}(t,t'),\rho(t)\right]_{\substack{ij\\kl}} \tag{3.45}$$

In order to evaluate the functional derivative acting on the S^{dyn} functions we use the following chain rule:

$$\frac{\delta}{\delta\phi_{kl}^{\mathrm{ext}}\left(t'\right)}=\int d\bar{t}\,\frac{\delta\rho_{mn}\left(\bar{t}\right)}{\delta\phi_{kl}^{\mathrm{ext}}\left(t'\right)}\frac{\delta}{\delta\rho_{mn}\left(\bar{t}\right)}, \tag{3.46}$$

so that

$$\frac{\delta}{\delta\phi_{kl}^{\mathrm{ext}}\left(t'\right)}S_{ji}^{\mathrm{dyn}}\left[\rho\right]\left(t\right)=\int d\bar{t}\,\left[K^{\mathrm{dyn}}\left(t,\bar{t}\right)\circ\tilde{\chi}\left(\bar{t},t'\right)\right]_{\substack{ji\\lk}}. \tag{3.47}$$

Thus, the final equation for the longitudinal two-times linear response function becomes

$$\frac{d}{dt}\tilde{\chi}\left(t,t'\right)+\mathrm{i}\left[h_{\mathrm{ext}}\left(t\right),\tilde{\chi}\left(t,t'\right)\right]+\mathrm{i}\left[K^{s}\circ\chi(t,t')+\mathbb{1}\delta\left(t-t'\right),\rho\left(t\right)\right]=-\int d\bar{t}\,\left[K^{\mathrm{dyn}}\left(t,\bar{t}\right)\circ\tilde{\chi}\left(\bar{t},t'\right)\right]. \tag{3.48}$$

As explained in Sec. 3.5, the non-local time dependence of the left-hand side of Eq. (3.48) can be simplified by using the adiabatic ansatz. The most complicated term remains the dynamical kernel, K^{dyn}, that we will extensively discuss in Sec. 3.4.5. Indeed, K^{dyn} is a common ingredient of the equations describing both the light absorption and emission.

3.4.4 Light emission

Thanks to the quantisation of the electromagnetic field, we can now derive a closed expression for the light-emission spectrum. As it will be clear shortly the present

formulation allows to introduce coherently the combined effects induced by the e-e and e-p coupling. This represents an important step forward compared to the state-of-the-art formulation and, more importantly, it allows an efficient "merging" with DFT.

In order to derive the expression for the light emission spectrum in terms of the density matrix and use Eq. (3.31) to create a link with the density-matrix equation of motion, we use here the Poynting vector. In its Hermitian form this vector is written as

$$\hat{\mathbf{S}}(1) = \frac{c}{8\pi}\left[\hat{\mathbf{E}}^\dagger(1)\times\hat{\mathbf{B}}(1) - \hat{\mathbf{B}}^\dagger(1)\times\hat{\mathbf{E}}(1)\right] = \frac{c}{8\pi}\left[\hat{\mathbf{E}}^\dagger(1)\times\hat{\mathbf{B}}(2) - \hat{\mathbf{B}}^\dagger(2)\times\hat{\mathbf{E}}(1)\right]\Big|_{2=1}. \quad (3.49)$$

The Poynting theorem relates the change in the energy of the energy density of the electromagnetic field $\langle\hat{u}(1)\rangle$ with the Poynting vector through its divergence

$$\frac{\partial\langle\hat{u}(1)\rangle}{\partial t_1} = -\langle\hat{\mathbf{J}}(1)\cdot\hat{\mathbf{E}}(1)\rangle - \frac{1}{c}\nabla_1\cdot\langle\hat{\mathbf{S}}(1)\rangle\,. \quad (3.50)$$

The first term on the right-hand-side of Eq. (3.50) reflects the amount of energy per time and per volume which is transferred to electrons through mechanical work, while the second term the energy which escapes the system as radiation. Thus, we can write the power spectrum of the system $I(1)$, i.e., the energy per time per volume which escapes the system due to the quantum correlations in the material as the Fourier transform of the divergence of $\langle\hat{\mathbf{S}}(1)\rangle$ with respect to time

$$I(\mathbf{r}_1,\omega) = \nabla\cdot\langle\hat{\mathbf{S}}(\mathbf{r}_1,\omega)\rangle_{\text{corr}}\,. \quad (3.51)$$

We now take the relations between the fields and the vector potential which, in Coulomb's gauge ($\nabla\cdot\mathbf{A}=0$), are given by

$$\hat{\mathbf{E}}(1) = -\frac{1}{c}\frac{\partial\hat{\mathbf{A}}(1)}{\partial t_1}, \quad (3.52a)$$

$$\hat{\mathbf{B}}(1) = \nabla\times\hat{\mathbf{A}}(1). \quad (3.52b)$$

By using Eqs. (3.52a) and (3.52b), we can write explicitly the expression for the lesser and greater transverse photon propagator as

$$\mathcal{D}^<_{\alpha\beta}(1,2) = \frac{1}{4\pi\mathrm{i}}\left[\langle\hat{A}_\beta(2)\hat{A}_\alpha(1)\rangle - \langle\hat{A}_\alpha(1)\rangle\langle\hat{A}_\beta(2)\rangle\right], \quad (3.53a)$$

$$\mathcal{D}^>_{\alpha\beta}(1,2) = \frac{1}{4\pi\mathrm{i}}\left[\langle\hat{A}_\alpha(1)\hat{A}_\beta(2)\rangle - \langle\hat{A}_\alpha(1)\rangle\langle\hat{A}_\beta(2)\rangle\right]. \quad (3.53b)$$

It is now possible to split the expectation value of the Poynting vector into two parts: a classical part which contains the information of the macroscopic effects

$$\langle \hat{S}_\alpha(1)\rangle_{\rm class} = \frac{1}{2}\sum_{\substack{\beta=1\\ \beta\neq\alpha}}^{3} \frac{\partial\,\langle \hat{A}_\beta(1)\rangle}{\partial t_1}\left[\frac{\partial\,\langle \hat{A}_\alpha(2)\rangle}{\partial r_{2,\beta}} - \frac{\partial\,\langle \hat{A}_\beta(2)\rangle}{\partial r_{2,\alpha}}\right], \tag{3.54}$$

and a contribution due solely to correlation effects

$$\langle \hat{S}_\alpha(1)\rangle_{\rm corr} = \frac{1}{2}\sum_{\substack{\beta=1\\ \beta\neq\alpha}}^{3} \frac{\partial}{\partial t_1}\left\{\frac{\partial}{\partial r_{2,\beta}}\left[\mathcal{D}^{>}_{\beta\alpha}(1,2)+\mathcal{D}^{<}_{\beta\alpha}(1,2)\right]\right.$$
$$\left. -\frac{\partial}{\partial r_{2,\alpha}}\left[\mathcal{D}^{>}_{\beta\beta}(1,2)+\mathcal{D}^{<}_{\beta\beta}(1,2)\right]\right\}\Big|_{2=1}. \tag{3.55}$$

Equation (3.55) demonstrates that the evaluation of the light emission spectrum is linked to the calculation of the lesser and greater transverse photon propagators that can be rewritten in terms of the advanced/retarded counterparts and the transverse response function [11]

$$\overleftrightarrow{\mathcal{D}}^{\gtrless}(1,2) = \overleftrightarrow{\mathcal{D}}^{r}(1,3)\overleftrightarrow{P}^{\gtrless}(3,4)\overleftrightarrow{\mathcal{D}}^{a}(4,2). \tag{3.56}$$

The problem of calculating the advanced and retarded photon propagators is itself a complicated issue. Here we assume to be interested in systems where the renormalisation of the photons can be neglected. This is the case of simple solids and molecules where the electronic polarisation effects on the electromagnetic field can be assumed to be negligible. We start, then, from an independent particle approximation for $\mathcal{D}^{a/r}$:

$$\mathcal{D}^{r}_{\alpha\beta}(\mathbf{r},t) = -\frac{\mathrm{i}c^2}{2}\sum_I \tau^I_{\alpha\beta}\left[\bar{\xi}_I(\mathbf{r})e^{-\mathrm{i}\omega_I t} - \text{H.c.}\right]\theta(t), \tag{3.57a}$$

$$\mathcal{D}^{a}_{\alpha\beta}(\mathbf{r},t) = \frac{\mathrm{i}c^2}{2}\sum_I \tau^I_{\alpha\beta}\left[\bar{\xi}_I(\mathbf{r})e^{-\mathrm{i}\omega_I t} - \text{H.c.}\right]\theta(-t). \tag{3.57b}$$

In Eqs. (3.57a) and (3.57a′) we have introduced the single free photon wavefunction, $\bar{\xi}_I(\mathbf{r}) \equiv 2\pi/\left(\Omega\omega_{\mathbf{q}+\mathbf{G}}\right)e^{i\mathbf{r}\cdot(\mathbf{q}+\mathbf{G})}$. We remind here the convention introduced in Sec.3.1 to label the photon state as $I \equiv (\mathbf{q},\mathbf{G})$. By using Eqs. (3.57a) and (3.57b),

we rewrite Eq. (3.55) only in terms of $P^{\gtrless}_{\alpha\beta}$:

$$\mathcal{D}^{>}_{\alpha\beta}(1,2)+\mathcal{D}^{<}_{\alpha\beta}(1,2)=\frac{c^4}{4}\sum_{\substack{I,J\\ \alpha_1\alpha_2}}\int \mathrm{d}3\mathrm{d}4\,\left[\xi_I(\mathbf{r}_1-\mathbf{r}_3)e^{-\mathrm{i}\omega_I(t_1-t_3)}-\mathbf{H.c.}\right]\tau^I_{\alpha\alpha_1}$$
$$\times\left[P^{>}_{\alpha_1\alpha_2}(3,4)+P^{<}_{\alpha_1\alpha_2}(3,4)\right]\tau^J_{\alpha_2\beta}\left[\xi_J(\mathbf{r}_4-\mathbf{r}_2)e^{-\mathrm{i}\omega_I(t_4-t_2)}-\mathbf{H.c.}\right]\theta(t_1-t_3)\theta(t_2-t_4). \tag{3.58}$$

Equations (3.58) reduces the calculation of the light-emission spectrum, $I(\omega)$, to the evaluation of the equation of motion for $P^{\gtrless}_{\alpha\beta}(1,2)$. It is evident, then, that we can now follow a path quite similar to the longitudinal case by using a series of chain rules to close the equation of motion in an algebraic form. Indeed, we start by the $P^{\gtrless}_{\alpha\beta}(1,2)$ definition:

$$P_{\alpha\beta}(\mathbf{r}_1,t_1;\mathbf{r}_2,t_2)=-\frac{4\pi}{c}\frac{\delta\left\langle J^{\mathrm{ind}}_{\alpha}(\mathbf{r}_1,t_1)\right\rangle}{\delta\left\langle A_{\beta}(\mathbf{r}_2,t_2)\right\rangle}, \tag{3.59}$$

and by rewriting the induced current as

$$J^{\mathrm{ind}}_{\alpha}(\mathbf{r},t)=\mathrm{i}\Pi_{\alpha}(\mathbf{r},\mathbf{r}')G(\mathbf{r},t;\mathbf{r},t')\big|_{\substack{\mathbf{r}'=\mathbf{r}\\ t'=t^+}}=-\Pi_{\alpha}(\mathbf{r},\mathbf{r}')\rho(\mathbf{r},\mathbf{r}';t)\big|_{\mathbf{r}'=\mathbf{r}}. \tag{3.60}$$

Then, by using Eq. (2.9) and expanding the density-matrix in the single-particle basis we can rewrite the induced current in terms of $\rho(t)$

$$J^{\mathrm{ind}}_{\alpha}(\mathbf{r},t)=-\sum_{ij}\Pi_{ij,\alpha}(\mathbf{r})\rho_{ji}(t), \tag{3.61}$$

where $\Pi_{ij,\alpha}(\mathbf{r})=\Pi_{\alpha}(\mathbf{r},\mathbf{r}')\phi^*_i(\mathbf{r})\phi_j(\mathbf{r}')\big|_{\mathbf{r}'=\mathbf{r}}$. We also expand the variations of $\langle A_\alpha(1)\rangle$ in a photon basis

$$\delta\left\langle A_{\alpha}(\mathbf{r},t)\right\rangle=\frac{1}{2}\sum_{I}\left[\xi_I(\mathbf{r})\delta A_{I,\alpha}(t)+\mathbf{H.c.}\right]. \tag{3.62}$$

where $\xi_I(\mathbf{r})=\left(\frac{8\pi c^2}{\Omega\omega_I}\right)^{1/2}e^{i\mathbf{r}\cdot(\mathbf{q}+\mathbf{G})}$. By using Eqs. (3.62) and (3.61) we can rewrite Eq. (3.59) as

$$-\frac{4\pi}{c}\sum_{ij}\Pi_{ij,\alpha}(\mathbf{r})\delta\rho_{ji}(t)=\frac{1}{2}\sum_{I}\int \mathrm{d}t'\mathrm{d}\mathbf{r}'\,P_{\alpha\beta}(\mathbf{r},t;\mathbf{r}',t')\left[\xi_I(\mathbf{r})\delta A_{I,\beta}(t)+\mathbf{H.c.}\right]. \tag{3.63}$$

We can now recast the functional derivative with respect to δA as

$$-\frac{4\pi}{c}\sum_{ij}\Pi_{ij,\alpha}(\mathbf{r})\frac{\delta\rho_{ji}(t)}{\delta A_{I,\beta(t')}}=\frac{1}{2}\int \mathrm{d}\mathbf{r}'P_{\alpha\beta}(\mathbf{r},t;\mathbf{r}',t')\xi_I(\mathbf{r}'), \tag{3.64}$$

and its adjoint

$$-\frac{4\pi}{c}\sum_{ij}\Pi_{ij,\alpha}(\mathbf{r})\frac{\delta\rho_{ji}(t)}{\delta A^{*}_{I,\beta(t')}}=\frac{1}{2}\left[\int \mathrm{d}\mathbf{r}' P_{\alpha\beta}(\mathbf{r},t;\mathbf{r}',t')\xi_I(\mathbf{r}')\right]^{*}. \tag{3.65}$$

At this point we can define the I-th component of the transverse linear response function as

$$\mathbf{P}^I_{ij}(t,t')=\frac{\delta\rho_{ij}(t)}{\delta\mathbf{A}_I(t')}. \tag{3.66}$$

This means that we can use the same procedure as we did for the electronic polarisation function χ [see, for example, Eq. (3.43)] and write

$$\frac{\delta}{\delta\mathbf{A}_I(t')}\left[h_{\mathrm{ext}}(t),\rho(t)\right]_{ji}=\delta(t-t')\left[\mathbf{p}^I,\rho(t)\right]_{ji}+\left[h_{\mathrm{ext}}(t),\frac{\delta\rho(t)}{\delta\mathbf{A}_I(t')}\right]_{ji}, \tag{3.67}$$

with

$$\mathbf{p}^I_{ij}=-\frac{\mathrm{i}}{c}\int \mathrm{d}\,\mathbf{r}\phi^{*}_j(\mathbf{r})\xi_I(\mathbf{r})\nabla\phi_j(\mathbf{r}). \tag{3.68}$$

In Eq. (3.67) we have used the compact notation defined by Eq. (C.4) in order to simplify the notation. The terms involving the functional derivatives of the COHSEX and dynamical kernels will follow the same procedure of the longitudinal case. In the case of the COHSEX kernel contribution, indeed, we have that

$$\frac{\delta S^{\mathrm{coh}}_{ji}(t)}{\delta\mathbf{A}_I\left(t'\right)}=\int \mathrm{d}\bar{t}\,\frac{\delta\rho_{mn}\left(\bar{t}\right)}{\delta\mathbf{A}_I\left(t'\right)}\frac{\delta S^{\mathrm{coh}}_{ji}(t)}{\delta\rho_{mn}\left(\bar{t}\right)}=\left[K_s\circ\frac{\delta\rho\left(t\right)}{\delta\mathbf{A}_I\left(t'\right)},\rho(r)\right]_{ji}, \tag{3.69}$$

and for the dynamical kernel we will write

$$\frac{\delta S^{\mathrm{dyn}}_{ji}(t)}{\delta\mathbf{A}_I\left(t'\right)}=\int \mathrm{d}\bar{t}\left(K^{\mathrm{dyn}}(t,\bar{t})\circ\frac{\delta\rho\left(\bar{t}\right)}{\delta\mathbf{A}_I\left(t'\right)}\right)_{ji}. \tag{3.70}$$

We can now derive the final equation of motion for $\mathbf{P}^I_{ij}(t,t')$ in similarity with what we did for $\chi(t,t')$

$$\begin{aligned}\frac{d}{dt}\mathbf{P}^I\left(t,t'\right)+\mathrm{i}\left[h_{\mathrm{ext}}\left(t\right),\mathbf{P}^I\left(t,t'\right)\right]+\mathrm{i}\left[K_s\circ\mathbf{P}^I(t,t')+\delta(t-t')\mathbf{p}^I,\rho(t)\right]=\\ -K^{\mathrm{dyn}}\left(t\right)\circ\mathbf{P}^I\left(t,t'\right).\end{aligned} \tag{3.71}$$

Equation (3.71) represents another important result of this work. It derives a closed equation for the transverse response function and, in turns, it provides a

sound scheme to calculate the photoluminescence spectrum. As this equation is derived in a scheme where e-e and e-p are included this means that, physically, we have all essential ingredients of the dynamics. The carriers excited by the primary pump pulse will, then, relax, dissipate and participate in bound electron-hole pairs before recombining and emitting light.

A final methodological remark is due. Equation (3.71) is for the response function defined in Eq. (3.64). An equivalent equation can be derived for its complex conjugate, defined by Eq. (3.64′). The only difference with Eq. (3.71) would be that the matrix elements $\mathbf{p}^I_{ij}$ must be replaced with $\mathbf{q}^I_{ij} = -\frac{\mathrm{i}}{c}\int \mathrm{d}\mathbf{r}\, \phi^*_j(\mathbf{r})\xi^*_I(\mathbf{r})\nabla\phi_j(\mathbf{r})$.

3.4.5 The dynamical two-particle kernel

A common ingredient of Eq. (3.73) and Eq. (3.71) is the dynamical kernel K, defined in Eq. (3.47) as $\frac{\delta S^{\mathrm{dyn}}_{ji}[\rho](t)}{\delta\rho_{mn}(\bar{t})}$. We have now all ingredients to analyse the physical contents of K^{dyn} and interpret its properties.

The problem is now how to calculate this functional derivative and how to use the LIA.

If we look back into Eq. (3.29) and Fig. 3.2, we see how to evaluate the functional derivative of Eq. (3.47). The point is what happens if we apply the LIA. Indeed we have two possibilities: to apply the LIA before taking the functional derivative; or to apply it after the derivative.

As we will show shortly, this corresponds to neglect specific diagrams in the equation for the two-particle Green's function. In order to do so, let us follow a diagrammatic path. If we start from Fig. 3.2 we see that the derivative $\frac{\delta}{\delta\rho_{mn}(\bar{t})}$ can be applied both on ρ and $\overline{\rho}$. Graphically this corresponds to *open* the diagram as schematically shown in Fig. 3.4.

We clearly see that two kinds of interactions contribute to the dynamical kernel: an electron-hole pair interaction [Fig. 3.4(a)], and a simple e-e [Fig. 3.4(b)] or hole-hole [Fig. 3.4(c)] interaction mediated by a generic boson, shown in the bottom right of Fig. 3.4. The electron-hole interaction is, in the equilibrium language, the well-known dynamical part of the screened electron-hole interaction. This has been studied in the framework of the BSE and showed to be connected and compensated with the dynamical self-energy effects [66, 67].

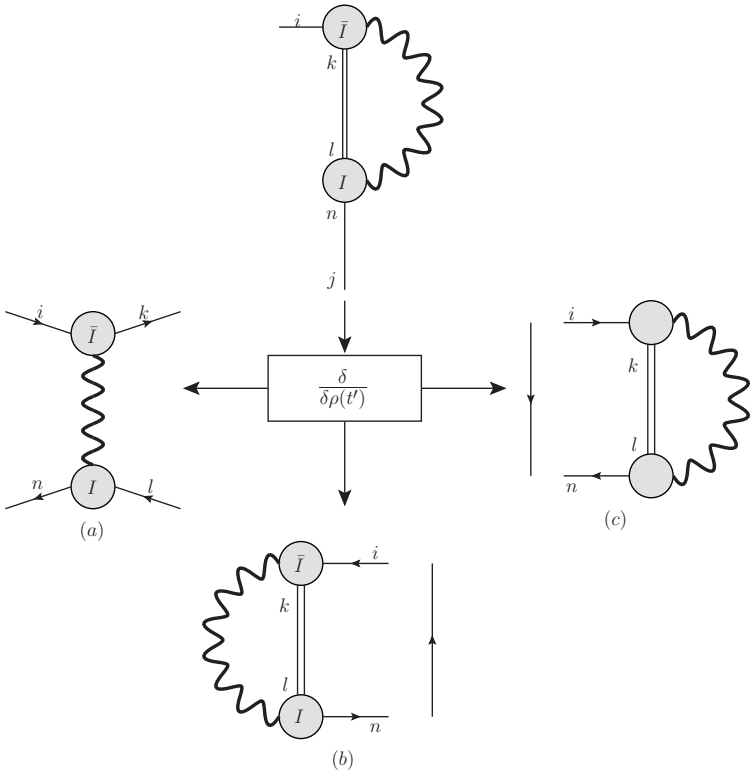

Figure 3.4: Diagrammatic contributions to the dynamical kernel K^{dyn} resulting from the application of the functional derivative to S^{dyn}, within the GW approximation.

Now, if we apply the LIA *before* taking the functional derivative we notice that the Fig. 3.4(a) disappears as it comes from the internal density matrix that, in Eq. (3.34) is approximated by its diagonal. Instead if we apply the LIA *after* the functional derivative the two internal density matrices in Figs. 3.4(b) and 3.4(c) are approximated by occupation factors.

If we take the path of applying the LIA *before* doing the functional derivative we get a closed expression for K^{dyn}:

$$K^{\mathrm{dyn}}_{\substack{ji\\lk}}\left(t,\bar{t}\right) \approx K^{\mathrm{dyn}}_{\substack{ji\\lk}}\left(t\right)\delta\left(t-\bar{t}\right) = \delta\left(t-\bar{t}\right)\Big[\delta_{il}\left(\gamma^{(-)}_{ilk}\left(t\right)+\tilde{\gamma}^{(-)}_{jlk}\left(t\right)\right)+ \delta_{jk}\left(\left(\gamma^{(+)}_{lki}\left(t\right)+\tilde{\gamma}^{(+)}_{lki}\left(t\right)\right)\Big], \quad (3.72)$$

which allows us to simplify the equation of motion for the longitudinal two-times

response function, turning Eq. (3.48) into

$$\frac{d}{dt}\tilde{\chi}\left(t,t'\right)+\mathrm{i}\left[h_{\mathrm{ext}}\left(t\right),\tilde{\chi}\left(t,t'\right)\right]+\mathrm{i}\left[K^{s}\circ\tilde{\chi}(t,t')+\mathbb{1}\delta\left(t-t'\right),\rho\left(t\right)\right]= \\ -K^{\mathrm{dyn}}\left(t\right)\circ\tilde{\chi}\left(t,t'\right). \quad (3.73)$$

Equation (3.73) allows a simple and immediate physical interpretation as the γ function simply representing a time-dependent relaxation of the polarisation that appears as a time-dependent broadening of the corresponding absorption peaks.

3.5 The frequency representation of the transient absorption and luminescence spectra

In the equilibrium limit it is well known that the response function depends on the time difference and therefore it can be easily transformed in frequency space by applying a Fourier transform. This is a natural consequence of the time-translational invariance of the theory and reflects the fact the the energy of the system is conserved.

Out-ofequilibrium the energy of the electronic and nuclear sub-system is not conserved anymore as it flows back and forth to the electromagnetic field. As a consequence both χ and P are complex two-times functions. The next step is to use the adiabatic ansatz (see Sec. 3.4.1) to change Eqs. (3.48) and (3.71) in order to have algebraic equations for χ and $P^{I,\alpha}$, as is in the state-of-the-art equilibrium case.

In the adiabatic ansatz, $\rho(t)$ and $A_{I,\alpha}(t)$ will change slowly in time. For times $(t,t')\approx\tau$ (with τ the pump-probe time delay) the response functions can be taken as a function of the relative time coordinate

$$\chi(t,t')\approx\chi^{\tau}(t-t'), \quad (3.74a)$$

$$\mathbf{P}^{I}(t,t')\approx\mathbf{P}^{I,\tau}(t-t'). \quad (3.74b)$$

Since in the adiabatic regime the density changes slowly in time, as long as the conditions described in Sec. 3.4.1 (a more detailed description can be found in Ref. [41]), the dynamic kernel of Eq. (3.48) can also be taken as a function of the

relative time coordinate. Thus, we can finally rewrite Eq. (3.48) into an algebraic form for the frequency dependent response function

$$-\mathrm{i}\omega\tilde{\chi}^{\tau}(\omega)+\mathrm{i}\left[h_{\mathrm{ext}}(\tau),\tilde{\chi}^{\tau}(\omega)\right]+\mathrm{i}\left[K_s^{\tau}\circ\tilde{\chi}^{\tau}(\omega)+1,\rho(\tau)\right]=-K^{\mathrm{dyn},\tau}(\omega)\circ\tilde{\chi}^{\tau}(\omega). \quad (3.75)$$

The question now is how to bypass the calculation of the one-particle density matrix $\rho(\tau)$ so that we can have an equation in which the only unknown quantity is the response function. In the equilibrium limit, we can always rotate the Hamiltonian h_{ext} and the density into a basis where both would be diagonal, but this is not possible in non-equilibrium processes. Therefore, by following Ref. [41], we consider an orthogonal matrix $O(\tau)$ which rotates the Hamiltonian to the equilibrium basis and brings $h_{\mathrm{ext}}(\tau)$ to its diagonal form

$$\left[O^{\dagger}(\tau)h_{\mathrm{ext}}(\tau)O(\tau)\right]_{ij}=\delta_{ij}\epsilon_i(\tau). \quad (3.76)$$

In this new basis, the Eq. (3.75) reads as

$$\left[\omega-\Delta\epsilon(\tau)+\mathrm{i}K^{\mathrm{dyn},\tau}(\omega)\right]\circ\chi^{\tau}(\omega)=\left[K_s^{\tau}\circ\chi(\omega)+1,\rho(\tau)\right]. \quad (3.77)$$

Here we have defined the energy tensor $\Delta\epsilon(\tau)_{\substack{ij\\pq}}=\left[\epsilon_i(\tau)-\epsilon_j(\tau)\right]1_{\substack{ij\\pq}}$. Following this definition we can write the NEQ response function χ_0^{τ} as

$$\chi_0^{\tau}(\omega)=-\left[\omega-\Delta\epsilon(\tau)+\mathrm{i}K^{\mathrm{dyn},\tau}(\omega)\right]^{-1}\circ[\rho(\tau),1]. \quad (3.78)$$

If we now use the property

$$[\rho(\tau),K_s^{\tau}\circ\tilde{\chi}^{\tau}(\omega)]=[\rho(\tau),1]\circ K_s^{\tau}\circ\chi^{\tau}(\omega), \quad (3.79)$$

we can finally obtain a Dyson-type equation for $\tilde{\chi}^{\tau}(\omega)$

$$\chi^{\tau}(\omega)=\tilde{\chi}_0^{\tau}(\omega)+\chi_0^{\tau}(\omega)\circ K_s^{\tau}\circ\chi^{\tau}(\omega). \quad (3.80)$$

If we apply the same process to the transverse response function, we see that its differential equation, Eq. (3.71), becomes

$$\begin{aligned}-\mathrm{i}\omega\mathbf{P}^{I,\tau}(\omega)+\mathrm{i}\left[h_{\mathrm{ext}}(\tau),\mathbf{P}^{I,\tau}(\omega)\right]+\mathrm{i}\left[K_s^{\tau}\circ\mathbf{P}^{I,\tau}(\omega)+\mathbf{p}^{I,\tau},\rho(\tau)\right]&\\ =-K^{\mathrm{dyn},\tau}(\omega)\circ\mathbf{P}^{I,\tau}(\omega)& \quad (3.81)\end{aligned}$$

and after reverting to the basis where $h_{\mathrm{ext}}(\tau)$ is diagonal and following the same procedure we used to arrive at Eq. (3.80), we obtain the desired Dyson-type equation for $\mathbf{P}^{I,\tau}(\omega)$

$$\mathbf{P}^{I,\tau}(\omega) = \mathbf{P}_0^{I,\tau}(\omega) + \tilde{\chi}_0^{\tau}(\omega) \circ K_s^{\tau} \circ \mathbf{P}^{I,\tau}(\omega) \tag{3.82}$$

with the NEQ $\mathbf{P}_0^{I,\tau}(\omega)$ being

$$\mathbf{P}_0^{I,\tau}(\omega) = -\Big[\omega - \Delta\epsilon(\tau) + \mathrm{i}K^{\mathrm{dyn},\tau}(\omega)\Big]^{-1} \circ [\rho(\tau), \mathbf{p}^{I,\tau}]. \tag{3.83}$$

Equation (3.83) represents another crucial result of this work. It provides, indeed, the basis for a fully *ab-initio* implementation of the transient photoluminescence spectrum. This will allow to extend what has been already done previously [68] in the transient absorption case. Unfortunately, however, $\mathbf{P}^{I,\tau}(\omega)$ is an intrinsically retarded function, and as we see from Eq. (3.55) we need the equations for the lesser and greater counterparts. In the next chapters we show how to circumvent this problem and obtain the expression for the power spectrum.

Chapter 4

The structure of the vectorial BSE

"How do you know I'm mad?"
said Alice.
"You must be," said the Cat, "or
you wouldn't have come here."

Lewis Carroll, *Alice in Wonderland*

In Subsec. 3.4.4 we have shown how to obtain an equation of motion for the retarded NEQ vectorial linear response function. However, we need the information about the lesser and greater photon polarisation functions, especially the contributions coming from electronic transitions of out-of-equilibrium electrons. We can obtain this information by looking into the pole structure of a vectorial BSE equation for the electromagnetic vertex.

4.1 The vectorial BSE for the electromagnetic vertex

In the electronic case the linear response function is closely connected with the two-particle correlation function, L, which is defined as

$$L(1,2;3,4) = \frac{\delta G(1,2)}{\delta U(4,3)}, \tag{4.1}$$

where U is the total electronic potential defined in Eq. (2.40). This function's equation of motion is called the Bethe-Salpeter equation

$$L(1,2;3,4) = L_0(1,2;3,4) + L_0(1,5;3,6)\Xi(6,7;5,8)L(8,2;7,4), \tag{4.2}$$

where the BSE kernel is written as

$$\Xi(6,7;5,8) = \frac{\delta\Sigma(6,5)}{\delta G(8,7)} \approx \mathrm{i}\left[W(6,5)\delta(6,8)\delta(5,7) - v(6,8)\delta(5,6)\delta(7,8)\right], \tag{4.3}$$

and the non-interacting correlation function L_0 is given by

$$L_0(1,2;3,4) = G(1,3)G(4,2). \tag{4.4}$$

In Eq. (4.3) we are following the approximation of ignoring the contributions from the term $\frac{\delta W(1,2)}{\delta G(3,4)}$ [55], thus avoiding contributions from higher-order vertex corrections.

The linear-response function χ used in Sections 3.4 and 3.5 [see Eqs. (3.42a) and (3.42b)] is connected with the two-particle correction function through the relation $\chi(t,t') = L(t,t^+;t',t'^+)$. In those Sections we saw that when dealing with electromagnetic fields we needed to define a vectorial response function [Eq. (3.66)] which is connected to the transverse polarisation [Eq. (2.61)]. This suggests that we should introduce a general three-point photon polarisation function

$$P_{\alpha\beta}(1,2;3) = -\frac{4\pi\mathrm{i}}{c}\Pi_\alpha(1,2)\frac{\delta G(1,2)}{\delta A_\beta(3)}, \tag{4.5}$$

which then by itself introduces a pair-photon correlation function $\boldsymbol{\mathcal{L}}$, which we define as

$$\boldsymbol{\mathcal{L}}(1,2;3) = \frac{\delta G(1,2)}{\delta \mathbf{A}(3)}. \tag{4.6}$$

We can show that $\boldsymbol{\mathcal{L}}$ follows a Bethe-Salpeter equation similar to that of L. We start by using again Eq.(2.43)

$$\begin{aligned}\boldsymbol{\mathcal{L}}(1,2;3) &= -G(1,4)\frac{\delta G^{-1}(4,5)}{\delta \mathbf{A}(3)}G(5,2)\\ &= \left[\boldsymbol{\Pi}(4,4')G(1,4)G(5,2)\right]\delta(4,3)\delta(4,5)|_{4'=4} + G(1,4)\frac{\Sigma(4,5)}{\delta G(6,7)}\frac{\delta G(6,7)}{\delta \mathbf{A}(3)}G(5,2)\\ &= \boldsymbol{\mathcal{L}}_0(1,2;3) + L_0(1,5;2,4)\Xi(4,7;5,6)\boldsymbol{\mathcal{L}}(6,7;3),\end{aligned} \tag{4.7}$$

which introduces the zeroth-order pair-photon correlation function $\boldsymbol{\mathcal{L}}_0$

$$\boldsymbol{\mathcal{L}}_0(1,2;3) = \left[\boldsymbol{\Pi}(3,3')G(1,3)G(3',2)\right]|_{3'=3}, \tag{4.8}$$

for which we can use the non-interacting picture as the starting point. A diagrammatic representation of this equation can be seen in Fig. 4.1.

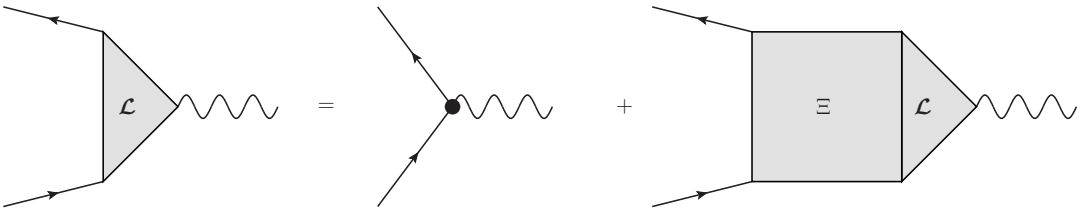

Figure 4.1: Diagrammatic representation of the BSE for the transverse vertex. As before the bullet represents a $\boldsymbol{\Pi}$ differential operator.

4.1.1 The basis expansion for the photon vertex

Before we can proceed we need to study the expansion form of $\boldsymbol{\mathcal{L}}(1,2;3)$ as we did in Subsec. 3.4.4 for the expansion of the transverse polarisation. Using a basis expansion for $G(1,2)$ and $\mathbf{A}(3)$ [see Eq.(3.2) and Eq.(3.62)] we arrive at

$$\begin{aligned}\boldsymbol{\mathcal{L}}(1,2;3) &= \sum_{i,j}\sum_{I}\phi_i(\mathbf{r}_1)\phi_j^*(\mathbf{r}_2)\xi_I^*(\mathbf{r}_3)\frac{\delta G_{ij}(t_1,t_2)}{\delta \mathbf{A}_I(t_3)} \\ &= \sum_{i,j}\sum_{I}\phi_i(\mathbf{r}_1)\phi_j^*(\mathbf{r}_2)\xi_I^*(\mathbf{r}_3)\boldsymbol{\mathcal{L}}_{ij,I}(t_1,t_2;t_3).\end{aligned} \tag{4.9}$$

With this expansion we can obtain a relation between the time-dependent coefficients of $\boldsymbol{\mathcal{L}}_0$, which we write as $\boldsymbol{\mathcal{L}}^0_{ij,I}(t_1,t_2;t_3)$, and the time-dependent coefficients of $L^0_{\substack{ij\\kl}}(t_1,t_2;t_3,t_4)$. We obtain that

$$\begin{aligned}\boldsymbol{\mathcal{L}}_0(1,2;3) &= \left[\boldsymbol{\Pi}(3,3')G(1,3)G(3',2)\right]|_{3'=3} \\ &= \sum_{\substack{ij\\kl}}\phi_i(\mathbf{r}_1)\left[\boldsymbol{\Pi}(3,3')\phi_k(\mathbf{r}_3')\phi_j^*(\mathbf{r}_3)\right]|_{3'=3}\phi_l(\mathbf{r}_2)G_{ij}(t_1,t_3)G_{kl}(t_3,t_2) \\ &= \sum_{uv}\sum_{I}\phi_u(\mathbf{r}_1)\phi_v^*(\mathbf{r}_2)\xi_I^*(\mathbf{r}_3)\boldsymbol{\mathcal{L}}^0_{uv,I}(t_1,t_2;t_3) \Rightarrow \\ &\Rightarrow \boldsymbol{\mathcal{L}}^0_{ij,I}(t_1,t_2;t_3) = \sum_{kl} L^0_{\substack{ik\\lj}}(t_1,t_2;t_3,t_4)\boldsymbol{\Pi}_{kj,I},\end{aligned} \tag{4.10}$$

where we have

$$\mathbf{\Pi}_{kj,I} = \int \mathrm{d}\mathbf{r}\, \xi_I(\mathbf{r}) \left[\mathbf{\Pi}(\mathbf{r},\mathbf{r}')\phi_k(\mathbf{r}')\phi_j^*(\mathbf{r})\right] |_{\mathbf{r}'=\mathbf{r}}. \tag{4.11}$$

This is a useful step as the L_0 and L functions have already been extensively studied within various approximations, so Eq. (4.10) allows us to reuse those results.

4.1.2 The matrix form for the BSE

To continue with the derivation of a matrix expression for the pair-photon BSE we recall the definition of Ξ in Eq. (4.3), with which we write

$$\boldsymbol{\mathcal{L}}(1,2;3) = \boldsymbol{\mathcal{L}}_0(1,2;3) + \mathrm{i}\left[L_0(1.5;2,4)W(4,5)\boldsymbol{\mathcal{L}}(4,5;3) - L_0(1,4;2,4)w(4,6)\boldsymbol{\mathcal{L}}(6,6;3)\right]. \tag{4.12}$$

Herein we focus only on the electronic dynamics when evaluating the contributions to the transverse vertex.

The COHSEX approximation is a good starting point for the screened interaction W, which can be expanded together with the Coulomb interaction w as

$$W(1,2) = \frac{\delta(t_1-t_2)}{\Omega N}\sum_{\mathbf{q}}\sum_{\mathbf{G}\mathbf{G}'} W_{\mathbf{G}\mathbf{G}'}(\mathbf{q}) e^{\mathrm{i}[(\mathbf{q}+\mathbf{G})\cdot\mathbf{r}_1 - (\mathbf{q}+\mathbf{G}')\cdot\mathbf{r}_2]}, \tag{4.13}$$

$$w(1,2) = \frac{\delta(t_1-t_2)}{\Omega N}\sum_{\mathbf{q}}\sum_{\mathbf{G}} \frac{4\pi}{|\mathbf{q}+\mathbf{G}|^2} e^{\mathrm{i}(\mathbf{q}+\mathbf{G})\cdot(\mathbf{r}_1-\mathbf{r}_2)}. \tag{4.14}$$

Together with Eqs. (4.10) and (4.12) we arrive at the diagrammatic contributions for the matrix elements $\boldsymbol{\mathcal{L}}_{\substack{n_1\mathbf{k}_1 \\ n_2\mathbf{k}_1-\mathbf{q}}, I}(t_1,t_2;t_3)$, which are shown in Fig. 4.2.

We can now evaluate each contribution individually. The first term coming Fig. 4.2 [subfigure a)] is simply the non-interacting $\boldsymbol{\mathcal{L}}_0$ expressed in Eq. (4.10). The second term [subfigure b)] arises from the contribution of the static screened interaction W, and is expressed by

$$\begin{aligned}\frac{1}{\Omega N}\sum_{n_4 n_5}\sum_{\mathbf{G}_4\mathbf{G}_5}\sum_{\mathbf{q}'}\sum_{I}\int \mathrm{d}4\mathrm{d}5\, &\phi_{n_1\mathbf{k}_1}(\mathbf{r}_1)\phi^*_{n_1\mathbf{k}_1}(\mathbf{r}_4)\phi_{n_2\mathbf{k}_1-\mathbf{q}}(\mathbf{r}_5)\phi^*_{n_2\mathbf{k}_1-\mathbf{q}}(\mathbf{r}_2)\phi_{n_4\mathbf{k}_1-\mathbf{q}}(\mathbf{r}_4)\\ &\times \phi^*_{n_5\mathbf{k}_1-\mathbf{q}-\mathbf{q}'}(\mathbf{r}_5) G_{n_1\mathbf{k}_1}(t_1,t_2)G_{n_2\mathbf{k}_2-\mathbf{q}}(t_5,t_2)W_{\mathbf{G}_4\mathbf{G}_5}(\mathbf{q})e^{\mathrm{i}[(\mathbf{q}+\mathbf{G})\cdot\mathbf{r}_4-(\mathbf{q}+\mathbf{G}')\cdot\mathbf{r}_5]}\\ &\times \xi_I(\mathbf{r}_3)\boldsymbol{\mathcal{L}}_{\substack{n_4\mathbf{k}_1-\mathbf{q}' \\ n_5\mathbf{k}_1-\mathbf{q}-\mathbf{q}'}, I}(t_4,t_5;t_3)\delta(t_4-t_5).\end{aligned} \tag{4.15}$$

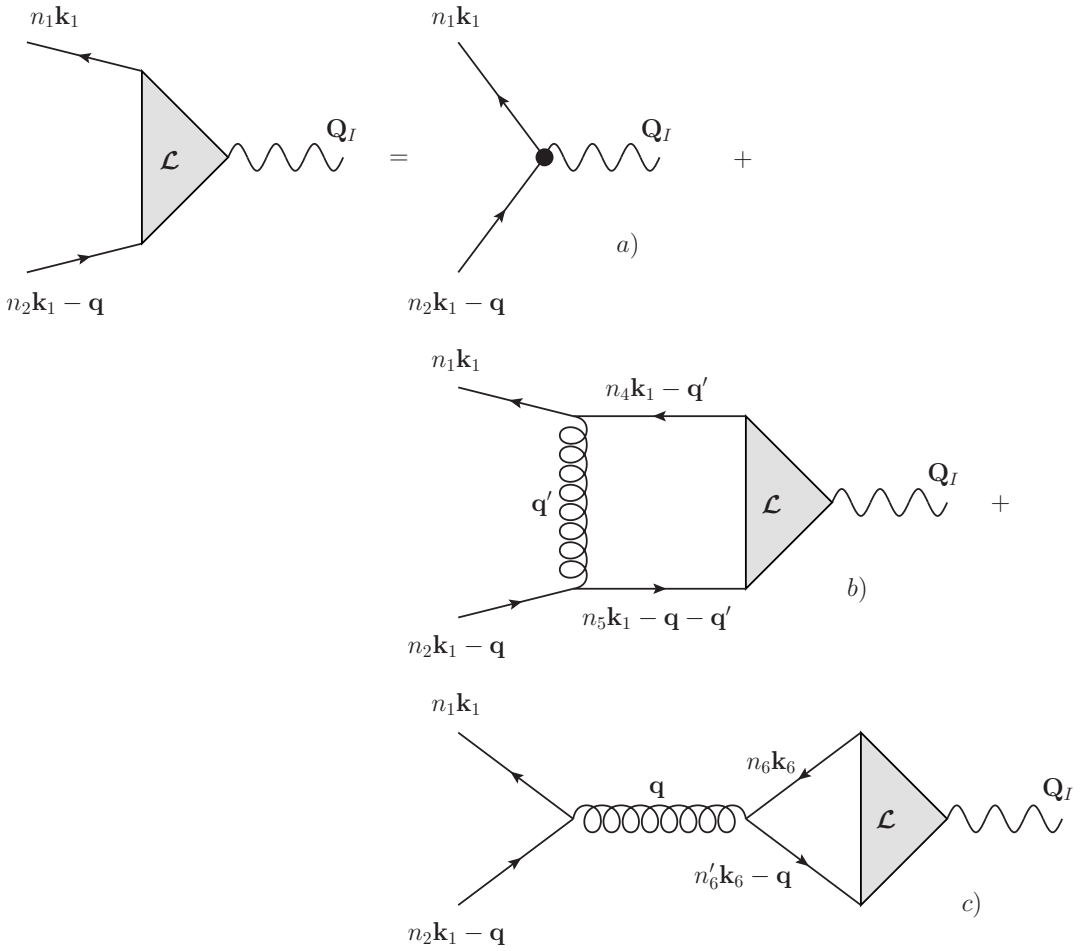

Figure 4.2: Diagrammatic contributions for $\mathcal{L}$. Diagram a) corresponds to the non-interacting part $\mathcal{L}_0$, where the bullet represents a $\mathbf{\Pi}$ differential operator. Diagrams b) and c) are, respectively, the contributions from the static screened interaction W and the Coulomb potential w defined in Eq. (4.13) and (4.14).

We can rewrite Eq. (4.15) in a more compact expression, obtaining

$$\sum_{n_4 n_5} \sum_{\mathbf{q}'} \sum_{I} W_{\substack{n_1 n_4 \\ n_2 n_5}}(\mathbf{k}_1, \mathbf{q}, \mathbf{q}') L^0{}_{\substack{n_1 \mathbf{k}_1 \\ n_2 \mathbf{k}_1 - \mathbf{q}}}(t_1, t_4; t_2, t_4) \boldsymbol{\mathcal{L}}_{\substack{n_4 \mathbf{k}_1 - \mathbf{q}' \\ n_5 \mathbf{k}_1 - \mathbf{q} - \mathbf{q}', I}}(t_4, t_4; t_3), \tag{4.16}$$

where we defined the matrix element of W as

$$W_{\substack{n_1 n_4 \\ n_2 n_5}}(\mathbf{k}_1, \mathbf{q}, \mathbf{q}') = \sum_{\mathbf{G}_4 \mathbf{G}_5} \rho_{n_1 n_4}(\mathbf{k}_1, \mathbf{q}, \mathbf{G}_4) \left[\rho_{n_2 n_5}(\mathbf{k}_1, \mathbf{q} - \mathbf{q}', \mathbf{G}_5)\right]^* W_{\mathbf{G}_4 \mathbf{G}_5}(\mathbf{q}), \tag{4.17}$$

with

$$\rho_{n_1 n_4}(\mathbf{k}_1, \mathbf{q}, \mathbf{q}', \mathbf{G}_4) = \int \mathrm{d}\mathbf{r}_4 \, \phi_{n_4 \mathbf{k}_1 - \mathbf{q}'}(\mathbf{r}_4) \phi^*_{n_1 \mathbf{k}_1}(\mathbf{r}_4) e^{\mathrm{i}(\mathbf{q} + \mathbf{G}) \cdot \mathbf{r}_4}. \tag{4.18}$$

The same procedure can be used for the contributions which arise from the Coulomb potential, which are represented in diagram c) of Fig. 4.2.

In full, like in Eq. (4.15), the contribution from the Coulomb interaction is written as

$$\begin{aligned} \frac{1}{\Omega N} \sum_{n_6 n_6'} \sum_{\mathbf{G}} \sum_{\mathbf{k}_6} \sum_{I} \int \mathrm{d}4\mathrm{d}6 \, \phi_{n_1 \mathbf{k}_1}(\mathbf{r}_1) \phi^*_{n_1 \mathbf{k}_1}(\mathbf{r}_4) \phi_{n_2 \mathbf{k}_1 - \mathbf{q}}(\mathbf{r}_4) \phi^*_{n_2 \mathbf{k}_1 - \mathbf{q}}(\mathbf{r}_2) \phi_{n_6 \mathbf{k}_6}(\mathbf{r}_6) \\ \times \phi^*_{n_6 \mathbf{k}_6 - \mathbf{q}}(\mathbf{r}_6) G_{n_1 \mathbf{k}_1}(t_1, t_2) G_{n_2 \mathbf{k}_2 - \mathbf{q}}(t_5, t_2) \frac{4\pi}{|\mathbf{q} + \mathbf{G}|^2} e^{\mathrm{i}(\mathbf{q} + \mathbf{G}) \cdot (\mathbf{r}_4 - \mathbf{r}_6)} \\ \times \xi_I(\mathbf{r}_3) \boldsymbol{\mathcal{L}}_{\substack{n_6 \mathbf{k}_6 \\ n_6' \mathbf{k}_6 - \mathbf{q}, I}}(t_6, t_6; t_3) \delta(t_4 - t_6), \end{aligned} \tag{4.19}$$

which we can then bring into compact from by writing

$$\sum_{n_6 n_6'} \sum_{\mathbf{k}_6} \sum_{I} V_{\substack{n_1 n_6 \\ n_2 n_6'}}(\mathbf{k}_1, \mathbf{k}_6, \mathbf{q}) L^0{}_{\substack{n_1 \mathbf{k}_1 \\ n_2 \mathbf{k}_1 - \mathbf{q}}}(t_1, t_4; t_2, t_4) \boldsymbol{\mathcal{L}}_{\substack{n_6 \mathbf{k}_6 \\ n_6' \mathbf{k}_6 - \mathbf{q}, I}}(t_4, t_4; t_3). \tag{4.20}$$

Here the matrix elements of the Coulomb interaction are given by

$$V_{\substack{n_1 n_6 \\ n_2 n_6'}}(\mathbf{k}_1, \mathbf{k}_6, \mathbf{q}) = \frac{1}{\Omega N} \sum_{\mathbf{G}} \rho_{n_2 n_1}(\mathbf{k}_1, \mathbf{q}, \mathbf{G}) \left[\rho_{n_6' n_6}(\mathbf{k}_6, \mathbf{q}, \mathbf{G})\right]^* \frac{4\pi}{|\mathbf{q} + \mathbf{G}|^2}. \tag{4.21}$$

By inserting the matrix elements of W and w into Eq. (4.12) we arrive at the finite momentum BSE for the matrix elements of $\boldsymbol{\mathcal{L}}$

$$\begin{aligned} \boldsymbol{\mathcal{L}}_{\substack{n_1 \mathbf{k}_1 \\ n_2 \mathbf{k}_1 - \mathbf{q}, I}}(t_1, t_2; t_3) = \boldsymbol{\mathcal{L}}^0_{\substack{n_1 \mathbf{k}_1 \\ n_2 \mathbf{k}_1 - \mathbf{q}, I}}(t_1, t_2; t_3) + \mathrm{i} L^0{}_{\substack{n_1 \mathbf{k}_1 \\ n_2 \mathbf{k}_1 - \mathbf{q}}}(t_1, t_4; t_2, t_4) \\ \times \sum_{n_4 n_5} \Bigg[\sum_{\mathbf{q}'} W_{\substack{n_1 n_4 \\ n_2 n_5}}(\mathbf{k}_1, \mathbf{q}, \mathbf{q}') \boldsymbol{\mathcal{L}}_{\substack{n_4 \mathbf{k}_1 - \mathbf{q}' \\ n_5 \mathbf{k}_1 - \mathbf{q} - \mathbf{q}', I}}(t_4, t_4; t_3) - \\ 2 \sum_{\mathbf{k}_4} V_{\substack{n_1 n_4 \\ n_2 n_5}}(\mathbf{k}_1, \mathbf{k}_4, \mathbf{q}) \boldsymbol{\mathcal{L}}_{\substack{n_4 \mathbf{k}_4 \\ n_5 \mathbf{k}_4 - \mathbf{q}, I}}(t_4, t_4; t_3) \Bigg]. \end{aligned} \tag{4.22}$$

Similarly to what is done in literature for the density-density correlation function L (see, for instance, Ref. [15]), we take the optical limit by doing $\mathbf{q} \to \mathbf{0}$, thus arriving at the zero momentum BSE

$$\begin{aligned}\boldsymbol{\mathcal{L}}_{\substack{n_1\mathbf{k}_1\\ n_2\mathbf{k}_1},I}(t_1,t_2;t_3) = \boldsymbol{\mathcal{L}}^0_{\substack{n_1\mathbf{k}_1\\ n_2\mathbf{k}_1},I}(t_1,t_2;t_3) + \mathrm{i}L^0_{\substack{n_1\mathbf{k}_1\\ n_2\mathbf{k}_1}}(t_1,t_4;t_2,t_4) \\ \times \sum_{n_4 n_5}\left[\sum_{\mathbf{q}'} W^{n_1 n_4}_{n_2 n_5}(\mathbf{k}_1,0,\mathbf{q}')\boldsymbol{\mathcal{L}}_{\substack{n_4\mathbf{k}_1-\mathbf{q}'\\ n_5\mathbf{k}_1-\mathbf{q}'},I}(t_4,t_4;t_3) - \right. \\ \left. 2\sum_{\mathbf{k}_4} V^{n_1 n_4}_{n_2 n_5}(\mathbf{k}_1,\mathbf{k}_4,0)\boldsymbol{\mathcal{L}}_{\substack{n_4\mathbf{k}_4\\ n_5\mathbf{k}_4},I}(t_4,t_4;t_3)\right]. \quad (4.23)\end{aligned}$$

Here the factor 2 before the contributions from the Coulomb potential accounts for the spin. We can rewrite Eq. (4.23) into a compact form by defining the matrix elements of the kernel as

$$\Xi^{n_1 n_4}_{n_2 n_5}(\mathbf{k}_1,\mathbf{k}_4) = W^{n_1 n_4}_{n_2 n_5}(\mathbf{k}_1,0,\mathbf{k}-\mathbf{k}_4) - 2V^{n_1 n_4}_{n_2 n_5}(\mathbf{k}_1,\mathbf{k}_4,0) \quad (4.24)$$

and thus bring Eq. (4.23) into a more familiar form

$$\begin{aligned}\boldsymbol{\mathcal{L}}_{\substack{n_1\mathbf{k}_1\\ n_2\mathbf{k}_1},I}(t_1,t_2;t_3) = \boldsymbol{\mathcal{L}}^0_{\substack{n_1\mathbf{k}_1\\ n_2\mathbf{k}_1},I}(t_1,t_2;t_3) \\ + \mathrm{i}L^0_{\substack{n_1\mathbf{k}_1\\ n_2\mathbf{k}_1}}(t_1,t_4;t_2,t_4)\sum_{n_4 n_5}\sum_{\mathbf{k}_4}\Xi^{n_1 n_4}_{n_2 n_5}(\mathbf{k}_1,\mathbf{k}_4)\boldsymbol{\mathcal{L}}_{\substack{n_4\mathbf{k}_4\\ n_5\mathbf{k}_4},I}(t_4,t_4;t_3). \quad (4.25)\end{aligned}$$

Due to the definition of the transverse polarisation in Eq. (2.61) we need to take the limit where $t_2 \to t_1^+$ of Eq. (4.25) [check Eqs. (3.59) and (3.60)]. Here we assume that the adiabatic approximation defined in Sec. 3.4.1 is valid, so that we can take the Fourier transform with respect to $t_1 - t_3$ and obtain

$$\boldsymbol{\mathcal{L}}^{\tau}_{K,I}(\omega) = \boldsymbol{\mathcal{L}}^{0,\tau}_{K,I}(\omega) + L^{0,\tau}_{K}(\omega)\sum_{K'}\Xi_{K,K'}\boldsymbol{\mathcal{L}}^{\tau}_{K',I}(\omega), \quad (4.26)$$

where we introduce a notation in which $K = \{n_1 n_2 \mathbf{k}_1\}$ and $K' = \{n_4 n_5 \mathbf{k}_4\}$.

4.2 The BSE for the lesser and greater vectorial vertex

The equations in the previous section are only valid for retarded functions. Since we are interested in the lesser and greater functions we must go back into the

contour defined transverse polarisation $\overleftrightarrow{P}$ which we can write as

$$P_{\alpha\beta}(\underline{1},\underline{2}) = -\frac{4\pi i}{c}\Pi_{\alpha}(1,1')\frac{\delta G(\underline{1},\underline{1}')}{\delta \mathbf{A}_{\beta}(\underline{3})}\bigg|_{\underline{1}'=\underline{1}} = -\frac{4\pi i}{c}\Pi_{\alpha}(1,1')\boldsymbol{\mathcal{L}}_{\beta}(\underline{1},\underline{1}';\underline{2})\bigg|_{\underline{1}'=\underline{1}}. \quad (4.27)$$

We define $\tau_i \in C$ as the time variable over the Keldysh contour in Fig. 2.1. Due to the nature of the COHSEX approximation, $W(1,2)$ and $w(1,2)$ are static [see Eqs. (4.13) and (4.14)] and so we can write for $\boldsymbol{\mathcal{L}}$[1]

$$\boldsymbol{\mathcal{L}}(\tau_1,\tau_2;\tau_3) = \boldsymbol{\mathcal{L}}_0(\tau_1,\tau_2;\tau_3) + L_0(\tau_1,\tau_4;\tau_4,\tau_2)\Xi\boldsymbol{\mathcal{L}}(\tau_4,\tau_4;\tau_3). \quad (4.28)$$

Then, using the analytic continuation rules from Langreth theorem [11][2] yields the equation of motion for $\boldsymbol{\mathcal{L}}^{\lessgtr}$

$$\boldsymbol{\mathcal{L}}^{\lessgtr}(t_1,t_2;t_3) = \boldsymbol{\mathcal{L}}_0^{\lessgtr}(t_1,t_2;t_3) + L_0^{r}(t_1,t_4;t_4,t_2)\Xi\boldsymbol{\mathcal{L}}^{\lessgtr}(t_4,t_4;t_3) + L_0^{\lessgtr}(t_1,t_4;t_4,t_2)\Xi\boldsymbol{\mathcal{L}}^{a}(t_4,t_4;t_3), \quad (4.29)$$

as well as the equation of motion for $\boldsymbol{\mathcal{L}}^{r/a}$

$$\boldsymbol{\mathcal{L}}^{r/a}(t_1,t_2;t_3) = \boldsymbol{\mathcal{L}}_0^{r/a}(t_1,t_2;t_3) + L_0^{r/a}(t_1,t_4;t_4,t_2)\Xi\boldsymbol{\mathcal{L}}^{r/a}(t_4,t_4;t_3). \quad (4.30)$$

Finally we assume the same approximations which led to Eq. (4.26) and take the Fourier transform, thus arriving at the frequency dependent equations for $\boldsymbol{\mathcal{L}}^{\lessgtr,\tau}$

$$\boldsymbol{\mathcal{L}}^{\lessgtr,\tau}(\omega) = \boldsymbol{\mathcal{L}}_0^{\lessgtr,\tau}(\omega) + L_0^{r,\tau}(\omega)\Xi\boldsymbol{\mathcal{L}}^{\lessgtr,\tau}(\omega) + L_0^{\lessgtr,\tau}(\omega)\Xi\boldsymbol{\mathcal{L}}^{a,\tau}(\omega), \quad (4.31)$$

and $\boldsymbol{\mathcal{L}}^{r/a,\tau}$

$$\boldsymbol{\mathcal{L}}^{r/a,\tau}(\omega) = \boldsymbol{\mathcal{L}}_0^{r/a,\tau}(\omega) + L_0^{r/a,\tau}(\omega)\Xi\boldsymbol{\mathcal{L}}^{r/a,\tau}(\omega). \quad (4.32)$$

We can use Eq. (4.32) to invert Eq. (4.31) in order to separate the two equations. We start from

$$\left[\delta_{KK'} - L_K^{0r,\tau}(\omega)\Xi_{KK'}\right]\boldsymbol{\mathcal{L}}_{K',I}^{\lessgtr,\tau}(\omega) = L_K^{0\lessgtr,\tau}(\omega)\left[\boldsymbol{\Pi}_{K,I} + \Xi_{KK'}\boldsymbol{\mathcal{L}}_{K,I}^{a,\tau}(\omega)\right], \quad (4.33)$$

and then take advantage of the fact that (here we use Einstein's summation convention)

$$\Xi_{K'K''}\boldsymbol{\mathcal{L}}_{K'',I}^{a,\tau}(\omega) = \left[1 - \Xi L^{0a,\tau}(\omega)\right]^{-1}_{K'K''}\Xi_{K''K'''}\boldsymbol{\mathcal{L}}_{K''',I}^{0a,\tau}(\omega). \quad (4.34)$$

[1] Here we are ignoring the K labels in the matrix elements in order to no overburden the notation. We re-introduce them back at the end.

[2] See Tab. A.1.

Since we can always write $\left[1-\Xi L^{0a,\tau}(\omega)\right]^{-1}_{K'K''} = \sum_{n=0}^{+\infty}[\Xi L^{0a,\tau}(\omega)]^n_{K'K''}$, we can rework Eq. (4.34) and replace it in Eq. (4.33) to arrive at

$$\boldsymbol{\mathcal{L}}^{\lessgtr,\tau}_K(\omega) = \left[1-L^{0r,\tau}(\omega)\Xi\right]^{-1}_{KK'} L^{0\lessgtr}_{K'}(\omega)\left[1-\Xi L^{0a,\tau}(\omega)\right]^{-1}_{K'K''}\boldsymbol{\Pi}_{K'',I}. \tag{4.35}$$

4.3 The pole structure of the vectorial vertex and the nature of the selected transitions

To analyse the pole structure of $\boldsymbol{\mathcal{L}}$ in Eq. (4.35) we start from the non-interacting picture for the electron correlation functions. With this, we can rewrite the matrix elements in Eq. (4.35) as

$$\begin{aligned}\left[1-L^{0r,\tau}(\omega)\Xi\right]_{KK'} &= \delta_{KK'} - L^{0r,\tau}_K(\omega)\Xi_{KK'} = \delta_{KK'} - \frac{R^\tau_K}{\omega-\Omega^\tau_K+i\eta}\Xi_{KK'} = \\ &= \frac{1}{\omega-\Omega^\tau_K+i\eta}\left[\delta_{KK'}(\omega-\Omega^\tau_K+i\eta) - R^\tau_K\Xi_{KK'}\right] = \frac{1}{\omega-\Omega^\tau_K+i\eta}M^{r,\tau}_{KK'}(\omega),\end{aligned} \tag{4.36}$$

and as

$$\begin{aligned}\left[1-\Xi L^{0a,\tau}(\omega)\right]_{KK'} &= \delta_{KK'} - \Xi_{KK'}L^{0a,\tau}_{K'}(\omega) = \delta_{KK'} - \Xi_{KK'}\frac{R^\tau_{K'}}{\omega-\Omega_{K'}-i\eta} = \\ &= \frac{1}{\omega-\Omega^\tau_{K'}-i\eta}\left[\delta_{KK'}(\omega-\Omega^\tau_{K'}-i\eta) - \Xi_{KK'}R^\tau_{K'}\right] = \frac{1}{\omega-\Omega^\tau_{K'}-i\eta}M^{a,\tau}_{KK'}(\omega),\end{aligned} \tag{4.37}$$

where we have that $R^\tau_K = f^\tau_{n_1\mathbf{k}} - f^\tau_{n_2\mathbf{k}}$ and that $\Omega^\tau_K = \epsilon_{n_1\mathbf{k}}(\tau) - \epsilon_{n_2\mathbf{k}}(\tau)$. We have also defined the retarded and advanced matrices $M^{r,\tau}$ and $M^{a,\tau}$ as

$$M^{r,\tau}_{KK'}(\omega) = \delta_{KK'}(\omega-\Omega^\tau_K+i\eta) - R^\tau_K\Xi_{KK'} \tag{4.38a}$$

$$M^{a,\tau}_{KK'}(\omega) = \delta_{KK'}(\omega-\Omega^\tau_K-i\eta) - \Xi_{KK'}R^\tau_{K'}. \tag{4.38b}$$

If we look closely to the necessary algebraic steps that we can change Eq. (4.35) into

$$\boldsymbol{\mathcal{L}}^{\lessgtr,\tau}_K(\omega) = [M^{r,\tau}(\omega)]^{-1}_{KK'}(\omega-\Omega^\tau_{K'}+i\eta)L^{0\lessgtr,\tau}_{K'}(\omega)(\omega-\Omega^\tau_{K'}-i\eta)\,[M^{a,\tau}(\omega)]^{-1}_{K'K''}\boldsymbol{\Pi}_{K'',I}. \tag{4.39}$$

By taking the $L^{0\lessgtr,\tau}_{K'}(\omega)$ in the non-interacting picture we arrive at a simpler equation for $\boldsymbol{\mathcal{L}}^{\lessgtr,\tau}(\omega)$[1]

$$\boldsymbol{\mathcal{L}}^{\lessgtr,\tau}_{K,I}(\omega) = -\frac{2\mathrm{i}\eta}{\pi}\left[M^{r,\tau}(\omega)\right]^{-1}_{KK'} R^{\lessgtr,\tau}_{K'}\left[M^{a,\tau}(\omega)\right]^{-1}_{K'K''}\boldsymbol{\Pi}_{K'',I}. \tag{4.40}$$

where we defined

$$R^{<,\tau}_{K} = f^{\tau}_{n_1\mathbf{k}}(1-f^{\tau}_{n_2\mathbf{k}}), \tag{4.41a}$$

$$R^{>,\tau}_{K} = f^{\tau}_{n_2\mathbf{k}}(1-f^{\tau}_{n_1\mathbf{k}}). \tag{4.41b}$$

As we can see from (4.35) we need to evaluate the inverse matrices of $M^{r/a,\tau}(\omega)$. This is usually dealt with by defining an auxiliar excitonic Hamiltonian

$$H^{r,\tau}_{KK'} = \Omega^{\tau}_{K}\delta_{KK'} + R^{\tau}_{K}\Xi_{KK'} \tag{4.42a}$$

$$H^{a,\tau}_{KK'} = \Omega^{\tau}_{K}\delta_{KK'} + \Xi_{KK'}R^{\tau}_{K'}, \tag{4.42b}$$

and so we can deal with the problem of evaluating their inverse matrices using diagonalisation or inversion methods. We discuss some of these methods in Appendix D.

We are now able to study the position of the peaks in the spectrum within different levels of approximation for the interaction between the carriers.

4.3.1 System of non-interacting particles

Let's begin with the case of non-interacting particles by taking $\Xi = 0$ in Eqs. (4.38a) and (4.38b). This changes (4.40) into

$$\boldsymbol{\mathcal{L}}^{\lessgtr,\tau}_{K,I}(\omega) = -2\mathrm{i}R^{\lessgtr,\tau}_{K}\boldsymbol{\Pi}_{K,I}\delta\left(\omega-\Omega_K\right), \tag{4.43}$$

which means that the poles of the spectrum lies on top of the energy differences between two electronic levels.

In Fig. 4.3 we separate between a situation where the system is at equilibrium [subfigure a)] and another where there is a population of carriers [subfigure b)].

[1] We used the representation of the Dirac delta function in which

$$\delta(x) = \lim_{\eta\to 0^+}\frac{1}{\pi}\frac{\eta}{x^2+\eta^2}.$$

For the former case, if we recall the definitions of Ω_K^τ and $R_{K'}^{\lessgtr,\tau}$ we can arrive at the following conclusion: $\boldsymbol{\mathcal{L}}^{<,\tau}$ only has contributions in which $f_{n_1\mathbf{k}}(\tau) = 1$ and $f_{n_2\mathbf{k}}(\tau) = 0$, which then means that $\Omega_K = \epsilon_{n_1\mathbf{k}} - \epsilon_{n_2\mathbf{k}} < 0$. So, for a system at equilibrium, $\boldsymbol{\mathcal{L}}^{<,\tau}$ only has contributions for negative ω. Applying the same analysis to $\boldsymbol{\mathcal{L}}^{>,\tau}$, we arrive at the conclusion that the only contributions to this function are from terms which have $f_{n_1\mathbf{k}}(\tau) = 0$ and $f_{n_2\mathbf{k}}(\tau) = 1$. This however means that $\Omega_K = \epsilon_{n_1\mathbf{k}} - \epsilon_{n_2\mathbf{k}} > 0$, and thus $\boldsymbol{\mathcal{L}}^{>,\tau}$ only has contributions for positive ω.

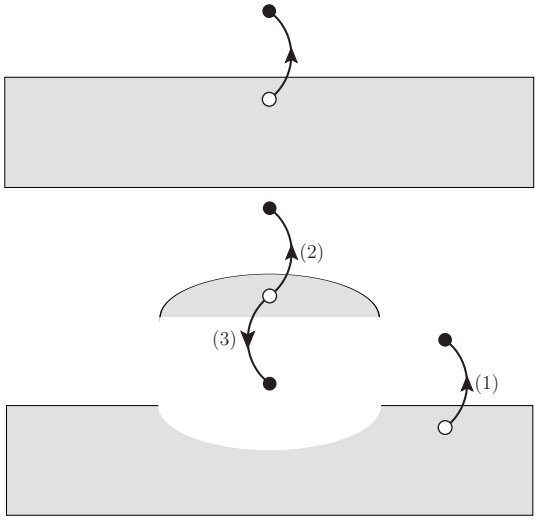

Figure 4.3: Schematic representation of the possible electronic transitions in a system at equilibrium, a), and out-of-equilibrium, b). The white bullet represents the hole created by an electron when absorbing or emitting a photon and the black bullet the final state of the electron.

For the out-of-equilibrium case the situation is slightly more complex. The existence of an electronic population in the conduction bands introduces two more possible transitions, labeled (2) and (3) in Fig. 4.3. The transitions labeled as (1) and (2) are of the same kind as the the one for a system at equilibrium, which we have already discussed in the previous paragraph. Their contributions to $\boldsymbol{\mathcal{L}}^{<,\tau}$ are only for $\omega < 0$, while for $\boldsymbol{\mathcal{L}}^{>,\tau}$ they contribute only when $\omega > 0$. For the transition labeled as (3) the situation is different. For the function $\boldsymbol{\mathcal{L}}^{<,\tau}$, the occupation functions demand that $\Omega_K = \epsilon_{n_1\mathbf{k}} - \epsilon_{n_2\mathbf{k}} > 0$. So these transitions only contribute for the elements of $\boldsymbol{\mathcal{L}}^{<,\tau}$ for which ω is positive. In a similar fashion these transitions

contribute to $\boldsymbol{\mathcal{L}}^{>,\tau}$ only when ω is negative.

In summary, the analysis of the polar structure of the non-interacting $\boldsymbol{\mathcal{L}}^{\lessgtr,\tau}$ functions allowed us to reach the following conclusion: for negative ω, $\boldsymbol{\mathcal{L}}^{<,\tau}$ contains information on electronic transitions in which the electron absorbs a photon and moves to a state of higher energy while $\boldsymbol{\mathcal{L}}^{>,\tau}$ contains information on transitions where the electron emits a photon and decays to a state with lower energy; for positive ω, $\boldsymbol{\mathcal{L}}^{<,\tau}$ contains information on transitions where there is the emission of a photon and $\boldsymbol{\mathcal{L}}^{>,\tau}$ has the information on transitions where a photon is absorbed.

4.3.2 The Tamm-Dancoff approximation and beyond

While the non-interacting particle picture is useful, we can also study what happens when we stay within the framework of the BSE. Usually we are interested in computing the set of eigenvalues and eigenvectors of the excitonic Hamiltonian of Eq. (4.42a), $\{E_\lambda, A^K_\lambda\}$, in order to obtain the absorption spectrum, which involves the retarded function L^r

$$L^r_{K,K'}(\omega) = \sum_{\lambda,\lambda'} \frac{A^K_\lambda S^{-1}_{\lambda,\lambda'} A^{K'}_{\lambda'}}{\omega - E_\lambda + \mathrm{i}\eta} R^r_{K'}, \tag{4.44}$$

where $R^r_{K'} = f_{n_3\mathbf{k}'} - f_{n_4\mathbf{k}'}$[1] controls the eigenvalues E_λ which can have a non-zero contribution for the absorption spectrum. If the system is at equilibrium, the only possible contributions are pairs whose quantum numbers follow $(n_3, n_4) \in \{(c,v),(v,c)\}$, where c/v stands for a conduction/valence band, respectively. Physically this reflects the fact that only electron-hole pairs can contribute to the absorption spectrum. The excitonic Hamiltonian is then divided in four blocks

$$H^{\text{exc}} = \begin{pmatrix} H^{\text{res}}_{(v,c,\mathbf{k}),(v',c',\mathbf{k})} & H^{\text{coupling}}_{(v,c,\mathbf{k}),(c',v',\mathbf{k})} \\ -\left(H^{\text{coupling}}_{(v,c,\mathbf{k}),(c',v',\mathbf{k})}\right)^* & -\left(H^{\text{res}}_{(v,c,\mathbf{k}),(v',c',\mathbf{k})}\right)^* \end{pmatrix} \tag{4.45}$$

where we have the resonant and the coupling parts of the Hamiltonian, respectively

$$H^{\text{res}}_{(v,c,\mathbf{k}),(v',c',\mathbf{k})} = (\epsilon_{c\mathbf{k}} - \epsilon_{v\mathbf{k}})\delta_{c,c'}\delta_{v,v'} + \Xi_{(v,c,\mathbf{k}),(v',c',\mathbf{k})}, \tag{4.46}$$

[1] Here we take $K' = \{n_3, n_4, \mathbf{k}'\}$.

and

$$H^{\text{coupling}}_{(v,c,\mathbf{k}),(v',c',\mathbf{k})} = \Xi_{(v,c,\mathbf{k}),(c',v',\mathbf{k})} \tag{4.47}$$

Due to the signs in Eq. (4.45) and to the fact that H^{res} is Hermitian while H^{coupling} is symmetric, Eq. (4.45) is not necessarily Hermitian. The bottom right block of Eq. (4.45) is called the anti-resonant Hamiltonian since, as the resonant part contains transitions from a valence to a conduction band, the transitions from a conduction to a valence band contribute to the anti-resonant part. This goes to the point made in the previous section, i.e., a resonant transition in absorption is an anti-resonant transition in emission, and vice-versa.

If we ignore the coupling blocks, i.e., the interaction between excitations and de-excitations, we get what is called the Tamm-Dancoff approximation (TDA) [54]. Within this approximation the resonant and anti-resonant parts of H^{exc} are completely decoupled and the absorption and emission peaks are at the symmetric positions in the energy spectrum. The eigenvalues E_λ are then selected, in the case of PL, by the occupation factors $R^{\lessgtr,\tau}_K$ and their strength altered by the $\mathbf{\Pi}_{K,I}$ matrix elements, while for absorption they are selected by the R^{τ}_K factors and the strength of the peaks is altered the dipolar matrix elements.

The validity of the TDA is controlled by the strength of the coupling blocks, in which the dominant contribution is the Hartree term in Eq. (4.24). The strength of the Hartree contribution depends on the inhomogeneity of the electronic density (and thus on the strength of the local fields). As such, for systems which are highly inhomogeneous the TDA eventually fails [69]. The TDA is also known for failing to take into account plasmonic excitations [70], since oscillations of the charge density involve both excitations and de-excitations.

In this work we stay within the TDA. Since in this approximation Eq. (4.45) is hermitian a simple relation between $M^{r,\tau}(\omega)$ and $M^{a,\tau}(\omega)$ holds (see Appendix D). When coming to applications, we must check its validity by comparing the results for absorption within TDA and the full excitonic Hamiltonian.

At this stage we know which non-equilibrium quantities have the information we want to study. The last remaining step is to derive a connection between the $\mathcal{L}^{\lessgtr}$ functions and the macroscopic observable, which we have defined in Eq. (3.51) as the divergence of the Poynting vector.

Chapter 5

Connection to observables

"-so long as I get SOMEWHERE." Alice added as an explanation.
"Oh, you're sure to do that," said the Cat "if only you walk long enough."

Lewis Carroll, *Alice in Wonderland*

5.1 Revisiting the Poynting vector

The information on the analytic properties of the $\mathcal{L}^{\lessgtr}$ functions plays a crucial role in this chapter, as we derive a connection between the macroscopic observable and the microscopic dynamics. However, we must first perform some transformations to the correlation part of the Poynting vector, $\langle \hat{\mathbf{S}}(1) \rangle_{\text{corr}}$ [as defined in Eq. (3.55)]. These transformations allow us to choose which of the $\mathcal{L}^{\lessgtr}$ functions to keep and finally arrive at the expression for the power spectrum.

We start by noticing that we can rewrite Eq. (3.55) in a tensorial form

$$\langle \hat{S}_{\alpha}(1) \rangle_{\text{corr}} = \frac{1}{2} \sum_{\substack{\beta=1 \\ \beta \neq \alpha}}^{3} \left[S_{\beta\beta\alpha}(1,2) - S_{\alpha\beta\beta}(1,2) \right] |_{2=1}, \tag{5.1}$$

allowing us to focus on the simplification of the third-order tensor $S_{\alpha\beta\gamma}(1,2)$, which,

if we take into account Eq. (3.58) is given by

$$S_{\alpha\beta\gamma}(1,2) = \frac{\partial}{\partial t_1}\left\{\frac{\partial}{\partial r_{2,\alpha}}\left[\mathcal{D}^{>}_{\beta\gamma}(1,2) + \mathcal{D}^{<}_{\beta\gamma}(1,2)\right]\right\}$$
$$= \sum_{\alpha_1,\alpha_2=1}^{3}\left[\frac{\partial}{\partial t_1}\mathcal{D}^{0r}_{\beta\alpha_1}(1-3)\right]\left[P^{>}_{\alpha_1,\alpha_2}(3,4) + P^{<}_{\alpha_1,\alpha_2}(3,4)\right]\left[\frac{\partial}{\partial r_{2,\alpha}}\mathcal{D}^{0a}_{\alpha_2\gamma}(4-2)\right]. \quad (5.2)$$

We now re-write the independent particle-photon propagators of Eqs. (3.57a) and (3.57b) into

$$\mathcal{D}^{0r}_{\beta,\alpha_1}(1-3) = \frac{\mathrm{i}c^2}{2}\sum_{I,s} s\tau^{I}_{\beta,\alpha_1}\bar{\xi}_{sI}(\mathbf{r}_1-\mathbf{r}_3)e^{-\mathrm{i}s\omega_I(t_1-t_3)}\theta(t_1-t_3) \quad (5.3a)$$

$$\mathcal{D}^{0a}_{\alpha_2,\gamma}(4-2) = -\frac{\mathrm{i}c^2}{2}\sum_{J,s'} s'\tau^{J}_{\alpha_2,\gamma}\bar{\xi}_{s'J}(\mathbf{r}_4-\mathbf{r}_2)e^{-\mathrm{i}s'\omega_J(t_4-t_2)}\theta(t_4-t_2), \quad (5.3b)$$

which brings Eq. (5.2) in a more compact form

$$S_{\alpha\beta\gamma}(1,2) = -\frac{c^4}{4}\sum_{I,s}\sum_{J,s'}\omega_I Q_{J,\alpha}\bar{\xi}_{sI}(\mathbf{r}_1)\bar{\xi}_{s'J}(-\mathbf{r}_2)e^{-\mathrm{i}s\omega_I t_1}e^{\mathrm{i}s'\omega_J t_2}\mathcal{F}^{\beta,\gamma}_{\substack{s,s'\\I,J}}(t_1,t_2). \quad (5.4)$$

Here we should point out quickly that, since $s, s' = \pm 1$, then $s^2 = s'^2 = 1$. The function $\mathcal{F}$ absorbs most of the parcels in Eq. (5.4) that are not dependent on $\mathbf{r}_1$ or $\mathbf{r}_2$

$$\mathcal{F}^{\beta,\gamma}_{\substack{s,s'\\I,J}}(t_1,t_2) = \int \mathrm{d}\mathbf{r}_3\mathrm{d}\mathbf{r}_4\int_{-\infty}^{t_1}\mathrm{d}t_3\int_{-\infty}^{t_2}\mathrm{d}t_4\, e^{-\mathrm{i}s\mathbf{Q}_I\cdot\mathbf{r}_3}e^{\mathrm{i}s\omega_I t_3}e^{\mathrm{i}s'\mathbf{Q}_J\cdot\mathbf{r}_4}e^{-\mathrm{i}s'\omega_J t_4}$$
$$\sum_{\alpha_1,\alpha_2=1}^{3}\tau^{I}_{\beta,\alpha_1}\tau^{J}_{\alpha_2,\gamma}\left[P^{>}_{\alpha_1,\alpha_2}(3,4) + P^{<}_{\alpha_1,\alpha_2}(3,4)\right], \quad (5.5)$$

and we use it to separate the integrals which are not important for the computation of the divergence of the Poynting vector. We can take the 2→1 limit and evaluate the spatial derivative of Eq. (5.2)

$$\frac{\partial S_{\alpha\beta\gamma}(1,1)}{\partial r_{1,\sigma}} = -\frac{\mathrm{i}c^4}{4}\sum_{I,s}\sum_{J,s'}\omega_I Q_{J,\alpha}(sQ_{I,\sigma} - s'Q_{J,\sigma})\bar{\xi}_{sI}(\mathbf{r}_1)\bar{\xi}_{s'J}(-\mathbf{r}_1)$$
$$e^{-\mathrm{i}s\omega_I t_1}e^{\mathrm{i}s'\omega_J t_1}\mathcal{F}^{\beta,\gamma}_{\substack{s,s'\\I,J}}(t_1,t_2), \quad (5.6)$$

which we are going to use to evaluate the macroscopic average. But before doing so, we must eliminate some spurious terms in Eq. (5.6). These were introduced

between Eq. (5.1) and Eq. (5.4),when we wrote the Fourier expansion of $\langle \hat{S}(1) \rangle_{\text{corr}}$ as the limit of the expansion of the tensor $S_{\alpha\beta\gamma}(1,2)$. We can see that if we compare the expansion of a single-coordinate function, which we call $A(\mathbf{r})$, as a limit when $\mathbf{r}' = \mathbf{r}$ of the expansion of a two-coordinate function, which we call $A(\mathbf{r}, \mathbf{r}')$[1], we arrive at

$$\begin{aligned} A(\mathbf{r}) &= \frac{1}{2\Omega} \sum_{\mathbf{G}} \sum_{\mathbf{q}} \sum_{s} e^{\mathrm{i}s\mathbf{r}\cdot(\mathbf{q}+\mathbf{G})} A_s(\mathbf{q}+\mathbf{G}) \\ &= \frac{2\Omega}{4\Omega^2} \sum_{\mathbf{G}\mathbf{G}'} \sum_{\mathbf{q}\mathbf{q}'} \sum_{ss'} \delta_{s,-s'} \delta_{\mathbf{q},\mathbf{q}'} \delta_{\mathbf{G},\mathbf{G}'} e^{\frac{\mathrm{i}}{2}[s\mathbf{r}\cdot(\mathbf{q}+\mathbf{G}) - s'\mathbf{r}'\cdot(\mathbf{q}'+\mathbf{G}')]} A_s(\mathbf{q}+\mathbf{G})|_{\mathbf{r}'=\mathbf{r}} \\ &= \frac{1}{4\Omega^2} \sum_{\mathbf{G}\mathbf{G}'} \sum_{\mathbf{q}\mathbf{q}'} \sum_{ss'} e^{\frac{\mathrm{i}}{2}[s\mathbf{r}\cdot(\mathbf{q}+\mathbf{G}) - s'\mathbf{r}'\cdot(\mathbf{q}'+\mathbf{G}')]} A_{ss'}\left[s(\mathbf{q}+\mathbf{G}), s'(\mathbf{q}'+\mathbf{G}')\right]|_{\mathbf{r}'=\mathbf{r}}. \end{aligned} \tag{5.7}$$

This means that, in order for the two expressions to match, we must have the following relation between the two coefficients

$$A_{ss'}\left[s(\mathbf{q}+\mathbf{G}), s'(\mathbf{q}'+\mathbf{G}')\right] = 2\Omega \delta_{s,-s'} \delta_{\mathbf{q},\mathbf{q}'} \delta_{\mathbf{G},\mathbf{G}'} A_s(\mathbf{q}+\mathbf{G}). \tag{5.8}$$

As such, in Eq. (5.6) we must exclude all terms which would be eliminated by the Kronecker deltas and correct the volume and numerical factors. Doing so leads to the result

$$\left.\frac{\partial S_{\alpha\beta\gamma}(1,2)}{\partial r_{1,\sigma}}\right|_{2=1} = -4\mathrm{i}\pi^2 c^4 \sum_{I,s} s \frac{Q_{I,\alpha} Q_{I,\sigma}}{\omega_I} e^{\mathrm{i}s(\mathbf{r}\cdot\mathbf{Q}_I - \omega_I t_1)} \underset{I,I}{F^{\beta,\gamma}_{s,-s'}}(t_1,t_1). \tag{5.9}$$

If we now combine Eq. (5.9) with Eq. (5.1) we arrive at

$$\begin{aligned} \nabla \cdot \langle \hat{\mathbf{S}}(1) \rangle_{\text{corr}} = -4\mathrm{i}\pi^2 c^4 \sum_{\substack{\beta=1 \\ \beta\neq\alpha}}^{3} \sum_{I,s} \frac{s e^{\mathrm{i}s(\mathbf{r}\cdot\mathbf{Q}_I - \omega_I t_1)}}{\omega_I} \times \\ \left[Q_{I,\beta} Q_{I,\alpha} \underset{I,I}{F^{\beta,\alpha}_{s,-s'}}(t_1,t_1) - Q_{I,\alpha} Q_{I,\alpha} \underset{I,I}{\mathcal{F}^{\beta,\beta}_{s,-s'}}(t_1,t_1) \right]. \end{aligned} \tag{5.10}$$

By observation we see that we can include the term with $\beta = \alpha$ in the equation above, as it is equivalent to adding zero. This allows us to further simplify the expression for $\nabla \cdot \langle \hat{\mathbf{S}}(1) \rangle_{\text{corr}}$, since

$$\sum_{\alpha=1}^{3} Q_{I,\alpha} \tau^I_{\alpha_2,\alpha} = \sum_{\alpha=1}^{3} Q_{I,\alpha} \left(\delta_{\alpha_2,\alpha} - \frac{Q_{I,\alpha_2} Q_{I,\alpha}}{\mathbf{Q}_I^2} \right) = Q_{I,\alpha} - \frac{Q_{I,\alpha_2} \mathbf{Q}_I^2}{\mathbf{Q}_I^2} = 0, \tag{5.11}$$

[1] We are excluding the time coordinates here, but the conclusions remain valid nonetheless.

and

$$\sum_{\alpha,\beta=1}^{3} Q_{I,\alpha}Q_{I,\alpha}\tau^{I}_{\beta,\alpha_1}\tau^{I}_{\alpha_2,\beta} = \sum_{\alpha=1}^{3} Q_{I,\alpha}\left(\delta_{\alpha_2,\alpha} - \frac{Q_{I,\alpha_2}Q_{I,\alpha}}{\mathbf{Q}_I^2}\right)\left(\delta_{\alpha_2,\alpha} - \frac{Q_{I,\alpha_2}Q_{I,\alpha}}{\mathbf{Q}_I^2}\right)$$
$$= \mathbf{Q}_I^2\left(\delta_{\alpha_1,\alpha_2} - 2\frac{Q_{I,\alpha_2}Q_{I,\alpha_1}}{\mathbf{Q}_I^2} + \frac{Q_{I,\alpha_2}Q_{I,\alpha_1}}{\mathbf{Q}_I^2}\right) = \mathbf{Q}_I^2\tau^{I}_{\alpha_1,\alpha_2}. \quad (5.12)$$

Equations (5.11) and (5.12) further simplify Eq. (5.10) into

$$\nabla\cdot\langle\hat{\mathbf{S}}(1)\rangle_{\text{corr}} = 2\mathrm{i}\pi^2c^2\sum_{\alpha_1,\alpha_2=1}^{3}\sum_{I,s}\omega_I s e^{\mathrm{i}s(\mathbf{r}\cdot\mathbf{Q}_I-\omega_I t_1)}\tau^{I}_{\alpha_1,\alpha_2}\times$$
$$\left[\tilde{P}^{>}_{\alpha_1,\alpha_2}(s\mathbf{Q}_I, s\omega_I; t_1) + \tilde{P}^{<}_{\alpha_1,\alpha_2}(s\mathbf{Q}_I, s\omega_I; t_1)\right], \quad (5.13)$$

where

$$\tilde{P}^{\lessgtr}_{\alpha_1,\alpha_2}(s\mathbf{Q}_I, s\omega_I; t_1) = \int \mathrm{d}\mathbf{r}_3\mathrm{d}\mathbf{r}_4\int_{-\infty}^{t_1}\mathrm{d}t_3\int_{-\infty}^{t_1}\mathrm{d}t_4\, e^{-\mathrm{i}s[\mathbf{Q}_I\cdot(\mathbf{r}_3+\mathbf{r}_4)-\omega_I(t_3+t_4)]}P^{\lessgtr}_{\alpha_1,\alpha_2}(3,4). \quad (5.14)$$

As we wrote in Subsection 3.4.4 we can equate Eq. (5.13) to the power spectrum. In practice however, we need to average over the unit cell, as it is done when evaluating the absorption spectrum [55]. This leads to the elimination of all contributions with G=0, and as such we obtain

$$I(\mathbf{r},t) = 2\mathrm{i}\pi^2c^2\sum_{\alpha_1,\alpha_2=1}^{3}\sum_{s}\int\frac{\mathrm{d}\mathbf{q}}{(2\pi)^3}\omega_{\mathbf{q}}s e^{\mathrm{i}s(\mathbf{r}\cdot\mathbf{q}-\omega_{\mathbf{q}}t)}\tau^{\mathbf{q}}_{\alpha_1,\alpha_2}\times$$
$$\left[\tilde{P}^{>}_{\alpha_1,\alpha_2}(s\mathbf{q}, s\omega_{\mathbf{q}}; t_1) + \tilde{P}^{<}_{\alpha_1,\alpha_2}(s\mathbf{q}, s\omega_{\mathbf{q}}; t_1)\right], \quad (5.15)$$

which is already in a Fourier expansion form. From Eq. (5.15) we can extract the amplitudes $I^{t_1}(\mathbf{q},\omega_q)$

$$I^{t_1}(\mathbf{q},\omega_q) = 4\pi^2c^2\sum_{\alpha_1,\alpha_2=1}^{3}\omega_{\mathbf{q}}\tau^{\mathbf{q}}_{\alpha_1,\alpha_2}\left[\tilde{P}^{>}_{\alpha_1,\alpha_2}(\mathbf{q},\omega_{\mathbf{q}}; t_1) + \tilde{P}^{<}_{\alpha_1,\alpha_2}(\mathbf{q},\omega_{\mathbf{q}}; t_1)\right], \quad (5.16)$$

of which we only need the imaginary part, as it can be seen through inspection of Eq. (5.15). We can now further simplify Eq. (5.16) by dealing with the time and space integrals which were absorbed in Eq. (5.14).

5.2 Selected transitions and light emission

We start by assuming that the conditions which validate the adiabatic approximation still hold (see Subsection 3.4.1), and use them to write for the transverse polarisation functions

$$P^{\lessgtr}_{\alpha\beta}(1,2) = P^{\lessgtr,\tau}_{\alpha\beta}(\mathbf{r}_1,\mathbf{r}_2;t_1-t_2). \tag{5.17}$$

This allows us to use the time-Fourier transform and eliminate the time-integrals, by writing them in a compact form

$$\int \frac{\mathrm{d}\omega}{2\pi} e^{-i\omega(t_1-t_2)} \tilde{f}_{\mathbf{q}}(\omega) \tilde{P}^{\lessgtr,\tau}_{\alpha\beta}(\mathbf{r}_1,\mathbf{r}_2;\omega) \tilde{\bar{f}}_{\mathbf{q}}(\omega), \tag{5.18}$$

where $\tilde{P}^{\lessgtr,\tau}_{\alpha\beta}(\mathbf{r}_1,\mathbf{r}_2;\omega)$ is the Fourier transform of $P^{\lessgtr,\tau}_{\alpha\beta}(\mathbf{r}_1,\mathbf{r}_2;t_1-t_2)$. The auxiliary functions $\tilde{f}_{\mathbf{q}}(\omega)$ and $\tilde{\bar{f}}_{\mathbf{q}}(\omega)$ are given by

$$\tilde{f}_{\mathbf{q}}(\omega) = \int_{-\infty}^{+\infty} \mathrm{d}\tau\, e^{\mathrm{i}\omega\tau} e^{-\mathrm{i}\omega_{\mathbf{q}}\tau}\theta(\tau) = \lim_{\eta\to 0^+} \frac{\mathrm{i}}{\omega-\omega_{\mathbf{q}}+\mathrm{i}\eta} \tag{5.19a}$$

$$\tilde{\bar{f}}_{\mathbf{q}}(\omega) = \int_{-\infty}^{+\infty} \mathrm{d}\tau\, e^{\mathrm{i}\omega\tau} e^{\mathrm{i}\omega_{\mathbf{q}}\tau}\theta(-\tau) = -\lim_{\eta\to 0^+} \frac{\mathrm{i}}{\omega+\omega_{\mathbf{q}}-\mathrm{i}\eta}. \tag{5.19b}$$

If we use Eqs. (5.19a) and (5.19b) and recall that we can always write that

$$\frac{1}{z\pm\mathrm{i}\eta} = \frac{1}{z} \mp \mathrm{i}\pi\delta(z=0), \tag{5.20}$$

we can obtain the expression

$$\begin{aligned}\lim_{\eta\to 0^+} \int \frac{\mathrm{d}\omega}{2\pi} \frac{1}{\omega-\omega_{\mathbf{q}}+\mathrm{i}\eta} \tilde{P}^{\lessgtr,\tau}_{\alpha\beta}(\mathbf{r}_1,\mathbf{r}_2;\omega) \frac{1}{\omega+\omega_{\mathbf{q}}-\mathrm{i}\eta} = \\ = \int \frac{\mathrm{d}\omega}{2\pi} P^{\lessgtr,\tau}_{\alpha\beta}(\mathbf{r}_1,\mathbf{r}_2;\omega) \left[\frac{1}{(\omega-\omega_{\mathbf{q}})(\omega+\omega_{\mathbf{q}})} + \pi^2\delta(\omega-\omega_{\mathbf{q}})\delta(\omega+\omega_{\mathbf{q}}) \right. \\ \left. -\mathrm{i}\pi\frac{\delta(\omega-\omega_{\mathbf{q}})}{\omega+\omega_{\mathbf{q}}} + \mathrm{i}\pi\frac{\delta(\omega+\omega_{\mathbf{q}})}{\omega-\omega_{\mathbf{q}}} \right].\end{aligned} \tag{5.21}$$

The term on the right-hand-side of Eq. (5.21) with the product of two delta functions has no contributions to the sum, as it implies that $\omega_{\mathbf{q}} = -\omega_{\mathbf{q}} \Rightarrow \omega_{\mathbf{q}} = 0$, and this is canceled out by the $\omega_{\mathbf{q}}$ factor in Eq. (5.15). Therefore the only terms which survive in Eq. (5.21) are

$$\int \frac{\mathrm{d}\omega}{2\pi} \frac{\tilde{P}^{\lessgtr,\tau}_{\alpha\beta}(\mathbf{r}_1,\mathbf{r}_2;\omega)}{\omega^2-\omega_{\mathbf{q}}^2} - \frac{\mathrm{i}}{4\omega_{\mathbf{q}}} \left[\tilde{P}^{\lessgtr,\tau}_{\alpha\beta}(\mathbf{r}_1,\mathbf{r}_2;\omega_{\mathbf{q}}) + \tilde{P}^{\lessgtr,\tau}_{\alpha\beta}(\mathbf{r}_1,\mathbf{r}_2;-\omega_{\mathbf{q}}) \right]. \tag{5.22}$$

To proceed further we must look into the properties of the transverse polarisation function and its Fourier transform. Since $P^{\lessgtr}$ is a real function, if we rewrite its Fourier transform $\tilde{P}^{\lessgtr}$ as[1]

$$\tilde{P}^{\lessgtr}(\omega) = \tilde{P}_1^{\lessgtr}(\omega) + \mathrm{i}\tilde{P}_2^{\lessgtr}(\omega), \tag{5.23}$$

where $P_1^{\lessgtr}$ and $P_2^{\lessgtr}$ are also real, then these two functions must obey the following properties regarding their parity

$$\tilde{P}^{\lessgtr}(-\omega) = \left[\tilde{P}^{\lessgtr}(\omega)\right]^* \Rightarrow \begin{cases} \tilde{P}_1^{\lessgtr}(\omega) = \tilde{P}_1^{\lessgtr}(\omega) \\ \tilde{P}_2^{\lessgtr}(\omega) = -\tilde{P}_2^{\lessgtr}(-\omega) \end{cases} . \tag{5.24}$$

An immediate consequence of the parity of $\tilde{P}_1^{\lessgtr}$ and $\tilde{P}_2^{\lessgtr}$ is that we can reduce the last two terms in Eq. (5.22) to

$$-\frac{\mathrm{i}}{4\omega_{\mathbf{q}}}\left[\tilde{P}^{\lessgtr}(\omega_{\mathbf{q}}) + \tilde{P}^{\lessgtr}(-\omega_{\mathbf{q}})\right] = -\frac{\mathrm{i}}{2\omega_{\mathbf{q}}}\tilde{P}_1^{\lessgtr}(\omega_{\mathbf{q}}). \tag{5.25}$$

The relations in Eq. (5.24) are also extremely useful, as they reduce the integral in Eq. (5.22) to a Kramers-Kronig relation between $\tilde{P}_1^{\lessgtr}$ and $\tilde{P}_2^{\lessgtr}$[2]

$$\begin{aligned}\int_{-\infty}^{+\infty}\frac{\mathrm{d}\omega}{2\pi}\frac{\tilde{P}^{\lessgtr}(\omega)}{\omega^2-\omega_{\mathbf{q}}^2} &= \int_0^{+\infty}\frac{\mathrm{d}\omega}{2\pi}\frac{\tilde{P}^{\lessgtr}(\omega)}{\omega^2-\omega_{\mathbf{q}}^2} + \int_{-\infty}^{0}\frac{\mathrm{d}\omega}{2\pi}\frac{\tilde{P}^{\lessgtr}(\omega)}{\omega^2-\omega_{\mathbf{q}}^2} = \\ &= \int_0^{+\infty}\frac{\mathrm{d}\omega}{2\pi}\frac{\tilde{P}^{\lessgtr}(\omega)+\tilde{P}^{\lessgtr}(-\omega)}{\omega^2-\omega_{\mathbf{q}}^2} = \left(-\frac{\pi}{2\omega_{\mathbf{q}}}\right)\left(-\frac{2\omega_{\mathbf{q}}}{\pi}\right)\int_0^{+\infty}\frac{\mathrm{d}\omega}{\pi}\frac{\tilde{P}_1^{\lessgtr}(\omega)}{\omega^2-\omega_{\mathbf{q}}^2} = \\ &= -\frac{\tilde{P}_2^{\lessgtr}(\omega)}{2\omega_{\mathbf{q}}}\end{aligned} \tag{5.26}$$

This means that the only surviving contributions arising from the time-integrals can be written as

$$-\frac{\mathrm{i}}{2\omega_{\mathbf{q}}}\left[\tilde{P}^{\lessgtr,\tau}_{1,\alpha_1\alpha_2}(\mathbf{r}_3,\mathbf{r}_4;\omega_{\mathbf{q}}) - \mathrm{i}\tilde{P}^{\lessgtr,\tau}_{2,\alpha_1\alpha_2}(\mathbf{r}_3,\mathbf{r}_4;\omega_{\mathbf{q}})\right] = -\frac{\mathrm{i}}{2\omega_{\mathbf{q}}}\left[\tilde{P}^{\lessgtr,\tau}_{\alpha_1,\alpha_2}(\mathbf{r}_3,\mathbf{r}_4;\omega_{\mathbf{q}})\right]^*, \tag{5.27}$$

and we can use this result to connect the power spectrum with the BSE equations.

[1] Here we are only interested in the analytic properties of $\tilde{P}$, so for now we ignore its dependencies on other coordinates.

[2] In order to use the Kramers-Kronig relations, $\tilde{P}$ must be analytical either in the upper or the lower-half of the complex plane. This is indeed the case since we can obtain $\tilde{P}$ from $\boldsymbol{\mathcal{L}}$ by using Eq. (4.5) and through what we have seen in Section 4.3 we can separate $\boldsymbol{\mathcal{L}}$ into two components, one which is analytical in the upper-half and another which is analytical in the lower-half.

5.3 The power spectrum

We are now ready to use the information obtained in Section 4.3 to select which of the lesser and greater transverse polarisation functions we keep in order to study the emission spectrum. As we saw there, for positive frequencies it is the $\boldsymbol{\mathcal{L}}^{<}$ function which has the contributions coming from light emission due to electronic transitions, while $\boldsymbol{\mathcal{L}}^{>}$ has the contributions coming from light absorption. Since we are interested in studying the signal coming from photoluminescence, we can disregard the terms involving $P^{>}$ and study only the ones with $P^{<}$. We begin by rewriting Eq. (5.14) as

$$\begin{aligned}\tilde{P}^{<,\tau}_{\alpha_1,\alpha_2}(\mathbf{q}, s\omega_{\mathbf{q}}) &= -\frac{\mathrm{i}}{2\omega_{\mathbf{q}}}\int \mathrm{d}\mathbf{r}_3\mathrm{d}\mathbf{r}_4\, e^{-\mathrm{i}\mathbf{q}\cdot(\mathbf{r}_3+\mathbf{r}_4)}\left[P^{<}_{\alpha_1,\alpha_2}(\mathbf{r}_3,\mathbf{r}_4;\omega_q)\right]^* \\ &= -\frac{\mathrm{i}\Omega}{8\pi c^2}\frac{1}{2}\int \mathrm{d}\mathbf{r}_3\mathrm{d}\mathbf{r}_4\,\xi^*_{\mathbf{q}}(\mathbf{r}_3)\xi^*_{\mathbf{q}}(\mathbf{r}_4)\left[P^{<,\tau}_{\alpha_1,\alpha_2}(\mathbf{r}_3,\mathbf{r}_4;\omega_q)\right]^* \\ = \frac{\Omega}{2c^3}\int \mathrm{d}\mathbf{r}_3\,\xi^*_{\mathbf{q}}(\mathbf{r}_3)\sum_{i,j}\Pi^*_{ij,\alpha_1}(\mathbf{r}_3,\mathbf{r}_3)\left[\mathcal{L}^{<,\tau}_{ij,\alpha_2}(\mathbf{q},\omega_q)\right]^* &= \frac{\Omega}{2c^3}\sum_{i,j}\left[\Pi^{\mathbf{q}}_{ij,\alpha_1}\mathcal{L}^{<,\tau}_{ij,\alpha_2}(\mathbf{q},\omega_q)\right]^*,\end{aligned} \tag{5.28}$$

where we have used the fact that

$$\frac{1}{2}\int \mathrm{d}\mathbf{r}_2\, P^{<}_{\alpha\beta}(1,2)\xi_{\mathbf{q}}(\mathbf{r}_2) = -\frac{4\mathrm{i}\pi}{c}\sum_{ij}\Pi_{ij,\alpha}(\mathbf{r}_1)\mathcal{L}^{<,\tau}_{ij\mathbf{q},\beta}(t_1,t_1';t_2)\Big|_{t_1'=t_1^+}. \tag{5.29}$$

By inserting Eq. (5.28) into Eq. (5.16) we obtain the final expression for the Fourier amplitudes of $I^{\tau}(\mathbf{q},\omega_{\mathbf{q}})$

$$I^{\tau}(\mathbf{q},\omega_{\mathbf{q}}) = \frac{2\pi^2\Omega}{c}\sum_{\alpha_1,\alpha_2=1}^{3}\sum_{i,j}\omega_{\mathbf{q}}\tau^{\mathbf{q}}_{\alpha_1,\alpha_2}\left[\Pi^{\mathbf{q}}_{ij,\alpha}\mathcal{L}^{<,\tau}_{ij,\alpha_2}(\mathbf{q},\omega_q)\right]^*. \tag{5.30}$$

At this stage we must bear in mind that we are only interested in the imaginary parts of the Fourier amplitudes and we have to take the limit $\mathbf{q}\to 0$. This last step is in line with what is done when evaluating absorption, since the photon's momentum is much smaller than that of the electrons. In order to eliminate potential divergences, we redefine the $\boldsymbol{\Pi}_{ij,\mathbf{q}}$ matrix elements [which are present in both Eq. (5.30) and in the definition of $\boldsymbol{\mathcal{L}}$ in Eq. (4.40)] by writting

$$\Pi^{\mathbf{q}}_{ij,\alpha} = \int \mathrm{d}\mathbf{r}\,\xi_{\mathbf{q}}(\mathbf{r})\Pi_{ij,\alpha}(\mathbf{r},\mathbf{r}')|_{\mathbf{r}=\mathbf{r}'} \to \left(\frac{8\pi c^2}{\Omega\omega_{\mathbf{q}}}\right)^{\frac{1}{2}}\Pi^{\mathbf{q}}_{ij,\alpha}, \tag{5.31}$$

where now

$$\Pi^{\mathbf{q}}_{ij,\alpha} = \int \mathrm{d}\mathbf{r}\, e^{i\mathbf{r}\cdot\mathbf{q}} \Pi_{ij}(\mathbf{r},\mathbf{r}')|_{\mathbf{r}=\mathbf{r}'}. \tag{5.32}$$

This means that we can write the power spectrum as a function of $\mathbf{q}$ and $\omega_{\mathbf{q}}$ as

$$I^{\tau}(\mathbf{q},\omega_{\mathbf{q}}) = -16\pi^3 c \sum_{\alpha_1,\alpha_2=1}^{3} \sum_{i,j} \tau^{\mathbf{q}}_{\alpha_1,\alpha_2} \Im\left[\Pi^{\mathbf{q}}_{ij,\alpha_1} \mathcal{L}^{<,\tau}_{ij,\alpha_2}(\mathbf{q},\omega_q)\right], \tag{5.33}$$

where $\Im[z]$ stands for the imaginary part of z. All terms in Eq. (5.33) are now regular in $\mathbf{q}$, except $\tau^{\mathbf{q}}_{\alpha_1,\alpha_2}$ which is ill-defined for when $\mathbf{q} \to 0$. We can circumvent this divergence by assuming that the contribution of a Fourier amplitude $I^{\tau}(\mathbf{q},\omega_{\mathbf{q}})$ of a given $\mathbf{q}$ vector is in fact an integral in a close vicinity of the end point of this vector. We are going to consider this region as a small sphere of radius R_q centred at the end point of $\mathbf{q}$. If we ignore the dependencies of all terms besides the $\tau^{\mathbf{q}}$ matrix inside this sphere, we obtain that the contribution of a $\mathbf{q}$ point is given by

$$\int_{R_q} \mathrm{d}\mathbf{q}\, \tau^{\mathbf{q}}_{\alpha_1,\alpha_2} = \delta_{\alpha_1,\alpha_2} \frac{8\pi}{9} R^3_{\mathbf{q}} = \delta_{\alpha_1,\alpha_2} I^{\mathbf{q}}_{\alpha_1}. \tag{5.34}$$

At long last, we have reached one of the main goals of this work: to obtain an expression from which we can evaluate the photoluminescence signal of a given material. We take the limit $\mathbf{q} \to 0$ and treat $\omega_{\mathbf{q}}$ as an independent variable[1] which we will now call simply ω. With this we can write the power spectrum as

$$I^{\tau}(\omega) = -16\pi^3 c \sum_{\alpha=1}^{3} \sum_{i,j} I_{\alpha} \Im\left[\Pi_{ij,\alpha} \mathcal{L}^{<,\tau}_{ij,\alpha}(\omega)\right]. \tag{5.35}$$

This is the expression which was implemented in YAMBO. In the next chapter we will look into the results which were obtained in the test calculations we performed on monolayer systems of hBN and of WS_2. We should point out that, besides the approximations we have made with respect to the momentum of the photon, this expression if valid for whichever level of theory one would like to use to compute $\mathcal{L}^{<,\tau}_{ij,\alpha}(\omega)$: a system of non-interacting particles; within the excitonic description coming from the BSE; or any other approximation used to describe the two-particle interactions in the material.

[1] Do recall that, while $\mathbf{q}$ can be very small with respect to the electron's momentum, the energy of the associated photon can be quite large, as it is multiplied by the speed of light, c.

5.4 Computational prescription to evaluate the TR-PL spectrum

The technical details of the implementation into YAMBO are presented in Appendix D.

In the following chapter we present the results from the application of these equations to 2D systems. A schematic representation of the steps involved in the computation of a PL spectrum is given in Fig. 5.1. The first step is the computation of the ground state with DFT for a given exchange-correlation potential V_{xc}. This yields the Kohn-Sham eigenstates and eigenvalues, ϕ_i^{KS} and ϵ_i^{KS}, respectively.

The electron-phonon coupling constants, usually named $g_{\boldsymbol{kk'p}}$, and the phonon modes are computed within DFPT, using both the V_{xc} and the ϵ_i^{KS}. These are used later in the time-dependent propagation to include the dissipation of energy from the carriers' scattering with the lattice.

Two more objects have to be computed before the time-dependent calculation can be run. The first one is the quasi-particle G_0W_0 corrections to the energy levels. This allows us to perform the time-run with reasonable values for the band gap, which are usually underestimated within DFT.

The second object is obtained in the run named "Collisions" in Fig. 5.1. Here we evaluate the static components of the self-energy and store them for later usage. This is possible within the COHSEX approximation as it was shown in Sec. 3.1, and as it has been already shown in Ref. [15]. These matrix elements do not change during the time-propagation and as such can be safely stored to quickly update the self-energy.

In parallel to the G_0W_0 quasi-particle corrections we also evaluate the corrections to the energy levels coming from the COHSEX approximation at $t = 0$, $\Delta\epsilon^{\text{X}}(t = 0)$. These are used later in the computation of the PL spectrum.

The databases with the "Collisions", $g_{\boldsymbol{kk'p}}$ coupling constants, G_0W_0 quasi-particle corrections, and the DFT quantities all enter in the time-propagation calculation. Here we specify the characteristics of the laser field[1], such as the

[1] Or of the two laser fields, if we wish to simulate a pump-and-probe experiment.

intensity, energy of excitation, damping, and starting time. During the computation, YAMBO will output at previously specified instants the carrier occupations at that time, $f_i(T)$.

It is these time-dependent occupations which allow us to evaluate the COHSEX corrections to the energy levels at the same instant, $\Delta\epsilon^{\mathrm{X}}(t=T)$. From the latter, together with the $\Delta\epsilon^{\mathrm{X}}(t=0)$ and the $\Delta\epsilon_i^{GW}$ we can evaluate correctly the renormalisation of the band gap at each instant when computing the PL spectrum.

With all of these components ready, we can finally proceed to the actual calculation of the PL spectrum, given by Eq. (5.35). The $f_i(T)$ provide the electronic configuration of the system at a specific instant, while the three databases with the corrections to the energy levels update correctly the electronic energies at the same instant. Again, together with the DFT quantities, we compute the BSE kernel[1], invert it, and obtain the spectrum for that specific instant. By repeating this procedure for other instants, we can simulate a time-dependent PL experiment.

[1]Here we can re-use the electronic screening computed during the COHSEX run with the time-dependent occupations.

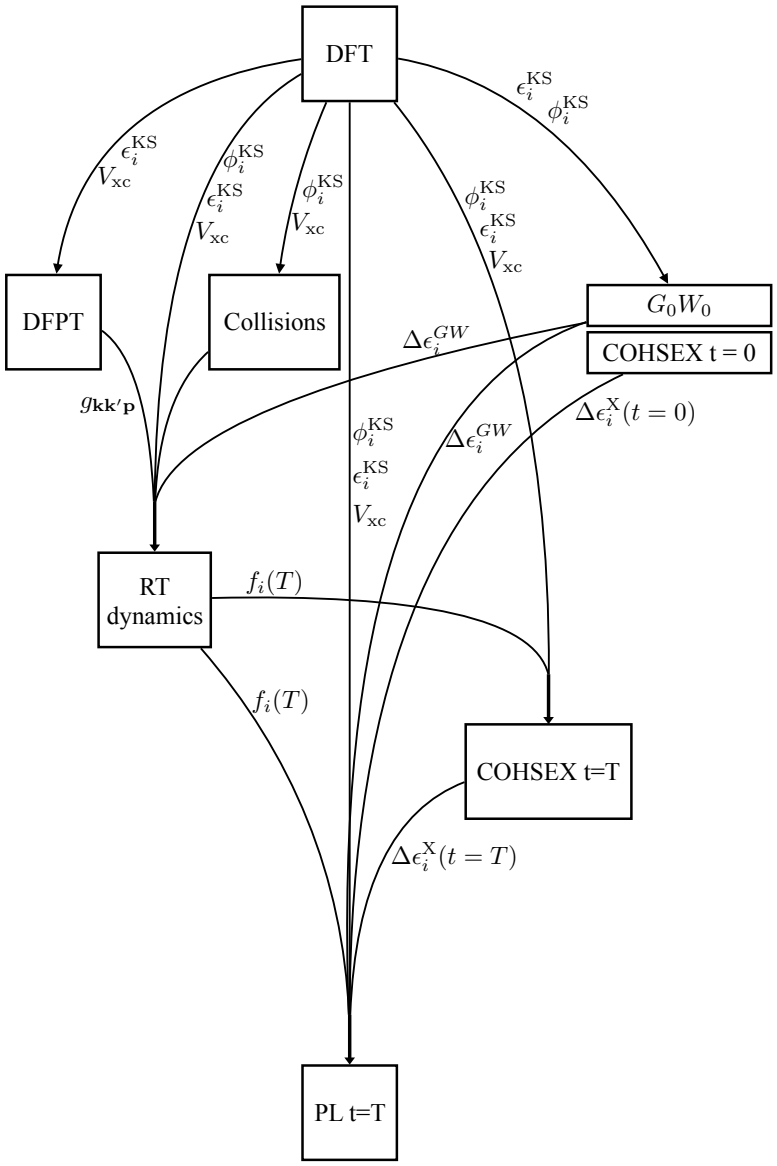

Figure 5.1: Computational diagram representing the necessary steps for a full TR-PL simulation with YAMBO. The starting point (DFT calculation) generates the Kohn-Sham eigenvalues, ϵ_i^{KS}, and eigenstates, ϕ_i^{KS}, for a given exchange-correlation potential, V_{xc}. These are used to compute the quasi-particle G_0W_0 and COHSEX (at t=0) corrections, $\Delta\epsilon_i^{GW}$ and $\Delta\epsilon^{\mathrm{X}}(t=0)$, the electron-phonon coupling constants, $g_{\boldsymbol{kk'p}}$, and the static components of the self-energy. The latter together with the $g_{\boldsymbol{kk'p}}$ and the DFT results are used in the time propagation of the BKE, which generates the time-dependent occupations, $f_i(T)$. These are used to recompute the energy levels renormalisation at a time T, $\Delta\epsilon^{\mathrm{X}}(t=T)$, and entre together with the $f_i(T)$, $\Delta\epsilon_i^{GW}$, $\Delta\epsilon^{\mathrm{X}}(t=0)$, and the DFT output in the computation of the PL spectrum at a given instant, T.

Chapter 6

Application to 2D systems

"And out of all the sweat and swearing and mathematics had come this... thing, dropping words across the world as softly as starlight."

Sir Terence David John "Terry" Pratchett,*"Going Postal"*

In this chapter we present and analyse numerical results for the PL spectrum obtained with the open source code YAMBO when computing the PL spectrum. We performed tests on two monolayer systems: hBN and WS_2.

6.1 hBN tests

Here we analyse the results for a simple controlled test in which the system is prepared as a laser by inverting manually the population at the band gap minimum. We expect that the laser emits at the gap energy. This was a qualitative test used to check the results against the physical intuition we have of the phenomena.

The ground state of the hBN monolayer was computed using the open source code QUANTUM ESPRESSO [71]. This is a plane wave code, i.e., the KS eigenstates are expanded in a plane wave basis. Details on the parameters used to compute the ground state as well as PL related quantities can be found in Appendix E. We obtained a direct gap of 4.74 eV at K, far away from the experimental value of

$\sim$6 eV found in literature [72]. However, as we were more interested in obtaining consistent results rather than comparing with experiments, no quasi-particle (QP) corrections to the KS bandstructure was applied. Once the ground state was obtained, we used YAMBO to create an artificial excited state, by moving an electron from the 4^{th} to the 5^{th} band at the K-point[1]. We then used YAMBO to compute the PL signal and the transient absorption within both the non-interacting particle approximation and the BSE, and compared the results with the equilibrium absorption. Again, we recall that our results are limited to the TDA, as explained in section 4.3. The computed results for hBN were obtained using the diagonalisation solver for the BSE matrix (see Appendix D).

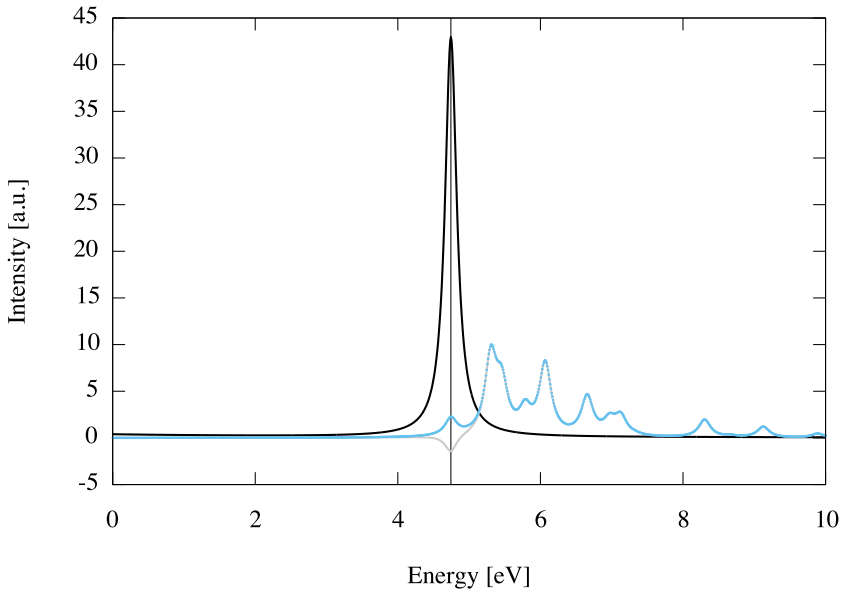

Figure 6.1: PL (solid black line) and transient absorption (solid grey line) for the artificial excited state created in a monolayer of hBN by pumping an electron from the 4^{th} to the 5^{th} band at the K-point and computed within the non-interacting particle approximation. The vertical line indicates the PL peak and the matching negative transient absorption peak at 4.74 eV. The dotted blue line is the equilibrium absorption spectrum computed within the non-interacting particle approximation.

In Figs. 6.1 and 6.2 we plot the calculated spectra for the non-interacting particle calculations and the BSE, respectively.

[1]Note that this procedure is much simpler than the one described in Sec. 5.4 and illustrated in Fig. 5.1, as it is used to create an artificial excited state, and not to do a realistic TR-PL simulation.

The obtained transient absorption spectrum at the independent particle level in Fig 6.1 (solid grey line) matches the equilibrium results (dotted blue line) except for the 4.74 eV peak. Here the transient spectrum shows a negative peak. This feature is a characteristic signature of population inversion, in which all electrons were moved from a valence state to a conduction one[1]. An experimental setup with this configuration would measure a gain in the electric field, which means that the system is emitting light. This is precisely what we obtain with the PL spectrum (solid black line) in Fig. 6.1. There is a single emission peak at the energy corresponding to the population inversion in the transient absorption spectrum. Moreover, the peak is precisely at the position of the direct band gap. This is to expect really, at least at IP level since we are inverting the population at the direct gap.

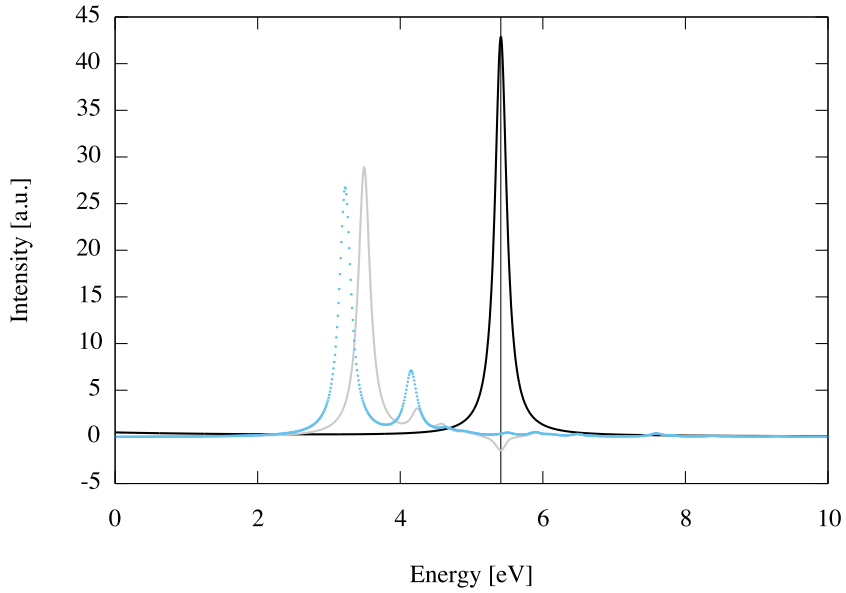

Figure 6.2: PL (solid black line) and transient absorption (solid grey line) for the artificial excited state created in a monolayer of hBN by pumping an electron from the 4^{th} to the 5^{th} band at the K-point and computed using the BSE. The vertical line indicates the PL peak and the matching negative transient absorption peak at 5.41 eV. The dotted blue line is the equilibrium absorption spectrum computed with the BSE.

[1] In other words, it is similar to a laser system

In Fig. 6.2 the computed spectra at the BSE level show a blue shift between the equilibrium and the transient absorption spectra. The change in the peaks is expected, as we are changing the occupations which enter in the BSE matrix (see Section 4.3), but not renormalising the gap (see Subsection 6.2.3). In spite of those differences in the absorption, for the PL we obtain results similar to those in Fig. 6.1, i.e., there is a single emission peak detected in the PL spectrum corresponding to a negative peak in the transient absorption, but now at 5.41 eV.

Next we compare the results given by the inversion and diagonalisation solvers (see Appendix D). For the non-interacting particle approximation (not shown) no differences were found between the two spectra. Instead, in Fig. 6.3 there are some slight differences in the strength of the single peak, as well as in the tail coming from the negative frequencies. Since the inversion solver is the easiest to analyse we decided, after checking its validity, to use it for the calculations on WS_2.

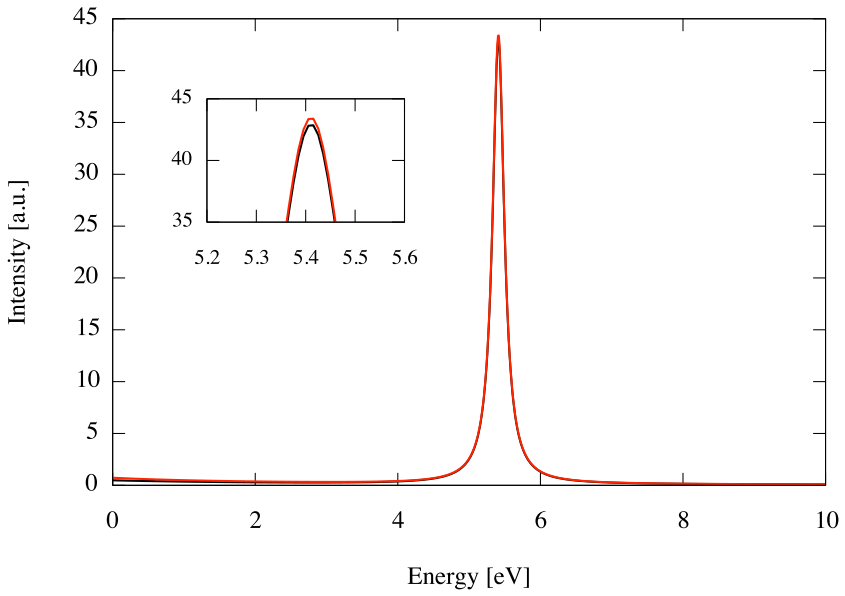

Figure 6.3: BSE PL results obtained via the inversion (solid black line) and diagonalisation (solid red line) solvers for the hBN monolayer with the same excited state as in Fig. 6.1 and Fig. 6.2. The inset plot is a close in on the top of the peak.

One aspect which we have not mentioned yet is the non-zero PL spectral intensity at 0 eV in Figs. 6.1, 6.2, and 6.3 are a numerical artefact. We plot in Fig. 6.4 the spectra for both positive and negative energies. In the inset the figure shows

the signal contamination from the much higher peaks from negative energies (for instance, the strongest peak is almost on hundred times higher than the peaks at positive energies).

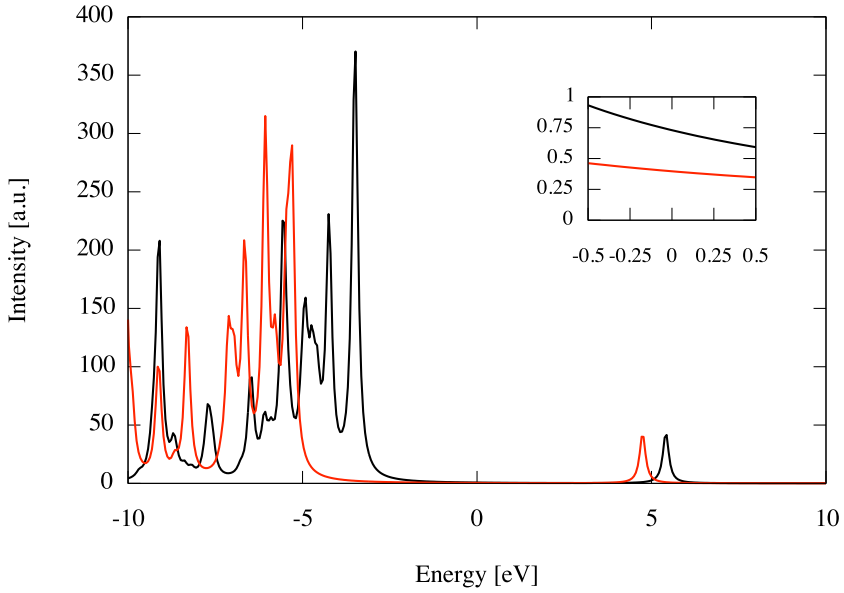

Figure 6.4: IP (solid red line) and BSE (solid black line) PL results for the hBN monolayer with the same excited state as in Fig. 6.1 and Fig. 6.2. The spectra for negative frequencies is also plotted. The inset plot is a close in on the Lorentzian tails close to 0 eV.

In conclusion, the laser system we set up emits at the energies where population inversion was created, which checks against the expected behaviour.

6.2 Preliminary results on WS_2

In recent years there has been an extraordinary increase in studies of optical and electronic properties of 2D materials, especially group-VI transition metal dichalcogenides (TMDs). In these compounds at the band edge are controlled by two non-equivalent energy valleys occurring at the +K and -K points. Together with spin-orbit coupling effects, this symmetry breaking allows one to control the population of carriers at each valley, thus creating a way to store binary information [73] and use TMDs in semiconducting devices [74].

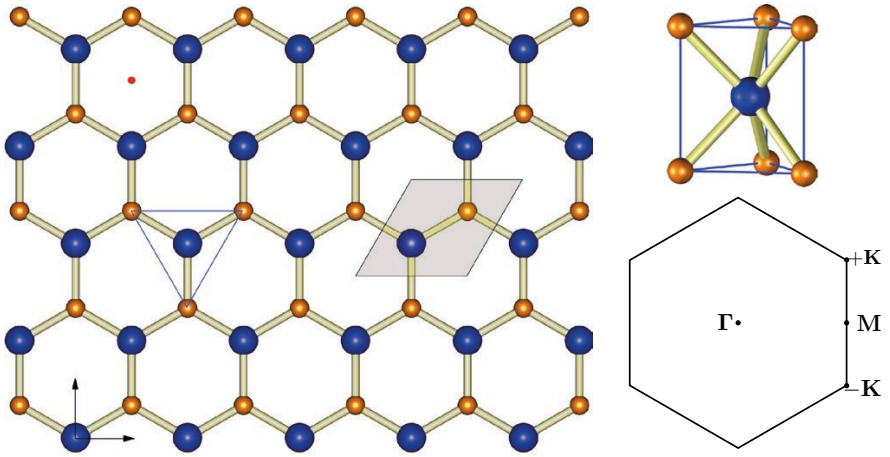

Figure 6.5: WS_2 monolayer and lateral view (taken from Ref. [73]) and Brillouin zone. Blue spheres depict W atoms, while golden spheres depict S atoms.

A common way to research TMDs is by photoluminescence. Some remarkable results regarding valley polarisation [75, 76] have shown that high-fidelity valley initialisation is possible with optical injection (i.e., creation of different valley populations through circularly polarised light). Other highly interesting results obtained from PL spectroscopy have shown that, contrary to what is usually expected, an increase in temperature can in fact magnify the PL signal of WSe_2 [77].

Two important aspects should pointed out: first, since everything is still at an experimental stage, the results which are presented are not at convergence; second, of the three possible scattering channels, e-p, e-γ, and e-e we are only considering e-p in the time-propagation calculations. The e-e channel can be deactivated since the number of electrons promoted to the conduction bands is not high enough for the interactions between them to be relevant. In the e-γ case, the code is still experimental, so it was turned off to reduce further instabilities in the results. Without the e-γ channel we should expect the strength of our signals to saturate after a certain time, as electrons cannot move down from the conduction bands into the valence states.

The aim of the study is then twofold: firstly to check if the code works as expected, for instance, if we can reproduce the physical picture of the phenomenon and possibly compare our results against experimental data; secondly to start the

computational study PL in TMDs, in order to provide some understanding of experimental results.

Here we used again the code QUANTUM ESPRESSO to compute the ground state of the WS_2 monolayer. We obtained an LDA gap of 1.50 eV which was corrected with a scissor operator of 1.05 eV obtained from a G_0W_0 quasiparticle calculation, thus yielding a total band gap of 2.55 eV. Again, details on the numerical parameters which were used in the calculations can be found in Appendix E.

In order to check the validity of the TDA, we first computed the equilibrium absorption spectrum. The results are presented in Fig. 6.6, where the peaks' positions do not change between the TDA (solid red line) to the full BSE (solid black line). The relative change in the intensity shown in the inset does not go beyond 10%. As such, we decided to proceed with the calculations within the TDA.

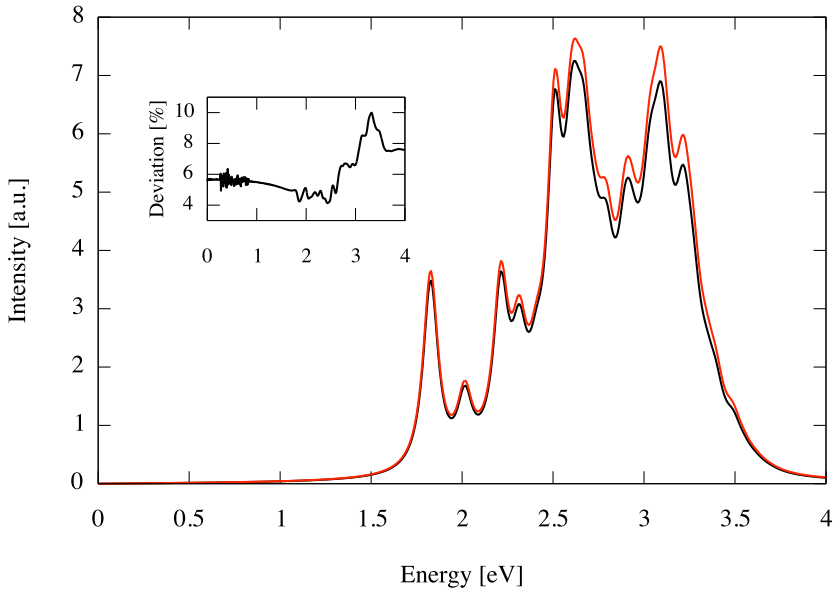

Figure 6.6: Absorption spectrum evaluated within the TDA (solid red line) and the full BSE Hamiltonian (solid black line) for the WS_2 monolayer. Inset - change in the intensity of the full BSE results relative to the TDA ones.

6.2.1 Time-dependent runs

We want to see how the PL signal changes with the characteristic of the laser (central frequency and pulse duration) and with the temperature.

The profile of the laser pulse used in the simulations was that of a plane wave modulated by a gaussian function,

$$E(t) = E_0 \sin\left[\omega_0 \left(t - T_0\right)\right] e^{-\frac{(t-T_0)^2}{2\sigma_t^2}}, \tag{6.1}$$

where ω_0 is the central frequency of the laser pulse, T_0 the starting time, σ_t the damping, and E_0 the magnitude of the electric field. The starting time for each laser pulse is chosen in YAMBO according to

$$T_0 = \frac{\pi}{\omega_0} \mathrm{Nint}\left(\frac{2\omega_0\sigma_t}{\pi}\right), \tag{6.2}$$

where $\mathrm{Nint}(x)$ represents the closest integer to x. The magnitude of the electric field is related with the intensity of the laser pulse, I_0, by

$$I_0 = \frac{c}{8\pi} E_0^2. \tag{6.3}$$

In Tab. 6.1 we summarise the different conditions we explored in our simulations. The strategy for the computation of the PL spectrum is the one already explained

Table 6.1: Simulation conditions used for the time-dependent runs on WS_2. The exponent at each damping value represents the assigned test name in this work.

Central frequency [eV]	Temperature [K]	Intensity [kW/m^2]	Damping [fs]	Fluence [nJ/cm^2]
1.826	4.0	10^5	100.0^{A} 50.00^{B} 25.00^{C}	8861.79 4431.00 2215.52
1.826	100.0 300.0^{E}	10^5	100.0^{D}	8861.79
2.200	4.0	10^5	100.0^{F}	8861.79

in Sec. 5.4 and depicted in Fig. 5.1. Note that PL calculations were performed with the electron system at 0 K, in order to isolate effects of broadening in the energy bands.

6.2.1.1 Effects of the pulse duration

In Fig. 6.8 we have the evolution of the carriers in the band structure at given instants for the test labeled as A in Tab. 6.1. The corresponding spectra at each instant are plotted in Fig. 6.9 for the IP case and in Fig. 6.10 for the BSE. Carrier populations are created in a region nearby the K point and that they decay to the edges of the bands at K. Both the PL spectra in Figs. 6.9 and 6.10 reflect the characteristics of the carriers' evolution in time. The long laser pulse creates a narrow excitation region in the band structure[1] which is characterised by the strong main peaks in both the IP and BSE cases.

In both approximations emission is negligible up to 200 fs. For IP we observe that after 400 fs the system emits a photon at 2.32 eV. As time evolves, the peak is red-shifted and its intensity increases. Regarding the BSE results in Fig. 6.10, there is a strong peak at 1.82 eV which position remains constant for the duration of the time-dependent run. We argue that the shoulder at approximately 2 eV is a numerical artefact which should disappear when converging the results with respect to the k-point grid.

Just to reinforce a previous point, in Fig. 6.7 we plotted the PL spectrum for the case A at 1200 fs. The intensity of the spectrum is about sixty times stronger for negative energies than for positive ones. This high intensity creates a tail which contaminates the signal for positive frequencies, as depicted in the inset. To remove this tail we fitted a Lorentzian distribution to the region of the spectrum close to 0 eV and then removed it from the signal.

We compare now the results obtained for the test case A with those from test cases B and C. In Tab. 6.1 they differ only in the values for the damping of the laser field and thus in the fluence. From Figs. 6.11 and 6.14 we see that there are no striking differences in the regions where the carrier populations are created. The fact that there is already light emission at 200 fs in Figs. 6.12 and 6.13 and Figs. 6.15 and 6.16 is due to Eq. (6.2). Since σ_t is shorter, YAMBO choses earlier starting times for the laser pulses of cases B and C.

In Figs. 6.12 and 6.13 and Figs. 6.15 and 6.16 the broadening of the peaks increases with the decrease in the laser damping. This is expected, since a shorter

[1]For a gaussian curve the uncertainty principle yields $\sigma_t \sigma_E = \frac{1}{2}$, where σ_E and σ_t are the uncertainties in energy and time, respectively.

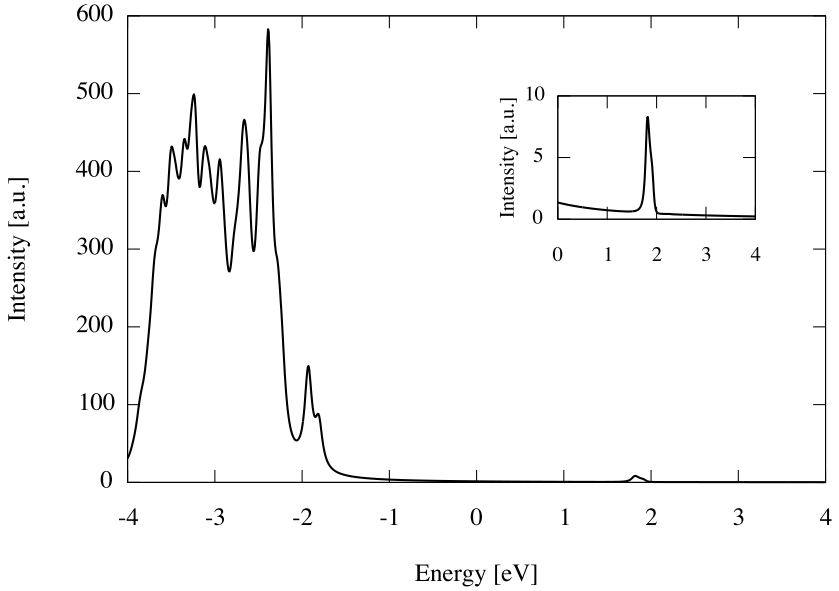

Figure 6.7: Full BSE photoluminescence spectra for case A in Tab. 6.1 at 1200 fs. Inset - region of positive frequencies only.

uncertainty in time, σ_t, is translated into a larger uncertainty in energy, σ_E. Hence the broadening of the peaks in Figs. 6.12 and 6.13 where the damping is 50 fs will be larger than the ones in Figs. 6.9 and 6.10, and the broadening of peaks in Figs. 6.15 and 6.16 will be the largest of the three cases.

To better illustrate the changes in the energy the highest peak (EHP) and its intensity (IHP), their evolution in time is plotted in Fig. 6.17 for both the IP and BSE results. The data in Figs. 6.17a, 6.17c, and 6.17e show that there is a significant reduction in the intensity of the PL signal with the fluence of the laser. This result is expected, since the higher the fluence, the higher the number of electrons which are excited to the conduction bands, and so the higher the PL signal.

Regarding the EHP, subfigures b), d), and f) of Fig. 6.17 show that the change in the EHP for the IP case is more pronounced for the case A of Tab. 6.1 (about 0.20 eV) than for cases B (about 0.18 eV) and C (about 0.05 eV). This is again related to the changes in fluence between each laser pulse. The pulses which transfer more energy to the system create higher densities of carriers. This then leads to a higher renormalisation of the energy levels, and thus a higher renormalisation of the band gap.

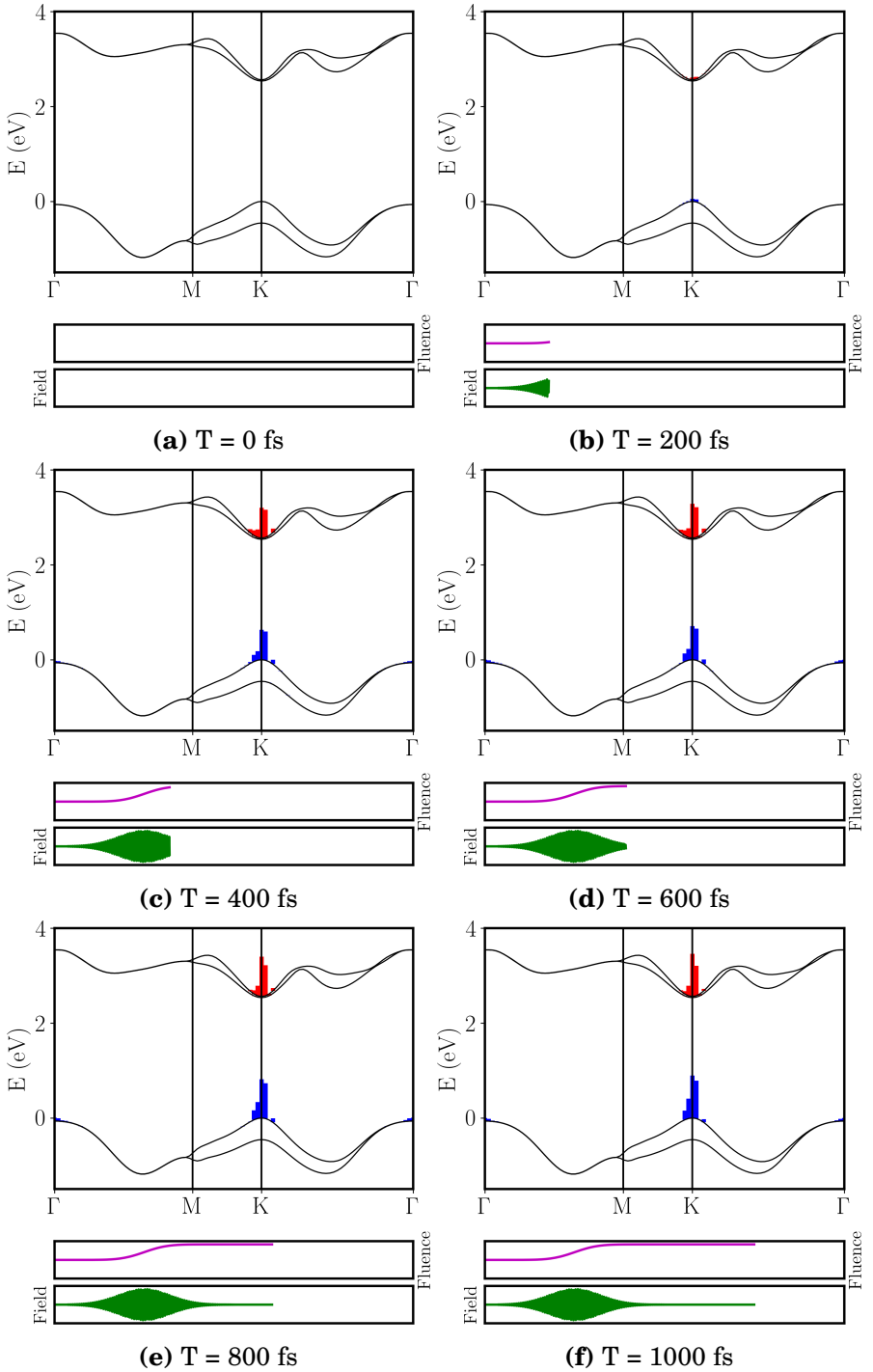

(a) T = 0 fs **(b)** T = 200 fs

(c) T = 400 fs **(d)** T = 600 fs

(e) T = 800 fs **(f)** T = 1000 fs

Figure 6.8: Evolution in time of the carrier occupations on the band structure for case A in Tab. 6.1. Blue columns represent holes, while electrons are represented by red columns. The green line represents the laser profile and the purple on the evolution in time of the fluence.

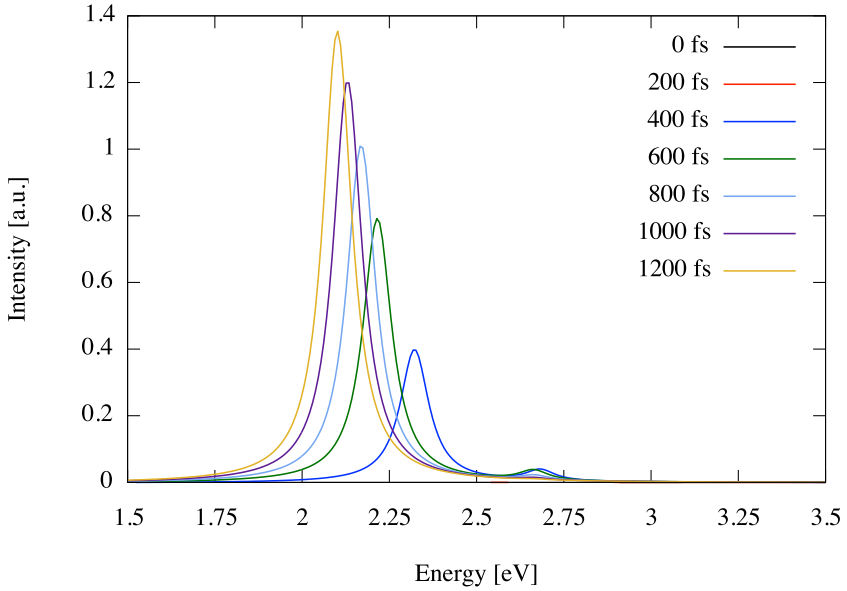

Figure 6.9: Non-interacting photoluminescence spectra for case A in Tab. 6.1. Results are plotted from 0 to 1200 fs in intervals of 200 fs. The 0 an 200 fs lines do not appear because there is no signal at those instants.

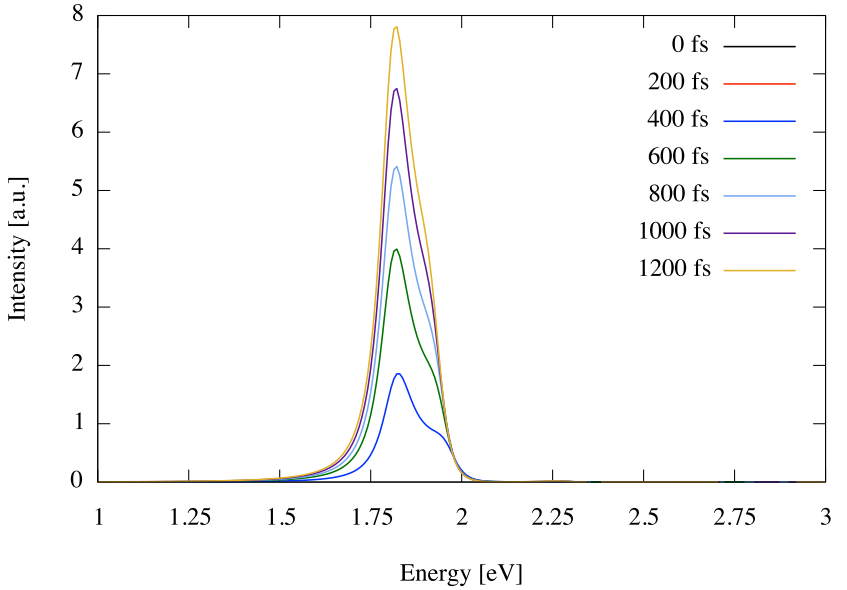

Figure 6.10: BSE photoluminescence spectra for case A in Tab. 6.1. Results are plotted from 0 to 1200 fs in intervals of 200 fs. The 0 an 200 fs lines do not appear because there is no signal at those instants.

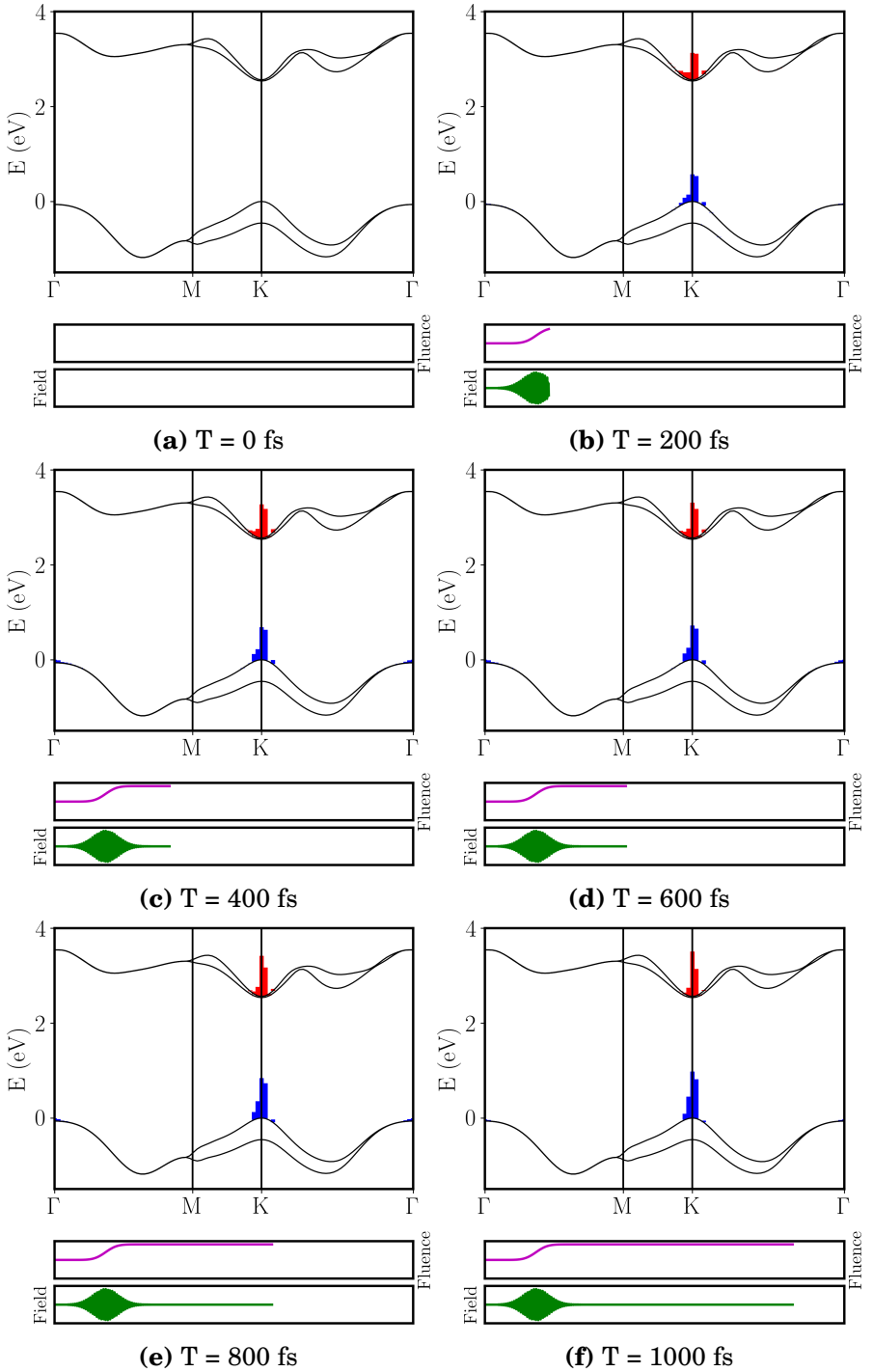

(a) T = 0 fs **(b)** T = 200 fs

(c) T = 400 fs **(d)** T = 600 fs

(e) T = 800 fs **(f)** T = 1000 fs

Figure 6.11: Evolution in time of the carrier occupations on the band structure for case B in Tab. 6.1. Blue columns represent holes, while electrons are represented by red columns. The green line represents the laser profile and the purple on the evolution in time of the fluence.

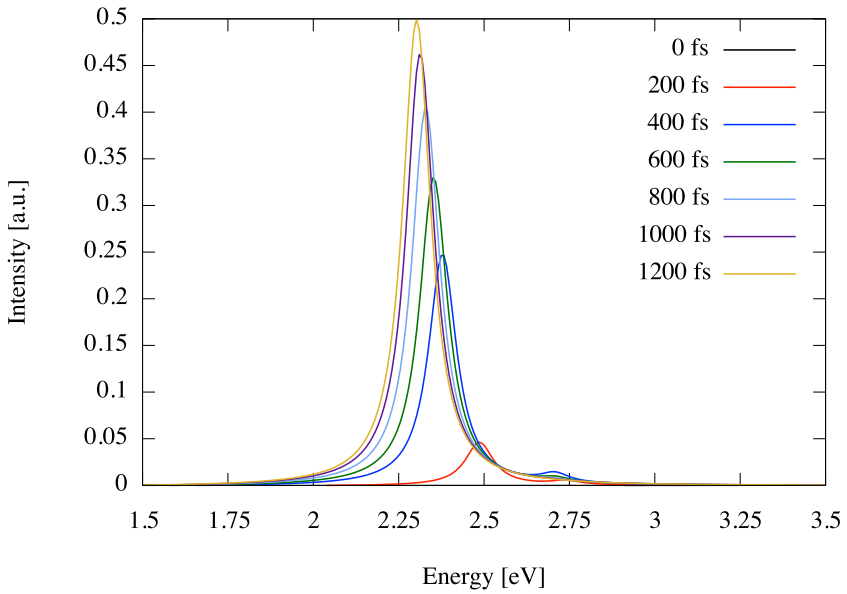

Figure 6.12: Non-interacting photoluminescence spectra for case B in Tab. 6.1. Results are plotted from 0 to 1200 fs in intervals of 200 fs.

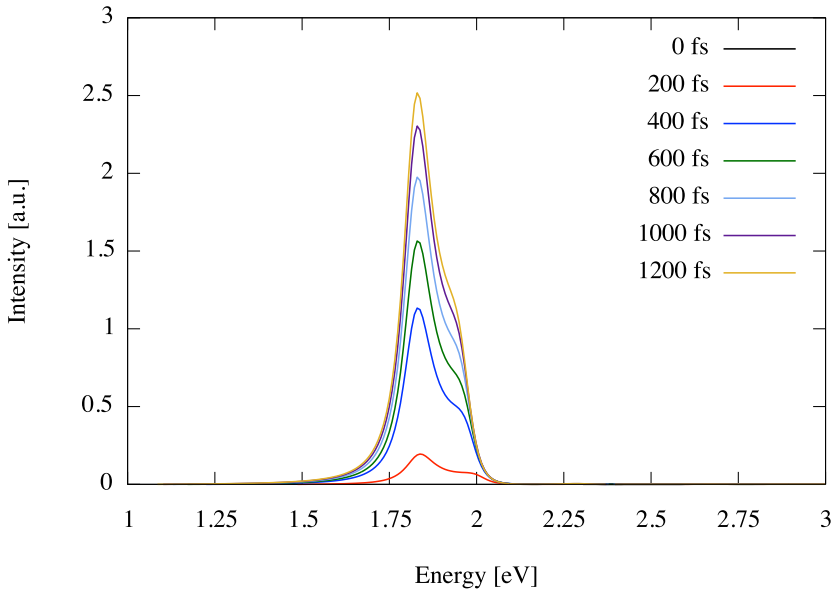

Figure 6.13: BSE photoluminescence spectra for case B in Tab. 6.1. Results are plotted from 0 to 1200 fs in intervals of 200 fs.

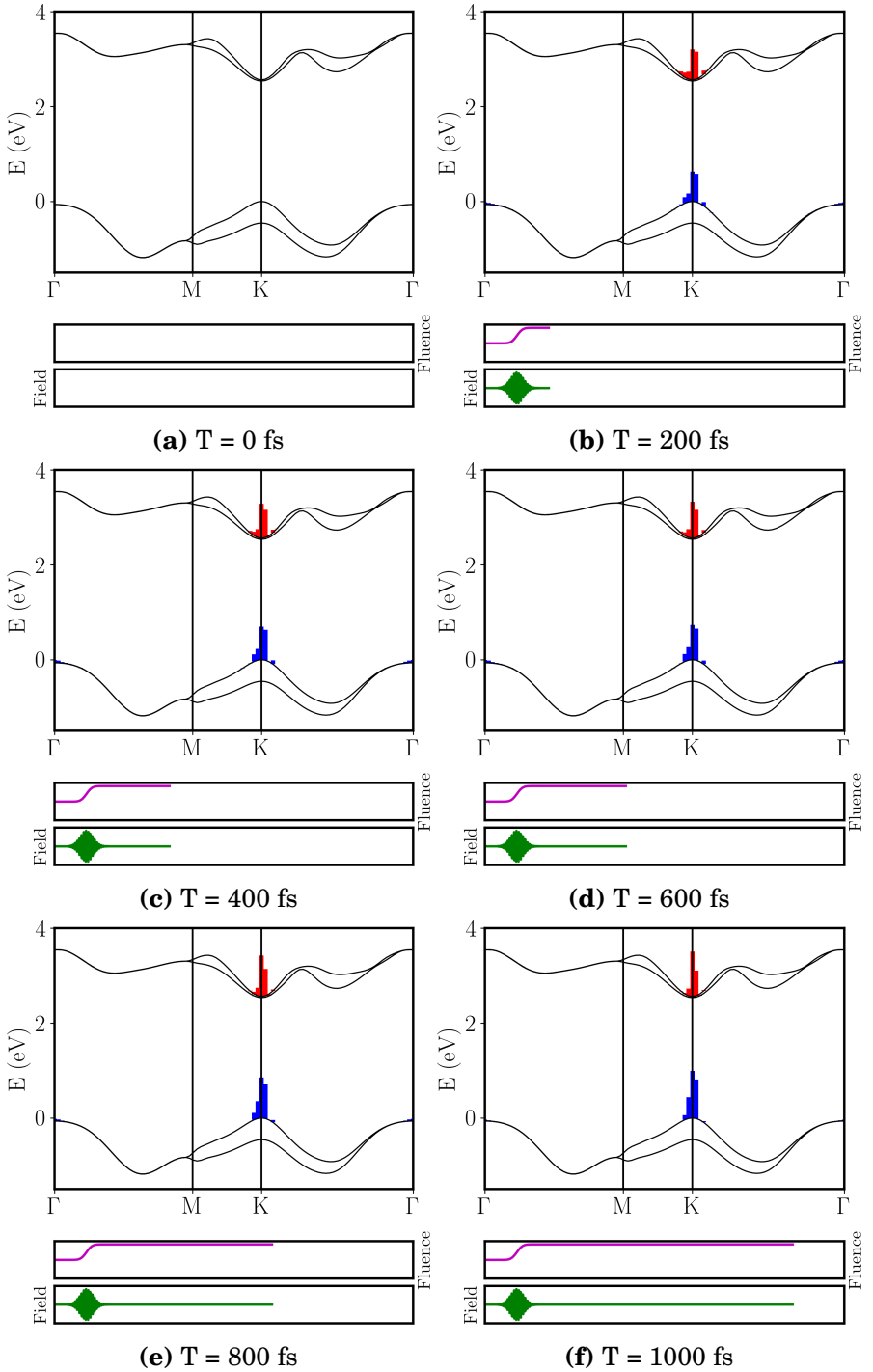

(a) T = 0 fs **(b)** T = 200 fs

(c) T = 400 fs **(d)** T = 600 fs

(e) T = 800 fs **(f)** T = 1000 fs

Figure 6.14: Evolution in time of the carrier occupations on the band structure for case C in Tab. 6.1. Blue columns represent holes, while electrons are represented by red columns. The green line represents the laser profile and the purple on the evolution in time of the fluence.

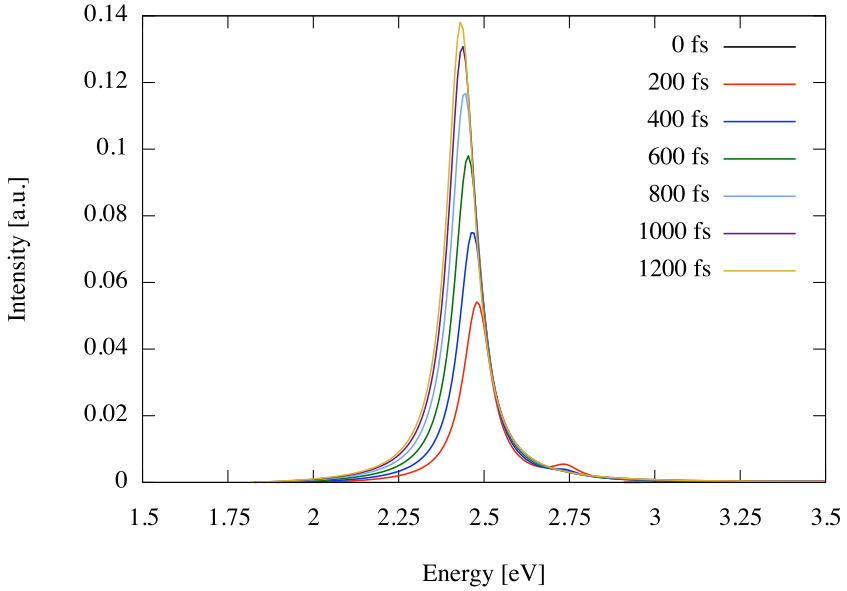

Figure 6.15: Non-interacting photoluminescence spectra for case C in Tab. 6.1. Results are plotted from 0 to 1200 fs in intervals of 200 fs.

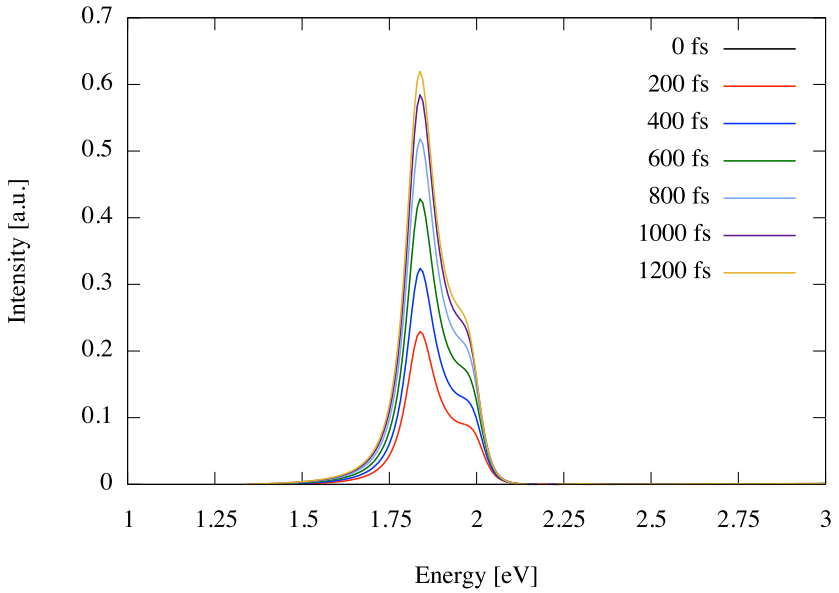

Figure 6.16: BSE photoluminescence spectra for case C in Tab. 6.1. Results are plotted from 0 to 1200 fs in intervals of 200 fs.

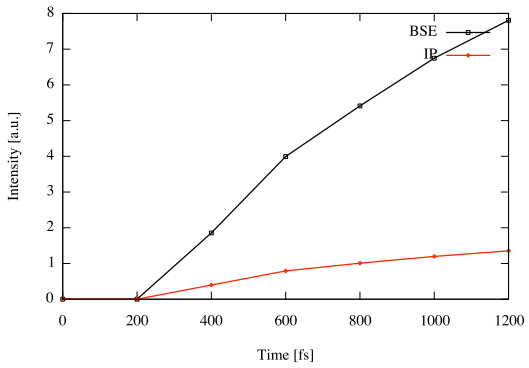

(a) IHP over time for test A

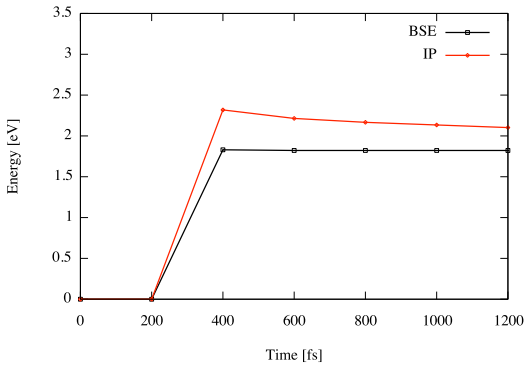

(b) EHP over time for test A

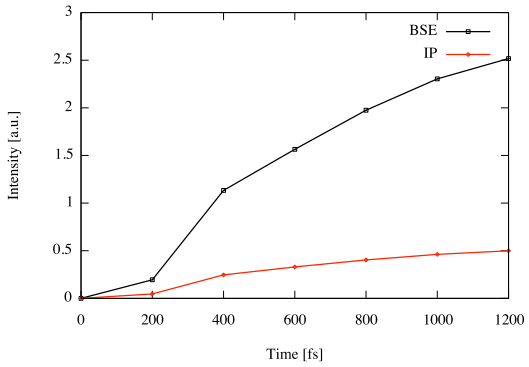

(c) IHP over time for test B

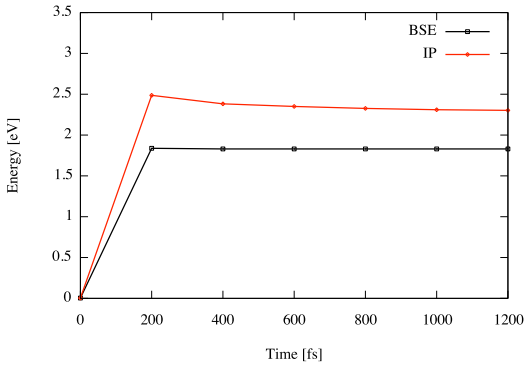

(d) EHP over time for test B

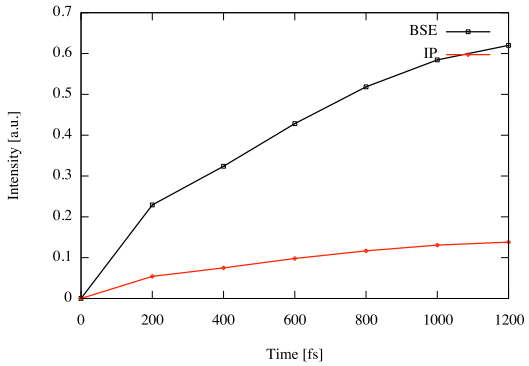

(e) IHP over time for test C

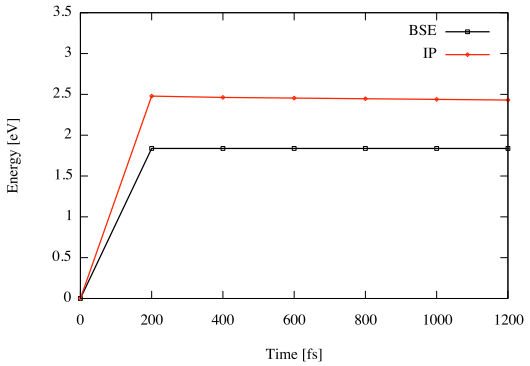

(f) EHP over time for test C

Figure 6.17: Evolution in time of the intensity of the maximum peak (IHP) and energy of the maximum peak (EHP) for the tests A, B, C of Table 6.1 within the non-interacting approximation (IP) (solid red line) and BSE (solid black line).

For the BSE, the change in the EHP is almost imperceptible from subfigures b), d), and f) of Fig. 6.17. In fact, within the precision of the code, the EHP changes

about 0.01 eV for cases A and B, and we register no change for case C. The changes relative to the equilibrium values, 1.84 eV for the optical gap and 2.55 eV for the quasi-particle band gap are shown in Tab. 6.2 and again show that the higher the fluence, the higher the renormalisation.

Table 6.2: Change energy of the highest peak (EHP) for the calculated IP and BSE spectra at 1200 fs for the cases A, B, and C of Tab. 6.1.

Test case	IP [eV]	BSE [eV]
A	2.10	1.82
B	2.30	1.83
C	2.43	1.84

6.2.1.2 Effect of the temperature

We then moved on to test cases D and E, in which the laser frequency and pulse duration are the same as in test case A, but the system's temperature during the time-propagation is 100.0 K and 300.0 K, respectively. Snapshots of the carrier dynamics can be seen in Figs. 6.18 and 6.21 for the cases D and E, and the PL signals are presented in Figs. 6.19 and 6.20 for test D, and Figs. 6.22 and 6.23 for test D. The evolution of the IHP and EHP is shown in Fig. 6.24.

Regarding the overall shape of the PL spectrum, there are some differences between the signals for cases A (4.0 K), D (100.0 K), and E (300.0 K). As it is shown in Fig. 6.24a, while the initial growth rate of the signal appears to be similar for A and D, for both the IP and BSE results the signal approaches saturation much faster than in case A, where the time-dependent simulation was performed at 4.0 K. The faster saturation of the signal for IP can be understood since with higher temperature the e-p transition matrix elements are larger, thus the probability of emitting a phonon is higher and more scattering terms are allowed than at low temperature. The reduction in the intensity of the maximum peak is also expected, as it is known that an increase in temperature will, in general, bleach the emission peaks. Regarding the change in the position of the peaks, the behaviour is almost identical to the one observed in test A (Fig. 6.17b). The IP peaks change from 2.33 eV to 2.20 eV, while the BSE peaks go from 1.83 eV to 1.82 eV.

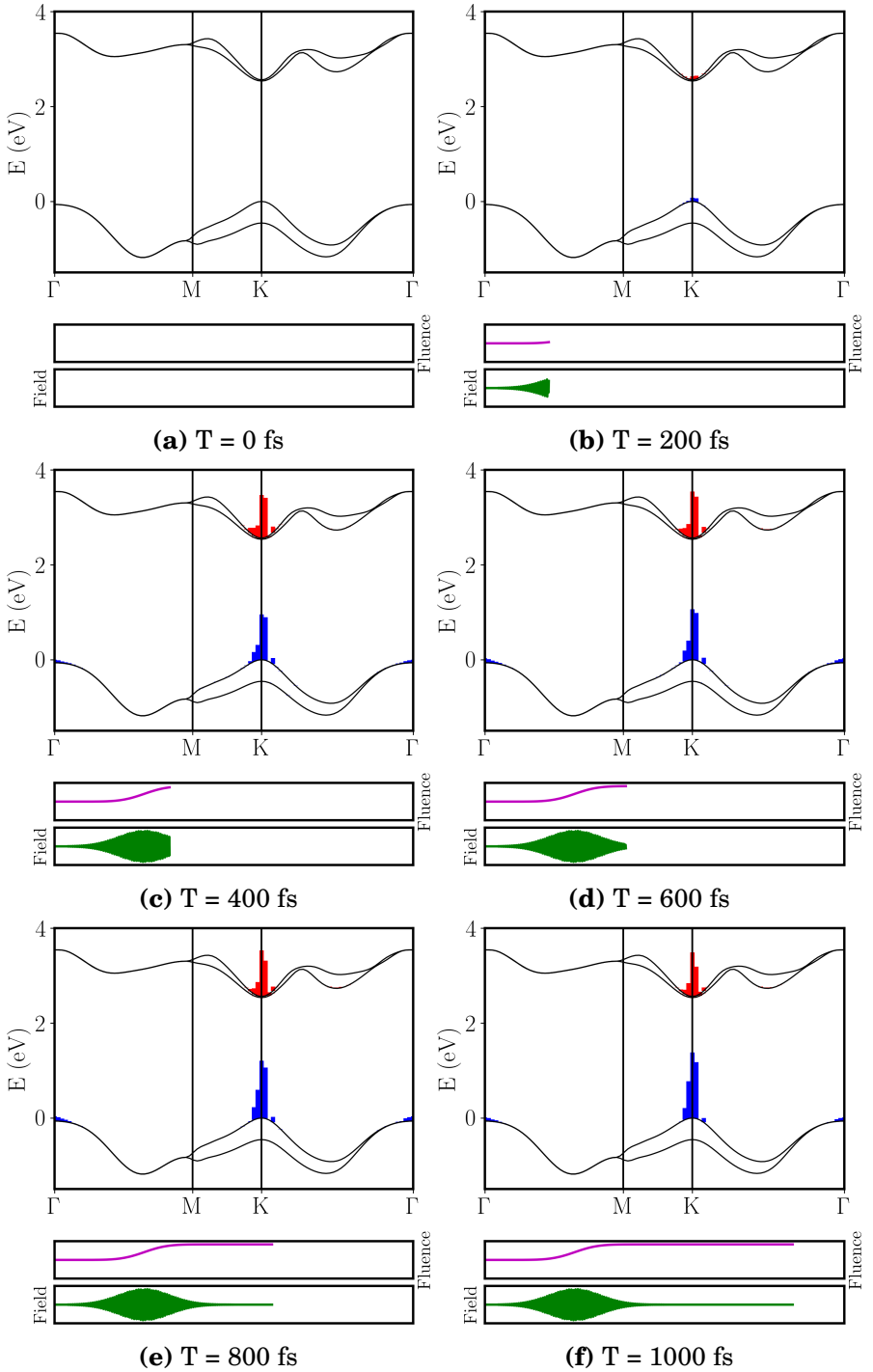

(a) T = 0 fs **(b)** T = 200 fs

(c) T = 400 fs **(d)** T = 600 fs

(e) T = 800 fs **(f)** T = 1000 fs

Figure 6.18: Evolution in time of the carrier occupations on the band structure for case D in Tab. 6.1. Blue columns represent holes, while electrons are represented by red columns. The green line represents the laser profile and the purple on the evolution in time of the fluence.

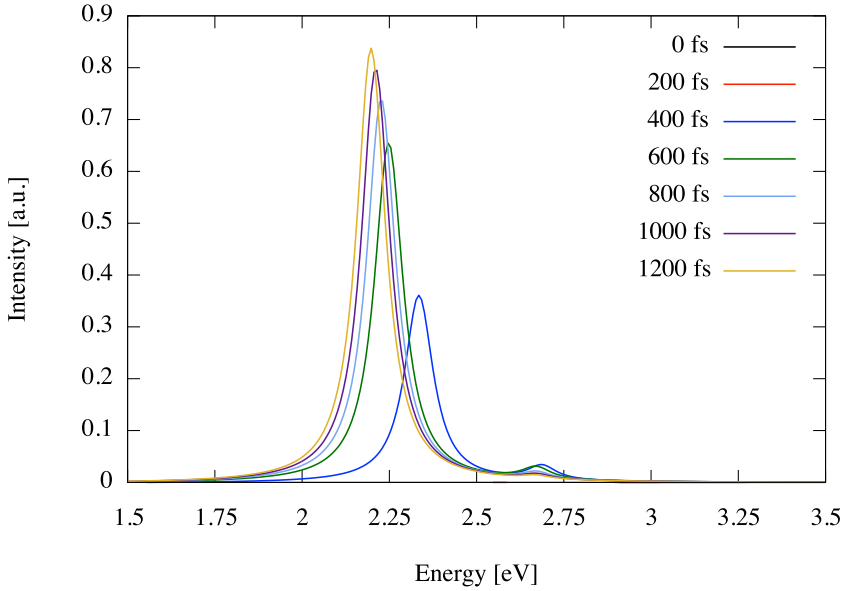

Figure 6.19: Non-interacting photoluminescence spectra for case D in Tab. 6.1. Results are plotted from 0 to 1200 fs in intervals of 200 fs. The 0 an 200 fs lines do not appear because there is no signal at those instants.

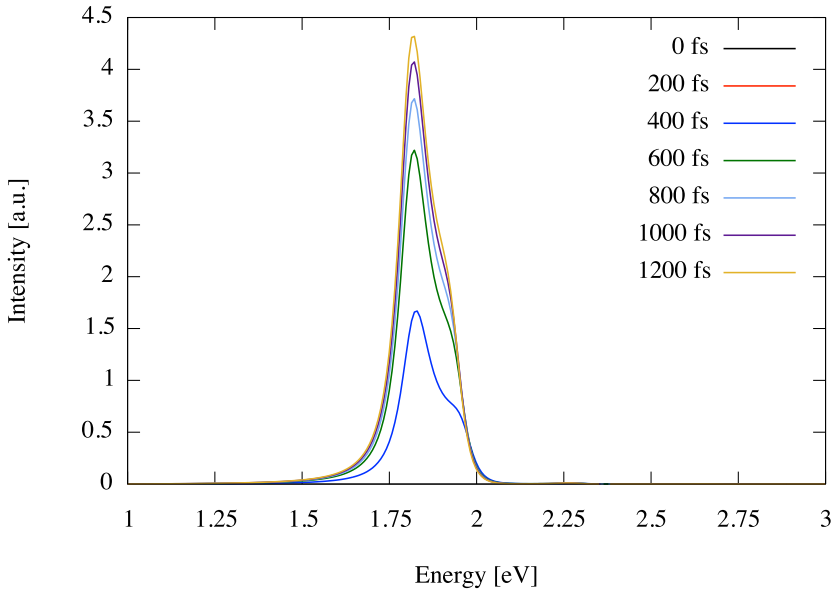

Figure 6.20: BSE photoluminescence spectra for case D in Tab. 6.1. Results are plotted from 0 to 1200 fs in intervals of 200 fs. The 0 an 200 fs lines do not appear because there is no signal at those instants.

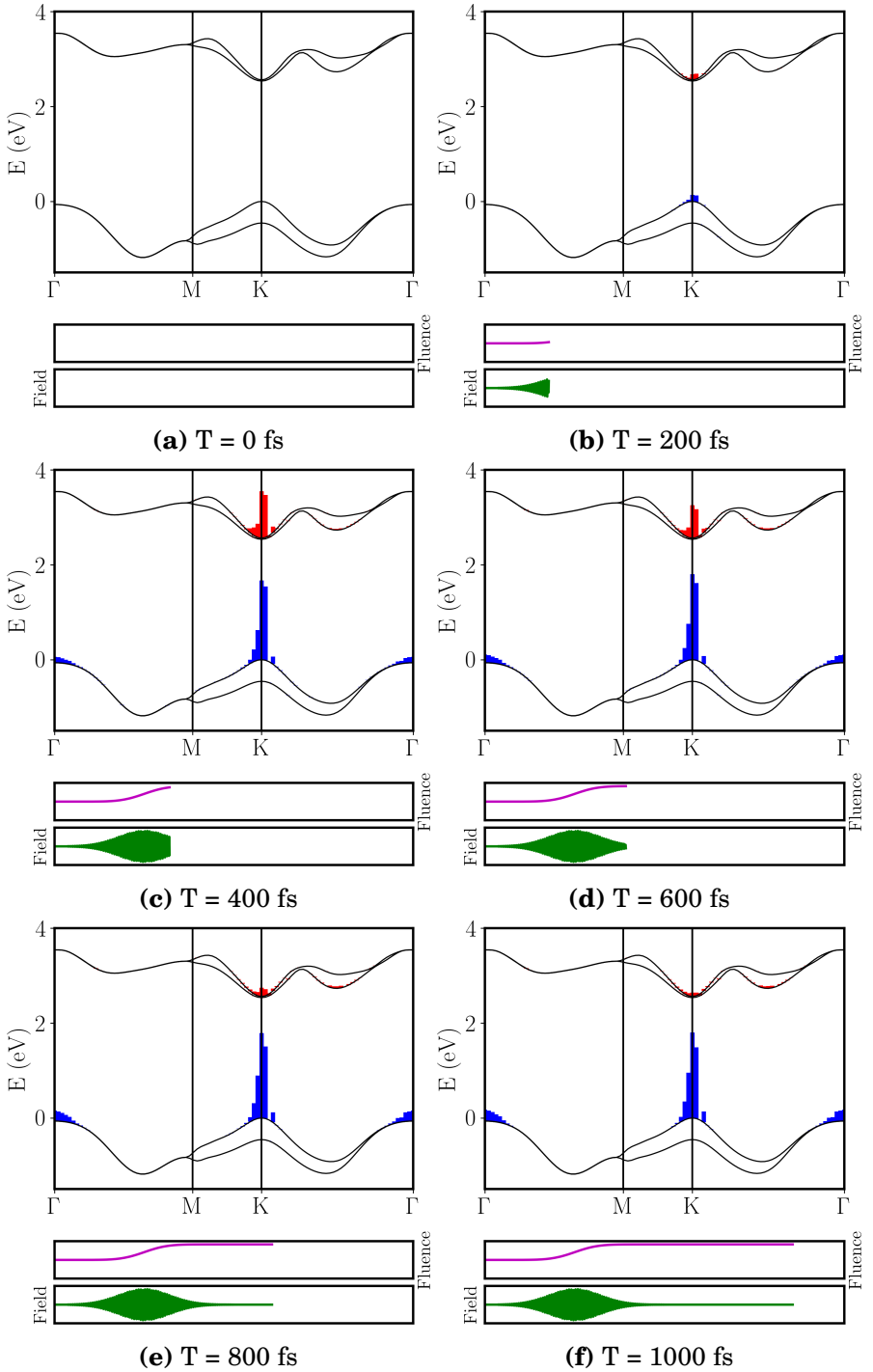

(a) T = 0 fs **(b)** T = 200 fs

(c) T = 400 fs **(d)** T = 600 fs

(e) T = 800 fs **(f)** T = 1000 fs

Figure 6.21: Evolution in time of the carrier occupations on the band structure for case E in Tab. 6.1. Blue columns represent holes, while electrons are represented by red columns. The green line represents the laser profile and the purple on the evolution in time of the fluence.

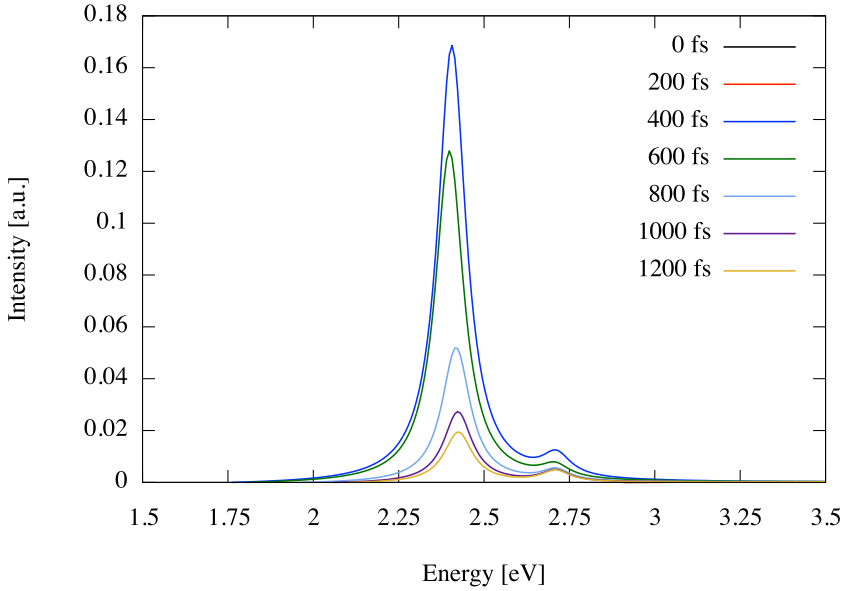

Figure 6.22: Non-interacting photoluminescence spectra for case E in Tab. 6.1. Results are plotted from 0 to 1200 fs in intervals of 200 fs. The 0 an 200 fs lines do not appear because there is no signal at those instants.

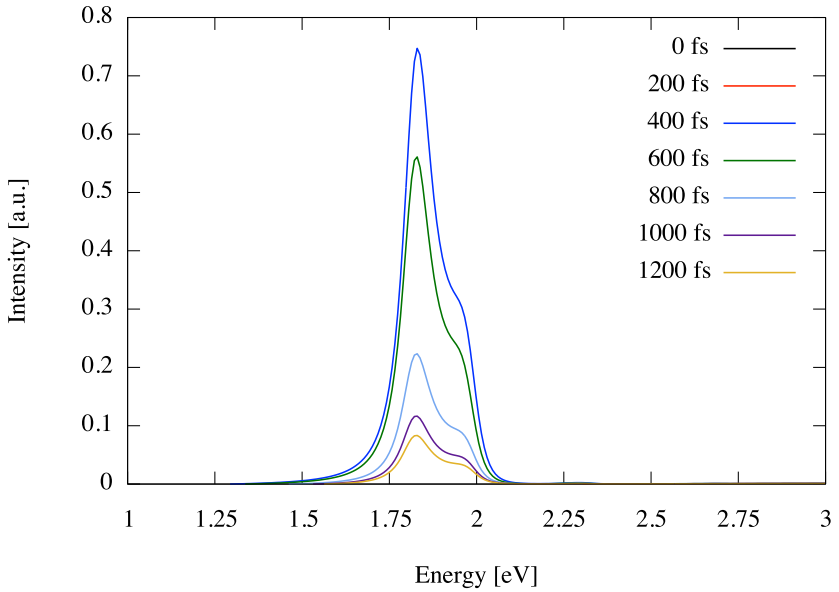

Figure 6.23: Non-interacting and BSE photoluminescence spectra for case E in Tab. 6.1. Results are plotted from 0 to 1200 fs in intervals of 200 fs. The 0 an 200 fs lines do not appear because there is no signal at those instants.

The results for case E in Figs. 6.22 and 6.23 are more striking. The increase in temperature leads not only to a comparative reduction of the signal's intensity at 400 fs, but also to a sharp decay in intensity of the main peak with time. As shown in Fig. 6.21, at 300.0 K the electrons in the conduction bands can absorb phonons and move to other valleys, thus decreasing the contributions to the exciton. This explain both the decrease in overall intensity and the decrease of the signal with time. Note that this happens in both the IP and BSE results. The emission energies for the IP and BSE results remain practically constant during the time-propagation at 2.42 eV and 1.83 eV, respectively.

Although less visible, in Figs 6.18e and 6.18f there is also a small reduction on the amount of electrons in the conduction states at K and a slight increase in the occupations of the states in the nearby conduction valley. The difference between the evolution in Fig. 6.18 and Fig. 6.21 are naturally due to the diferences in temperature, since in systems at low temperature the absorption of a phonon is much less likely than in systems at higher temperatures.

Table 6.3: Change energy of the highest peak (EHP) for the calculated IP and BSE spectra at 1200 fs for cases A to E of Tab. 6.1.

Test case	IP [eV]	BSE [eV]
A	2.10	1.82
B	2.30	1.83
C	2.43	1.84
D	2.20	1.82
E	2.42	1.83

Table 6.3 shows a comparison between the long-term peak positions coming from the IP and BSE results for cases A to E. The effects of increasing the temperature of the system appear to be similar to those of reducing the fluence of the laser. We can understand it by observing the evolution of the carriers in Fig. 6.21.

The difference between tests D and E is likely related to the dispersion of the electrons in the conduction states. At 300 K they are much more dispersed than at 100 K, while the holes stay at the edges near K and Γ. The interaction between

the holes and a much less denser cloud of excited electrons should be much weaker and should reduce the renormalisation of the gap.

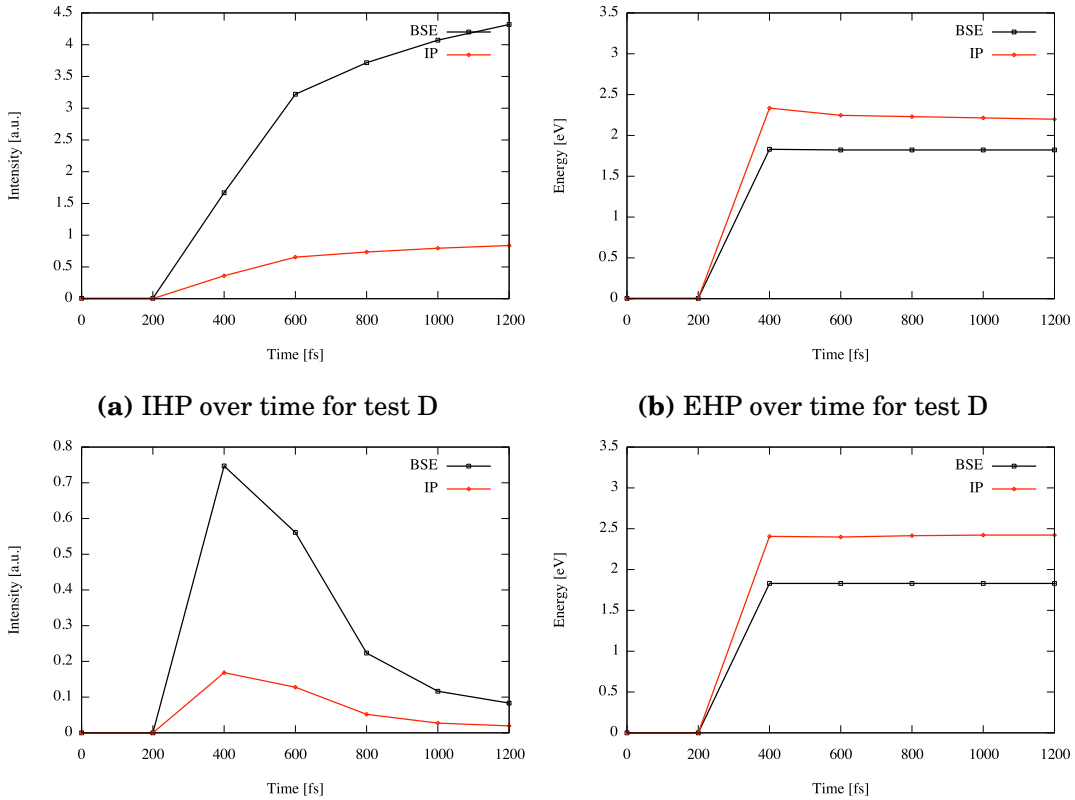

(a) IHP over time for test D

(b) EHP over time for test D

(c) IHP over time for test E

(d) EHP over time for test E

Figure 6.24: Evolution in time of the intensity of the maximum peak (IHP) and energy of the maximum peak (EHP) for the tests D and E of Table 6.1 within the non-interacting approximation (IP) (solid red line) and BSE (solid black line).

6.2.1.3 Effect of the central frequency

In test case F the central frequency of the laser field is changed from 1.826 eV to 2.2 eV, thus being closer to the energy of the B exciton of WS_2. The damping, fluence, and intensity of the laser field are the same as in case A. The change in the laser frequency causes an immediate alteration in the time-evolution of the carrier density, as shown in Fig. 6.25. Not only are the carriers much more dispersed at the beginning, but also their density is smaller.

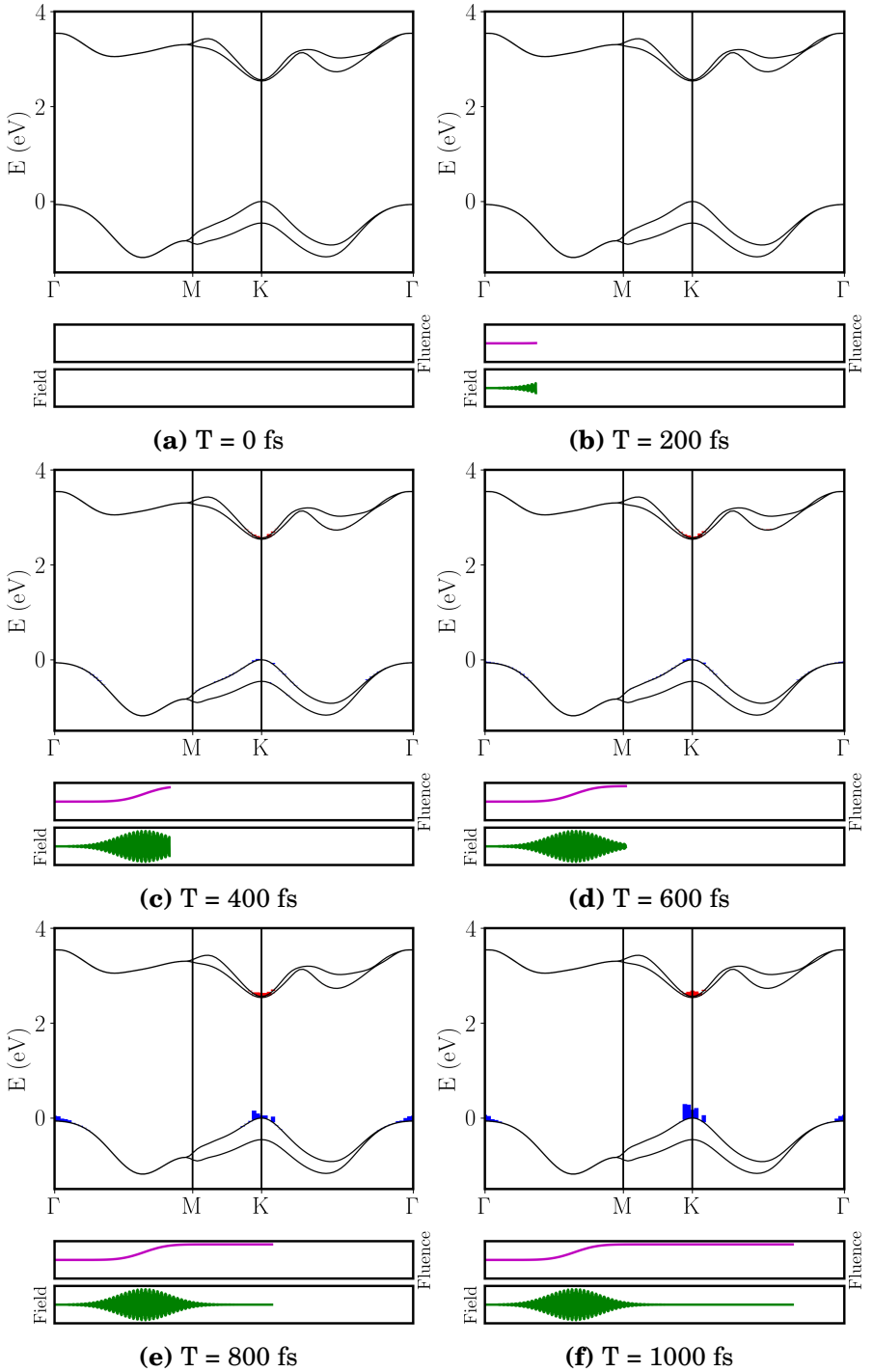

(a) T = 0 fs **(b)** T = 200 fs

(c) T = 400 fs **(d)** T = 600 fs

(e) T = 800 fs **(f)** T = 1000 fs

Figure 6.25: Evolution in time of the carrier occupations on the band structure for case F in Tab. 6.1. Blue columns represent holes, while electrons are represented by red columns. The green line represents the laser profile and the purple on the evolution in time of the fluence.

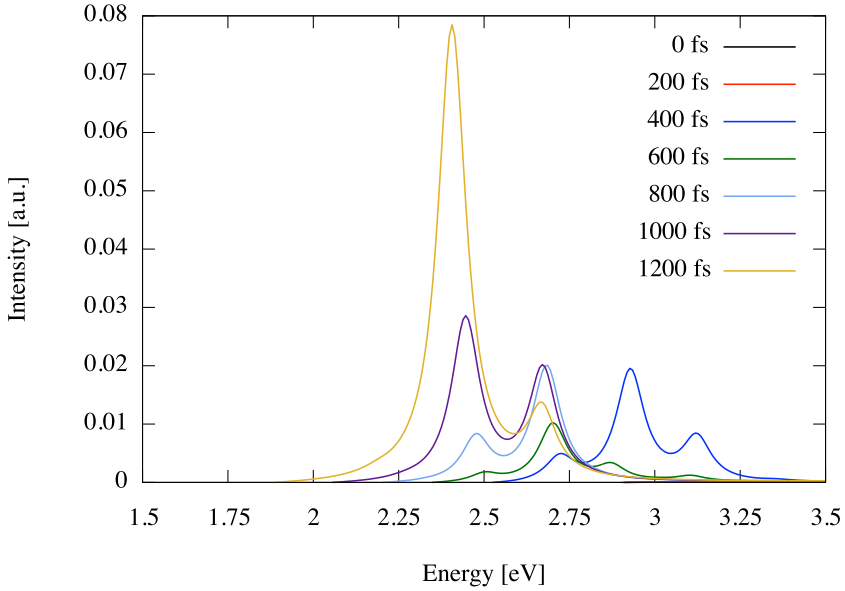

Figure 6.26: Non-interacting photoluminescence spectra for case F in Tab. 6.1. Results are plotted from 0 to 1200 fs in intervals of 200 fs. The 0 an 200 fs lines do not appear because there is no signal at those instants.

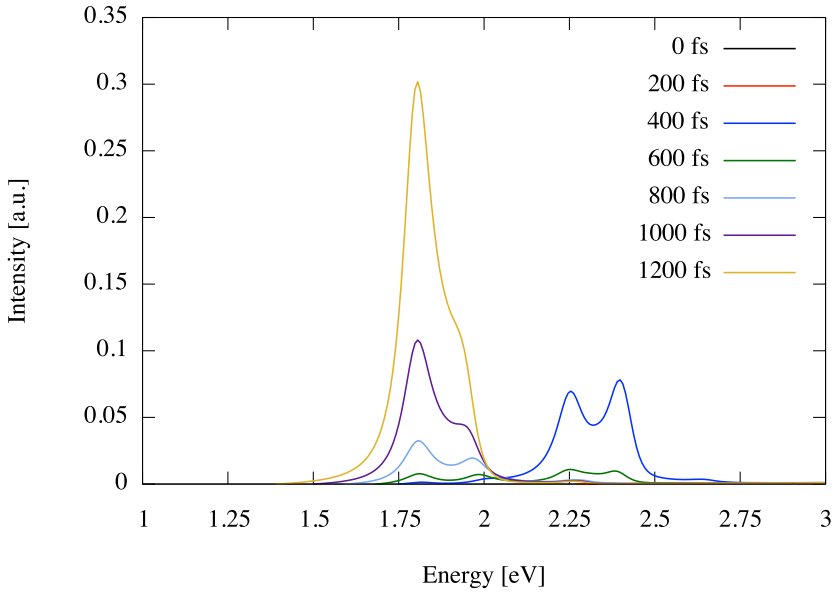

Figure 6.27: BSE photoluminescence spectra for case F in Tab. 6.1. Results are plotted from 0 to 1200 fs in intervals of 200 fs. The 0 an 200 fs lines do not appear because there is no signal at those instants.

In Fig. 6.25, where the system is excited at 2.2 eV, there is at first (between 200 fs and 400 fs) a population of excited carriers is created at much higher energies (around 2.9 eV for IP and 2.40 eV for the BSE). Over time the carriers move towards the band edges (Fig. 6.25d) and the signal changes dramatically. In particular, looking at the BSE, after 600 fs the peaks at 2.2 eV are almost negligible and small peaks appear close to the region of the A exciton. At later times those peaks grow in intensity and after 1200 fs only a peak at 1.81 eV is visible (but for the shoulder) for the BSE results, while for IP a peak at 2.41 eV surges. This is consistent with the carrier distribution in Fig 6.25.

An immediate result is that saturation of the signal happens at much later times than what we had observed for the cases in which the system was excited at 1.826 eV. Since electrons are excited at higher energies, it is expected that it would take longer for them to reach the edges of the bands.

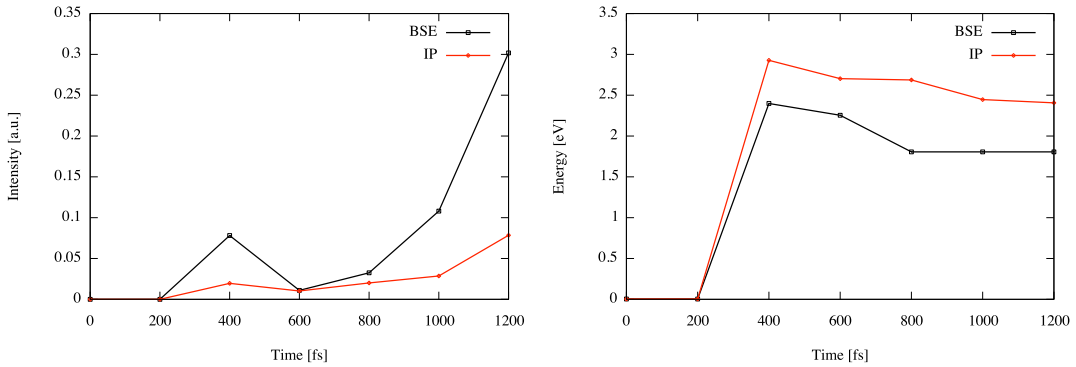

(a) IHP over time for test F

(b) EHP over time for test F

Figure 6.28: Evolution in time of the intensity of the maximum peak (IHP) and energy of the maximum peak (EHP) for the test F of Table 6.1 within the non-interacting approximation (IP) (solid red line) and BSE (solid black line).

In Fig. 6.28a the evolution in time of the IHP reflects the behaviour of the emission spectra shown in Figs. 6.26 and 6.27. The same happens with the changes over time in the EHP in Fig. 6.28b. Our interpretation is as follows: initially, the laser pulse creates a density of carriers at the B exciton of WS_2. Radiative transitions between the A and B excitons are forbidden, due to the spin selection rules. However, it is still possible for electrons to transfer energy to the lattice by e-p

interaction. Eventually the population of carriers responsible for the B exciton decays and moves down towards the band edges. It is then that the A exciton begins to be populated and the system starts to emit at this energy.

In Tab. 6.4 the positions of the peaks for the IP and BSE results for tests A and F are compared. The BSE results do not change significantly, while the IP value is closer in fact to that of case C in Tab. 6.2. The fluence is the same for cases A and F, so the difference should be we are exciting close to the B exciton.

If the transitions which populate the B exciton are much less probable than the transitions which populate the A exciton, the end result will be that fewer carriers will receive energy from the laser field, regardless of the value of the fluence. So the resulting signal and the effects from gap renormalisation and change in the screening should be weaker.

Table 6.4: Change energy of the highest peak (EHP) for the calculated IP and BSE spectra at 1200 fs for cases A, and F of Tab. 6.1.

Test case	IP [eV]	BSE [eV]
A	2.10	1.82
F	2.41	1.81

6.2.2 Comparison with experimental data

The comparison with experimental data is difficult because of the plethora of experimental results with slight different conditions and results. In literature experimental PL peaks ranging, for instance, from about 2.02589 eV [78] to 1.93725 eV [79]. Thus, the results which we have obtained are underestimated by 0.1 to 0.2 eV with respect to experiments. In any case the results which were presented here are not yet fully converged. Errors mays be originated, for instance, from the G_0W_0 at zero-field and have no connection with the description of PL.

One of the main experimental features which is observed in emission experiments is a Stokes-shift between the absorption and emission peaks [80][1]. However there is some debate regarding the occurence of these shifts in transition metal

[1]Blue-shifts in emission regarding absorption are called anti-Stokes shift, in which the electrons decay into a state with lower energy than the one from which they were before excitation.

dichalcogenides, namely WS_2[1], with reports of no Stokes shift observed [78, 79, 83] and of large Stokes shifts close to 0.1 eV [81]. The occurrence of these shifts has been linked to the doping of the sample and the presence of impurities and in fact has been seen to depend on the quality of the sample and the level of doping [78].

In our simulations we have found very small red-shifts in the PL peaks in comparison to the equilibrium absorption threshold, with a maximum shift of 0.03 eV. These small shifts can be understood by looking into the changes we are introducing in the system in each case (e.g. density of carriers, changes in temperature) and are smaller than what has been attributed to the presence of dopants or structural defects in the samples used in experiments.

In order to compare with experimental data, we decided to carry out another simulation with a laser field with the same damping and intensity as case A, but with central frequency of 2.54 eV, the same excitation energy of the pump used in Ref. [84]. The obtained spectrum is presented in Figs. 6.30 and 6.31, and in Fig 6.29 the evolution of the density of carriers is depicted. In Fig. 6.32a we present the evolution of the IHP and in Fig. 6.32b the changes in time of the EHP.

Before commenting on the results for the excitation at 2.54 eV we should point out that, at difference with the other spectra, here we had to choose a smaller damping for the Lorentzian curves used to computationally emulate the Dirac-delta functions[2]. This was needed since the emission signal was much weaker. In fact the signal from the negative frequencies was harder to extract without corrupting the output from YAMBO.

The evolution of the carriers in Fig. 6.29 shows that we have two effects acting simultaneously: the increase of the central frequency, which allows more electrons over wider regions of the Brillouin zone to be promoted to the conduction bands; and the occupation of states in other conduction valleys besides the one at K, due to the increase in temperature. Carriers then move towards the band edges, but a small population of electrons remains trapped in the valley between K and Γ. However, the number of electrons which remain in the band edge at K is larger than what was observed in case F, where the temperature was also at 300 K, so the gap renormalisation and change in the screening should be larger.

[1] Similar reports exist for MoS_2 as well [81, 82].

[2] Recall that a Dirac-delta function can be written as the following limit $\delta(x) = \lim_{\eta\to 0^+} \frac{1}{\pi}\frac{\eta}{x^2+\eta^2}$.

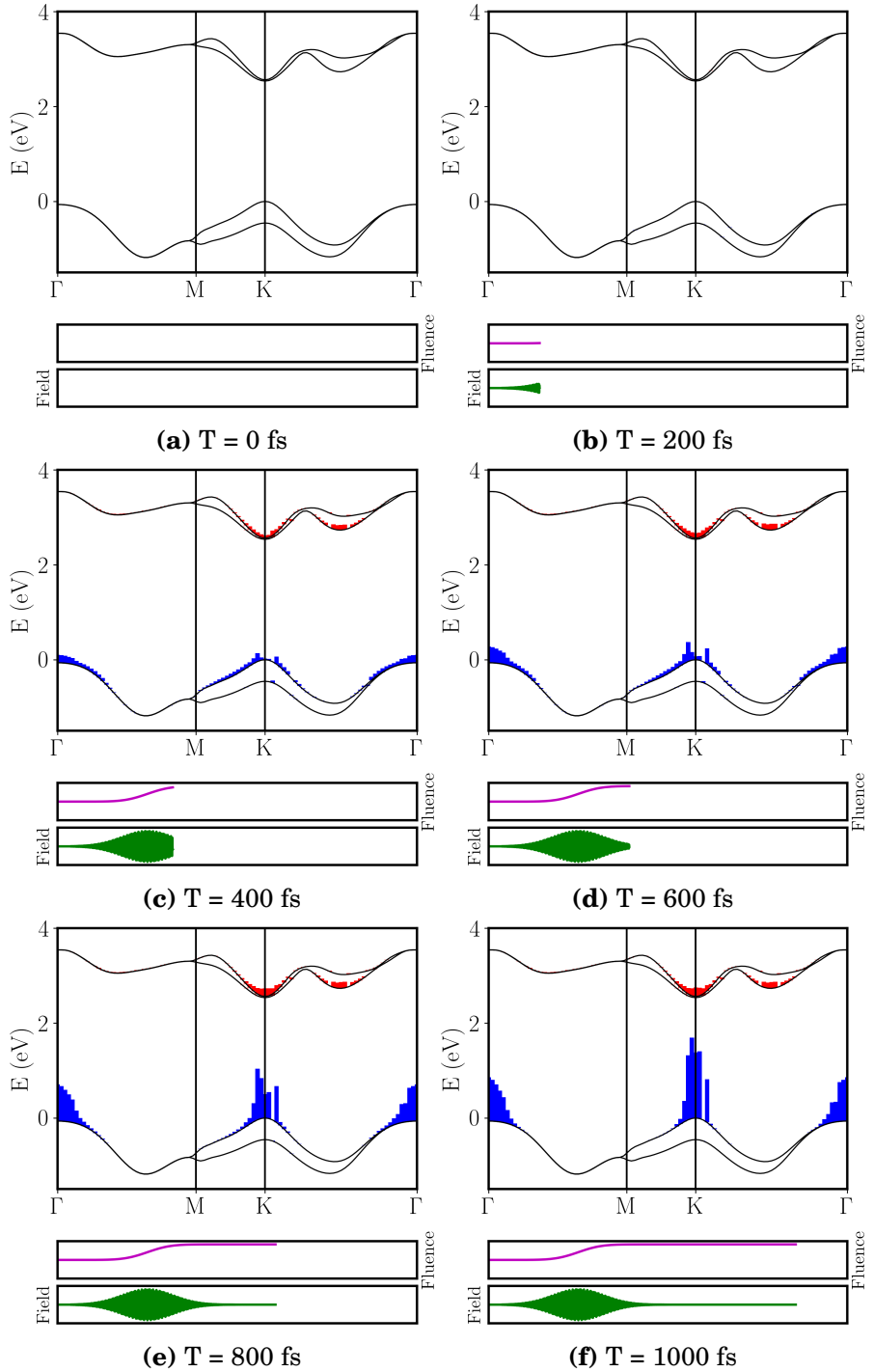

(a) T = 0 fs **(b)** T = 200 fs

(c) T = 400 fs **(d)** T = 600 fs

(e) T = 800 fs **(f)** T = 1000 fs

Figure 6.29: Evolution in time of the carrier occupations on the band structurefor the laser with intensity of 10^5 kW/m^2, 100 fs damping, and energy at 2.54 eV, at a temperature of 300.0K. Blue columns represent holes, while electrons are represented by red columns. The green line represents the laser profile and the purple on the evolution in time of the fluence.

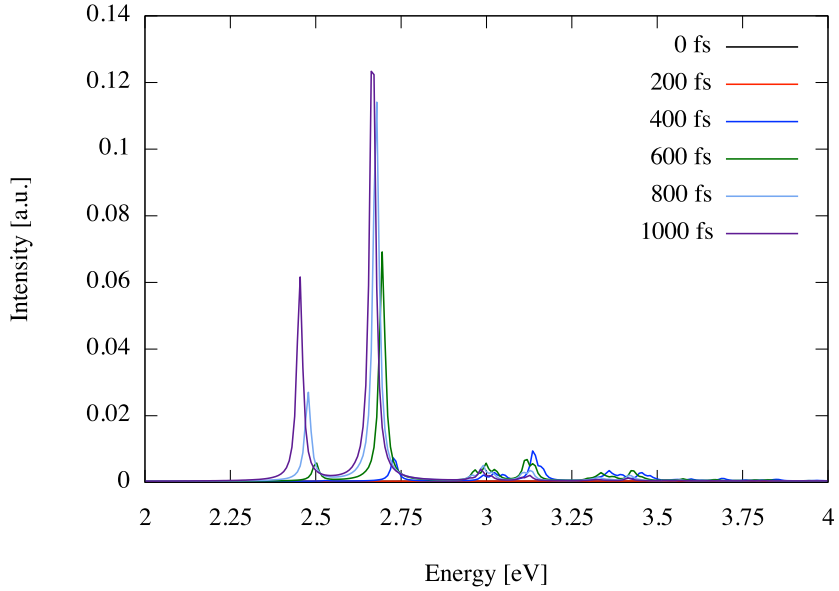

Figure 6.30: Non-interacting photoluminescence spectra for the laser with intensity of 10^5 kW/m^2, 100 fs damping, and energy at 2.54 eV, at a temperature of 300.0K. The results are plotted from 0 fs to 1000 fs in intervals of 200 fs.

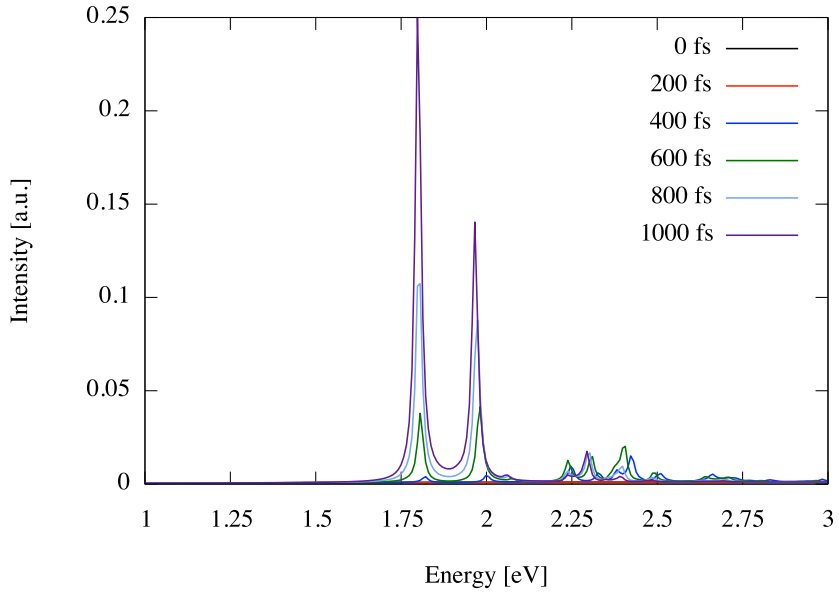

Figure 6.31: BSE photoluminescence spectra for the laser with intensity of 10^5 kW/m^2, 100 fs damping, and energy at 2.54 eV, at a temperature of 300.0K. The results are plotted from 0 fs to 1000 fs in intervals of 200 fs.

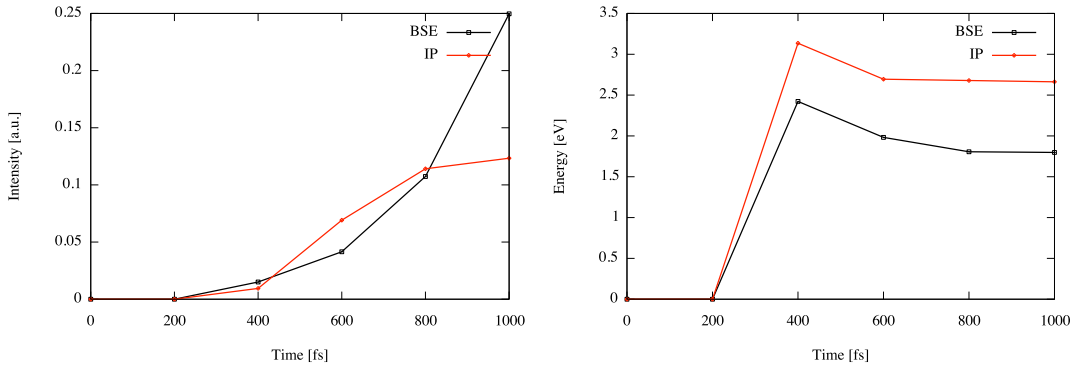

(a) IHP over time for test E

(b) EHP over time for test E

Figure 6.32: Evolution in time of the intensity of the maximum peak (IHP) and energy of the maximum peak (EHP) for the tests C and D of Table 6.1 within the non-interacting approximation (IP) (solid red line) and BSE (solid black line).

Coming to the result, the evolution in time of the spectra is similar to the one observed in Figs. 6.26 and 6.27. The laser creates at the beginning a small population of carriers (hence the weakness of the emission signal) which then decays into the minimum of the conduction band. For the BSE results there is still the existence of the shoulder peak above the A exciton energy, but far below the energy of the B exciton. In Fig. 6.32a the signal for the BSE results takes much longer to saturate than in case A, but behaves closely to case F, as a result from the fact that electrons have been moved higher in the band structure. The energy of the highest peak for the BSE results converges towards the 1.80 eV, while for the IP results it approaches the 2.66 eV. Although it appears that this is inconsistent with what was discussed before (a stronger gap renormalisation was expected), we should point out that up to 1000 fs the main peak in the IP is not the peak with the lowest energy. A longer time propagation would probably see a flip in the relative intensity of the peaks at 2.45 eV and 2.66 eV, and the energy of the strongest would then be close to the former. This would be consistent with what has been discussed so far in this work.

In Ref. [84] the energies experimentally obtained for the A and B excitons were 1.95 eV and 2.236 eV, respectively, while the direct band gap obtained was 2.05 eV. As such, we are not able to continue comparing our results with theirs.

6.2.3 Effects from the BSE kernel, screening, and energy levels' renormalisation

Here we analyse how the different contributions from the band gap renormalisation and the time-dependent occupations affect the emission spectrum. In Figs 6.33 and 6.34 we plotted how the spectrum at 1200 fs for case A changes if we update the BSE kernel (K), the residues (R), the electronic screening (S) which are affected by the time-dependent occupations and the electronic levels' energies (E)[1].

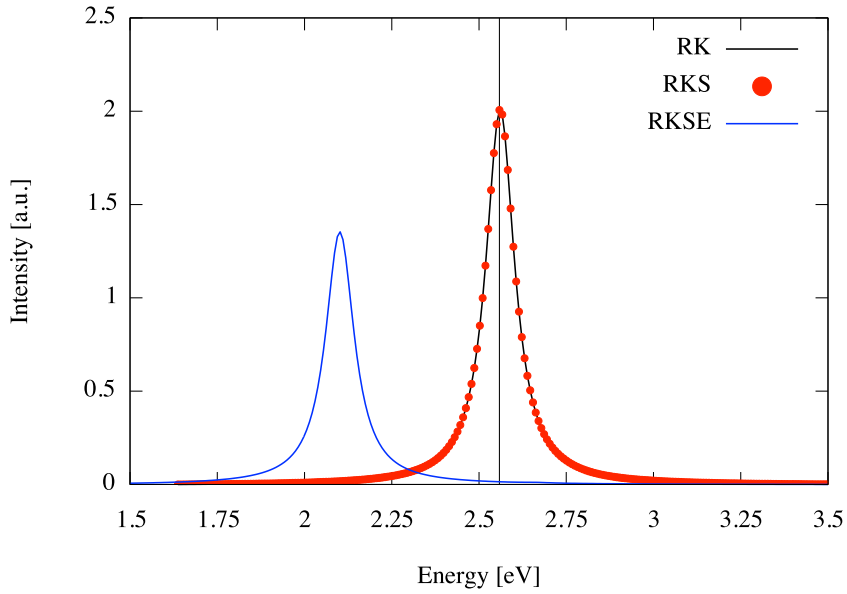

Figure 6.33: Non-interacting photoluminescence spectra for case A in Tab. 6.1. The plotted results are for the electronic configuration of the system at 1200 fs. The characters R, K, S, and E represent which quantities were updated for the calculation. R - residues; K - BSE kernel; S - screening; E - energies. The vertical black line marks the IP absorption thresholds.

As it can be seen for the IP case in Fig. 6.33, updating the kernel and the residues, but not the electronic screening (solid black line) does not change the resulting spectrum when compared with updating all the three quantities (red dots). This is in fact an expected result since in the IP approximation for $\mathcal{L}^<$ in Eq. (4.43)

[1]Note that, at this stage in YAMBO, R and K must always be updated together or the run will halt and output an error.

the positions of the peaks are given just by the energy levels for unscreened electrons. As such, only the update of the energy levels' renormalisation should affect the spectrum, which is what we see in the solid red line in Fig. 6.33.

For the BSE results in Fig. 6.34, when only the kernel and the residues were updated (solid black line) with the time-dependent occupations we obtain a significantly weaker emission peak with a blue-shift with respect to that of the equilibrium absorption threshold (marked by the vertical black line). Physically this means that the electron would decay into a state with lower energy than the one from which it was excited, or that it gained energy. Since we are exciting electrons close to the energy of the A exciton of WS_2 at the K point, we do not expect to see a significant blue-shift in the energy (or even, for that matter, a red shift).

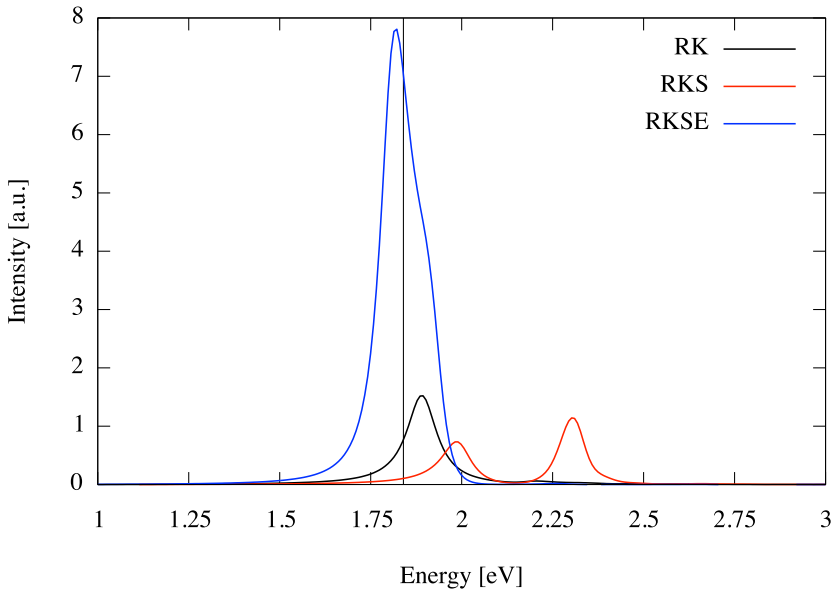

Figure 6.34: BSE photoluminescence spectra for case A in Tab. 6.1. The plotted results are for the electronic configuration of the system at 1200 fs. The characters R, K, S, and E represent which quantities were updated for the calculation. R - residues; K - BSE kernel; S - screening; E - energies. The vertical black line marks the BSE absorption threshold.

If the occupations in the screening are updated, but the energies used are those from equilibrium (solid red line) the results worsen. Not only the blue-shift is larger than in the previous case, but also we observe the presence of a second

peak at higher energies with higher intensity, which is a highly unphysical result. However, if all quantities are updated, all the blue shifts are cancelled and the highest emission peak is almost on top of the absorption one, only about 0.01 eV red-shifted. Again, we attribute the shoulder structure due to poor convergence with the k-point grid.

Next we compare in Fig. 6.35 the effects of updating different quantities for the case D (temperature at 100.0 K) and in Fig. 6.36 the results for case F (central frequency of 2.2 eV). Clearly in Fig. 6.35 the changes in the PL spectrum due to the update in the screening are weaker than what we observed in Fig. 6.34. However, the renormalisation of the electronic energy levels is also weaker and the two effects appear to cancel out, and we recover for the same EHP for the BSE result as in the case A. For the case E, where the pump energy was at 2.2 eV, the cancelation effects between the screening and the energies renormalisation is much weaker.

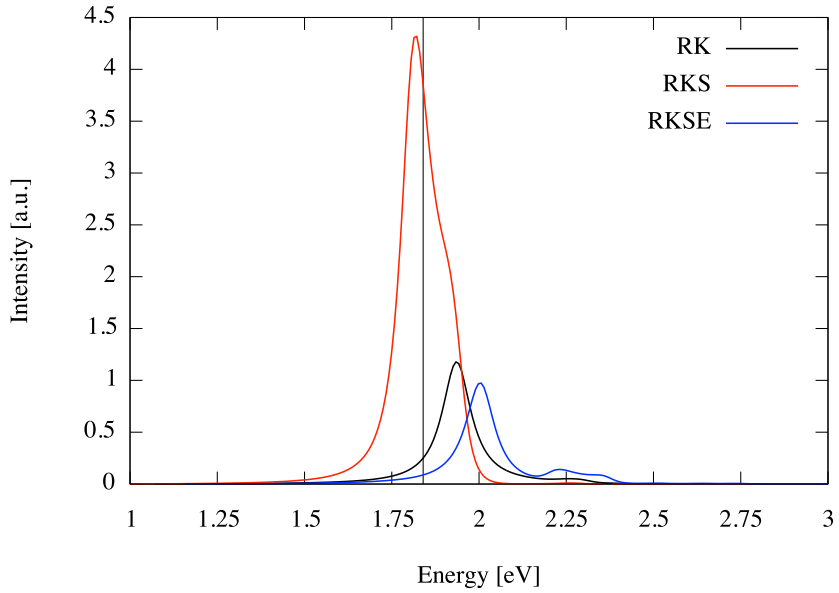

Figure 6.35: BSE photoluminescence spectra at 1200 fs for case D of Tab. 6.1. The solid black line represents the results when only the BSE kernel (K) and the residues (R) are updated, while in the solid blue line the screening (S) is also updated, and in the solid blue line the kernel, residues, screening, and energies are all updated. The vertical black line marks the BSE absorption threshold.

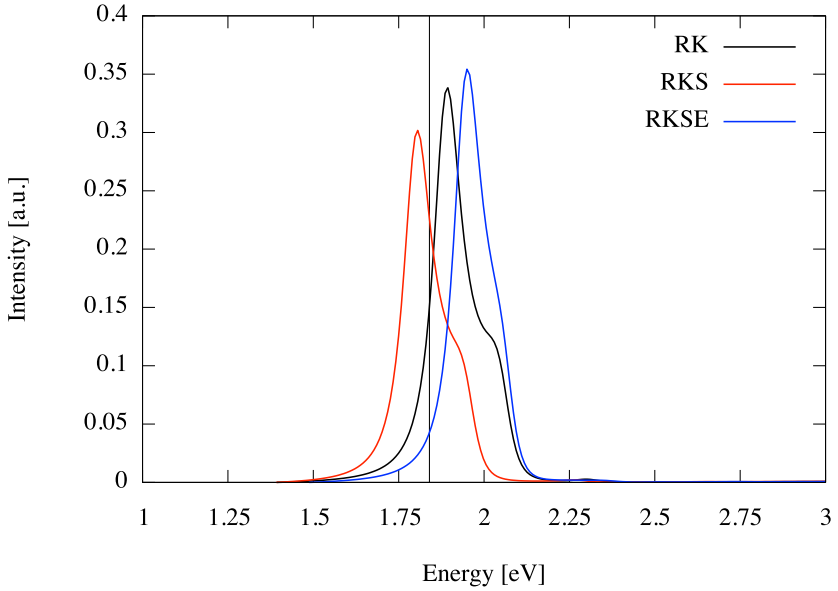

Figure 6.36: BSE photoluminescence spectra at 1200 fs for case F of Tab. 6.1. The solid black line represents the results when only the BSE kernel (K) and the residues (R) are updated, while in the solid blue line the screening (S) is also updated, and in the solid blue line the kernel, residues, screening, and energies are all updated. The vertical black line marks the BSE absorption threshold.

6.3 Conclusions

Following the analysis of the results, we believe that, at the current stage the code properly describes the dynamics of the system, when matched against our physical intuition.

Regarding the IP and BSE results, we conclude that an accurate description of the positions of the spectral peaks can be obtained only within the BSE. Nevertheless the IP results capture for most cases (in fact, all but the one in Fig. 6.32a) a behaviour emission energies for the IP and BSE results remain practically to the BSE data, but with different intensities for the peaks.

Finally we have shown the necessity of the computational scheme depicted in Fig. 5.1. Without the update of the residues, BSE kernel, screening, and energies the results would have been unphysical in some cases, or would exhibit small anti-Stokes shifts.

Chapter 7

Conclusions and further work

7.1 Main conclusions

We started this work with the intent of developing a coherent theoretical and computational framework which could be used to compute the photoluminescence spectrum of realistic systems and to simulate time-resolved photoluminescence experiments.

To reach that goal, we began in Chapter 2 by including in the Hamiltonian all the necessary interaction terms between electrons, phonons, and photons at a second quantisation level. By writing the propagators on the Keldysh contour and using the functional derivative technique, we were able to derive a set of equations which extends the one of Hedin's to the case in which all particles (not just the electrons) are quantised.

We then proceeded on obtaining the equation of motion for the electronic propagator in Chapter 3 by performing the analytic continuation from the complex plane into the real axis. We have shown that all the interactions between electrons and phonons, electrons and photons, and electrons and electrons can be written in a GW like form. This meant that we could derive a complete general form for the scattering elements which play an important role in the non-equilibrium dynamics controlled by the Baym-Kadanoff equation. We further simplified the functional dependence of the scattering terms by using the generalised Baym-Kadanoff ansatz and the Complete Collision approximation, thus making these terms functionals of the density matrix only and removing their dependence on the memory

of the interactions in the system.

By taking into consideration the typical experimental conditions in which TR-PL experiments are performed, we introduced the Low-intensity approximation. This approximation allowed us to recover a simple Boltzman-like equation, but in which the lifetimes for each form of interaction which concerns electrons are time-dependent. Following that, we have shown how to compute the transient absorption spectrum and proved that we can, in fact, recover the Baym-Kadanoff equation in frequency space.

The next step was to derive a connection between the two-particle correlation function and the emission spectrum. We did so in Chapter 4 by, at first, studying the Bethe-Salpeter equation for the electron-photon correlation function $\mathcal{L}^{\lessgtr}$. We have shown how to solve the BSE for this function with a static screening and studied its pole structure within the non-interacting and Tamm-Dancoff approximations, so as to determine which function has the information on the emission spectrum of a given material. Following this study, in Chapter 5 we derived a connection between the microscopic quantities in $\mathcal{L}^{\lessgtr}$ and the macroscopic observable, the divergence of the Poynting vector.

With the theoretical part settled, we then moved on the implementation in YAMBO and testing of the developed routines. We first tested the code in a hBN monolayer in Chapter 6, where a population of excited carriers was artificially created by pumping electrons from the top of the valence band to the bottom of the conduction band. We observed the inversion of population by computing the transient absorption spectrum and obtaining a negative absorption peak. When compared with the emission spectrum, we observed that the position of the PL peak corresponded to the negative peak in the transient absorption. This proved that YAMBO was outputting an emission spectrum in the correct region.

We then moved on with the testing of the code on a WS_2 monolayer with a series of different laser pumps and with the system at different temperatures during the time-propagation. Here we followed the prescription depicted in Fig. 5.1. We observed that YAMBO was reproducing expected behaviour of the PL with the pulse duration of the laser pump, namely that the intensity of the emission spectrum and that the renormalisation of the electronic energy levels would be smaller if the generated density of carriers were also to be diminished.

We have also analysed the change in the results with the increase in temperature and with a laser frequency larger than the energy of the A exciton. We observed that the increase in temperature would have the expected effect of bleaching the intensity of the PL signal, this effect being much stronger at room temperature than at 100.0 K. Regarding the increase in the excitation energy, we observed that this would reduce the density of excited carriers and the effects of the screening in the PL spectrum.

The diversity of existing experimental data on the PL spectrum of WS_2 makes it somewhat difficult to really compare our results with the ones in literature. Nevertheless the position of the emission peak from our simulation underestimates by 0.1 - 0.2 eV the experimental measures. Regarding the presence of a Stokes-shift between the equilibrium absorption and the PL emission, we observe a maximum change of about 0.03 eV, an order of magnitude smaller than that attributed to impurities and defects in the samples.

We therefore believe that we have achieved the proposed goals of this work. A complete theoretical framework which properly describes photoluminescence was obtained and the implemented computational routines give results which reasonably describe the expected changes in the spectrum due to the evolution in time of the carrier dynamics, and the changes due to temperature, central frequency, and fluence.

7.2 Future work

The next immediate step would be to complete the testing of the electron-photon lifetimes which were implemented in YAMBO and to perform time-dependent simulations with these decay channels activated. At the current stage, with only the electron-phonon decay channel we can only aim to describe the initial period of a TR-PL experiment. For longer time-scales, the electron-photon interaction becomes dominant over the electron-phonon and thus is key to simulate the carrier dynamics.

Another important step would be to converge our spectra with respect to the k-point mesh. With the present choice of k-grid the emission peak position is converged, but there are still artefacts due to artificial confinement of the excitonic

wavefunction. Performing longer time-dependent simulations and evaluating the PL spectrum at more instants can also provide better description of TR-PL experiments. Special attention should be given to the cases in which the system is excited above the energy of the A exciton. As we saw in Fig. 6.24c at the initial stages there should be a temporary decrease in the PL signal, as the emission of phonons destroys the B exciton and carriers move downwards in the band structure towards the A exciton. If such a result can be reproduced experimentally it would be a strong validation of our results.

We should also turn our attention to other transition metal dichalcogenides. Interesting results have been obtained for WSe_2, where the increase in temperature actually enhances the photoluminescence signal, instead of bleaching it [77]. This effect has been attributed to the valley dynamics which is characteristic of WSe_2 and it is a potentially interesting effect to reproduce.

Another step for a later stage would be to introduce the electron-phonon interaction in the BSE kernel. This would allow for phonon assisted photoluminescence and the detection of satellite peaks, besides the main emission peak.

Appendix A

The Many Body problem

A.1 The Many-body problem at equilibrium

Consider a system of N electrons and M nuclei in condensed matter or molecular physics. For all the practical purposes nuclei can be considered as point like charges and the electrostatic interaction between electrons and nuclei can be described using the usual Coulomb potential, in a full non-relativistic scheme. The full Hamiltonian of the system, in the real space representation, is [85] (in atomic units)[1]

$$\hat{H} = -\sum_{i=1}^{N} \frac{\nabla_i^2}{2} - \sum_{A=1}^{M} \frac{\nabla_A^2}{2m_A} - \sum_{i,A=1}^{N,M} \frac{Z_A}{|\mathbf{R}_A - \mathbf{r}_i|} + \frac{1}{2} \sum_{\substack{i,j=1 \\ i \neq j}}^{N} \frac{1}{|\mathbf{r}_i - \mathbf{r}_j|} + \frac{1}{2} \sum_{\substack{A,B=1 \\ A \neq B}}^{M} \frac{Z_A Z_B}{|\mathbf{R}_A - \mathbf{R}_B|}, \tag{A.1}$$

where m_A is the relative mass of the nucleus with respect to the electron, Z_A is the atomic number of the nucleus, $\mathbf{R}_A$ represents the nuclear space-coordinates and $\mathbf{r}_i$ represents the space coordinates of each electron.

The usual approach is to introduce the Born-Oppenheimer approximation [85] in order to solve the time-independent Schrödinger equation. One writes the wave function $\Psi(\mathbf{r}_i, \mathbf{R}_A)$ as

$$\Psi(\mathbf{r}_i, \mathbf{R}_A) = \psi(\mathbf{r}_i; \mathbf{R}_A)\chi(\mathbf{R}_A) \tag{A.2}$$

[1] Atomic units $\hbar = m_e = e = 4\pi\epsilon_0 = 1$ will be used almost in the entire thesis, except in some specific parts where the reader will be warned.

where $\psi(\mathbf{r}_i;\mathbf{R}_A)$ is a function of the set of coordinates $\mathbf{r}_i$ and depends parametrically on $\mathbf{R}_A$ and $\chi(\mathbf{R}_A)$ is an explicit function of $\mathbf{R}_A$.

As the nucleus' mass is greater than that of the electrons (a proton's mass is about 1830 times the mass of an electron) the time it takes for the electrons to readjust their position in response to the nuclear motion can be neglected. This means that we consider that the electrons move adiabatically with the nuclei. Also, due to their much larger mass, the nuclei wave function will be extremely more localized, almost like the classical description of point charges. So there must be a region in space where

$$|\nabla_A \chi(\mathbf{R}_A)| \gg |\nabla_A \psi(\mathbf{r}_i;\mathbf{R}_A)| \tag{A.3}$$

Therefore, when applying the operator of the nuclei kinetic energy to the wave function, we can ignore the variation of the electronic part in comparison with the nuclear one. This will lead to the following equation

$$\frac{\left[\hat{T}_e + \hat{V}_{ee}(\mathbf{r}_i) + \hat{V}_{eN}\left(\mathbf{r}_i,\mathbf{R}_A\right)\right]\psi(\mathbf{r}_i;\mathbf{R}_A)}{\psi(\mathbf{r}_i;\mathbf{R}_A)} + \frac{\left[\hat{T}_N + \hat{V}_{NN}(\mathbf{R}_A)\right]\chi(\mathbf{R}_A)}{\chi(\mathbf{R}_A)} = E \tag{A.4}$$

where we can identify the following operators as, respectively, the electron kinetic energy

$$\hat{T}_e = -\sum_{i=1}^{N} \frac{\nabla_i^2}{2}, \tag{A.5}$$

the electron-nuclei potential

$$\hat{V}_{eN}\left(\mathbf{r}_i,\mathbf{R}_A\right) = -\sum_{i,A=1}^{N,M} \frac{Z_A}{|\mathbf{R}_A - \mathbf{r}_i|}, \tag{A.6}$$

the electron-electron potential

$$\hat{V}_{ee}(\mathbf{r}_i) = \frac{1}{2}\sum_{\substack{i,j=1 \\ i\neq j}}^{N} \frac{1}{|\mathbf{r}_i - \mathbf{r}_j|}, \tag{A.7}$$

the nuclei-nuclei potential

$$\hat{V}_{NN}(\mathbf{R}_A) = \frac{1}{2}\sum_{\substack{A,B=1 \\ A\neq B}}^{M} \frac{Z_A Z_B}{|\mathbf{R}_A - \mathbf{R}_B|}, \tag{A.8}$$

and the nuclei kinetic energy

$$\hat{T}_N = -\sum_{A=1}^{M} \frac{\nabla_A^2}{2m_A}. \tag{A.9}$$

By defining a parametric function

$$\epsilon(\mathbf{R}_A) = E - \frac{\left[\hat{T}_N + \hat{V}_{NN}(\mathbf{R}_A)\right]\chi(\mathbf{R}_A)}{\chi(\mathbf{R}_A)} \tag{A.10}$$

equation (A.3) can be decoupled in one equation for the nuclei and one equation for the electrons, respectively

$$\left[\hat{T}_N + \hat{V}_{NN}(\mathbf{R}_A) + \epsilon(\mathbf{R}_A)\right]\chi(\mathbf{R}_A) = E\chi(\mathbf{R}_A) \tag{A.11a}$$

$$\left[\hat{T}_e + \hat{V}_{ee}(\mathbf{r}_i) + \hat{V}_{eN}(\mathbf{r}_i, \mathbf{R}_A)\right]\psi(\mathbf{r}_i; \mathbf{R}_A) = \epsilon(\mathbf{R}_A)\psi(\mathbf{r}_i; \mathbf{R}_A) \tag{A.11b}$$

Although a quantum mechanical treatment for the nuclei is possible under such approximation, they are most often considered as classical particles described by Newtonian Mechanics. So now, we only have to find solutions for the Eq. (A.11b), which can be re-written more simply by omitting the parametric dependence on $\mathbf{R}_A$

$$\hat{H}_e\psi_n(\mathbf{r}_i) = \left[\hat{T}_e + \hat{V}_{ee}(\mathbf{r}_i) + \hat{V}_{eN}(\mathbf{r}_i)\right]\psi_n(\mathbf{r}_i) = \epsilon_n\psi_n(\mathbf{r}_i) \tag{A.12}$$

Although it looks simple, Eq. (A.12) is only solvable, either numerically or arithmetically, for simple models or cases with few electrons. In order to circumvent this problem, physicists and quantum chemists developed approximation methods. Below I give a short introduction to the main points of two of the most used full *ab-initio* theories in solid state Physics: DFT and MBPT.

A.1.1 Density functional Theory

The purpose of Density Functional Theory is to replace the need of the full wavefunction of the system by the ground state density. This is possible thanks to the Hohenberg-Kohn (HK) theorems [86]. The first HK theorem states

First HK theorem. *In a finite system with N interacting electrons the external potential $v(\mathbf{r})$, and therefore the ground state energy E_0 are unique functionals of the ground state density $n_0(\mathbf{r})$.*

This proves that there is an one-to-one correspondence between the ground state energy and the external potential, so that we can express all quantities as a functional of the ground state density. The second theorem states that

Second HK theorem. *The ground state energy E_0 can be obtained variationally and to the exact ground state density n_0 corresponds to the exact ground state energy.*

As a consequence, if we are able to express the energy of the system as a functional of the density, we can obtain the ground state energy just by plugging in the ground state density. Now all that is needed is a method through which n_0 can be evaluated.

This need arises from the fact that, although the Hohenberg-Kohn theorems allow us to write a variational equation to solve the problem using the ground state density, this is a complicate task and to avoid this we actually uses the auxiliary Kohn-Sham (KS) system, where the interacting system is replaced by a non-interacting one where the particles obey N-independent Schrödinger equations

$$\left[-\frac{\nabla^2}{2} + v_s(\mathbf{r})\right]\phi_i(\mathbf{r}) = \epsilon_i\phi_i(\mathbf{r}), \tag{A.13}$$

and the electronic density is written as

$$n_s(\mathbf{r}) = \sum_{i=1}^{N} \theta_i |\phi_i(\mathbf{r})|^2, \tag{A.14}$$

with θ_i being the occupation function for the state with index i. A fundamental point of the KS auxiliary system is that the ground state density given by Eq. (A.14) is in fact equal to that of the real system, $n(\mathbf{r})$. The potential in the equation is the Kohn-Sham potential and is defined as

$$v_s[n](\mathbf{r}) = v[n](\mathbf{r}) + \int d^3r' \frac{n(\mathbf{r}')}{|\mathbf{r} - \mathbf{r}'|} + v_{xc}[n](\mathbf{r}), \tag{A.15}$$

with v_{xc} being the exchange-correlation potential. This quantity is defined by the expression

$$v_{xc}[n](\mathbf{r}) = \frac{\delta E_{xc}[n]}{\delta n(\mathbf{r})} \tag{A.16}$$

where the exchange-correlation functional E_{xc}, which is given by

$$E_{xc}[n] = T[n] - T_s[n] + W[n] - E_H[n], \tag{A.17}$$

is introduced. This functional is the central piece for the approximations to the many-body interactions in the theory. Basically, it expresses the difference between what is unknown (the kinetic and potential energy of the real system) and what can be known (the kinetic and potential energy of the auxilliary system). The kinetic energy of the KS-system is an explicit functional of the orbitals

$$T_s[n] = -\frac{1}{2}\sum_{i=1}^{N}\int d^3r \phi_i^\dagger[n](\mathbf{r})\nabla^2\phi_i[n](\mathbf{r}), \tag{A.18}$$

but due to the HK theorems, it will also be an implicit functional of the ground state density. $E_H[n]$ is the classical Coulomb energy or the Hartree energy

$$E_H[n] = \frac{1}{2}\iint d^3r d^3r' \frac{n(\mathbf{r})n(\mathbf{r}')}{|\mathbf{r}-\mathbf{r}'|}. \tag{A.19}$$

The exchange-correlation energy is subject to approximations since it contains the many-body interactions. One of the simplest approximations corresponds to the Local-density approximation (LDA), proposed in 1965 by Kohn and Sham. The idea is to approximate the xc energy of the inhomogeneous electron cloud to the exchange-correlation energy of the homogeneous electron liquid, e_{xc}^{HEG} [87]

$$E_x^{LDA}[n] = \int \mathrm{d}^3r\, e_{xc}^{HEG}(n)|_{n=n(\mathbf{r})}. \tag{A.20}$$

The exchange part has an explicit formula while the correlation part is usually obtained via parametrizations of Monte-Carlo simulations. Usual parametrizations are present in the PZ81 [88] and PW92 [89] functionals. Another order of functionals uses the density's gradient uses the generalised gradient approximation (GGA)[90], where

$$E_{xc}^{GGA}[n] = \int d^3r e_{xc}(n(\mathbf{r}), \nabla n(\mathbf{r})). \tag{A.21}$$

Expansions in this case are built by introducing terms which satisfy some known exact properties and, as there is no recipe for it, sometimes one uses a set of empirical parameters. Commonly used functionals are PW91 [91, 92] and PBE [93].

The next step on the ladder has the Meta-GGAs functionals, in which one includes more terms

$$E_{xc}^{MGGA}[n] = \int d^3r e_{xc}^{MGGA}(n, \nabla n, \nabla^2 n, \tau) \tag{A.22}$$

with $\tau = \frac{1}{2}\sum_{i=1}^{N} \theta_i |\nabla \phi_i(\mathbf{r})|^2$. However, as we have already stated, the fact that DFT is a ground state theory makes it unsuitable to describe excitonic effects. For that we need to use an excited state approach, such as MBPT, which is the choice of this thesis.

A.1.2 Green's function and Hedin's equations at equilibrium

A different approach to the Many-body problem involves the use of the single particle Green's function. It is based on the second quantisation method, with which we can write the electronic Hamiltonian in Eq. (A.12) as

$$\hat{H}_e = \int \mathrm{d}\mathbf{r} \hat{\psi}^\dagger(\mathbf{r}) h(\mathbf{r}) \hat{\psi}(\mathbf{r}) + \frac{1}{2}\int \mathrm{d}\mathbf{r}\mathrm{d}\mathbf{r}' \hat{\psi}^\dagger(\mathbf{r})\hat{\psi}^\dagger(\mathbf{r}') v(\mathbf{r},\mathbf{r}')\hat{\psi}(\mathbf{r}')\hat{\psi}(\mathbf{r}), \tag{A.23}$$

in which $h(\mathbf{r})$ contains the single-particle terms and $v(\mathbf{r},\mathbf{r}')$ the two-particle terms. Here we introduced also the electron creation operator $\hat{\psi}^\dagger(\mathbf{r})$ and the electron annihilation operator $\hat{\psi}(\mathbf{r})$. Fundamental to this theory is an auxiliary external potential $U(\mathbf{r}, t)$ which allows us to use a time-dependent external Hamiltonian $\hat{H}'(t)$

$$\hat{H}'(t) = \int \mathrm{d}\mathbf{r}\, \hat{\psi}^\dagger(\mathbf{r}) U(\mathbf{r}, t) \hat{\psi}(\mathbf{r}), \tag{A.24}$$

and which we can set to zero at the end. With a time-dependent perturbation we can use the interaction picture[1] with which we can describe the time-dependence of the field operators

$$\hat{\psi}_I(1) = \exp\left\{i\hat{H}_I(t_1)\right\} \hat{\psi}(\mathbf{r}_1) \exp\left\{-i\hat{H}_I(t_1)\right\}, \tag{A.25}$$

where we use the notation in which $i = \mathbf{r}_i, t_i$ and the subscript I means that the operator $\hat{H}'$ is written in the interaction picture. These elements allow us to define the single-particle Green's function, G(1,2)

$$G(1,2) = -i\frac{\langle N|\mathrm{T}\left[\hat{S}\hat{\psi}_I(1)\hat{\psi}_I^\dagger(2)\right]|N\rangle}{\langle N|\mathrm{T}[\hat{S}]|N\rangle}, \tag{A.26}$$

[1] See Appendix C for information on time-evolution pictures and the first and second quantisation.

where $|N\rangle$ is the N-electron unperturbed ground state and T is the time-ordering operator [54]. We also have the electron creation and annihilation operators, $\hat{\psi}_I^\dagger$ and $\hat{\psi}_I$, in the interaction picture and the time-evolution operator

$$\hat{S} = \exp\left\{-i\int_{-\infty}^{+\infty} \mathrm{d}t'\, \hat{H}_I'(t')\right\}. \tag{A.27}$$

All these definitions allow us to derive the equation of motion for G

$$\left[i\frac{\partial}{\partial t_1} - h(1) - U(1)\right] G(1,2) = \delta(1,2) + \int \mathrm{d}3\, \Sigma(1,3)G(3,2). \tag{A.28}$$

The self-energy Σ in the equation above is given by

$$\Sigma(1,2) = i\int \mathrm{d}3\mathrm{d}4\, G(1,4)W(1^+,3)\Gamma(4,2;3), \tag{A.29}$$

where $1^+ = (\mathbf{r}_1, t_1 + 0^+)$ and we have introduced the screened interaction W

$$W(1,2) = w_0(1,2) + \int \mathrm{d}(34)\, W(1,3)p_e(3,4)w_0(4,2), \tag{A.30}$$

the irreducible vertex

$$\gamma(1,2;3) = \delta(1,2)\delta(1,3) + \int \mathrm{d}(4567)\, \frac{\delta\Sigma(1,2)}{\delta G(4,5)} G(4,6)G(7,5)\gamma(6,7;3), \tag{A.31}$$

and the irreducible polarisability P which is expressed by

$$p_e(1,2) = -\mathrm{i}\int \mathrm{d}(34)\, G(1,3)G(4,1^+)\gamma(3,4;2). \tag{A.32}$$

If we rewrite Eq. (A.28) into

$$G(1,2) = G_0(1,2) + \int \mathrm{d}(34)\, G_0(1,3)\Sigma(3,4)G(4,2), \tag{A.33}$$

by taking $G_0(1,2) = [i\partial_{t_1} - h(1) - U(1)]^{-1}\,\delta(1,2)$ we arrive at the set of five integro-differential equations called Hedin's equations, which can be solved self-consistently and which can be schematically represented in Fig. A.1 A usual approximation to the Hedin's equations is to disregard the contributions from the second term in the irreducible vertex in Eq. (A.31), in what is known as the GW approximation. This reduces the number of equations to four and has been extensively studied [14].

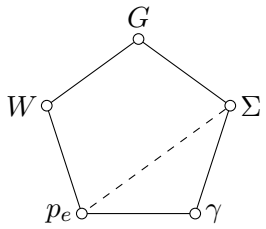

Figure A.1: Schematic representation of formulations of Hedin's equations. The dashed lines correspond to the GW approximation in which the contributions from the vertex are ignored.

A.2 The Many-body problem in out-of-equilibrium systems

One of the fundamental differences between the description of a system at equilibrium and another which is out-of-equilibrium is the assumption that, given enough time, the configuration of the system will go back to being that of the ground state. In fact, in most out-of-equilibrium cases it does not. The starting point for extending both DFT and MBPT to out-of-equilibrium systems is the same: we begin by dividing our Hamiltonian into two pieces

$$\hat{H} = \hat{H}_e + \hat{H}'(t) \tag{A.34}$$

where $\hat{H}_e$ is the electronic Hamiltonian in Eq. (A.12) and the new term, $\hat{H}'(t)$ is a time-dependent Hamiltonian, which is assumed to vanish at any instant $t < t_0$[1]. This term can represent any out-of-equilibrium driving perturbation, such as an electric field, a light excitation pulse, etc. This is the starting point to extend both DFT and MBPT to out-of-equilibrium systems.

A.2.1 Time-dependent Density functional theory

DFT can be extended to the time-dependent regime, where the Hamiltonian contains an explicitly time-dependent scalar potential $v(\mathbf{r}, t)$. The evolution of the

[1]At difference with the fictitious perturbation introduced in Eq. (A.24) this is not a fictitious term which we set to zero at the end, but the responsible for driving the system out-of-equilibrium.

system is now governed by the time-dependent Schödinger equation

$$\hat{H}\left|\Psi\right\rangle = i\frac{\partial}{\partial t}\left|\Psi\right\rangle, \tag{A.35}$$

which is used to propagate an initial state $|\Psi_0\rangle$ from an instant t_0 to t_1. It is usually convenient to consider that for $t < t_0$ the system was in the ground state under the effect of a static potential $v_0(\mathbf{r})$ and that at t_0 a time-dependent component is switched on. Analytically, this is expressed as

$$v(\mathbf{r},t) = v_0(\mathbf{r}) + \theta(t-t_0)v_1(\mathbf{r},t). \tag{A.36}$$

As in DFT, the key idea is to establish the density of the system (now time-dependent), $n(\mathbf{r},t)$, as the key ingredient from which all observables can be evaluated once they are written as a functional of the density. In 1984 [94], Runge and Gross proved that, under certain conditions, the mapping between the time-dependent potential and density could be inverted and stated what is known as the Runge-Gross theorem [94]

Runge-Gross theorem. *Two densities $n(\mathbf{r},t)$ and $n'(\mathbf{r},t)$, evolving from a common initial many-body state Ψ_0 under the influence of two different potentials $v(\mathbf{r},t)$ and $v'(\mathbf{r},t) \neq v(\mathbf{r},t) + c(t)$ (both assumed to be Taylor-expandable around t_0), will start to become different infinitesimally later than t_0. Therefore, there is a one-to-one correspondence between densities and potentials, for any fixed initial many-body state.*

Another important result is the van Leeuwen theorem [95] which is stated as follows

van Leeuwen theorem. *For a time-dependent density $n(\mathbf{r},t)$ associated with a many-body system with a given particle-particle interaction, external potential and initial state, there is a different many-body system with another particle-particle interaction and time-dependent external potential (up to a $c(t)$ function) which reproduces the same time-dependent density. The initial state of the system Ψ_0 must be chosen such that it correctly gives the same density and its time-derivative at the initial time t_0*

This theorem gives the theoretical justification for the use of the Kohn-Sham auxiliary system, in which the particle-particle interaction is null. Time-dependent

KS simulations usually start with a ground state calculation using Eq. (A.13) with the ground state density given by Eq. (A.14) and the ground state KS potential by Eq. (A.15). Right after the instant t_0, the time-dependent part of the potential begins to act. The KS eigenvectors follow the time-dependent KS equation

$$\left[-\frac{\nabla^2}{2} + v_s[n](\mathbf{r},t)\right]\varphi_i(\mathbf{r},t) = i\frac{\partial}{\partial t}\varphi_i(\mathbf{r},t), \tag{A.37}$$

given that $\varphi_i(\mathbf{r},t_0) = \phi_i(\mathbf{r})$. The time-dependent density is given by

$$n(\mathbf{r},t) = \sum_{i=1}^{N}\theta_i|\varphi_i(\mathbf{r},t)|^2 \tag{A.38}$$

and the effective KS potential in (A.37) is given by

$$v_s[n](\mathbf{r},t) = v(\mathbf{r},t) + \int d^3r\frac{n(\mathbf{r}',t)}{|\mathbf{r}-\mathbf{r}'|} + v_{xc}[n](\mathbf{r},t). \tag{A.39}$$

It is important to say that the exchange-correlation potential used for the ground state calculation and the time-dependent exchange-correlation potential used for the time propagation must match at the initial time in order to guarantee that the density remains static if no time-dependent potential is applied to the system at $t > t_0$ or to any sudden change at $t = t_0$.

It should also be stated that starting from the ground state is not actually necessary [96]. The equations will still hold if one starts from another energy configuration as long as the many-body wave function is still a Slater determinant. The only difference is that in this case the potential will be a functional of the initial state.

A.2.2 Time evolution picture and the Green function

One of the most important points in the construction of the MBPT in A.1.2 is the possibility of building the $\hat{S}$ operator in Eq. (A.27). This operator allows us to build an interaction picture with which we can propagate in time the electronic operators. However, it rests upon the assumption that at a sufficiently large time the system will go back to its ground state, which is not valid anymore. This is a critical point, since it is the fact that we can create such a time-evolution operator that, together with the time-ordering operator, allow us to derive Hedin's equations of Fig. A.1.

This problem can be solved, however, with the introduction of the Keldysh contour [97]. We will not show in this chapter how to use this concept and how to derive the equivalent equations to the ones in Hedin's set, since in the next chapter we use all of the necessary concepts to arrive at a full description of a non-equilibrium process which treats quantistically electrons. photons and the effects from the nuclei (phonons). For now, it suffices to say that such procedure[1] will lead to a set of equations which look almost the same as the Eq. (A.29) to Eq. (A.33), the only difference being that the time-arguments are now complex

$$\Sigma(\underline{1},\underline{2}) = i\int \mathrm{d}\underline{3}\mathrm{d}4\, G(\underline{1},\underline{4})W(\underline{1}^{+},\underline{3})\Gamma(\underline{4},\underline{2};\underline{3}), \tag{A.40}$$

$$W(\underline{1},\underline{2}) = w_0(\underline{1},\underline{2}) + \int \mathrm{d}(\underline{34})\, W(\underline{1},\underline{3})p_e(\underline{3},\underline{4})w_0(\underline{4},\underline{2}), \tag{A.41}$$

$$\gamma(\underline{1},\underline{2};\underline{3}) = \delta(\underline{1},\underline{2})\delta(\underline{1},\underline{3}) + \int \mathrm{d}(\underline{4567})\,\frac{\delta\Sigma(\underline{1},\underline{2})}{\delta G(\underline{4},\underline{5})}G(\underline{4},\underline{6})G(\underline{7},\underline{5})\gamma(\underline{6},\underline{7};\underline{3}), \tag{A.42}$$

$$p_e(\underline{1},\underline{2}) = -i\int \mathrm{d}(\underline{34})G(\underline{1},\underline{3})G(\underline{4},\underline{1}^{+})\gamma(\underline{3},\underline{4};\underline{2}), \tag{A.43}$$

$$G(\underline{1},\underline{2}) = G_0(\underline{1},\underline{2}) + \int \mathrm{d}(\underline{34})\, G_0(\underline{1},\underline{3})\Sigma(\underline{3},\underline{4})G(\underline{4},\underline{2}), \tag{A.44}$$

and so we use the notation in which $\underline{i} = \mathbf{r}_i, \tau_i$, with τ_i lying on the complex contour.

In order to transpose from the equations defined on the contour to the ones in which the time-arguments are real, which is called analytic continuation, we must employ the set of rules known as the Langreth theorem [11], which we summarise in Table A.1.

[1] Here I am referring only to the effects coming from the electron-electron interaction.

Table A.1: Langreth theorem and rules for analytic continuation [11].

Contour	Real axis
$C = \int_C AB$	$C^{\lessgtr} = \int_t [A^r B^{\lessgtr} + A^{\lessgtr} B^a]$ $C^{r/a} = \int_t A^{r/a} B^{r/a}$
$D = \int_C ABC$	$D^{\lessgtr} = \int_t [A^r B^r C^{\lessgtr} + A^r B^{\lessgtr} C^a + A^{\lessgtr} B^a C^a]$ $D^{r/a} = \int_t A^{r/a} B^{r/a} C^{r/a}$
$C(\tau, \tau') = A(\tau, \tau') B(\tau, \tau')$	$C^{\lessgtr}(t, t') = A^{\lessgtr}(t, t') B^{\lessgtr}(t, t')$ $C^{r/a}(t, t') = A^{<}(t, t') B^{r/a}(t, t') + A^{r/a}(t, t') B^{<}(t, t')$ $+A^{r/a}(t, t') B^{r/a}(t, t')$
$D(\tau, \tau') = A(\tau, \tau') B(\tau', \tau)$	$D^{\lessgtr}(t, t') = A^{\lessgtr}(t, t') B^{\gtrless}(t', t)$ $D^{r}(t, t') = A^{<}(t, t') B^{a/r}(t', t) + A^{r/a}(t, t') B^{<}(t', t)$

Appendix B

The merging with Density–Functional Theory

In order to merge the BKE in the general DFT scheme we follow the same strategy used in the standard MBPT approach [14]. This is based on the use of the Kohn–Sham (KS) Hamiltonian, $h_{\rm KS}$ as the reference single particle Hamiltonian. This means, in practice, that in Eq. (2.1a) the h operator is replaced by

$$h_{\rm KS}\phi_i(\mathbf{r}) = \left[-\frac{\nabla^2}{2} + v_{\rm ext}\left(\mathbf{r}\right) + v_{\rm H}\left[\rho\right]\left(\mathbf{r}\right) + v_{\rm xc}\left[\rho\right]\left(\mathbf{r}\right)\right]\phi_i(\mathbf{r}) = \epsilon_i^{\rm KS}\phi_i(\mathbf{r}), \tag{B.1}$$

with $v_{\rm H}$ and $v_{\rm xc}$ the Hartree and the exchange–correlation potentials which, in DFT, are functional of the electronic density $\rho\left(\mathbf{r}\right)$. Then, ϕ_i represents the basis of wave functions used in Eqs. (3.1) and (3.2).

DFT is a mean-field theory, where the electronic system is described by a group of pseudo non–interacting particles which move under the influence of the $v_{\rm xc}$ potential that already contains some of the e–e correlation effects. This initial correlation already present in the KS Hamiltonian has several important consequences in the electronic [27] and also in the phononic dynamics [30].

As far as the electronic dynamics is concerned, $v_{\rm xc}$ can lead to subtle double–counting problems that are safely removed by defining, in Eq. (2.34),

$$h_{\rm ext} = h_{\rm KS} - v_{\rm xc}. \tag{B.2}$$

Another important ingredient of the present approach are the phonon modes. These, within the DFT scheme, are obtained by considering the total Hamiltonian H as a functional of the atomic positions $\{\mathbf{R}\}$. The problem of finding the

phonon modes reduces to the self–consistent calculation of derivatives of H. Indeed, if DFT is a self–consistent theory, DFPT [24, 25] is its extension to take into account, self–consistently, the effect of static perturbations (like nuclear displacements). In this case, DFPT provides an exact description of phonons within the limits of a static and adiabatic approach.

Thus DFT and DFPT provide all ingredients of the present theory and allow a full *ab–initio* implementation. Indeed, as discussed in chapter 3, we have that for each element of the theory we can define a DFT/DFPT counterpart:

(a) As far as the single–particle electronic basis is concerned the KS wave–functions ϕ_i represent a natural definition. In this basis all standard MBPT machinery can be used to calculate the ingredients of standard Hedin's equations [14];

(b) In the e–p case phonons and e–p interaction matrix elements can be easily calculated within DFTP. Indeed, in this case, the ionic potential V_n appearing in Eq. (3.16) is

$$V_n(\mathbf{r}) \Rightarrow V_{\text{scf}}(\mathbf{R},\mathbf{r}) = v_{\text{H}}(\mathbf{r}) + v_{\text{xc}}(\mathbf{r}) - \sum_{\mathbf{R}} \frac{Z_{\mathbf{R}}}{|\mathbf{r}-\mathbf{R}|}, \tag{B.3}$$

and the phonon frequencies can be safely calculated within DFPT.

These simple connections demonstrate that, by simply implementing the NEGF framework in a KS basis, we can extend the predictive power of the many–body technique beyond the standard and well–known equilibrium limit.

Appendix C

Conventions for linear algebra operations

In the derivation of the equations of the Sec. 3.5 we introduced the following *ad–hoc* notation for the generic products of matrices

$$(M \circ V)_{pq} \equiv \underset{mn}{M_{pq}} V_{nm}, \tag{C.1}$$

$$(T \circ M \circ V) \equiv T_{pq} \underset{mn}{M_{qp}} V_{nm}, \tag{C.2}$$

$$(M \circ N)^{mn}_{rs} \equiv \underset{pq}{M^{mn}} \underset{rs}{N^{qp}}, \tag{C.3}$$

$$[N, V]^{mn}_{pq} = -[V, N]^{mn}_{pq} \equiv \underset{pq}{N_{mi}} V_{in} - V_{mi} \underset{pq}{N_{in}}. \tag{C.4}$$

$$[N, V]_{mn} = -[V, N]_{mn} \equiv N_{mi} V_{in} - V_{mi} N_{in}. \tag{C.5}$$

Appendix D

Inversion methods for the BSE matrix and the PL spectrum

Despite de relative simplicity of the final form of our equations, they must still be readied to be implemented in the subroutines of YAMBO. Here we follow Dr. Andrea Marini's notes on how this was done.

D.1 Symmetrisation of $\mathcal{L}^<$

We have, from Eq. (5.35) the connection between the power spectrum $I^\tau(\omega)$ and the electron-photon correlation function $\mathcal{L}^<$

$$I^\tau(\omega) = -16\pi^3 c \sum_{\alpha=1}^{3} \sum_{i,j} I_\alpha \Im \left[\Pi_{ij}^\alpha \mathcal{L}_{ij,\alpha}^{<,\tau}(\omega) \right], \tag{D.1}$$

and from Eq. (4.35) we now how to evaluate $\mathcal{L}^<$ by using

$$\boldsymbol{\mathcal{L}}_K^{\lessgtr,\tau}(\omega) = \left[1 - L^{0r,\tau}(\omega)\Xi\right]^{-1}_{KK'} L^{0\lessgtr}_{K'}(\omega) \left[1 - \Xi L^{0a,\tau}(\omega)\right]^{-1}_{K'K''} \boldsymbol{\Pi}_{K'',I}, \tag{D.2}$$

with

$$L_K^{0,r/a}(\omega) = \frac{\mathrm{i}R_K}{\omega - \Omega_K \pm \mathrm{i}\eta}. \tag{D.3}$$

However, in YAMBO we use a symmetric form for the correlation functions and the associated quantities which follows[1]

$$L_{KK'} = \sqrt{R_K}\tilde{L}_{KK'}\sqrt{R_{K'}}, \tag{D.4}$$

[1]From here on we are interested in algebraic transformations to the matrices and vectors involved in the computation of $\boldsymbol{\mathcal{L}}^<$, so we will ignore their dependence in ω so as to not overburden

which, as we can see, preserves the BSE equation for $\tilde{L}^{r/a}$

$$\begin{aligned}\sqrt{R_K}\tilde{L}_{KK'}\sqrt{R_{K'}} &= \sqrt{R_K}\tilde{L}^0_{KK'}\sqrt{R_{K'}}\delta_{KK'} \\ &\quad + \sqrt{R_K}\tilde{L}^0_K\sqrt{R_K}\Xi_{KK'}\sqrt{R_{K'}}\tilde{L}_{K'K''}\sqrt{R_{K''}} \\ &\quad \Rightarrow \tilde{L}_{KK'} = \tilde{L}^0_K + \tilde{L}^0_K\tilde{\Xi}_{KK'}\tilde{L}_{K'K''}. \quad \text{(D.5)}\end{aligned}$$

With these symmetric functions we must change the matrices which are to be inverted in Eq. (D.2) into

$$\left[1 - \tilde{L}^{0r}\tilde{\Xi}\right]_{KK'} = \tilde{L}^{0r}_K\left[\left(\tilde{L}^{0r}\right)^{-1}_K\delta_{KK'} - \tilde{\Xi}_{KK'}\right] = \tilde{L}^{0r}_K\tilde{M}^r_{KK'} \quad \text{(D.6a)}$$

$$\left[1 - \tilde{\Xi}\tilde{L}^{0a}\right]_{KK'} = \left[\left(\tilde{L}^{0a}\right)^{-1}_K\delta_{KK'} - \tilde{\Xi}_{KK'}\right]\tilde{L}^{0a}_{K'} = \tilde{M}^a_{KK'}\tilde{L}^{0a}_{K'}, \quad \text{(D.6b)}$$

which then symmetrises Eq. (D.2)

$$\begin{aligned}\boldsymbol{\mathcal{L}}^<_{K,I} &= (M^r)^{-1}_{KK_1}\left(L^{0r}_{K1}\right)^{-1}L^{0<}_{K_1}\left(L^{0a}_{K_1}\right)^{-1}\left(M^{0a}\right)^{-1}_{K_1K_2}\boldsymbol{\Pi}_{K_2,I} \\ &= \sqrt{R_K}\left(\tilde{M}^r\right)^{-1}_{KK_1}\left(\tilde{L}^{0r}_{K1}\right)^{-1}\frac{L^{0<}_{K_1}}{R_{K_1}}\left(\tilde{L}^{0a}_{K_1}\right)^{-1}\left(\tilde{M}^{0a}\right)^{-1}_{K_1K_2}\sqrt{R_{K_2}}\boldsymbol{\Pi}_{K_2,I} \quad \text{(D.7)}\end{aligned}$$

where

$$L^{0\lessgtr}_K(\omega) = \pm 2\mathrm{i}R^{\lessgtr}_K\Re\left[\tilde{L}^{0r}_K(\omega)\right] = \pm 2\mathrm{i}R^{\lessgtr}_K A_K(\omega) \quad \text{(D.8)}$$

and where we have defined the spectral function $A_K(\omega)$, which for a system of independent particles is given by $A_K(\omega) = \pi\delta(\omega - \Omega_K)$. In this form, the power spectrum is given by

$$I^\tau(\omega) = -32\pi^3 c\sum_{\alpha=1}^{3}\sum_K I_\alpha\Re\left[\Pi^\alpha_K\mathcal{L}^{<,\tau}_{K,\alpha}(\omega)\right]. \quad \text{(D.9)}$$

D.2 Diagonalisation of the BSE kernel

Diagonalisation algorithms are based on the fact that we can always write $\tilde{M}^{r/a}_{KK'}(\omega)$ using an excitonic basis, as described in Section 4.3.2. If the matrices are hermitian (which holds up to and including the TDA), we have that

$$\left[\tilde{M}^{r/a}(\omega)\right]^{-1}_{KK'} = \mathrm{i}\sum_\lambda\frac{\langle K|\lambda\rangle\langle\lambda|K\rangle}{\omega - E_\lambda \pm \mathrm{i}\eta}, \quad \text{(D.10)}$$

the notation. We will recover it when appropriate. Also, unless otherwise stated, we use Einstein's summation convention.

which brings Eq. (D.1) into

$$I(\omega) = -32\pi^3 c \sum_{\alpha=1}^{3} I_\alpha \sum_{K,K',K''} \sum_{\lambda_1,\lambda_2} \sqrt{R_K}\sqrt{R_{K'}} \times \frac{\eta}{\pi} \Re \left[\Pi^*_{K,\alpha} \frac{\langle K|\lambda_1\rangle \langle \lambda_1|K\rangle}{\omega - E_{\lambda_1} + \mathrm{i}\eta} \frac{R^<_{K'}}{R_{K'}} \frac{\langle K|\lambda_2\rangle \langle \lambda_2|K\rangle}{\omega - E_{\lambda_2} - \mathrm{i}\eta} \Pi_{K'',\alpha} \right], \quad \text{(D.11)}$$

with $\eta \to 0$. Here we assume that the dominant contributions are those for which $\lambda_1 = \lambda_2$ and that the remaining part, which we will call $\Delta I^\tau(\omega)$, is negligible. This transforms Eq. (D.11) into

$$\begin{aligned} I(\omega) = -32\pi^3 c \sum_{\alpha=1}^{3} I_\alpha \sum_{K,K',K''} \sum_{\lambda} \sqrt{R_K}\sqrt{R_{K'}} \\ \times \Re \left[\Pi^*_{K,\alpha} \langle K|\lambda\rangle \langle \lambda|K\rangle \frac{R^<_{K'}}{R_{K'}} \langle K|\lambda\rangle \langle \lambda|K\rangle \Pi_{K'',\alpha} \right] \delta(\omega - E_\lambda) + \Delta I(\omega) \\ = \sum_\lambda \Theta_\lambda \delta(\omega - E_\lambda) + \Delta I(\omega) \quad \text{(D.12)} \end{aligned}$$

which means that the spectrum peaks will lie on top of the exciton energies and that their strength is given by Θ_λ. On a short note, it is easy to see what would be the shape of the power spectrum for the non-interacting particle case just by doing $|\lambda\rangle \to |K\rangle$, which yields

$$\begin{aligned} I^\tau_{\mathrm{IP}}(\omega) = -32\pi^3 c \sum_{\alpha=1}^{3} I_\alpha \sum_K \sum_\lambda \Re \left[\Pi^*_{K,\alpha} R^<_K \Pi_{K,\alpha} \frac{\eta}{\pi} \frac{1}{(\omega - E_K)^2 + \eta^2} \right] \\ = -32\pi^3 c \sum_{\alpha=1}^{3} I_\alpha \sum_K |\Pi_{K,\alpha}|^2 R^<_K \delta(\omega - E_K) \quad \text{(D.13)} \end{aligned}$$

Besides neglecting the coupling in Ξ, and we recall that

$$\mathrm{i}\Xi = \begin{pmatrix} R & C \\ C^* & R^* \end{pmatrix}, \quad \text{(D.14)}$$

we can in YAMBO decide if we wish to keep the anti-resonant part as well. In YAMBO the anti-resonant part can be included in $L^{0r/a}$ by writing

$$L^{0r/a}_K(\omega) = \mathrm{i} f_K \left[\frac{1}{\omega - \Omega_K + \mathrm{i}\eta} - \frac{1}{\omega + \bar{\Omega}_K - \mathrm{i}\eta} \right], \quad \text{(D.15)}$$

thus meaning that the spectral function will be

$$A_K(\omega) = \delta(\omega - \Omega_K) + \delta(\omega + \Omega_K). \quad \text{(D.16)}$$

Here we point out that YAMBO will use the resonant Ω_K for the resonant and anti-resonant components. Finally, using this decomposition we get that

$$\Theta_\lambda|_{\text{res}} = \Theta_\lambda|_{\text{anti-res}}. \tag{D.17}$$

D.3 Inversion of the BSE kernel

The inversion method does not rely on an excitonic decomposition of the $M^{r/a}$ matrices, as it directly computes their inverse and uses them in

$$I^\tau(\omega) = -32\pi^3 c \sum_{\alpha=1}^{3} \sum_{K K_1 K_2} I_\alpha \Re\Big[\Pi^*_{K,\alpha} \left(M^r(\omega)\right)^{-1}_{K K_1} \left(L^{0r}_{K1}(\omega)\right)^{-1} R^<_{K_1} A_{K_1}(\omega) \times \left(L^{0a}_{K_1}(\omega)\right)^{-1} \left(M^a(\omega)\right)^{-1}_{K_1 K_2} \Pi_{K_2,\alpha}\Big] \tag{D.18}$$

to compute the power spectrum. However, we may run into potential numerical problems if we keep the following product

$$\left(L^{0r}_K(\omega)\right)^{-1} A_K(\omega) \left(L^{0a}_K(\omega)\right)^{-1} \tag{D.19}$$

in its unsimplified form. This can be avoided by redefining A_K and $L^{0r/a}_K$ as

$$A_K(\omega) = -\frac{1}{\pi}\Re\left[A^0_K(\omega)\right] = \frac{1}{\pi}\Im\left[\bar{A}^{0r}_K(\omega)\right] \tag{D.20a}$$

$$L^{0r/a}_K(\omega) = \mathrm{i}\bar{L}^{0r/a}_K(\omega) \tag{D.20b}$$

where $\bar{A}^{0r}_K$ and $\bar{L}^{0r/a}_K$ are the quantities which are actually evaluated by YAMBO. Equation (D.20b) also means that

$$L^{0a}_K(\omega) = -\left[L^{0r}_K(\omega)\right]^* \Rightarrow L^{0a}_K(\omega) = \mathrm{i}\left[\bar{L}^{0r}_K(\omega)\right]. \tag{D.21}$$

So, if we define the following product

$$l_K(\omega) = \left(L^{0r}_K(\omega)\right)^{-1} R^<_K A_K(\omega) \left(L^{0a}_K(\omega)\right)^{-1}, \tag{D.22}$$

we easily obtain that

$$l_K(\omega) = -\frac{R^<_K A_K(\omega)}{|\bar{L}^{0r}_K(\omega)|^2} = -\frac{\eta}{\pi}\frac{f_{c\mathbf{k}}(1-f_{v\mathbf{k}})}{(f_{c\mathbf{k}}-f_{v\mathbf{k}})^2}, \tag{D.23}$$

where we took $K = \{c, v, \mathbf{k}\}$. This brings Eq. (D.18) into a shortened form where we can easily apply a perturbative expansion for the inverses of each matrix, as we can see in the following

$$\begin{aligned} I^{\tau}(\omega) &= -32\pi^3 c \sum_{\alpha=1}^{3} \sum_{K,K_1,K_2} I_\alpha \Re\left[\langle \Pi_K^\alpha | \, M^{r,-1}_{KK_1}(\omega) l_{K_1}(\omega) M^{a,-1}_{K_1K_2}(\omega) \, |\Pi^\alpha_{K_2}\rangle\right] \\ &= -32\pi^3 c \sum_{\alpha=1}^{3} \sum_{K,K_1,K_2} I_\alpha \sum_{n,n'=0}^{\infty} \Re\left[\langle \Pi_K^\alpha | \, S^r_K \left[\Xi_{KK_1} S^r_{K_1}\right]^n l_{K_1}(\omega) \right. \\ &\qquad \left. \times \left[S^a_{K_2} \Xi_{K_1K_2}\right]^{n'} S^a_{K_2} \, |\Pi^\alpha_{K_2}\rangle\right], \end{aligned} \tag{D.24}$$

where $S^{r/a}_K$ are the residues for the zeroth order.

The number of operations can be further reduced if we recall that up to, and including, the TDA, Ξ is hermitian. Thus $\Xi^*_{KK'} = \Xi_{K'K}$ and we obtain M^a from M^r simply by doing

$$[M^a_{KK'}]^* = \mathrm{i}\left[\left(\bar{L}^{0a}_K\right)^{-1,*} \delta_{KK'} - \Xi^*_{KK'}\right] = \mathrm{i}\left[\left(\bar{L}^{0r}_K\right)^{-1} \delta_{KK'} - \Xi_{K'K}\right] = -\bar{M}^r_{K'K}, \tag{D.25}$$

where $\bar{M}^r$ is the YAMBO quantity given by

$$M^r_{KK'} = -\mathrm{i}\left(\bar{L}^{0r}_K\right)^{-1} \delta_{KK'} + \mathrm{i}\Xi_{KK'} = -\mathrm{i}\left[\left(\bar{L}^{0r}_K\right)^{-1} \delta_{KK'} - \Xi_{KK'}\right] = -\mathrm{i}\bar{M}^r_{KK'}. \tag{D.26}$$

Finally, the matrices for the anti-resonant part are simply given by

$$\begin{aligned} M^{r,\text{anti-res}}_{KK'}(\omega) &= \mathrm{i}\left[\left(\bar{L}^{0r,\text{anti-res}}_K\right)^{-1} \delta_{KK'} - \Xi^*_{KK'}\right] \\ &= \mathrm{i}\left[-\frac{f_{v\mathbf{k}} - f_{c\mathbf{k}}}{\omega + \Omega_K + \mathrm{i}\eta}\delta_{KK'} - \Xi^*_{KK'}\right] \\ &= \mathrm{i}\left[\frac{f_{v\mathbf{k}} - f_{c\mathbf{k}}}{-\omega - \Omega_K + \mathrm{i}\eta} - \Xi^*_{KK'}\right] = \mathrm{i}\left[\bar{M}^{r,\text{res}}(-\omega)\right]^\dagger_{K'K}. \end{aligned} \tag{D.27}$$

D. INVERSION METHODS FOR THE BSE MATRIX AND THE PL SPECTRUM

Appendix E

Parameters used in the calculations

E.1 DFT calculations

Table E.1: Atomic and pseudo-potential data for the ground-state of hBN.

Atom	Atomic mass	Functional type	Coordinates
B	10.811	PBE GGA (scalar-relativistic)	(0.0,0.0,0.5)
N	14.0067	PBE GGA (scalar-relativistic)	(1/3,2/3,0.5)

Table E.2: Cell and numerical parameters for the convergence of the ground-state of hBN.

Parameter	Value
k points	9 by 9
Cell type	Hexagonal
Cell's dimensions [bohr]	4.7
	2.5531
Wave function cutoff [Ry]	60
Convergence threshold	10^{-10}

E. PARAMETERS USED IN THE CALCULATIONS

Table E.3: Parameters for the expansion of the ground-state of hBN on a finer mesh.

Parameter	Value
k points	12 by 12
Number of bands	60
Convergence threshold	10^{-8}

Table E.4: Atomic and pseudo-potential data for the ground-state of WS_2.

Atom	Atomic mass	Functional type	Coordinates
W	183.84	Perdew-Zunger LDA (full relativistic)	(1/3,2/3,0.0)
S	32.065	Perdew-Zunger LDA (full relativistic)	(2/3,1/3,0.0742)
			(2/3,1/3,-0.0742)

Table E.5: Cell and numerical parameters for the convergence of the ground-state of WS_2.

Parameter	Value
k points	15 by 15
Cell type	Hexagonal
Cell's dimensions [bohr]	6.12192
	6.53389
Wave function cutoff [Ry]	110
Convergence threshold	10^{-10}

Table E.6: Parameters for the expansion of the ground-state of WS_2 on a finer mesh.

Parameter	Value
k points	24 by 24
Number of bands	150
Convergence threshold	10^{-8}

E.2 G_0W_0 quasi-particle corrections

Here and in Sections E.2, E.3, E.4, and E.5 the parameters are those defined and used in version 4.1.2 of YAMBO.

Table E.7: Numerical parameters for the G_0W_0 quasi-particle corrections on WS_2.

Parameter	Variable	Value
Random q-points in the BZ	RandQpts	1000000
Cutoff Geometry	CUTGeo	box z
Coulomb cutoff	CUTBox	38
Plane-waves	FFTGvecs	15 Ha
Response block size	NGsBlkXd	2500 mHa
GW bands range	GbndRnge	70
Polarisation function bands	BndsRnXd	70

E.3 COHSEX corrections

Table E.8: Common numerical parameters for the G_0W_0 quasi-particle corrections on WS_2 for both $t = 0$ and $t = T$.

Parameter	Variable	Value
Random q-points in the BZ	RandQpts	1000000
Coulomb interaction RS components	RandGvec	1
Cutoff Geometry	CUTGeo	box z
Coulomb cutoff	CUTBox	38 au
Plane-waves	FFTGvecs	10 Ha
Response block size	NGsBlkXs	1000 mHa
Screened interaction block size	EXXRLvcs	10 Ha
Polarisation function bands	BndsRnXs	70

E.4 BSE spectra

Table E.9: Numerical parameters for the BSE spectrum on hBN.

Parameter	Variable	Value
Plane-waves	FFTGvecs	10 Ha
BSE kernel mode	BSEmod	causal
BSE inversion	BSSmod	d
Exchange components	BSENGexx	10 Ha
Screened interaction block size	BSENGBlk	1 RL
BSE spectrum energy range	BEnRange	0 to 10 eV
BSE bands range	BSEBands	4 to 5
Polarization function bands	BndsRnXs	50
Response block size	NGsBlkXs	1 RL

Table E.10: Common numerical parameters for the BSE spectrum on WS_2 for both $t = 0$ and $t = T$.

Parameter	Variable	Value
Plane-waves	FFTGvecs	10 Ha
Exchange components	BSENGexx	10 Ha
Screened interaction block size	BSENGBlk	1000 mHa
Cutoff Geometry	CUTGeo	box z
Coulomb cutoff	CUTBox	38 au
Response block size	NGsBlkXs	1000 mHa
Polarisation function bands	BndsRnXs	60
BSE bands range	BSEBands	25 to 28
BSE kernel type	BSEmod	causal
BSE inversion solver	BSSmod	i
BSE inversion solver mode	BSSInvMode	f
BSE absorption threshold	BSEPSInvTrs	0.01
BSE PL threshold	BSPLInvTrs	0.01
BSE spectrum energy range	BEnRange	-4.0 to 4.0 eV

E.5 Real-time propagation

The set up of the field central frequency and damping is done with the variables Field1_Freq and Field1_Damp, respectively. The temperature of the phonon bath is set up via the BoseTemp variable.

Table E.11: Common numerical parameters for the real-time propagation on WS_2 for both $t = 0$ and $t = T$.

Parameter	Variable	Value
Plane-waves	FFTGvecs	10 Ha
Screened interaction block size	EXXRLvcs	1000 mHa
Exchange components	HARRLvcs	10 Ha
Correlation RL components	CORRLvcs	1000 mHa
BSE kernel bands	COLLBands	25 to 28
Response block size	NGsBlkXs	1000 mHa
Polarisation function bands	BndsRnXs	60
Random q-points in the BZ	RandQpts	1000000
Cutoff Geometry	CUTGeo	box z
Coulomb cutoff	CUTBox	38
E-p modes included	ElPhModes	1 to 9
Time step	RTstep	10 as
Simulation time	NETime	1.4 ps
Laser intensity	Field1_Int	10^5 kW cm^{-2}
Electric field direction	Field1_Dir	(0.0, 1.0, 0.0)
Laser polarisation	Field1_pol	linear
Laser profile	Field1_kind	QSSIN

E. PARAMETERS USED IN THE CALCULATIONS

List of Figures

List of Tables

List of Symbols, Acronyms, and Mathematical conventions

$p_{\mathrm{e}}(1,2)$	Reducible longitudinal polarisation.
$\boldsymbol{\mathcal{L}}(1,2;3)$	The pair-photon correlation function.
$\boldsymbol{\mathcal{L}}_0(1,2;3)$	The zeroth order pair-photon correlation function.
$\langle \hat{S}_\alpha(1) \rangle_{\mathrm{class}}$	Classical component of the Poyting vector, i.e., the pump laser field.
$\langle \hat{S}_\alpha(1) \rangle_{\mathrm{corr}}$	Microscopic component of the Poyting vector, .
$\underset{lk}{\chi_{ji}}(t,t')$	Matrix elements of the linear density-density reducible response function.
$\gamma(1,2,3)$	Reducible longitudinal vertex.
$\delta^{\perp}(1,2)$	Transverse Dirac-delta function.
$\varepsilon^{-1}_{\mathrm{RPA}}[\rho](\mathbf{r},\bar{\mathbf{r}})$	Inverse static dielectric function, computed within RPA.
Ω	Volume of the lattice.
$\omega_{\mathbf{q}}, \omega_{\mathbf{Q}}$	Energy of a photon of momentum $\mathbf{q}$ or $\mathbf{Q}$.
Ω_s	Volume of the unit cell.
$\theta(t-t')$	Heaviside step function.
$\hat{\phi}'(1)$	Scalar potential operator associated to the electronic charge density operator, $\hat{\rho}(1)$.

$\hat{\phi}(\mathbf{r})$	Scalar potential associated with the total charge density operator, $\hat{n}(\mathbf{r})$.
$\hat{\psi}(\mathbf{r})$, $\hat{\psi}^{\dagger}(\mathbf{r})$	Electron annihilation and creation field operators, respectively.
$\hat{\rho}(\mathbf{r})$	Electron density operator.
$\hat{d}$	Dipole operator
$\hat{d}_{\mathbf{q}\lambda}$, $\hat{d}^{\dagger}_{\mathbf{q}\lambda}$	Photon annihilation and creation operators, respectively.
$\hat{H}_{\text{ext}}(t)$	Time-dependent external Hamiltonian used in the functional derivative technique.
$\hat{n}(\mathbf{r}) = \hat{\rho}(\mathbf{r}) + \hat{N}(\mathbf{r})$	Total charge density operator.
$\hat{N}(\mathbf{R})$	Nuclear density operator.
$\hat{S}\left(t_{\alpha}, t_{\beta}\right)$	Contour defined time-evolution operator.
$\hat{u}(1)$	Electromagnetic energy density operator.
$\hat{V}_{n}(\mathbf{r})$	Potential associated to the nuclear density.
$\hat{\mathbf{A}}(\mathbf{r})$	Magnetic vector potential.
$\hat{\mathbf{B}}(1)$	The photon magnetic field operator.
$\hat{\mathbf{E}}(1)$	The photon electric field operator.
$\hat{\mathbf{J}}(\mathbf{r})$	Electron current-density operator.
$\hat{\mathbf{S}}(1)$	The Poyting vector operator.
$\hat{H}$	Full Hamiltonian of the system.
$\hat{h}(\mathbf{r}_i)$	Electron single-particle Hamiltonian.
$\hat{H}_0$	Non-interacting Hamiltonian.
$\hat{H}_{\text{e-e}}$	Electron-electron interaction Hamiltonian.

$\hat{H}_{\text{e-n}}$	Electron-nuclei interaction Hamiltonian.
$\hat{H}_{\text{n-n}}$	Nuclei-nuclei interaction Hamiltonian.
$\hat{H}_{\gamma}$	Free photon Hamiltonian.
$\hat{H}_{\text{e}-\gamma}$	Electron-photon interaction Hamiltonian.
$\hat{T}_{\text{e}}$	Electron kinetic energy operator.
$\hat{T}_{\text{n}}$	Nuclear kinetic energy operator.
$\mathbf{\Gamma}\left(1,2,3\right)$	Reducible transverse vertex.
$\mathbf{A}_{\text{ext}}(1)$, $\mathbf{J}_{\text{ext}}(1)$	External time-dependent magnetic vector potential and associated external time-dependent current density.
$\mathbf{J}_{\text{ind}}(1)$	Induced current-density.
$\mathfrak{G}^{\tau}\left(\omega\right)$	Absorption coefficient.
T_{C}	Contour time ordering operator.
$\overleftrightarrow{\mathcal{D}}\left(1,2\right)$	Photon propagator.
$\overleftrightarrow{\mathcal{D}}_{0}(1,2)$	Free photon propagator.
$\overleftrightarrow{P}\left(3,4\right)$	Reducible transverse polarisation.
$\partial_{\mathbf{q}\lambda}V_{\text{n}}\left(\mathbf{r}\right)=\mathbf{e}_{\mathbf{q}\lambda}\cdot\nabla V_{\text{n}}\left(\mathbf{r}\right)$	Derivative of the nuclear potential along the direction of the phonon mode with momentum $\mathbf{q}$ and branch λ.
$\phi_{\text{ext}}(1)$, $\rho_{\text{ext}}(1)$	External time-dependent potential and associated external time-dependent charge density
$\mathbf{R}$	Position of a nucleus.
$\Sigma(1,2)$	Full self-energy.
$\Sigma^{<}(1,2)$	Lesser self-energy.
$\Sigma^{>}(1,2)$	Greater self-energy.

$\Sigma^{\mathrm{a}}(1,2)$	Advanced self-energy.
$\Sigma^{\mathrm{r}}(1,2)$	Retarded self-energy.
$\Sigma_{\mathrm{H}}(1,2)$	Hartree component of the self-energy.
$\Sigma_{\mathrm{xc}}(1,2)$	Exchange-correlation component of the self-energy.
τ_{carr}	Time interval after which the laser induced oscillations in the occupations have disappeared.
τ_{pol}	Time interval after which the laser induced polarisation has decayed.
$\tilde{\chi}_{\substack{ji \\ lk}}(t,t')$	Matrix elements of the linear density-density irreducible response function.
$\tilde{\gamma}(1,2,3)$	Irreducible longitudinal vertex.
$\tilde{p}_{\mathrm{e}}(1,2)$	Irreducible longitudinal polarisation.
$\tilde{\mathbf{\Gamma}}(1,2,3)$	Irreducible transverse vertex.
$\overleftrightarrow{\tilde{P}}(3,4)$	Irreducible transverse polarisation.
$\Xi(1,2;3,4)$	The Bethe-Salpeter equation kernel.
$D(1,2)$	Nuclear density-density correlation function.
$d(T)$	Time-dependent expectation value of the dipole operator.
E_λ, A^K_λ	Excitonic eigenvalues and eigenvectors of the retarded excitonic Hamiltonian, $H^{r,\tau}_{KK'}$.
$G(1_\alpha, 2_\beta)$	Electron Green's function defined on the Keldysh contour.
$G^<(1,2)$	Electronic lesser Green's function.
$G^>(1,2)$	Electronic greater Green's function.

$G_{\mathrm{c}}(1,2)$	Electronic time-ordered Green's function.
$G_{\tilde{\mathrm{c}}}(1,2)$	Electronic anti-time-ordered Green's function.
$H^{\text{coupling}}_{(v,c,\mathbf{k}),(v',c',\mathbf{k})}$	Coupling part of the excitonic Hamiltonian.
$H^{\text{res}}_{(v,c,\mathbf{k}),(v',c',\mathbf{k})}$	Resonant part of the excitonic Hamiltonian.
$H^{r/a,\tau}_{KK'}$	Retarded/advanced excitonic Hamiltonian.
$I^{\tau}(\omega)$	Time-dependent photoluminescence spectrum.
$K = \{n_1 n_2 \mathbf{k}_1\}$	Electron-hole pair indices.
K^{dyn}	Dynamical kernel of the time-dependent Bethe-Salpeter equation.
k_{B}	Boltzman constant.
K_s	Static kernel of the time-dependent Bethe-Salpeter equation.
$L(1,2;3,4)$	The electron two-particle correlation function.
$L_0(1,2;3,4)$	The zeroth-order two-particle correlation function.
$M_{\mathbf{R}}$	Mass of a nucleus at $\mathbf{R}$.
$N_{\text{ext}}(\mathbf{R},t)$	Fictitious external density which affects only to the nuclei.
$N_I(\beta)$	Bose-Einstein distribution, with $\beta = 1/k_{\mathrm{B}}T_{\mathrm{lt}}$.
R^I_{ij}	Interaction coupling constants.
S^{dyn}	Dynamical part of the non-equilibrium integral.
$S\left[\{G\},\{\Sigma\}\right]$	Non-equilibrium collision integral.
S^{coh}	Coherent part of the non-equilibrium collision integral.
$S^{\text{dyn}}_{\mathrm{e}-\gamma}$	Electron-photon scattering channel component of the dynamical non-equilibrium collision integral.

S_{e-e}^{dyn}	Electron-electron scattering channel component of the dynamical non-equilibrium collision integral.
S_{e-p}^{dyn}	Electron-phonon scattering channel component of the dynamical non-equilibrium collision integral.
T_{lt}	Lattice temperature.
$U(1) = \phi_{\mathrm{ext}}(1) + \langle \hat{\phi}(1) \rangle_C$	The total longitudinal potential.
$v(\mathbf{r} - \mathbf{r}')$	Coulomb potential (spatial part only).
$W(1,2)$	Screened interaction.
$W_{\mathrm{e}}(1,2)$	Electronic component of the screening.
$W_{\mathrm{ph}}(1,2)$	Nuclear component of the screening.
$W_{\mathbf{G}\mathbf{G}'}(\mathbf{q})$	Matrix elements of the static screened interaction, $W(1,2)$.
$Z_{\mathbf{R}}$	Nuclear charge.
BKE	Baym-Kadanoff equations.
CCA	Completed collision approximation.
COHSEX	Coulomb Hole and Screened Exchange approximation for the self-energy.
DFPT	Density functional perturbation theory.
DFT	Density Functional Theory.
GBKA	Generalised Baym-Kadanoff ansatz.
GBKA	The Generalised Baym-Kadanoff ansatz.
LIA	The Low Intensity Approximation.
MBPT	Many-body perturbation theory
NEGF	Non-equilibrium Green's function.

NEQ	Non-equilibrium.
PL	Photoluminescence.
RPA	Random phase approximation.
SR-PL	Spatial-resolved photoluminescence.
TR-PL	Time-resolved photoluminescence.
TSR-PL	Time-spatial-resolved photoluminescence.

References

[1] Hiroki Uoyama, Kenichi Goushi, Katsuyuki Shizu, Hiroko Nomura, and Chihaya Adachi. **Highly efficient organic light-emitting diodes from delayed fluorescence.** *Nature*, **492**(7428):234–8, December 2012.

[2] Rudi Berera, Rienk van Grondelle, and John T. M. Kennis. **Ultrafast transient absorption spectroscopy: principles and application to photosynthetic systems**. *Photosynthesis Research*, **101**(2-3):105–118, sep 2009.

[3] Giuseppe Sansone, Thomas Pfeifer, Konstantinos Simeonidis, and Alexander I. Kuleff. **Electron Correlation in Real Time**. *ChemPhysChem*, **13**(3):661–680, feb 2012.

[4] J Herrmann, M Lucchini, S Chen, M Wu, A Ludwig, L Kasmi, K J Schafer, L Gallmann, M B Gaarde, and U Keller. **Multiphoton transitions for delay-zero calibration in attosecond spectroscopy**. *New Journal of Physics*, **17**(1):013007, jan 2015.

[5] Alexander I Kuleff and Lorenz S Cederbaum. **Ultrafast correlation-driven electron dynamics**. *Journal of Physics B: Atomic, Molecular and Optical Physics*, **47**(12):124002, jun 2014.

[6] S. M. Falke, C. A. Rozzi, D. Brida, M. Maiuri, M. Amato, E. Sommer, A. De Sio, A. Rubio, G. Cerullo, E. Molinari, and C. Lienau. **Coherent ultrafast charge transfer in an organic photovoltaic blend**. *Science*, **344**(6187):1001–1005, may 2014.

[7] FAUSTO ROSSI AND TILMANN KUHN. **Theory of ultrafast phenomena in photoexcited semiconductors**. *Reviews of Modern Physics*, **74**(3):895–950, aug 2002.

[8] FERENC KRAUSZ AND MISHA IVANOV. **Attosecond physics**. *Reviews of Modern Physics*, **81**(1):163–234, feb 2009.

[9] V M AXT AND S MUKAMEL. **Nonlinear optics of semiconductor and molecular nanostructures; a common perspective**. *Rev. Mod. Phys.*, **70**(1):145–174, jan 1998.

[10] L P KADANOFF AND G BAYM. *Quantum statistical mechanics*. W.A. benjamin, 1962.

[11] GEORGE PAL, YAROSLAV PAVLYUKH, WOLFGANG HÜBNER, AND HANS CHRISTIAN SCHNEIDER. **Optical absorption spectra of finite systems from a conserving Bethe-Salpeter equation approach**. *The European Physical Journal B*, **79**(3):327–334, oct 2011.

[12] G STEFANUCCI AND ROBERT VAN LEEUWEN. *Nonequilibrium Many-Body Theory of Quantum Systems*. Cambridge University Press, 2013.

[13] M BONITZ. *Quantum Kinetic Theory*. B.G.Teubner Stuttgart. Leipzig, 1998.

[14] GIOVANNI ONIDA, LUCIA REINING, AND ANGEL RUBIO. **Electronic excitations: density-functional versus many-body Green's-function approaches**. *Reviews of Modern Physics*, **74**(2):601–659, jun 2002.

[15] C. ATTACCALITE, M. GRÜNING, AND A MARINI. **Real-time approach to the optical properties of solids and nanostructures: Time-dependent Bethe-Salpeter equation**. *Phys. Rev. B*, **84**(24):245110, dec 2011.

[16] S. W. KOCH, M. KIRA, G. KHITROVA, AND H. M. GIBBS. **Semiconductor excitons in new light**. *Nature Materials*, **5**(7):523–531, jul 2006.

[17] HONGYAN SHI, RUSEN YAN, SIMONE BERTOLAZZI, JACOPO BRIVIO, BO GAO, ANDRAS KIS, DEBDEEP JENA, HUILI GRACE XING, AND LIBAI HUANG. **Exciton Dynamics in Suspended Monolayer and Few-Layer MoS 2 2D Crystals**. *ACS Nano*, **7**(2):1072–1080, feb 2013.

[18] GEORGE B NORRIS AND K K BAJAJ. **Exciton-plasma Mott transition in Si**. *Phys. Rev. B*, **26**(12):6706–6710, dec 1982.

[19] JACQUES LEFEBVRE AND PAUL FINNIE. **Excited Excitonic States in Single-Walled Carbon Nanotubes**. *Nano Letters*, **8**(7):1890–1895, 2008.

[20] T ICHIBAYASHI AND K TANIMURA. **Ultrafast Carrier Relaxation in Si Studied by Time-Resolved Two-Photon Photoemission Spectroscopy: Intravalley Scattering and Energy Relaxation of Hot Electrons**. *Physical Review Letters*, **102**(8):087403, feb 2009.

[21] DAVIDE SANGALLI AND ANDREA MARINI. **Ultra-fast carriers relaxation in bulk silicon following photo-excitation with a short and polarized laser pulse**. *EPL (Europhysics Letters)*, **110**(4):47004, may 2015.

[22] G.D. GILLILAND. **Photoluminescence spectroscopy of crystalline semiconductors**. *Materials Science and Engineering: R: Reports*, **18**(3-6):99–399, March 1997.

[23] R.M.DREIZLER AND E.K.U.GROSS. *Density Functional Theory*. Springer-Verlag, 1990.

[24] XAVIER GONZE. **Adiabatic density-functional perturbation theory**. *Physical Review A*, **52**(2):1096–1114, aug 1995.

[25] STEFANO BARONI, STEFANO DE GIRONCOLI, ANDREA DAL CORSO, AND PAOLO GIANNOZZI. **Phonons and related crystal properties from density-functional perturbation theory**. *Reviews of Modern Physics*, **73**(2):515–562, jul 2001.

[26] M. VAN SCHILFGAARDE, TAKAO KOTANI, AND S FALEEV. **Quasiparticle self-consistent GW theory.** *Physical review letters*, **96**(22):226402, jun 2006.

[27] F ARYASETIAWAN AND O GUNNARSSON. **The GW method**. *Reports Prog. Phys.*, **61**(3):237–312, mar 1998.

[28] P DANIELEWICZ. **Quantum theory of nonequilibrium processes, I**. *Annals of Physics*, **152**(2):239–304, feb 1984.

[29] ROBERT VAN LEEUWEN. **First-principles approach to the electron-phonon interaction**. *Physical Review B*, **69**(11):115110, mar 2004.

[30] ANDREA MARINI, S PONCÉ, AND X GONZE. **Many-body perturbation theory approach to the electron-phonon interaction with density-functional theory as a starting point**. *Physical Review B*, **91**(22):224310, jun 2015.

[31] S PONCÉ, G ANTONIUS, Y GILLET, P BOULANGER, J LAFLAMME JANSSEN, A MARINI, M CÔTÉ, AND X GONZE. **Temperature dependence of electronic eigenenergies in the adiabatic harmonic approximation**. *Phys. Rev. B*, **90**(21):214304, dec 2014.

[32] ELENA CANNUCCIA AND ANDREA MARINI. **Effect of the quantum zero-point atomic motion on the optical and electronic properties of diamond and trans-polyacetylene.** *Physical review letters*, **107**(25):255501, dec 2011.

[33] ANDREA MARINI. **Ab Initio Finite-Temperature Excitons**. *Physical Review Letters*, **101**(10):106405, sep 2008.

[34] G ANTONIUS, S PONCÉ, P BOULANGER, M CÔTÉ, AND X GONZE. **Many-Body Effects on the Zero-Point Renormalization of the Band Structure**. *Phys. Rev. Lett.*, **112**(21):215501, may 2014.

[35] FELICIANO GIUSTINO, STEVEN G LOUIE, AND MARVIN L COHEN. **Electron-Phonon Renormalization of the Direct Band Gap of Diamond**. *Physical Review Letters*, **105**(26):265501, dec 2010.

[36] MARIOS ZACHARIAS, CHRISTOPHER E PATRICK, AND FELICIANO GIUSTINO. **Stochastic Approach to Phonon-Assisted Optical Absorption**. *Physical Review Letters*, **115**(17):177401, oct 2015.

[37] PHILIP B ALLEN. **Theory of thermal relaxation of electrons in metals**. *Phys. Rev. Lett.*, **59**(13):1460–1463, sep 1987.

[38] S DAS SARMA, J K JAIN, AND R JALABERT. **Many-body theory of energy relaxation in an excited-electron gas via optical-phonon emission**. *Physical Review B*, **41**(6):3561–3571, feb 1990.

[39] MARCO BERNARDI, DEREK VIGIL-FOWLER, JOHANNES LISCHNER, JEFFREY B NEATON, AND STEVEN G LOUIE. **Ab Initio Study of Hot Carriers in the First Picosecond after Sunlight Absorption in Silicon**. *Phys. Rev. Lett.*, **112**(25):257402, jun 2014.

[40] ANDREA MARINI. **Competition between the electronic and phonon-mediated scattering channels in the outofequilibrium carrier dynamics of semiconductors: an ab-initio approach**. *Journal of Physics: Conference Series*, **427**:012003, mar 2013.

[41] E PERFETTO, D SANGALLI, A MARINI, AND G STEFANUCCI. **Non-equilibrium Bethe-Salpeter equation for transient photo-absorption spectroscopy**. *arXiv:1507.01786*, **92**(20):205304, jul 2015.

[42] K. HENNEBERGER AND H. HAUG. **Nonlinear optics and transport in laser-excited semiconductors**. *Physical Review B*, **38**(14):9759–9770, nov 1988.

[43] K HANNEWALD, S GLUTSCH, AND F BECHSTEDT. **Quantum-Kinetic Theory of Hot Luminescence from Pulse-Excited Semiconductors**. *Physical Review Letters*, **86**(11):2451–2454, mar 2001.

[44] M F PEREIRA AND K HENNEBERGER. **Microscopic theory for the influence of Coulomb correlations in the light-emission properties of semiconductor quantum wells**. *Physical Review B*, **58**(4):2064–2076, jul 1998.

[45] K. HANNEWALD, S. GLUTSCH, AND F. BECHSTEDT. **Quantum-kinetic study of femtosecond pump-and-probe spectra of bulk GaAs**. *Physical Review B*, **61**(16):10792–10802, apr 2000.

[46] K. HANNEWALD, S. GLUTSCH, AND F. BECHSTEDT. **Nonequilibrium photoluminescence excitation spectroscopy in GaAs: Bottleneck and memory effects**. *Physical Review B*, **67**(23):233202, jun 2003.

[47] G F Bertsch, J. I. Iwata, Angel Rubio, and K Yabana. **A real-space, rela-time method for the dielectric function**. *Phys. Rev. B*, **62**(12):7998–8002, may 2000.

[48] K Yabana, T Sugiyama, Y Shinohara, T Otobe, and G F Bertsch. **Time-dependent density functional theory for strong electromagnetic fields in crystalline solids**. *Phys. Rev. B*, **85**(4):45134, dec 2011.

[49] Carlo Andrea Rozzi, Sarah Maria Falke, Nicola Spallanzani, Angel Rubio, Elisa Molinari, Daniele Brida, Margherita Maiuri, Giulio Cerullo, Heiko Schramm, Jens Christoffers, and Christoph Lienau. **Quantum coherence controls the charge separation in a prototypical artificial light-harvesting system**. *Nature Communications*, **4**:1602, mar 2013.

[50] K Krieger, J K Dewhurst, P Elliott, S Sharma, and E K U Gross. **Laser-Induced Demagnetization at Ultrashort Time Scales: Predictions of TDDFT**. *Journal of Chemical Theory and Computation*, **11**(10):4870–4874, 2015.

[51] Michael Ruggenthaler, Johannes Flick, Camilla Pellegrini, Heiko Appel, Ilya V Tokatly, and Angel Rubio. **Quantum-electrodynamical density-functional theory: Bridging quantum optics and electronic-structure theory**. *Phys. Rev. A*, **90**(1):12508, jul 2014.

[52] Andrea Marini, Conor Hogan, Myrta Grüning, and Daniele Varsano. **yambo: An ab initio tool for excited state calculations**. *Computer Physics Communications*, **180**(8):1392 – 1403, 2009.

[53] Pedro Miguel M. C. de Melo and Andrea Marini. **Unified theory of quantized electrons, phonons, and photons out of equilibrium: A simplified ab initio approach based on the generalized Baym-Kadanoff ansatz**. *Phys. Rev. B*, **93**:155102, Apr 2016.

[54] Alexander L. Fetter, John Dirk Walecka, and Physics. *Quantum Theory of Many-Particle Systems (Dover Books on Physics)*. Dover Publications, 2003.

[55] G STRINATI. **Application of the Green's functions method to the study of the optical properties of semiconductors**. *La Rivista del Nuovo Cimento*, **11**(12):1–86, dec 1988.

[56] LARS HEDIN AND STIG LUNDQVIST. **Effects of Electron-Electron and Electron-Phonon Interactions on the One-Electron States of Solids**. In DAVID TURNBULL FREDERICK SEITZ AND HENRY EHRENREICH, editors, *Solid State Physics*, **23**, pages 1–181. Academic Press, 1970.

[57] GORDON BAYM. **Field-theoretic approach to the properties of the solid state**. *Annals of Physics*, **14**:1–42, 1961.

[58] P. LIPAVSKÝ, V. **SPIcKA**, AND B. VELICKÝ. **Generalized Kadanoff-Baym ansatz for deriving quantum transport equations**. *Physical Review B*, **34**(10):6933–6942, nov 1986.

[59] H. HAUG. **Interband Quantum Kinetics with LO-Phonon Scattering in a Laser-Pulse-Excited Semiconductor I. Theory**. *physica status solidi (b)*, **173**(1):139–148, sep 1992.

[60] HARTMUT HAUG AND CLAUDIA ELL. **Coulomb quantum kinetics in a dense electron gas**. *Physical Review B*, **46**(4):2126–2132, jul 1992.

[61] M BONITZ, D SEMKAT, AND H HAUG. **Non-Lorentzian spectral functions for Coulomb quantum kinetics**. *The European Physical Journal B*, **9**(2):309–314, may 1999.

[62] H. HAUG AND L. BÁNYAI. **Improved spectral functions for quantum kinetics**. *Solid State Communications*, **100**(5):303–306, nov 1996.

[63] H HAUG. **Interband Quantum Kinetics with LO-Phonon Scattering in a Laser-Pulse-Excited Semiconductor I. Theory**. *physica status solidi (b)*, **173**(1):139–148, sep 1992.

[64] S. LATINI, E. PERFETTO, A.-M. M. UIMONEN, R. VAN LEEUWEN, AND G. STEFANUCCI. **Charge dynamics in molecular junctions: Nonequilibrium Green's Function approach made fast**. *Physical Review B*, **89**(7):075306, nov 2013.

[65] Maurizia Palummo, Marco Bernardi, and Jeffrey C Grossman. **Exciton Radiative Lifetimes in Two-Dimensional Transition Metal Dichalcogenides**. *Nano Letters*, **15**(5):2794–2800, 2015.

[66] Andrea Marini and Rodolfo Del Sole. **Dynamical Excitonic Effects in Metals and Semiconductors**. *Physical Review Letters*, **91**(17):176402, oct 2003.

[67] F Bechstedt, K Tenelsen, B Adolph, and R Del Sole. **Compensation of Dynamical Quasiparticle and Vertex Corrections in Optical Spectra**. *Phys. Rev. Lett.*, **78**(8):1528–1531, feb 1997.

[68] Eva A. A. Pogna, Margherita Marsili, Domenico De Fazio, Stefano Dal Conte, Cristian Manzoni, Davide Sangalli, Duhee Yoon, Antonio Lombardo, Andrea C. Ferrari, Andrea Marini, Giulio Cerullo, and Deborah Prezzi. **Photo-Induced Bandgap Renormalization Governs the Ultrafast Response of Single-Layer MoS2**. *ACS Nano*, page acsnano.5b06488, dec 2015.

[69] Myrta Grüning, Andrea Marini, and Xavier Gonze. **Exciton-Plasmon States in Nanoscale Materials: Breakdown of the Tamm-Dancoff Approximation**. *Nano Letters*, **9**(8):2820–2824, 2009. PMID: 19637906.

[70] Valerio Olevano and Lucia Reining. **Excitonic Effects on the Silicon Plasmon Resonance**. *Phys. Rev. Lett.*, **86**:5962–5965, Jun 2001.

[71] Paolo Giannozzi, Stefano Baroni, Nicola Bonini, Matteo Calandra, Roberto Car, Carlo Cavazzoni, Davide Ceresoli, Guido L Chiarotti, Matteo Cococcioni, Ismaila Dabo, Andrea Dal Corso, Stefano de Gironcoli, Stefano Fabris, Guido Fratesi, Ralph Gebauer, Uwe Gerstmann, Christos Gougoussis, Anton Kokalj, Michele Lazzeri, Layla Martin-Samos, Nicola Marzari, Francesco Mauri, Riccardo Mazzarello, Stefano Paolini, Alfredo Pasquarello, Lorenzo Paulatto, Carlo Sbraccia, Sandro

SCANDOLO, GABRIELE SCLAUZERO, ARI P SEITSONEN, ALEXANDER SMOGUNOV, PAOLO UMARI, AND RENATA M WENTZCOVITCH. **QUANTUM ESPRESSO: a modular and open-source software project for quantum simulations of materials**. *Journal of Physics: Condensed Matter*, **21**(39):395502 (19pp), 2009.

[72] KUN BA, WEI JIANG, JINGXIN CHENG, JINGXIAN BAO, NINGNING XUAN, YANGYE SUN, BING LIU, AOZHEN XIE, SHIWEI WU, AND ZHENGZONG SUN. **Chemical and Bandgap Engineering in Monolayer Hexagonal Boron Nitride**. *Scientific Reports*, **7**:45584 EP –, 04 2017.

[73] JOHN R. SCHAIBLEY, HONGYI YU, GENEVIEVE CLARK, PASQUAL RIVERA, JASON S. ROSS, KYLE L. SEYLER, WANG YAO, AND XIAODONG XU. **Valleytronics in 2D materials**. *Nature Reviews Materials*, **1**:16055 EP –, 08 2016.

[74] MANISH CHHOWALLA, DEBDEEP JENA, AND HUA ZHANG. **Two-dimensional semiconductors for transistors**. *Nature Reviews Materials*, **1**:16052 EP –, 08 2016.

[75] HUALING ZENG, JUNFENG DAI, WANG YAO, DI XIAO, AND XIAODONG CUI. **Valley polarization in MoS2 monolayers by optical pumping**. *Nat Nano*, **7**(8):490–493, 08 2012.

[76] AARON M. JONES, HONGYI YU, NIRMAL J. GHIMIRE, SANFENG WU, GRANT AIVAZIAN, JASON S. ROSS, BO ZHAO, JIAQIANG YAN, DAVID G. MANDRUS, DI XIAO, WANG YAO, AND XIAODONG XU. **Optical generation of excitonic valley coherence in monolayer WSe2**. *Nat Nano*, **8**(9):634–638, 09 2013.

[77] F. WITHERS, O. DEL POZO-ZAMUDIO, S. SCHWARZ, S. DUFFERWIEL, P. M. WALKER, T. GODDE, A. P. ROONEY, A. GHOLINIA, C. R. WOODS, P. BLAKE, S. J. HAIGH, K. WATANABE, T. TANIGUCHI, I. L. ALEINER, A. K. GEIM, V. I. FALKO, A. I. TARTAKOVSKII, AND K. S. NOVOSELOV. **WSe2 Light-Emitting Tunneling Transistors with Enhanced Brightness at Room Temperature**. *Nano Letters*, **15**(12):8223–8228, 2015. PMID: 26555037.

[78] ZHUAN ZHU, JIANGTAN YUAN, HAIQING ZHOU, JONATHAN HU, JING ZHANG, CHENGLI WEI, FANG YU, SHUO CHEN, YUCHENG LAN, YAO YANG, YANAN WANG, CHAO NIU, ZHIFENG REN, JUN LOU, ZHIMING WANG, AND JIMING BAO. **Excitonic Resonant EmissionAbsorption of Surface Plasmons in Transition Metal Dichalcogenides for Chip-Level ElectronicPhotonic Integrated Circuits**. *ACS Photonics*, **3**(5):869–874, 2016.

[79] NAMPHUNG PEIMYOO, JINGZHI SHANG, CHUNXIAO CONG, XIAONAN SHEN, XIANGYANG WU, EDWIN K. L. YEOW, AND TING YU. **Nonblinking, Intense Two-Dimensional Light Emitter: Monolayer WS2 Triangles**. *ACS Nano*, **7**(12):10985–10994, 2013. PMID: 24266716.

[80] J.R. ALBANI. *Structure and Dynamics of Macromolecules: Absorption and Fluorescence Studies*. Elsevier Science, 2011.

[81] GOKI EDA AND STEFAN A. MAIER. **Two-Dimensional Crystals: Managing Light for Optoelectronics**. *ACS Nano*, **7**(7):5660–5665, 2013. PMID: 23834654.

[82] KIN FAI MAK, CHANGGU LEE, JAMES HONE, JIE SHAN, AND TONY F. HEINZ. **Atomically Thin MoS_2: A New Direct-Gap Semiconductor**. *Phys. Rev. Lett.*, **105**:136805, Sep 2010.

[83] WEIJIE ZHAO, ZOHREH GHORANNEVIS, LEIQIANG CHU, MINGLIN TOH, CHRISTIAN KLOC, PING-HENG TAN, AND GOKI EDA. **Evolution of Electronic Structure in Atomically Thin Sheets of WS2 and WSe2**. *ACS Nano*, **7**(1):791–797, 2013. PMID: 23256505.

[84] HUMBERTO R. GUTIÉRREZ, NESTOR PEREA-LÓPEZ, ANA LAURA ELÍAS, AYSE BERKDEMIR, BEI WANG, RUITAO LV, FLORENTINO LÓPEZ-URÍAS, VINCENT H. CRESPI, HUMBERTO TERRONES, AND MAURICIO TERRONES. **Extraordinary Room-Temperature Photoluminescence in Triangular WS2 Monolayers**. *Nano Letters*, **13**(8):3447–3454, 2013. PMID: 23194096.

[85] ATTILA SZABO AND NEIL S. OSTLUND. *Modern Quantum Chemistry: Introduction to Advanced Electronic Structure Theory*. Dover Publications, 1996.

[86] W. KOHN AND L. J. SHAM. **Self-Consistent Equations Including Exchange and Correlation Effects**. *Physical Review*, **140**(4A):A1133–A1138, nov 1965.

[87] C FIOLHAIS, F NOGUEIRA, AND MAL MARQUES. *A primer in density functional theory*. Springer, 1st edition, 2003.

[88] J. P. PERDEW. **Self-interaction correction to density-functional approximations for many-electron systems**. *Physical Review B*, **23**(10):5048–5079, May 1981.

[89] JOHN P. PERDEW AND YUE WANG. **Accurate and simple analytic representation of the electron-gas correlation energy**. *Physical Review B*, **45**(23):13244–13249, June 1992.

[90] ERICH RUNGE AND E. K. U. GROSS. **Density-Functional Theory for Time-Dependent Systems**. *Physical Review Letters*, **52**(12):997–1000, mar 1984.

[91] JOHN P. PERDEW, KIERON BURKE, AND MATTHIAS ERNZERHOF. **Generalized Gradient Approximation Made Simple**. *Physical Review Letters*, **77**(18):3865–3868, October 1996.

[92] JOHN P. PERDEW, KIERON BURKE, AND MATTHIAS ERNZERHOF. **Generalized Gradient Approximation Made Simple [Phys. Rev. Lett. 77, 3865 (1996)]**. *Physical Review Letters*, **78**(7):1396–1396, February 1997.

[93] JOHN P. PERDEW, KOBLAR A. JACKSON, MARK R. PEDERSON, D. J. SINGH, AND CARLOS FIOLHAIS. **Atoms, molecules, solids, and surfaces: Applications of the generalized gradient approximation for exchange and correlation**. *Physical Review B*, **46**(11):6671–6687, September 1992.

[94] ERICH RUNGE AND E. K. U. GROSS. **Density-Functional Theory for Time-Dependent Systems**. *Physical Review Letters*, **52**(12):997–1000, March 1984.

[95] ROBERT VAN LEEUWEN. **Mapping from Densities to Potentials in Time-Dependent Density-Functional Theory**. *Physical Review Letters*, **82**(19):3863–3866, May 1999.

[96] CARSTEN A. ULLRICH. *Time-Dependent Density-Functional Theory*. Oxford University Press, dec 2011.

[97] HARTMUT HAUG AND ANTTI-PEKKA JAUHO. *Quantum Kinetics in Transport and Optics of Semiconductors*, **123** of *Solid-State Sciences*. Springer Berlin Heidelberg, Berlin, Heidelberg, 2008.